

DOT/FAA/TCTT-25/25

Federal Aviation Administration
William J. Hughes Technical Center
Aviation Research Division
Atlantic City International Airport
New Jersey 08405

Development of a Titanium Alloy Ti-6Al-4V Generalized Yield Surface Material Model Used in LS-DYNA

June 2025

Technical Thesis

The research described in this report was funded by the FAA as part of its mission to improve aircraft safety. The views and opinions expressed are those of the author alone and do not necessarily represent the views of the FAA. The FAA assumes no liability for the contents or use thereof. The FAA has not edited or modified the contents of the report in any manner.



U.S. Department of Transportation
Federal Aviation Administration

NOTICE

This document is disseminated under the sponsorship of the U.S. Department of Transportation in the interest of information exchange. The U.S. Government assumes no liability for the contents or use thereof. The U.S. Government does not endorse products or manufacturers. Trade or manufacturers' names appear herein solely because they are considered essential to the objective of this report. The findings and conclusions in this report are those of the author(s) and do not necessarily represent the views of the funding agency. This document does not constitute FAA policy. Consult the FAA sponsoring organization listed on the Technical Documentation page as to its use.

This report is available at the Federal Aviation Administration William J. Hughes Technical Center's Full-Text Technical Reports page: actlibrary.tc.faa.gov in Adobe Acrobat portable document format (PDF).

Form DOT F 1700.7 (8-72)

Reproduction of completed page authorized

1. Report No. DOT/FAA/TCTT-25/25		2. Government Accession No.		3. Recipient's Catalog No.	
4. Title and Subtitle Development of a Titanium Alloy Ti-6Al-4V Generalized Yield Surface Material Model Used in LS-DYNA				5. Report Date June 2025	
				6. Performing Organization Code	
7. Author(s) Fabrizio Ragone				8. Performing Organization Report No.	
9. Performing Organization Name and Address George Mason University Center for Collision Safety and Analysis 4087 University Drive, Fairfax, VA 22030 USA				10. Work Unit No. (TRAIS)	
				11. Contract or Grant No. 692M152340003	
12. Sponsoring Agency Name and Address Federal Aviation Administration Aircraft Certification Service Policy and Innovation Division (AIR-600) 800 Independence Avenue SW Washington, DC 20591				13. Type of Report and Period Covered Technical Thesis	
				14. Sponsoring Agency Code AIR-625	
15. Supplementary Notes The FAA William J. Hughes Technical Center Aviation Research Division COR was Daniel Cordasco.					
16. Abstract This thesis is part of a collaborative effort involving George Mason University (GMU), The Ohio State University (OSU), the National Aeronautics and Space Administration (NASA) Glenn Research Center (GRC), and the Federal Aviation Administration (FAA) under the Aircraft Catastrophic Failure Prevention Program (ACFPP). The primary objective of this research is to address the challenge of uncontained turbine engine failure by developing material models in LS-DYNA that can accurately predict fragment impact and penetration of engine and aircraft structure in the event of failure. The focus of this work is material characterization of Ti-6Al-4V manufactured from a 0.5" thick plate, a material frequently used in the fan and compressor section of aircraft turbines. This study aims to create a Ti-6Al-4V model using the *MAT_224_GYS material model in the LS-DYNA explicit finite element analysis software. Coupon level test data was used to create strain rate and temperature dependent plasticity curves in both tension and compression. A triaxiality and Lode parameter dependent failure surface was also generated from an extensive series of fracture test specimens. The *MAT_224_GYS constitutive model describes the plasticity and ductile fracture behavior of metals as a function of stress state, strain rate, and temperature with a J3 dependent yield surface. It employs an isotropic and isochoric generalized yield function, with stress-state-dependent hardening. This allows for consideration of tensile and compressive asymmetry in the material response which is essential for hexagonal close packed metals like Ti-6Al-4V. The distortional hardening (stress-state dependent hardening) accounts for strain rate and thermal effects through tabulated input curves that define the yield dependence on strain rate and temperature. Additionally, the model incorporates adiabatic heating resulting from plastic deformation, leading to thermal softening effects. This thesis documents the integration of experimental data into the LS-DYNA material model input, providing a robust foundation for future applications in turbine engine fragment impact analysis.					
17. Key Words LS-DYNA, Ti-6Al-4V, MAT_224_GYS, Material Characterization, Turbine Engine Failure, Plasticity, Yield Surface, Failure Surface, Strain Rate, Impact, Simulation, Finite Element, Triaxiality, Lode, Ductile Fracture			18. Distribution Statement This document is available to the U.S. public through the National Technical Information Service (NTIS), Springfield, Virginia 22161. This document is also available from the Federal Aviation Administration William J. Hughes Technical Center at actlibrary.tc.faa.gov .		
19. Security Classif. (of this report) Unclassified		20. Security Classif. (of this page) Unclassified		21. No. of Pages 195	
				22. Price	



POLITECNICO
MILANO 1863

SCUOLA DI INGEGNERIA INDUSTRIALE
E DELL'INFORMAZIONE

Development of a Titanium Alloy Ti-6Al-4V Generalized Yield Sur- face Material Model Used in LS- DYNA

TESI DI LAUREA MAGISTRALE IN
AERONAUTICAL ENGINEERING - INGEGNERIA AERONAUTICA

Author: **Fabrizio Ragone**

Student ID: 221517

Advisor: Prof. Marco Anghileri

Co-advisors: Prof. Stefano Dolci

Academic Year: 2024-25

Ai miei genitori, Alba e Rodolfo.

A mio fratello Riccardo.

Abstract

This thesis is part of a collaborative effort involving George Mason University (GMU), Ohio State University (OSU), NASA Glenn Research Center(GRC), and the Federal Aviation Administration (FAA) under the Aircraft Catastrophic Failure Prevention Research Program (ACFPR). The primary objective of this research is to address the challenge of uncontained turbine engine failure by developing material models in LS-DYNA to support the FAA's certification-by-analysis initiative.

The focus of this work is the material characterization of Ti-6Al-4V, a material that represents the fragments impacting the engine casing in the event of turbine engine failure. This study aims to create a plasticity model and a failure surface using the *MAT_224_GYS material model.

The constitutive model describes the plastic behavior of metals as a function of stress state, strain rate, and temperature. It employs an isotropic and isochoric generalized yield function , with stress-state-dependent hardening. The distortional hardening (stress-state-dependent hardening) accounts for strain rate and thermal effects through tabulated input curves that define the yield dependence on strain rate and temperature. Additionally, the model incorporates adiabatic heating resulting from plastic deformation, leading to thermal softening effects.

By improving the accuracy of material modeling, this research contributes to the reduction of costly physical testing in favor of simulations. The ability to replace expensive experimental tests with reliable simulations supports a more cost-effective and efficient approach to aerospace certification processes. This thesis documents the integration of experimental data into the LS-DYNA material model input, providing a robust foundation for future applications in turbine engine failure analysis and certification.

Keywords: LS-DYNA, Ti-6Al-4V, Material Characterization, Turbine Engine Failure, Plasticity, Yield Surface, Failure Surface, High Strain Rate Analysis, Titanium Alloy.

Abstract in lingua italiana

Questa tesi è parte di un progetto di ricerca collaborativo che coinvolge la George Mason University (GMU), l'Ohio State University (OSU), il NASA Glenn Research Center (GRC) e la Federal Aviation Administration (FAA), nell'ambito del programma Aircraft Catastrophic Failure Prevention Research Program (ACFPR). L'obiettivo principale di questa ricerca è affrontare il problema del guasto non contenuto dei motori a turbina, sviluppando dei modelli di materiale in LS-DYNA per supportare l'iniziativa della FAA di certificazione attraverso l'analisi.

Il lavoro si concentra sulla caratterizzazione del materiale Ti-6Al-4V, un materiale utilizzato in ambito aeronautico e che rappresenta i frammenti che impattano il casing del motore a turbina in caso di guasto. Lo scopo di questo studio è la creazione di un modello di plasticità e di una superficie di rottura, utilizzando il modello *MAT_224_GYS. Il modello costitutivo descrive il comportamento plastico dei metalli in funzione dello stato di sforzo, della velocità di deformazione e della temperatura. Esso si basa su una funzione di snervamento generalizzata, isotropa e isocora, con un indurimento distorsionale. Vengono considerati gli effetti della velocità di deformazione e della temperatura mediante curve tabulate che definiscono la dipendenza del limite di snervamento da questi parametri. Inoltre, il modello include il riscaldamento adiabatico dovuto alla deformazione plastica, con conseguente riduzione della resistenza meccanica per effetti termici.

Attraverso il miglioramento della modellazione del materiale, questa ricerca contribuisce a ridurre la necessità di costosi test sperimentali, privilegiando l'uso di simulazioni. La possibilità di sostituire i test sperimentali con simulazioni affidabili rappresenta un approccio più economico ed efficiente per i processi di certificazione aerospaziale.

La tesi documenta inoltre l'integrazione dei dati sperimentali nel modello di materiale LS-DYNA, offrendo una solida base per future applicazioni nell'analisi dei guasti dei motori a turbina e nei processi di certificazione.

Parole chiave: LS-DYNA, Ti-6Al-4V, Caratterizzazione del materiale, Guasto del motore a turbina, Plasticità, Superficie di snervamento, Superficie di rottura, Analisi ad alti tassi di deformazione, Lega di titanio.

Contents

Abstract	iii
Abstract in lingua italiana	v
Contents	vii
Introduction	1
1 Literature Review	5
1.1 Titanium Alloys in Aerospace Applications	5
1.1.1 Titanium for Airframes	5
1.1.2 Titanium for Engines	6
1.1.3 Properties required for Titanium material in aircrafts	6
1.2 Material Stress-Strain Response and Fracture Behaviour	8
1.3 Material Modeling of Ti-6Al-4V 0.5 inch plate	11
2 Methodology for Material Model Creation	13
2.1 Material Model	14
2.1.1 Material Properties	14
2.1.2 Material Properties	14
2.1.3 Plasticity and Yield Stress Tables	14
2.1.4 Failure Criteria Tables	15
2.1.5 Thermal Effects and Energy Dissipation	15
2.1.6 Numerical Controls and Element Erosion	16
2.2 Stress-Strain Relationship	16
2.2.1 Revisiting Common Elastic-Plastic Modeling	16
2.2.2 Violations of Common Assumptions	19
2.2.3 Stress-Strain Relationship after Necking	21
2.3 Differences for Compression Tests	26

2.4	Isothermal Effects	26
2.5	Strain Rate Dependency	26
2.5.1	Tabulated Input	26
2.5.2	Strain Rate is not a Constant	27
2.5.3	High Strain-Rate Sensitivity	29
2.6	Conversion of Plastic Work into Heat (Taylor-Quinney Effect)	31
3	Material Model Creation by Simulation of Mechanical Property Tests	33
3.1	Test Data	33
3.2	Computational Infrastructure for LS-DYNA Simulations	36
3.3	Temperature Effect	37
3.3.1	Tension	38
3.3.2	Compression	46
3.4	Stress strain relationship at a single, nominal quasi-static strain rate	52
3.4.1	Tension	52
3.4.2	Compression	56
3.5	Stress strain tabulated input of multiple strain rates and temperatures . .	57
3.5.1	Tension	60
3.5.2	Compression	73
4	Methodology for Failure Model Creation	83
4.1	Failure Surface Overview	83
4.2	Failure Surface Generation	84
5	Failure Model Creation by Simulation of Mechanical Property Tests	89
5.1	Test specimen descriptions	90
5.1.1	SG1—Plane Stress Specimen (Pure Tension)	90
5.1.2	SG2—Plane Stress Specimen	91
5.1.3	SG3—Plane Stress Specimen	92
5.1.4	SG4—Plane Stress Specimen	92
5.1.5	SG5—Axisymmetric Specimen (Pure Tension)	93
5.1.6	SG6—Axisymmetric Specimen	94
5.1.7	SG7—Axisymmetric Specimen	94
5.1.8	SG8—Axisymmetric Specimen.	95
5.1.9	SG9—Axisymmetric Specimen	96
5.1.10	SG10—Axisymmetric Specimen	96
5.1.11	SG11—Plane Strain Specimen	97
5.1.12	SG12—Plane Strain Specimen	98

5.1.13	SG13—Plane Strain Specimen	99
5.1.14	LR1 – Combined (Tension/Torsion) Specimen	100
5.1.15	LR2 – Combined (Tension/Torsion) Specimen	101
5.1.16	LR3 – Torsion Specimen	101
5.1.17	LR4 – Combined (Compression/Torsion) Specimen	101
5.1.18	Punch: Unbacked	102
5.1.19	Punch: Backed tests	103
5.2	Simulation results of mechanical property tests	105
5.2.1	Failure surface generation	121
5.2.2	Simulation results with failure surface	122
5.3	Creation of a Temperature Scaling function	128
5.4	Creation of a Strain Rate Scaling function	130
5.5	Creation of an Element Size fracture regularization curve	133
6	Validation of the Model	137
6.1	NASA Ballistic Test Series	137
6.1.1	Adiabatic Shear Band	140
7	Conclusions and Future Developments	141
	Bibliography	143
A	Digital Image Correlation	147
A.1	Working Principle	147
A.2	Differences in SHPB Testing for Tensile and Compression Tests	147
A.3	DIC in Tensile and Compression Testing	148
A.4	Advantages and Limitations	149
A.5	DIC for Strain and Displacement Calculation	149
B	Split-Hopkinson Pressure Bar	151
B.1	Differences in SHPB Testing for Tensile and Compression Tests	151
B.1.1	Compression Testing with the SHPB	152
B.1.2	Tensile Testing with the SHPB	152
B.1.3	Material Behavior Under High Strain Rates	153
B.1.4	Geometrical Considerations	153

C Convexity Algorithm of the GYS Model	155
D Material Property Summary	157
E Vendor-Supplied Material Certifications	159
List of Figures	167
List of Tables	173
List of Symbols	175
List of Abbreviations	177
Acknowledgments	179

Introduction

The plastic behavior of materials has posed significant challenges for engineers and researchers over many decades. The sustained interest in this topic arises from its direct relevance to a wide range of engineering applications. Accurately predicting plastic deformation becomes particularly complex when materials are subjected to complex mechanical loading conditions, such as multi-axial stress states, high strain rates, and variable temperature conditions. The precise representation of stress, strain, and temperature fields within structural components is heavily dependent on the mathematical models or constitutive equations used to describe the plastic behavior of these materials.

Understanding the dynamic plastic deformation characteristics of materials is essential for the design of optimized engineering products. For several decades, one of the most critical areas of research in mechanics has been the design of lighter, more cost-effective structures capable of withstanding impact loading, without compromising structural performance, safety, or integrity. Applications involving dynamic plastic deformation and failure extend to various fields, including aircraft safety, spacecraft shielding, high-speed machining, and armor penetration. Specific examples of ductile dynamic deformation and failure applications include automotive crashworthiness, protection against uncontained engine debris in aerospace applications, fan blade containment during blade-out events, and defense-armor penetration.

Uncontained turbine engine debris presents a significant risk to aircraft, where high-energy fragments impacting the aircraft must be carefully considered. Damage from an engine rotor burst can be catastrophic, compromising structural integrity, initiating fires, endangering critical systems, and potentially resulting in loss of life.

As a result, there has been significant interest in methods that can improve the understanding of such events and enhance aircraft designs. Following a catastrophic uncontained fan disk failure in commercial passenger service in 1989, the Federal Aviation Administration (FAA) initiated the Uncontained Engine Debris Mitigation Program, part of the Aircraft Catastrophic Failure Prevention Program. This research program aimed to investigate methods for analyzing and mitigating uncontained engine debris. While absolute containment is understood to be unlikely, efforts have focused on minimizing

fragment energies and developing effective mitigation strategies within the aircraft. In addition, civil aviation authorities require that turbine engines in civil service be designed to contain the release of any single fan, compressor, or turbine blade. To demonstrate compliance, 14 CFR (Code of Federal Regulations) 33.94 mandates that every new civil engine design be tested to prove that the highest-energy blade will be contained. Once the containment of the highest-energy blade is successfully demonstrated, the other stages of the engine are certified through analysis. Due to the high cost, difficulty, and time demands of performing such tests, engine manufacturers aim to ensure that a new engine will pass the containment test on the first attempt. As a result, predictive numerical models and analyses of containment structures are used during the design process to minimize the risk of having to repeat the blade containment test.



Figure 1: Fan blade-off test of the Trent XWB.

Computational mechanics has evolved significantly, allowing for the efficient and accurate prediction of structural performance under impact loading when appropriate numerical techniques and material models are employed. A substantial body of literature exists concerning the assessment of dynamic plastic deformation and failure in the impact performance evaluation of aerospace materials and their ability to mitigate risks from uncontained engine debris. One widely used material model for simulating impact and penetration is the Johnson-Cook plasticity and fracture model, which defines the effective material flow stress as a function of strain rate, temperature, and effective plastic strain. However, the Johnson-Cook model does not differentiate between yielding in uniaxial ten-

sion and yielding in uniaxial compression. This implies that the model relies on classical J2 (Second Stress Tensor Invariant) plasticity and cannot capture yielding asymmetry or the strain-rate-dependent effect in uniaxial tension, uniaxial compression, or pure-shear stress states. To adequately model the deviations from classical J2 plasticity, a Generalized Yield Surface (GYS) is necessary. This modification ensures that the material model appropriately accounts for the stress-state dependence of initial yielding and subsequent plastic flow, improving its accuracy in simulating scenarios involving uncontained engine debris.

George Mason University (GMU), Ohio State University (OSU), NASA Glenn Research Center, and Federal Aviation Administration (FAA) - Aircraft Catastrophic Failure Prevention Research Program (ACFPR) has collaborated to develop new material models in LS-DYNA to support the FAA initiative on certification by analysis.

In this framework, this thesis is dedicated to the material characterization of the half-inch Ti-6Al-4V plate using the `*MAT_224_GYS` material model, addressing the asymmetry in its behavior in tension and compression.

1 | Literature Review

1.1. Titanium Alloys in Aerospace Applications

Commercially pure titanium and its alloys have emerged as fundamental materials in the aerospace industry due to their advantageous combination of low density, high mechanical strength and exceptional resistance to corrosion. In recent years, the utilization of Carbon Fiber Reinforced Plastics (CFRP) in airframe structures and engine components has significantly increased, primarily to enhance fuel efficiency. Consequently, the demand for titanium has also escalated, given its superior compatibility with CFRP in terms of corrosion resistance and thermal expansion properties [23].

The application of titanium has been particularly notable in modern fuel-efficient aircraft, such as the Airbus A350XWB, where the incorporation of CFRP is extensive. In this aircraft model, the titanium content has more than doubled in comparison to conventional designs.



Figure 1.1: Airbus A350 XWB.

1.1.1. Titanium for Airframes

The evolution of airframe structures has progressed significantly, transitioning through aluminum alloys to the current dominance of Carbon Fiber Reinforced Plastics (CFRP).

Simultaneously, high-strength sections such as frames and joints, once made of steel, have increasingly been replaced by titanium alloys, ensuring substantial weight reduction while maintaining structural integrity [46].

The integration of heterogeneous materials within an airframe demands meticulous design considerations to prevent galvanic corrosion caused by differences in electrochemical potential and to mitigate strain induced by varying coefficients of thermal expansion. As CFRP has become the primary structural material in modern aircraft, titanium alloys, which exhibit similar physical characteristics, have seen growing adoption in aerospace applications.

1.1.2. Titanium for Engines

Turbofan engines are composed of four primary sections, arranged sequentially from front to rear: the fan, compressor, combustion chamber, and turbine. Titanium alloys are predominantly employed in the fan and compressor sections, where operating temperatures remain relatively moderate (below 600°C), ensuring an optimal balance of strength, weight reduction, and corrosion resistance. Conversely, the turbine and combustion chamber, which are subjected to significantly higher temperatures, necessitate the use of nickel- or iron-based superalloys to withstand the extreme thermal and mechanical stresses encountered in these regions [38].

1.1.3. Properties required for Titanium material in aircrafts

Titanium alloys employed in airframes vary depending on the structural requirements of specific components. For instance, Ti-6Al-4V, an alloy composed of 6% aluminum (Al) and 4% vanadium (V) by weight, is commonly used in cockpit window frames, wing boxes, and fasteners. Other titanium alloys, such as Ti-3Al-2.5V, Ti-10V-2Fe-3Al, and Ti-15V-3Cr-3Sn-3Al, are used for hydraulic pipes, landing gear components, and structural ducts, respectively, owing to their optimized mechanical properties. The reduction of airframe maintenance costs can be effectively achieved through the use of materials exhibiting superior fatigue strength, resistance to crack propagation, high fracture toughness, and excellent corrosion resistance. Titanium alloys have become a material of choice in aerospace applications due to their exceptional mechanical properties and their compatibility with Carbon Fiber Reinforced Plastics (CFRP). This compatibility has further facilitated their widespread adoption in modern aircraft structures.

In aircraft engines, titanium alloys with enhanced strength and thermal resistance are preferred over commercially pure titanium. While aluminum alloys with high specific

strength are generally unsuitable for engine applications due to their sharp decline in mechanical properties above 200°C , titanium alloys retain superior strength-to-weight ratios even at elevated temperatures. Specifically, in the temperature range of $500\text{--}600^{\circ}\text{C}$, titanium alloys exhibit better specific strength than nickel-based superalloys, making them highly advantageous in aerospace applications [34].

Given the relatively moderate temperatures surrounding fan blades, Ti-6Al-4V is widely employed due to its superior specific strength and fatigue resistance. In small and medium-sized aircraft engines, solid forged fan blades are commonly used, whereas in larger engines, hollow fan blades are preferred to reduce overall weight while maintaining structural integrity. The fan disc, which secures the fan blades, is a critical safety component requiring materials with both high strength and toughness. As a result, titanium alloys such as Ti-6Al-4V and Ti-17 (Ti-5Al-2Sn-2Zr-4Cr-4Mo) are extensively utilized.



Figure 1.2: Rolls-Royce Trent 900 fan blades.

As temperatures in high-pressure compressors exceed those in low-pressure compressors, the selection of high-strength, heat-resistant materials becomes crucial. Ti-6Al-4V is typically used for low-pressure compressor blades, whereas high-pressure compressor components demand alloys with superior strength, fatigue resistance, and toughness at elevated temperatures. Examples include Ti-8Al-1Mo-1V and Ti-6Al-2Sn-4Zr-6Mo, which offer excellent high-temperature mechanical properties. Compressor discs, which must withstand high mechanical stresses and cyclic loading, require alloys with exceptional low-cycle fatigue and creep resistance. Consequently, Ti-6Al-2Sn-4Zr-2Mo-0.1Si and Ti-6Al-2Sn-4Zr-6Mo are commonly employed due to their superior thermal resistance and

durability [16].

The continued advancement of titanium alloys in aerospace applications is driven by their outstanding combination of lightweight properties, high strength, corrosion resistance, and compatibility with CFRP. As aircraft design evolves towards greater efficiency and durability, the role of titanium alloys in both structural and propulsion systems is expected to expand further.

1.2. Material Stress-Strain Response and Fracture Behaviour

Material stress-strain response and fracture behavior have been shown to depend on stress triaxiality [3, 22, 31], strain rate [26, 42], and temperature [27]. To model these effects, Johnson and Cook [24] developed a phenomenological material model that accounts for strain hardening, strain rate sensitivity, and thermal softening in plastic deformation, as described by the following equation:

$$\sigma = [A + B(\varepsilon_p)^n] [1 + C \ln(\dot{\varepsilon})] [1 - (T_H)^m], \quad (1.1)$$

where σ represents the equivalent true stress, ε_p is the equivalent plastic strain, and $\dot{\varepsilon}_p$ is the equivalent plastic strain rate. The term T_H represents the homologous temperature, defined as:

$$T_H = \frac{T - T_{ref}}{T_{melt} - T_{ref}}, \quad (1.2)$$

where T is the material temperature, T_{ref} is the reference temperature (commonly room temperature), and T_{melt} is the melting temperature. The parameters A , B , C , m , and n are material-specific constants that allow the model to be calibrated to experimental data. The first term in brackets accounts for strain hardening, the second for strain rate sensitivity, and the third for thermal softening.

Johnson and Cook further extended their plasticity model to predict fracture by introducing a damage parameter that accounts for the influence of stress triaxiality, strain rate, and temperature on the equivalent plastic strain at failure [24]. The damage accumulation is represented as:

$$D = \sum \frac{\Delta \varepsilon}{\varepsilon_p^f} \quad (1.3)$$

where D is the damage parameter, $\Delta \varepsilon$ is the increment of equivalent plastic strain per numerical integration cycle, and ε_p^f is the equivalent plastic strain at failure. The failure strain is expressed as:

$$\varepsilon_p^f = [D_1 + D_2 \exp(D_3 \tau)] [1 + D_4 \ln(\dot{\varepsilon})] [1 + D_5 T_H] \quad (1.4)$$

where τ is the stress triaxiality, defined as the ratio of mean stress to von Mises stress, and D_1, D_2, D_3, D_4 , and D_5 are material parameters. Damage accumulates over the simulation as plastic deformation progresses, and failure occurs when D reaches unity. Since ε_p^f is a function of stress triaxiality, strain rate, and temperature, its value varies dynamically during the simulation. An increase in ε_p^f results in a smaller damage increment per cycle, slowing the damage accumulation, while a decrease in ε_p^f leads to a faster accumulation of damage. This formulation allows the model to capture the effects of loading history on failure prediction.

A key limitation of the Johnson-Cook model [24] is that it is capable of scaling the magnitude of the stress-strain curves to incorporate strain rate and thermal effects. However it's not able to represent a change in the shape of the stress-strain curve.[40]. Another problem is its assumption that the fracture strain decreases exponentially with increasing triaxiality. Nevertheless, experimental results indicate that this is not universally valid. For instance, it has been observed that in tests on 2024 Aluminum, the fracture strain initially decreases with increasing triaxiality from a negative value to zero, then rises to a local peak at a triaxiality of 0.4 before decreasing again at higher triaxialities [2]. This behavior is too complex to be represented by the Johnson-Cook model.

To overcome this shortcoming, Bao and Wierzbicki [3] proposed dividing the triaxiality domain into three segments and fitting separate mathematical functions to each. Another alternative involves considering the effect of shear stress through the introduction of a deviatoric state parameter. Barsoum and Faleskog [5] employed the Lode parameter, μ , which is derived from the principal stresses:

$$\mu = \frac{2\sigma_2 - \sigma_1 - \sigma_3}{\sigma_1 - \sigma_3}. \quad (1.5)$$

Similarly, Wierzbicki et al. [45] introduced an alternative Lode parameter, L , defined in

terms of the third invariant of the deviatoric stress tensor:

$$L = \frac{27}{2} \frac{J_3}{\sigma_{vm}^3} \quad (1.6)$$

where J_3 is the third invariant of the deviatoric stress tensor.

The triaxiality parameter quantifies the proportion of hydrostatic tension or compression, influencing void growth and coalescence rates, while the Lode parameter determines the role of shear stresses in material failure mechanisms [22, 31]. When fracture strain is expressed as a function of both triaxiality and Lode parameter, it forms a three-dimensional fracture surface. The construction of such a surface necessitates experimental determination of the fracture strain over a wide range of stress states, including uniaxial tension, compression, torsion, and combined loading conditions [3–5, 45].

One approach to defining a fracture surface is to fit experimental data points to predefined mathematical formulations, as in the extended Mohr-Coulomb and Hosford-Coulomb models [1, 33]. This method requires relatively few tests but is constrained by the limitations of the governing equations. An alternative approach is to interpolate between tabulated experimental data points, as implemented in LS-DYNA's `*MAT_224` material model [21]. This interpolation enables a more detailed representation of material behavior but demands extensive testing across a broad range of stress states. Notably, `*MAT_224` adopts a convention where positive triaxiality corresponds to compression, which contrasts with the convention used in many other studies.

Beyond fracture modeling, `*MAT_224` allows for tabulated input of stress-strain curves at different strain rates and temperatures [21]. Unlike conventional mathematical models such as Johnson-Cook, which only scale the hardening curve, `*MAT_224` enables the representation of strain rate and temperature-dependent changes in the curve's shape.

To accurately calibrate material models for strain rate sensitivity, testing must be performed at various strain rates. Strain rates between 10^{-4} s^{-1} and 1 s^{-1} are typically achieved using hydraulic or servo-hydraulic load frames, while higher rates in the range of 10^1 to 10^2 s^{-1} require specialized equipment, such as modified split-Hopkinson bar (SHB) apparatus [19, 27]. For strain rates around 10^3 s^{-1} , conventional SHB experiments are commonly used [26].

1.3. Material Modeling of Ti-6Al-4V 0.5 inch plate

During the experimental characterization of the 0.5 inch Titanium Alloy Ti-6Al-4V plate conducted at Ohio State University (OSU), it became evident that the material exhibited an asymmetry in tensile and compressive yield. At the microscopic level, the observed anisotropy is believed to originate during the grain refinement process occurring in rolling, which introduces a visible directional dependence. Variations in the rolling process lead to differences in microstructure, ultimately affecting the material properties [44]. Moreover, metals such as magnesium and titanium alloys possess a hexagonal close-packed (HCP) crystal structure, which often results in a more pronounced strength differential due to different dominant plastic deformation mechanisms compared to face-centered cubic (FCC) metals, such as aluminum, or body-centered cubic (BCC) metals, such as steel [10]. Traditional isotropic material models can be calibrated to fit either tensile or compressive behavior, but not both simultaneously. In impact analysis, it is crucial to accurately capture both tension and compression in order to correctly predict deformation and failure across different impact velocities and projectile geometries. It was determined that a model based on J_2 plasticity could not accurately capture the plastic response observed under both tensile and compressive loading. Consequently, the development of a material model incorporating a J_3 (third deviatoric stress invariant) dependent yield surface was necessary.

The `*MAT_224_GYS` model retains the same fundamental structure as `*MAT_224`, but extends its capability by allowing input parameters to be specified separately for tension, compression, and shear. Unlike `*MAT_224`, which requires only two tables to define the rate- and temperature-dependent stress-strain behavior, `*MAT_224_GYS` introduces six independent input tables, each defining material behavior under tension, compression, and shear across varying rates and temperatures. Additionally, the model incorporates an internal convexity check routine to ensure a physically valid yield surface. If the yield surface, derived from the specified tensile, compressive, and shear yield stresses, lacks convexity, the model automatically adjusts the input curves to enforce a convex yield surface. Without this constraint, non-unique solutions could arise. If any of the six input tables is omitted, the model assumes isotropic behavior in the corresponding loading direction, filling the missing data automatically [8].

`*MAT_224_GYS` incorporates strain rate and temperature sensitivity, element regularization, and a failure surface defining plastic failure strain as a function of triaxiality and the Lode parameter.

2 | Methodology for Material Model Creation

The variation in measured properties of Ti-6Al-4V are influenced by various factors , such as manufacturing and post-processing procedures, or the test specimen's orientation relative to the plate's grain direction, among others. To reduce some of these differences, the Ti-6Al-4V material examined here is a 1/2-inch plate, produced by a single company (refer to Appendix E).

The 0.5-inch plate of Titanium Alloy Ti-6Al-4V exhibits tension-compression asymmetry in its plastic deformation behavior. Classical continuum mechanics does not predict an asymmetric isotropic flow law for metals, as conventional isotropic material models are typically capable of fitting only either tension or compression, but not both simultaneously. In the context of impact analysis, it is essential to accurately capture both tension and compression to predict the deformation and failure of materials subjected to various impact velocities and projectile shapes. To achieve this, the rate and temperature-dependent hardening law must be defined independently for the tension and compression directions.

At the microscopic level, the anisotropy is believed to originate during the grain refinement process in rolling, where a directional difference in material properties is evident. Variations in the rolling process lead to differences in the microstructure, which in turn result in disparities in the material's properties.

The 1/2-inch rolled Ti-6Al-4V plate is modeled using `*MAT_224_GYS` in LS-DYNA. The `*MAT_224_GYS` model is an isotropic elasto-visco-plasticity model with a J3-dependent yield surface (Third Stress Tensor Invariant). By utilizing J3 instead of J2 flow theory, this model facilitates the inclusion of tensile/compressive asymmetry in the material's response.

2.1. Material Model

The MAT_224_GYS model in LS-DYNA is an isotropic elastic-plastic material law with a J3-dependent yield surface. This material model accounts for tensile/compressive asymmetry, which is crucial for HCP metals like Ti-6Al-4V. The model supports solid elements and requires several input tables to define material behavior under different conditions. These tables control yield stress, failure criteria, thermal effects, and numerical stability.

	MID	RO	E	PR	CP	TR	BETA	NUMINT
1						0.0	1.0	1.0
2	LCK1	LCKT	LCF	LCG	LCH	LCI		
	0	0	0	0	0	0		
3	LCCR	LCCT	LCSR	LCST	IFLAG	SFIEPM	NITER	
					0	1.0	100.0	

Figure 2.1: MAT_224_GYS Model Definition.

2.1.1. Material Properties

2.1.2. Material Properties

- RO: Density.
- E: Young Modulus.
- PR: Poisson Ratio.

2.1.3. Plasticity and Yield Stress Tables

These tables define the material's elastic-plastic response under various loading conditions:

- LCK1: Strain Rate-Dependent Yield Stress (Table):
Defines, for each plastic strain rate, a load curve specifying the effective stress as a function of plastic strain.
- LCKT: Temperature-Dependent Yield Stress (Table):
Defines, for each temperature, a load curve specifying the effective stress as a function of plastic strain.
- LCCR: Compressive Yield Stress (Table):
Defines the compressive yield stress as a function of plastic strain or effective plastic

strain.

- **LCCT: Temperature-Dependent Compressive Yield Stress (Table):**
Defines compressive yield stress as a function of temperature.
- **LCSR: Shear Yield Stress (Table):**
Defines the shear yield stress as a function of plastic strain or effective plastic strain.
- **LCST: Temperature-Dependent Shear Yield Stress (Table):**
Defines shear yield stress as a function of temperature.

2.1.4. Failure Criteria Tables

These tables govern material failure under different loading conditions:

- **LCF: Triaxiality-Dependent Failure Strain (Curve/Table):**
Defines plastic failure strain as a function of triaxiality. Can be defined via a table for different Lode parameter values.
- **LCG: Strain Rate-Dependent Failure Strain (Curve):**
Defines plastic failure strain as a function of strain rate.
- **LCH: Temperature-Dependent Failure Strain (Curve):**
Defines plastic failure strain as a function of temperature.
- **LCI: Element Size-Dependent Failure Strain (Curve/Table):**
Defines plastic failure strain as a function of element size.

2.1.5. Thermal Effects and Energy Dissipation

These parameters and tables control how plastic work is converted into heat:

- **BETA: Taylor-Quinney Coefficient:**
Defines the fraction of plastic work converted into heat. Can be a constant or a table dependent on strain rate, temperature, and plastic strain.
- **CP: Specific Heat.**
- **TR: Room Temperature:**
Sets the initial temperature of the material.

2.1.6. Numerical Controls and Element Erosion

- **NUMINT:** Integration Point-Based Element Deletion:
Specifies how many integration points must fail before the element is deleted.
- **IFLAG:** Plastic Strain Definition for LCCR, LCCT, LCSR, LCST:
0: Compressive and shear yield stresses are defined as functions of plastic strain. 1: Defined as functions of effective plastic strain.
- **SFIEPM:** Plastic Multiplier Scaling Factor:
Adjusts the initial plastic multiplier estimation.
- **NITER:** Secant Iterations:
Controls the number of secant iterations in the numerical solution.

2.2. Stress-Strain Relationship

Accurately modeling materials requires a realistic stress-strain relationship. This report begins by discussing some common issues that can limit the accuracy of traditional material modeling methods, followed by an overview of the approach taken to model the titanium alloy Ti-6Al-4V.

The input parameters presented in this thesis in the units [mm], [ms], [kg], [kN].

2.2.1. Revisiting Common Elastic-Plastic Modeling

An examination of widely used plastic material modeling techniques reveals potential limitations and sources of error within the process. What follows is a detailed review of the elastic-plastic material modeling procedure, including common assumptions. The modeling process starts with a standardized tensile test, where a dogbone specimen is pulled at a constant grip speed within a test machine (see Figure 2.2). During this test, two measurements are taken: the force versus time, $F(t)$, measured by the test machine, and the displacement versus time, $D(t)$, measured by a gauge or extensometer attached to the specimen. These data points are then used to plot the force versus displacement curve.

Using the force-displacement curve, simple formulas allow calculation of engineering stress and strain as follows:

$$\sigma_{\text{eng}}(t) = \frac{F(t)}{A_0} \quad , \quad \varepsilon_{\text{eng}}(t) = \frac{L(t) - L_0}{L_0} = \frac{D(t)}{L_0} \quad (2.1)$$

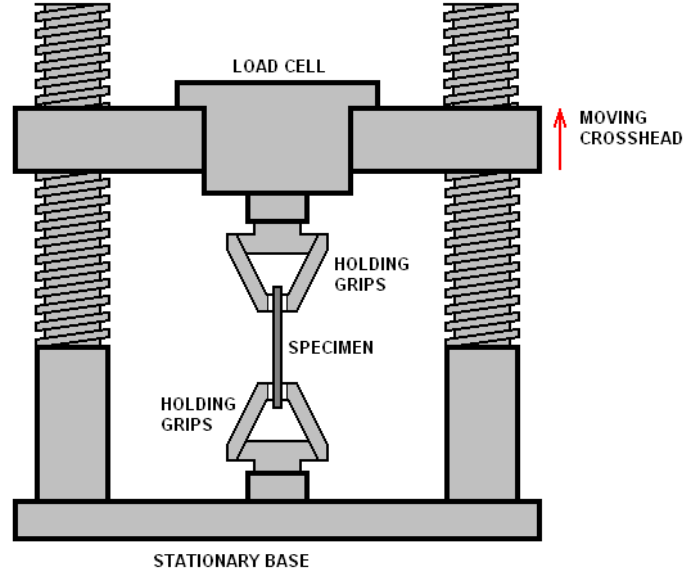


Figure 2.2: Standard tensile test.

where $\sigma_{\text{eng}}(t)$ is the engineering stress over time, ε_{eng} is the engineering strain, $F(t)$ is the axial force, A_0 is the initial cross-sectional area, $L(t)$ is the current gauge length, L_0 is the initial gauge length, and D is displacement.

From these, true stress and strain can be derived using:

$$\sigma = \sigma_{\text{eng}}(1 + \varepsilon_{\text{eng}}) \quad (2.2)$$

$$\varepsilon = \ln(1 + \varepsilon_{\text{eng}}) \quad (2.3)$$

These calculations rely on five assumptions (see Appendix A for details):

- **Assumption 1:** Stress $\sigma_{ij}(t)$ is uniform across the specimen's mid cross-section.
- **Assumption 2:** Cross-sectional area remains constant within the extensometer's measurement region.
- **Assumption 3:** Stress in transverse and thickness directions is zero.
- **Assumption 4:** Strain in transverse and thickness directions is $k\varepsilon_{11}$, with ε_{11} as longitudinal strain and $k \approx 0.5$.
- **Assumption 5:** Strain is uniformly distributed across the extensometer's measurement area.

Deviating from these assumptions may introduce errors into the calculated stress-strain relationship.

For Young's modulus, the elastic region of the final *MAT_224 Ti-6Al-4V model uses a value of 110 GPa.

In the plastic region, plastic strain ε_p is calculated as:

$$\varepsilon_p = \varepsilon - \frac{\sigma}{E} \quad (2.4)$$

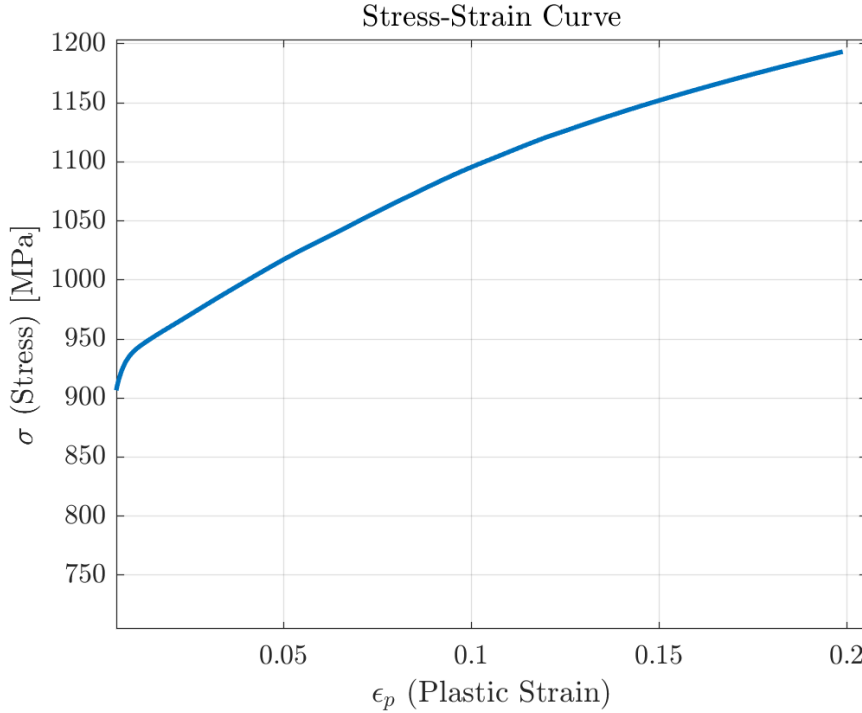


Figure 2.3: LS-DYNA input deck of a piecewise liner plasticity material model of a typical test result.

Under the five assumptions outlined in this section, the load curve representing longitudinal stress versus longitudinal plastic strain is equivalent to the relationship between effective plastic strain, $\varepsilon_{\text{eff}}^p$, and yield stress, σ_Y . This relationship will serve as the basis for analyzing deformation behavior beyond the elastic region.

The effective plastic strain, $\varepsilon_{\text{eff}}^p$, is a monotonically increasing scalar quantity, incrementally calculated based on $\dot{\varepsilon}_{ij}^p$, the plastic component of the rate of deformation tensor. In tensor notation, it is expressed as:

$$\varepsilon_{eff}^p \int_{t=0}^{t1} d\varepsilon_{eff}^p = \int_0^t \sqrt{\frac{2}{3} \dot{\varepsilon}_{ij}^p \dot{\varepsilon}_{ij}^p} dt \quad (2.5)$$

where $\varepsilon_{\text{eff}}^p$ denotes the effective plastic strain rate, and $\dot{\varepsilon}_{ij}^p$ represents the components of

the plastic strain rate tensor. If plastic deformation occurs at constant volume, then:

$$\dot{\varepsilon}_{ij}^p = \dot{\varepsilon}_1^p \begin{bmatrix} 1 & 0 & 0 \\ 0 & -0.5 & 0 \\ 0 & 0 & -0.5 \end{bmatrix} \Rightarrow \dot{\varepsilon}_{eff}^p = \dot{\varepsilon}_1^p \quad (2.6)$$

Additionally,

$$\varepsilon_{eff}^p = \int_{t=0}^{t1} d\varepsilon_{eff}^p = \int_0^t \dot{\varepsilon}_1^p dt = \varepsilon_1^p \quad (2.7)$$

The yield surface can be determined using Equation 15:

$$\sigma \leq \sigma_Y = f_h(\varepsilon_{eff}^p) \quad (2.8)$$

Where $f_h(\varepsilon_{eff}^p)$ represent the tabulated input and $f_h(0)$ is the yield stress that denotes the value of f_h when $\varepsilon_{eff}^p = 0$. This represents the starting point of the plastic strain versus stress curve.

The effective stress according to von Mises, σ_{vm} , is defined as follows:

$$\sigma_{vm} = \sqrt{\frac{1}{2}(\sigma_x - \sigma_y)^2 + (\sigma_y - \sigma_z)^2 + (\sigma_z - \sigma_x)^2 + 6\sigma_{xy}^2 + 6\sigma_{yz}^2 + 6\sigma_{zx}^2} \quad (2.9)$$

In case of uniaxial tension it becomes:

$$\sigma_{ij} = \sigma_1 \begin{bmatrix} 1 & 0 & 0 \\ 0 & 0 & 0 \\ 0 & 0 & 0 \end{bmatrix} \Rightarrow \sigma_{vm} = \sigma_1 (\sigma_1 > 0) \quad (2.10)$$

2.2.2. Violations of Common Assumptions

The standard approach for modeling elastic-plastic materials, as discussed in the previous section, becomes invalid after the onset of necking, since at least three out of five assumptions are violated.

Assumption 1 remains valid because the stress, $\sigma_{ij}(t)$, does not vary significantly across the cross-sectional area at any given time.

Assumption 4 is also valid because the material remains isotropic and plastically incom-

pressible after plastic instability begins.

Assumption 2 is invalid because the cross-sectional area becomes much smaller in the localized necking region and is thus not constant within the region spanned by an extensometer.

Assumption 3 is invalid due to the development of transverse stresses after the onset of necking, as well as additional stresses in the thickness direction with local necking. Consequently, after necking, the specimen no longer experiences a uniaxial stress condition.

Before necking, under uniaxial stress conditions, the only non-zero stress component is the axial stress, σ_l :

$$\sigma = \begin{pmatrix} \sigma_l & 0 & 0 \\ 0 & 0 & 0 \\ 0 & 0 & 0 \end{pmatrix} \quad (18)$$

After necking, a transverse stress, σ_t , develops because the material resists shrinking in the transverse direction:

$$\sigma = \begin{pmatrix} \sigma_l & 0 & 0 \\ 0 & \sigma_t & 0 \\ 0 & 0 & 0 \end{pmatrix} \quad (19)$$

As local necking progresses, additional stresses emerge in the thickness direction, denoted as σ_{tt} :

$$\sigma = \begin{pmatrix} \sigma_l & 0 & 0 \\ 0 & \sigma_t & 0 \\ 0 & 0 & \sigma_{tt} \end{pmatrix} \quad (2.11)$$

An accurate measurement of the longitudinal stress, σ_l , can be obtained by applying the instantaneous necking cross-sectional area (measured by digital imaging) in the stress calculation. However, it is not possible to measure the transverse stress, σ_t , nor the thickness stress, σ_{tt} . Therefore, the von Mises stress, σ_{vm} , is generally unknown after necking.

If the uniaxial stress assumption is still applied (assuming $\sigma_{vm} \approx \sigma$ after necking), and this incorrect von Mises stress versus effective plastic strain relationship is used to define the material behavior, the simulation result will deviate from the real test.

Assumption 5 is invalid because the strain is not uniform within the measuring distance of the extensometer. After the onset of necking, the necked region will have a higher strain than the rest of the specimen. An accurate strain measurement in the necking region can be obtained via digital image correlation (DIC).

2.2.3. Stress-Strain Relationship after Necking

To create a precise material model and simulate a tensile test in LS-DYNA, the following approach is applied:

1. Generate multiple post-necking plastic stress-strain curves by extrapolating from the pre-necking portion of the curve to use as input data.
2. Compare the simulated force-displacement curve to the test results and select the input curve that provides the closest match. For accuracy, ensure the complete specimen geometry is modeled precisely by measuring the actual specimen dimensions instead of relying on blueprint design values. At this stage, the strain-rate effect is not included in the simulation.
3. Input a single stress-strain curve corresponding to a specific strain rate, making the material model strain rate-independent. Consequently, the model will respond identically regardless of the loading speed, provided inertia effects are minimal. This strain rate independence allows the simulation to be run at an arbitrary (higher) loading speed, reducing simulation time compared to the actual test speed.
4. To apply the method safely, conduct multiple simulations to identify an appropriate artificial loading speed for the simulation.

The rate-independent material model will exhibit dynamic effects if subjected to very high loading speeds due to inertia. Therefore, begin with a high loading speed of 10 m/s and gradually reduce it until further reduction no longer changes the results. Use this final speed for the loading simulation; in this case, it was 1 m/s.

The necking point is identified by assuming that necking occurs at the maximum load. This point is given by the intersection between the true-strain versus true-stress curve and its own derivative, meaning that necking occurs where the true stress equals the tangent modulus:

$$\sigma = \frac{d\sigma}{d\varepsilon} \quad (2.12)$$

After identifying the necking point, only the portion of the stress-strain curve before

necking is used for further processing (see Figure 2.4).

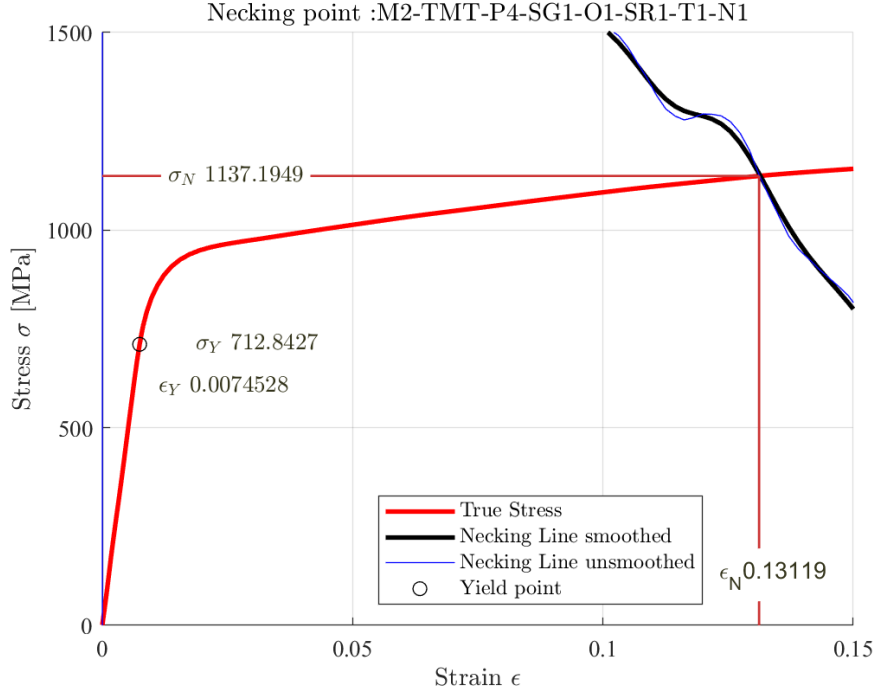


Figure 2.4: The necking judgment line and stress-strain curve.

The hardening curves beyond the necking point are extrapolated using the following formula:

$$\sigma = k[\varepsilon_e + \varepsilon_p]^n \quad (2.13)$$

where k , ε_e and n are fitting parameters. The exponent n is expected to vary between 0 and 1 because the hardening curve is expected to be monotonically increasing and to have a monotonically decreasing tangent.

At the necking point, the curve should be continuous:

$$A \equiv \sigma|_{\varepsilon=\varepsilon_0}, B \equiv \varepsilon|_{\varepsilon=\varepsilon_0} \quad (2.14)$$

and smooth:

$$A \equiv \sigma|_{\varepsilon=\varepsilon_0}, C \equiv \frac{d\sigma}{d\varepsilon}|_{\varepsilon=\varepsilon_0} \quad (2.15)$$

where A is the stress at necking, $B \equiv \varepsilon_0$ is the plastic strain at necking, and C is the slope (hardening modulus) at necking. Note that there are three variables but only two

boundary conditions. Therefore, the extrapolation is not uniquely defined, and one of the three parameters can be freely chosen; since it has a bounded domain, it is common to choose the exponent n . Given a specific n value, ε_e and k are determined the following relationship:

$$k = A \left(\frac{An}{C} \right)^{-n}, \varepsilon_e = \frac{An}{C} - B \quad (2.16)$$

Changing n value, different curves can be generated (See Figure 2.5).

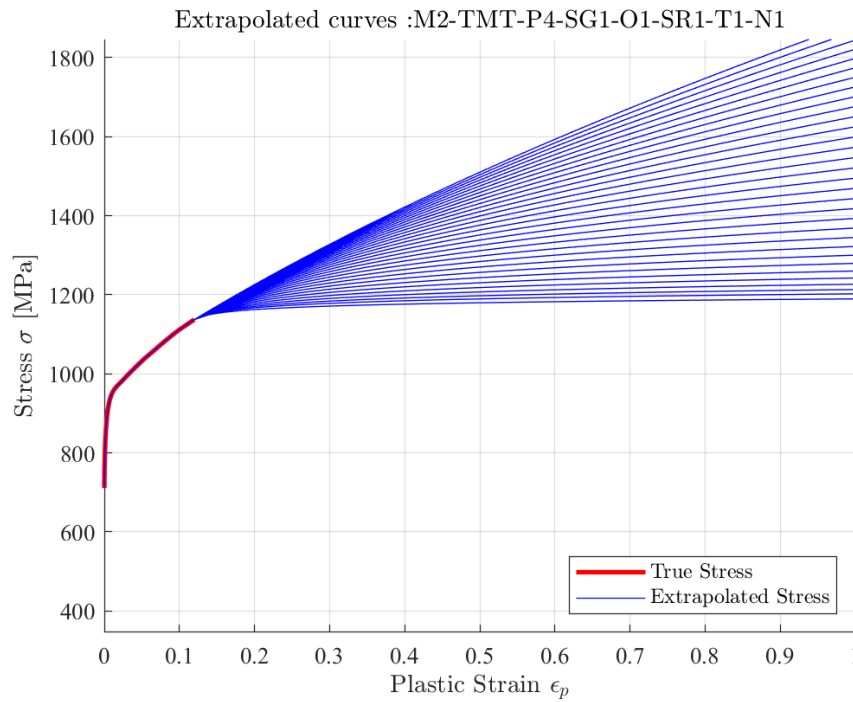


Figure 2.5: Plastic strain versus stress extrapolation curves.

Several candidate curves were selected from the generated plastic strain versus stress data (Figure 2.5), and these were then applied to the material model to simulate a tensile test (Figure 2.6). Additionally, Figure 2.7 illustrates the von Mises stress contour.

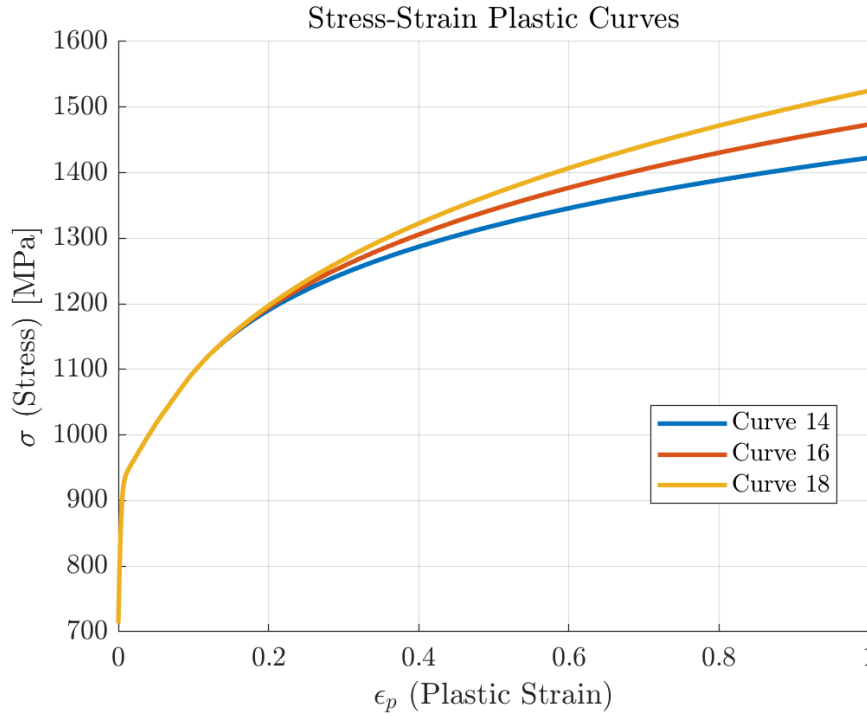


Figure 2.6: Candidate material plastic strain versus stress curves for tensile test simulation.

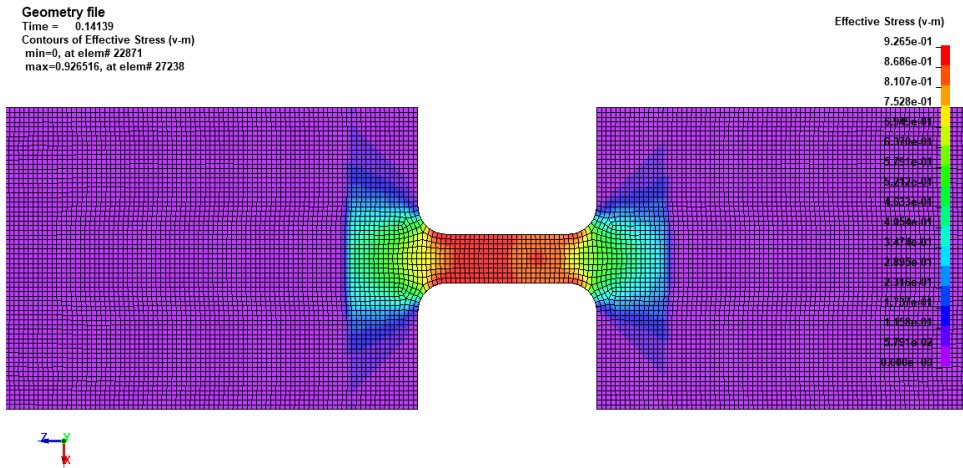


Figure 2.7: Von Mises stress contour of simulated tensile test.

The force-displacement curves from different simulations are compared with the actual tensile test data. Among them, the curve that provides the best displacement response that closely matches the experimental test is the number 16, indicating that it is a reliable estimate of the plastic strain-stress relationship Figure (2.8).

To further validate the results, the plastic strain contour in the load direction at failure

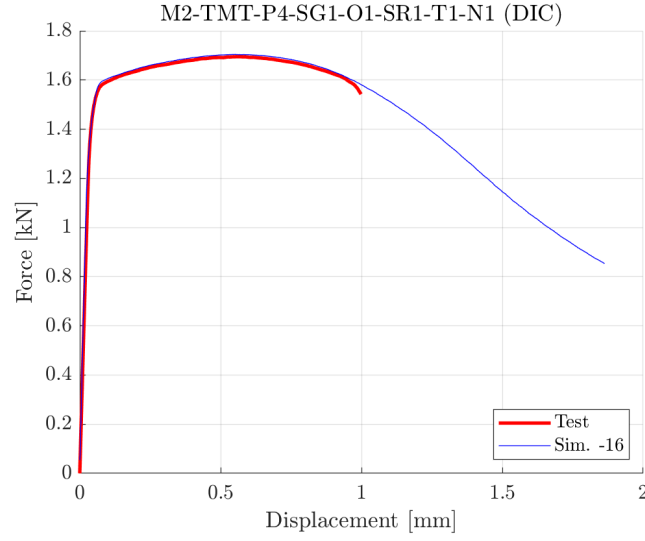


Figure 2.8: Force-displacement results from tensile test simulation.

in the simulation is compared with the longitudinal strain data from the physical test obtained by Digital Image Correlation (DIC), aiming for close alignment to confirm the accuracy of the stress-strain estimation (Figure 2.9).

The Digital Image Correlation (DIC) technique is explained in Appendix A.

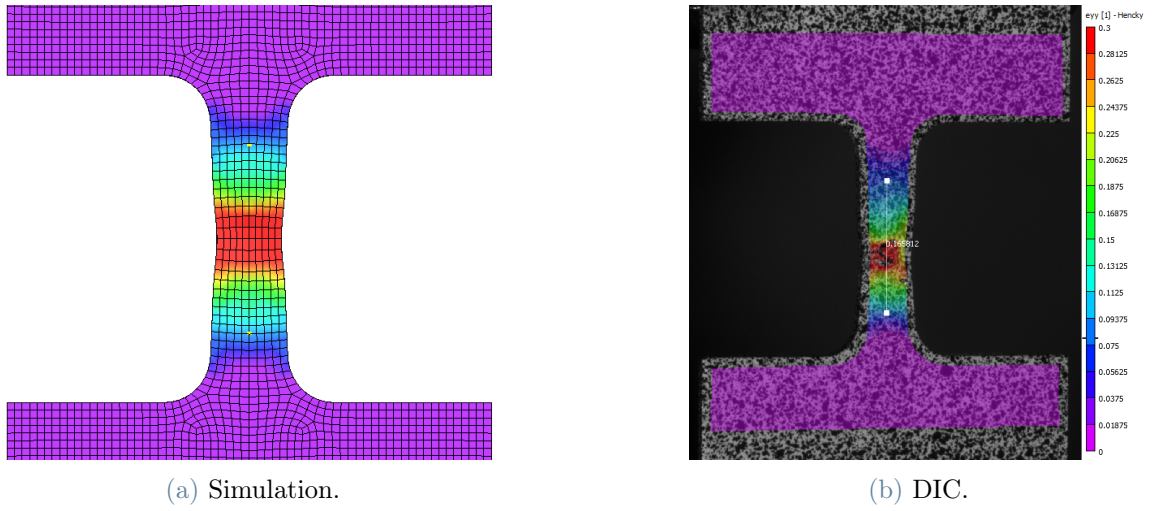


Figure 2.9: Strain comparison in the load direction at Room Temperature.

This process refines the raw data to enhance analysis convergence and execution, avoiding the inaccurate assumptions discussed in Section 2.2.2. The input data produced here aligns closely with the actual test data, removing high-frequency oscillations and negative slopes that could potentially hinder convergence.

2.3. Differences for Compression Tests

In compression tests, it is well established that no necking occurs. Unlike tension tests, the cross-sectional area of the specimen increases during deformation (barreling effect). Nevertheless, the adopted approach also involves generating extended stress-strain curves, extrapolated up to a strain value of $\varepsilon = 1$. This extension is applied to prevent numerical issues that may occur during LS-DYNA interpolation at higher strain values. While in tension tests the extrapolation holds a physical significance, in compression tests, its purpose is purely numerical.

2.4. Isothermal Effects

The approach outlined in Section 2.2.3 is applicable to all quasi-static, isothermal, uniaxial tests, regardless of the temperature at which they were conducted. For these tests to remain isothermal, they must be carried out at a sufficiently low strain rate, ensuring no thermomechanical coupling occurs during the experiment. The yield curve obtained through this method can then be associated with the specific temperature of the test, a requirement since *MAT_224 necessitates an isothermal input curve.

By following this approach, it is possible to build a table of isothermal, temperature-dependent yield curves by simulating each high- and low-temperature tensile test at a given strain rate, with no consideration of thermal coupling in the simulations. This table, alongside the rate-dependent yield curve table, can then serve as input for dynamic simulations where both thermal and strain-rate effects are present and interact—such as scenarios with high strain rates and rapid test completions, where the deformation process generates heat that cannot dissipate conductively due to time constraints.

2.5. Strain Rate Dependency

2.5.1. Tabulated Input

The rolled titanium alloy Ti-6Al-4V plate exhibits strain rate and temperature dependency in the plastic region:

$$\sigma_{ij} = \sigma_{ij}(\varepsilon_{ij}, \dot{\varepsilon}_{ij}, T) \quad (2.17)$$

Multiple tensile tests were conducted at various strain rates. Each test was processed using the method described in Section 2.2.3, with the resulting plastic strain versus stress curves shown in Figure 2.10. Each curve represents the relationship between plastic strain

and stress for a specific strain rate.

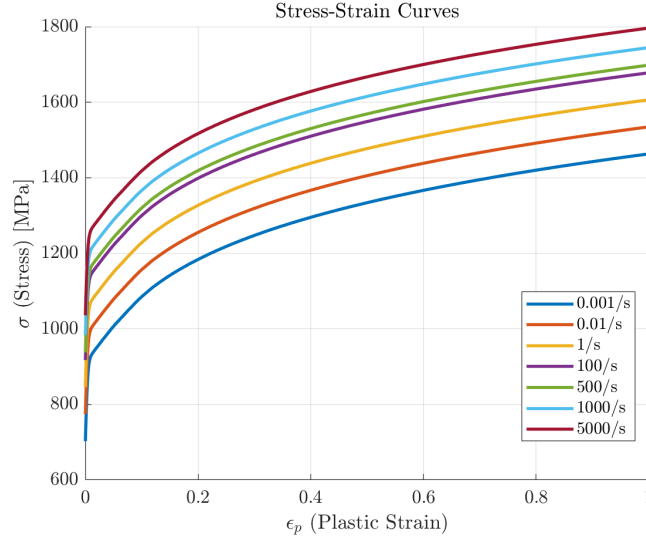


Figure 2.10: Plastic strain-stress relationship of rolled Ti-6Al-4V sheet under different strain rates.

These curves were compiled into a tabulated input for `*MAT_224`. Additional curves representing intermediate and higher strain rates were generated through interpolation and extrapolation, as outlined in Section 2.2.3. Intermediate curves are created internally by LS-DYNA through linear interpolation between user input curves. Unlike material models that rely on curve fitting to match an analytical formula to test data and derive material constants, this method reads all input curves to accurately generate an internal yield surface numerically.

2.5.2. Strain Rate is not a Constant

Initially, the strain rate is assumed to be the nominal strain rate of the test or the grip speed divided by the initial length of the sample monitored by the extensometer. However, this assumption is incorrect due to two influential factors. First we have:

$$\frac{d\varepsilon}{dt}(t) = \frac{1}{l(t)} \frac{dl}{dt} \quad (2.18)$$

This implies that the strain rate is not constant under constant grip speed. Although the strain rate is uniform across the sample until necking occurs, it decreases over time if the grip speed remains constant.

Second, after necking begins, all plastic deformation is localized within the necked region, while the plastic strain outside the neck remains unchanged. Consequently, the strain

rate in the necked area will increase and will no longer be uniform across the sample.

As illustrated in Figure 2.11, within the gauge length, L_0 , the specimen deforms uniformly before necking. After necking, the deformation is localized and only a small portion of the material at the necking point undergoes further deformation, while the rest remains under constant plastic strain.

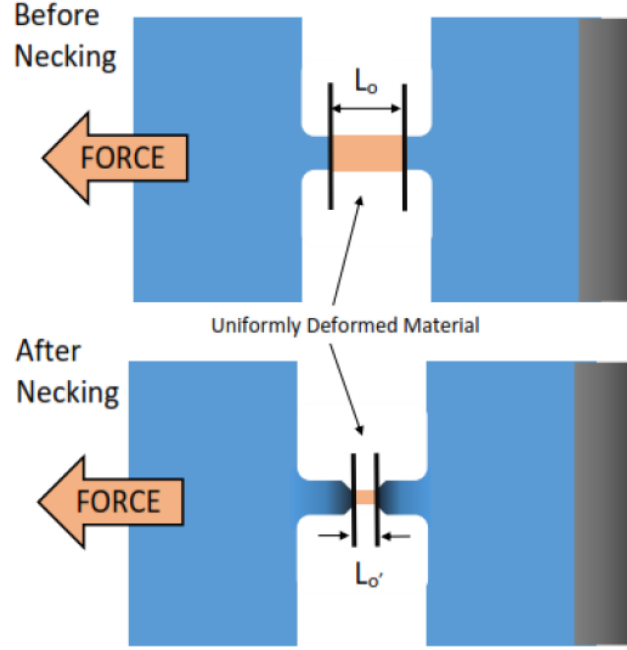


Figure 2.11: Length of uniformly deformed material significantly shortens post-necking.

Assuming deformation at the necking point is still uniform over a reduced length, L'_0 , the engineering strain rate before necking is:

$$\dot{\epsilon}_{\text{eng,bf}} = \frac{\dot{L}(t)}{L_0} \quad (2.19)$$

while the engineering strain rate after necking is:

$$\dot{\epsilon}_{\text{eng,af}} = \frac{\dot{L}(t)}{L'_0} \quad (2.20)$$

Thus, the engineering strain rate increases considerably in the necked area:

$$L'_0 \ll L_0 \Rightarrow \dot{\epsilon}_{\text{eng,af}} > \dot{\epsilon}_{\text{eng,bf}} \quad (2.21)$$

The same trend applies to the true strain rate, although it is more complex to demonstrate.

Other variations in the testing procedure, such as non-constant grip speed or non-fixed boundary conditions, may also affect the strain rate and cause the nominal strain rate to deviate from the actual physical value. Therefore, the displacement-time history from the test must be included in the numerical model to accurately replicate the strain rates observed in each test.

2.5.3. High Strain-Rate Sensitivity

When considering a Stress versus Strain Rate curve it is possible to distinguish three regions, each corresponding to a certain range of strain rate. These will be referred as regions I, II and IV following Rosenfield and Hann [39].

It has been observed that curves in region I are characterized by a small nearly constant slope (on a semi-logarithmic plot) and little temperature dependence; the dominant factor seems to be the internal stress fields due to dislocations: when the applied stress is only slightly greater than the amplitude of the internal stress, the strain rate sensitivity decreases [7].

The curves in region II are also linear (on a semi-logarithmic plot) but with a higher rate and temperature dependence (higher slope). It is generally accepted that at low temperatures the strain rate is controlled by the thermal activation of dislocation motion [9].

In region IV the rate dependency increases significantly, while the temperature dependence is unaffected. This is believed to be due to viscous resistance to dislocation motion, which becomes rate-controlling under these conditions.

As showed in the previous section the strain rate in a test with localization is not a constant. The localization is especially early and extreme in the Ti-6AL-4V tension tests with higher strain rate. The strain rate in the localization region can reach values significantly above the nominal strain rate for the sample. To account for this phenomenon, the strain rate was evaluated at a specific strain level, selected to be 2.5%. This choice was driven by the need to identify a strain value positioned between the yielding point and the necking point, ensuring both accuracy and the avoidance of potential initial oscillations in the high-strain-rate curves. This approach facilitates the development of strain rate sensitivity curves, which, for a GYS material model, must be constructed for both tension and compression.

It is important to note that these curves serve as an initial reference and starting point, but they come with limitations, as each test is characterized by a single strain rate,

even though it represents a broader range of values. The process is inherently iterative, with adjustments made to the strain-rate sensitivity curves until an optimal match with experimental data is achieved [13].

For this study, piecewise-defined curves were employed, consisting of three distinct regions, aligned with the previously presented theory.

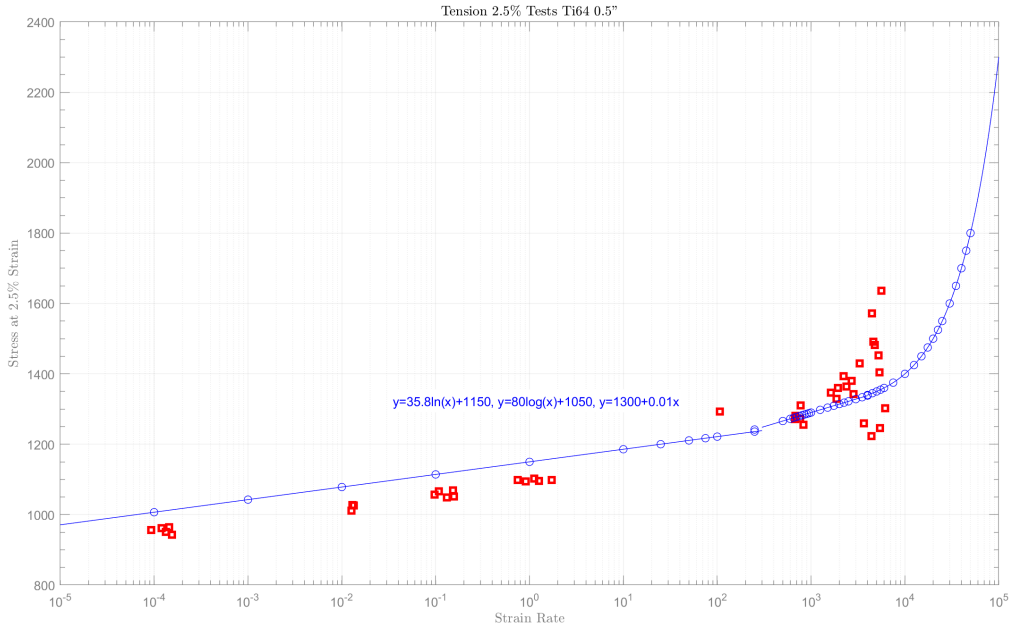


Figure 2.12: Strain-Rate sensitivity curve in tension.

It is worth noting that the graph itself is semi-logarithmic.

At higher strain rates, tests were conducted neither at a constant strain rate nor under isothermal conditions. Consequently, the quasistatic stress-strain curve was used as the baseline for all higher-rate curves. Each curve's stress values were shifted so that the stress at 2.5% strain matched the desired target value.

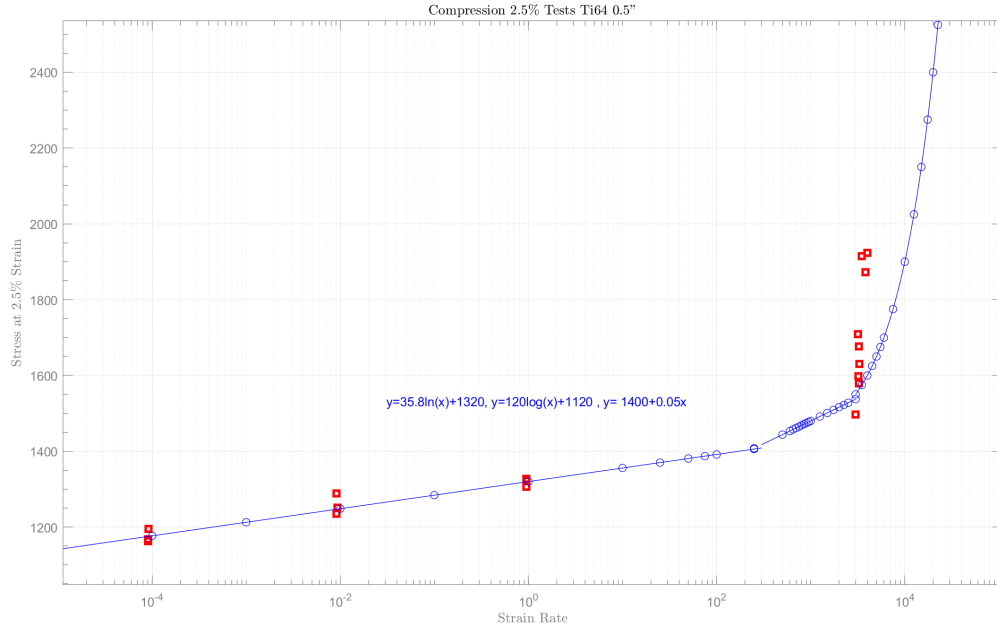


Figure 2.13: Strain-Rate sensitivity curve in compression.

2.6. Conversion of Plastic Work into Heat (Taylor-Quinney Effect)

In high strain rate tests, particularly within the localized necking region, there is not enough time for conduction to dissipate the heat generated by plastic deformation. As a result, the process becomes adiabatic, leading to a substantial local temperature increase in the specimen, significantly influencing material behavior at larger strains. Consequently, simulations of the tension tests are highly sensitive to the amount of energy generated by plastic work that is transformed into thermal energy.

The fraction of plastic work converted into thermal energy is described by the Taylor-Quinney coefficient, denoted as β . It is important to note that this coefficient is not constant but varies with strain rate and, to a lesser extent, with plastic strain.

For *MAT_224 it is possible to incorporate into simulations the calibrated effective TQC curves, giving the value of β for each given strain rate. Effective TQCs that consider heat conduction at different rates are required to accurately simulate dynamic processes that involve plastic deformation over a broad range of strain rates. For this thesis a specific curve has been used: Table 2.1.

Strain Rate [1/s]	β
1.00E-06	0.00
1.00E-05	0.00
1.00E-04	0.01
1.00E-03	0.03
1.00E-02	0.12
1.00E-01	0.38
2.50E-01	0.49
5.00E-01	0.56
1.00E+00	0.61
2.50E+00	0.65
5.00E+00	0.67
1.00E+01	0.68
1.00E+02	0.70
1.00E+03	0.70

Table 2.1: Taylor-Quinney Coefficient Curve.

The curve analyzed is the result of research carried out at the Center for Collision Safety and Analysis, dedicated to the development of these curves for various materials, including Ti-6Al-4V[36].

3 | Material Model Creation by Simulation of Mechanical Property Tests

The mechanical and chemical properties of the material provided by the manufacturer can be found in Appendix E and are reported in Tables 3.1, 3.2.

Property	Longitudinal Direction (L)	Transversal Direction (T)
Tensile Strength (MPa)	1022.91	1000.40
Yield Strength (MPa)	944.58	937.60
Elongation (%)	16	16

Table 3.1: Material Mechanical Properties.

Element	Chemical Composition (%)
N	0.006
C	0.0016
Fe	0.16
O	0.17
H	0.0085
Al	6.27
V	4.08
Y	0.0004

Table 3.2: Material Chemical Composition.

3.1. Test Data

The test data encompass information on time, force, and displacement. Each test is accompanied by a computer-aided design (CAD) image that illustrates the precise dimensions of the specimen as measured. For some of the tests DIC images are also available.

Table 3.3: Tension temperature tests series provided by OSU.

Series	Test Name	Stock	Specimen	Orientation	SR [1/s]	Temp. [°C]
Tension Temperature Series	M2-TMT-P4-SG1-O1-SR3-T2-N2	0.5"	Flat Dogbone	Rolled	1	200
	M2-TMT-P4-SG1-O1-SR3-T2-N3	0.5"	Flat Dogbone	Rolled	1	200
	M2-TMT-P4-SG1-O1-SR3-T2-N4	0.5"	Flat Dogbone	Rolled	1	200
	M2-TMT-P4-SG1-O1-SR3-T3-N2	0.5"	Flat Dogbone	Rolled	1	400
	M2-TMT-P4-SG1-O1-SR3-T3-N4	0.5"	Flat Dogbone	Rolled	1	400
	M2-TMT-P4-SG1-O1-SR3-T3-N5	0.5"	Flat Dogbone	Rolled	1	400
	M2-TMT-P4-SG1-O1-SR3-T4-N1	0.5"	Flat Dogbone	Rolled	1	600
	M2-TMT-P4-SG1-O1-SR3-T4-N2	0.5"	Flat Dogbone	Rolled	1	600
	M2-TMT-P4-SG1-O1-SR3-T4-N3	0.5"	Flat Dogbone	Rolled	1	600
	M2-TMT-P4-SG1-O1-SR3-T5-N2	0.5"	Flat Dogbone	Rolled	1	-50
	M2-TMT-P4-SG1-O1-SR3-T5-N3	0.5"	Flat Dogbone	Rolled	1	-50
	M2-TMT-P4-SG1-O1-SR3-T5-N4	0.5"	Flat Dogbone	Rolled	1	-50

Table 3.4: Compression strain rate tests series provided by OSU.

Series	Test Name	Stock	Specimen	Orientation	SR [1/s]	Temp. [°C]
Compression Strain Rate Series	M2-TMC-P4-SG1-O1-SR1-T1-N4	0.5"	Cylindrical	Rolled	0.0001	RT
	M2-TMC-P4-SG1-O1-SR1-T1-N5	0.5"	Cylindrical	Rolled	0.0001	RT
	M2-TMC-P4-SG1-O1-SR1-T1-N6	0.5"	Cylindrical	Rolled	0.0001	RT
	M2-TMC-P4-SG1-O1-SR2-T1-N1	0.5"	Cylindrical	Rolled	0.01	RT
	M2-TMC-P4-SG1-O1-SR2-T1-N3	0.5"	Cylindrical	Rolled	0.01	RT
	M2-TMC-P4-SG1-O1-SR2-T1-N4	0.5"	Cylindrical	Rolled	0.01	RT
	M2-TMC-P4-SG1-O1-SR3-T1-N2	0.5"	Cylindrical	Rolled	0.96	RT
	M2-TMC-P4-SG1-O1-SR3-T1-N4	0.5"	Cylindrical	Rolled	0.97	RT
	M2-TMC-P4-SG1-O1-SR3-T1-N5	0.5"	Cylindrical	Rolled	0.96	RT
	M2-TMC-P4-SG1-O1-SR4-T1-N1	0.5"	Cylindrical	Rolled	1474.00	RT
	M2-TMC-P4-SG1-O1-SR4-T1-N2	0.5"	Cylindrical	Rolled	818.00	RT
	M2-TMC-P4-SG1-O1-SR4-T1-N3	0.5"	Cylindrical	Rolled	1473.00	RT
	M2-TMC-P4-SG1-O1-SR5-T1-N2	0.5"	Cylindrical	Rolled	4084.00	RT
	M2-TMC-P4-SG1-O1-SR5-T1-N3	0.5"	Cylindrical	Rolled	3879.00	RT
	M2-TMC-P4-SG1-O1-SR5-T1-N5	0.5"	Cylindrical	Rolled	3980.00	RT
	M2-TMC-P4-SG1-O1-SR6-T1-N2	0.5"	Cylindrical	Rolled	7616.00	RT
	M2-TMC-P4-SG1-O1-SR6-T1-N3	0.5"	Cylindrical	Rolled	7199.00	RT
	M2-TMC-P4-SG1-O1-SR6-T1-N4	0.5"	Cylindrical	Rolled	7971.00	RT

Table 3.5: Tension strain rate tests series provided by OSU.

Series	Test Name	Stock	Specimen	Orientation	SR [1/s]	Temp. [°C]
Tension Strain Rate Series	M2-TMT-P4-SG1-O1-SR1-T1-N1	0.5"	Flat Dogbone	Rolled	0.0001	RT
	M2-TMT-P4-SG1-O1-SR1-T1-N2	0.5"	Flat Dogbone	Rolled	0.0001	RT
	M2-TMT-P4-SG1-O1-SR1-T1-N7	0.5"	Flat Dogbone	Rolled	0.0001	RT
	M2-TMT-P4-SG1-O1-SR1-T1-N8	0.5"	Flat Dogbone	Rolled	0.0001	RT
	M2-TMT-P4-SG1-O1-SR1-T1-N9	0.5"	Flat Dogbone	Rolled	0.0001	RT
	M2-TMT-P4-SG1-O1-SR2-T1-N7	0.5"	Flat Dogbone	Rolled	0.01	RT
	M2-TMT-P4-SG1-O1-SR2-T1-N8	0.5"	Flat Dogbone	Rolled	0.01	RT
	M2-TMT-P4-SG1-O1-SR2-T1-N9	0.5"	Flat Dogbone	Rolled	0.01	RT
	M2-TMT-P4-SG1-O1-SR2-T1-N1	0.5"	Flat Dogbone	Rolled	0.1095	RT
	M2-TMT-P4-SG1-O1-SR2-T1-N2	0.5"	Flat Dogbone	Rolled	0.1063	RT
	M2-TMT-P4-SG1-O1-SR2-T1-N3	0.5"	Flat Dogbone	Rolled	0.1045	RT
	M2-TMT-P4-SG1-O1-SR2-T1-N5	0.5"	Flat Dogbone	Rolled	0.1072	RT
	M2-TMT-P4-SG1-O1-SR2-T1-N6	0.5"	Flat Dogbone	Rolled	0.1113	RT
	M2-TMT-P4-SG1-O1-SR3-T1-N1	0.5"	Flat Dogbone	Rolled	1.0336	RT
	M2-TMT-P4-SG1-O1-SR3-T1-N2	0.5"	Flat Dogbone	Rolled	1.0138	RT
	M2-TMT-P4-SG1-O1-SR3-T1-N3	0.5"	Flat Dogbone	Rolled	0.9501	RT
	M2-TMT-P4-SG1-O1-SR3-T1-N4	0.5"	Flat Dogbone	Rolled	1.1304	RT
	M2-TMT-P4-SG1-O1-SR3-T1-N5	0.5"	Flat Dogbone	Rolled	1.1191	RT
	M2-TMT-P4-SG1-O1-SR4-T1-N1	0.5"	Flat Dogbone	Rolled	471.24	RT
	M2-TMT-P4-SG1-O1-SR4-T1-N2	0.5"	Flat Dogbone	Rolled	580.64	RT
	M2-TMT-P4-SG1-O1-SR4-T1-N3	0.5"	Flat Dogbone	Rolled	366.94	RT
	M2-TMT-P4-SG1-O1-SR4-T1-N4	0.5"	Flat Dogbone	Rolled	495.20	RT
	M2-TMT-P4-SG1-O1-SR4-T1-N5	0.5"	Flat Dogbone	Rolled		RT
	M2-TMT-P4-SG1-O1-SR4-T1-N6	0.5"	Flat Dogbone	Rolled	506.76	RT
	M2-TMT-P4-SG1-O1-SR4-T1-N7	0.5"	Flat Dogbone	Rolled	696.72	RT
	M2-TMT-P4-SG1-O1-SR5-T1-N1	0.5"	Flat Dogbone	Rolled	1572.15	RT
	M2-TMT-P4-SG1-O1-SR5-T1-N2	0.5"	Flat Dogbone	Rolled	913.38	RT
	M2-TMT-P4-SG1-O1-SR5-T1-N3	0.5"	Flat Dogbone	Rolled	1430.21	RT
	M2-TMT-P4-SG1-O1-SR5-T1-N4	0.5"	Flat Dogbone	Rolled	1987.73	RT
	M2-TMT-P4-SG1-O1-SR5-T1-N6	0.5"	Flat Dogbone	Rolled	2021.56	RT
	M2-TMT-P4-SG1-O1-SR5-T1-N8	0.5"	Flat Dogbone	Rolled	1677.09	RT
	M2-TMT-P4-SG1-O1-SR5-T1-N9	0.5"	Flat Dogbone	Rolled	1386.71	RT
	M2-TMT-P4-SG1-O1-SR6-T1-N1	0.5"	Flat Dogbone	Rolled	4233.75	RT
	M2-TMT-P4-SG1-O1-SR6-T1-N2	0.5"	Flat Dogbone	Rolled	6398.68	RT
	M2-TMT-P4-SG1-O1-SR6-T1-N4	0.5"	Flat Dogbone	Rolled	4692.35	RT
	M2-TMT-P4-SG1-O1-SR6-T1-N5	0.5"	Flat Dogbone	Rolled	5406.10	RT
	M2-TMT-P4-SG1-O1-SR6-T1-N6	0.5"	Flat Dogbone	Rolled	4555.10	RT
	M2-TMT-P4-SG1-O1-SR6-T1-N7	0.5"	Flat Dogbone	Rolled	4383.90	RT
	M2-TMT-P4-SG1-O1-SR7-T1-N1	0.5"	Flat Dogbone	Rolled	7711.20	RT
	M2-TMT-P4-SG1-O1-SR7-T1-N2	0.5"	Flat Dogbone	Rolled	5616.28	RT
	M2-TMT-P4-SG1-O1-SR7-T1-N4	0.5"	Flat Dogbone	Rolled	8400.46	RT
	M2-TMT-P4-SG1-O1-SR7-T1-N6	0.5"	Flat Dogbone	Rolled	7308.09	RT
	M2-TMT-P4-SG1-O1-SR7-T1-N7	0.5"	Flat Dogbone	Rolled	8131.96	RT

Table 3.6: Compression temperature tests series provided by OSU.

Series	Test Name	Stock	Specimen	Orientation	SR [1/s]	Temp. [°C]
Compression Temperature Series	M2-TMC-P4-SG1-O1-SR3-T2-N7	0.5"	Cylindrical	Rolled	1	200
	M2-TMC-P4-SG1-O1-SR3-T2-N8	0.5"	Cylindrical	Rolled	1	200
	M2-TMC-P4-SG1-O1-SR3-T2-N9	0.5"	Cylindrical	Rolled	1	200
	M2-TMC-P4-SG1-O1-SR3-T3-N1	0.5"	Cylindrical	Rolled	1	400
	M2-TMC-P4-SG1-O1-SR3-T3-N2	0.5"	Cylindrical	Rolled	1	400
	M2-TMC-P4-SG1-O1-SR3-T3-N3	0.5"	Cylindrical	Rolled	1	400
	M2-TMC-P4-SG1-O1-SR3-T3-N4	0.5"	Cylindrical	Rolled	1	400
	M2-TMC-P4-SG1-O1-SR3-T4-N1	0.5"	Cylindrical	Rolled	1	600
	M2-TMC-P4-SG1-O1-SR3-T4-N2	0.5"	Cylindrical	Rolled	1	600
	M2-TMC-P4-SG1-O1-SR3-T4-N3	0.5"	Cylindrical	Rolled	1	600
	M2-TMC-P4-SG1-O1-SR3-T5-N1	0.5"	Cylindrical	Rolled	1	-50
	M2-TMC-P4-SG1-O1-SR3-T5-N2	0.5"	Cylindrical	Rolled	1	-50
	M2-TMC-P4-SG1-O1-SR3-T5-N5	0.5"	Cylindrical	Rolled	1	-50
	M2-TMC-P4-SG1-O1-SR3-T5-N6	0.5"	Cylindrical	Rolled	1	-50

3.2. Computational Infrastructure for LS-DYNA Simulations

The Center for Collision Safety and Analysis (CCSA) operates its own high-performance cluster computer system dedicated to run LS-DYNA.

The system has twelve compute nodes by Supermicro; dual 16-core Intel Xeon Gold 6240 *Cascade Lake* processors and dual 32-core AMD EPYC 7153 processors are utilized, for a total of 512-cores. The cluster interconnect is Mellanox ConnectX-5 25 Gbps Ethernet. The cluster is managed with Bright Cluster Manager, jobs are managed by PBS Pro.

3.3. Temperature Effect

Numerous tests has been conducted at different temperature, for both tension and compression, in order to characterize the material behaviour in these different conditions and obtain stress-strain curve to use as input in the definition of the material (Tables 3.3, 3.6). The tests have been performed at 5 different temperatures : $T_1 = 293.15K$ (Room Temperature, RT), $T_2 = 493.15K$, $T_3 = 693.15K$, $T_4 = 893.15K$, $T_5 = 223.15K$.

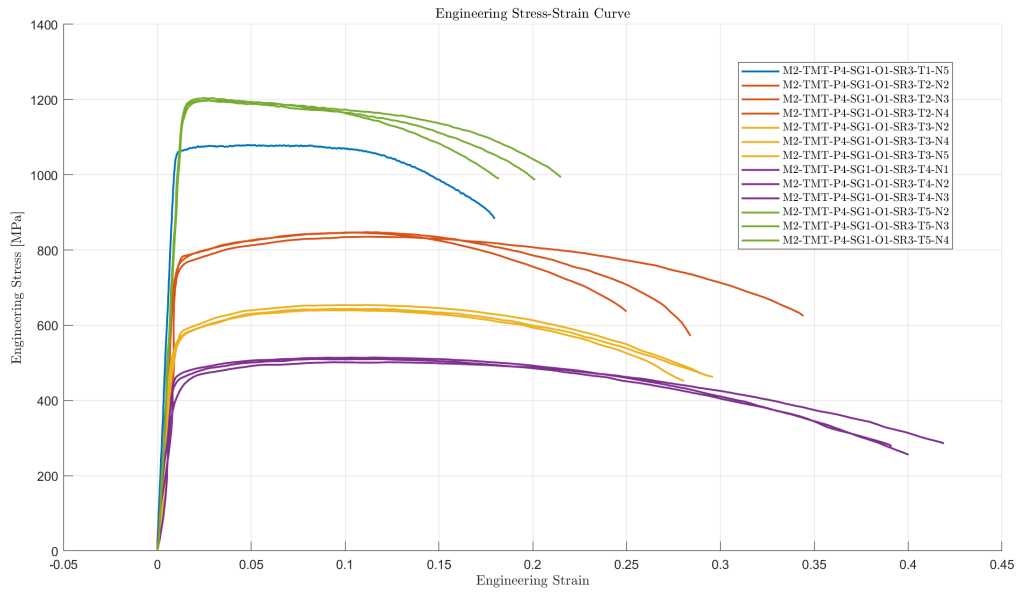


Figure 3.1: Temperature Effect for Tension tests.

All the tests have been simulated and one for each temperature has been selected to be used, considering the smoothness of the force-displacement curve and its value in order to choose the most reliable one.

The temperature effects were examined using `*MAT_224` models configured with single hardening curves corresponding to a strain rate of $1 s^{-1}$, which matches the rate at which all thermal tests were performed. Employing a single stress-strain curve ensures strain-rate insensitivity, allowing simulations to apply displacement at an accelerated grip speed of 1 m/s.

These simulations faithfully replicate the geometry of the physical test specimens.

The units used in the models are [kg], [mm], [ms], [kN], and [GPa].

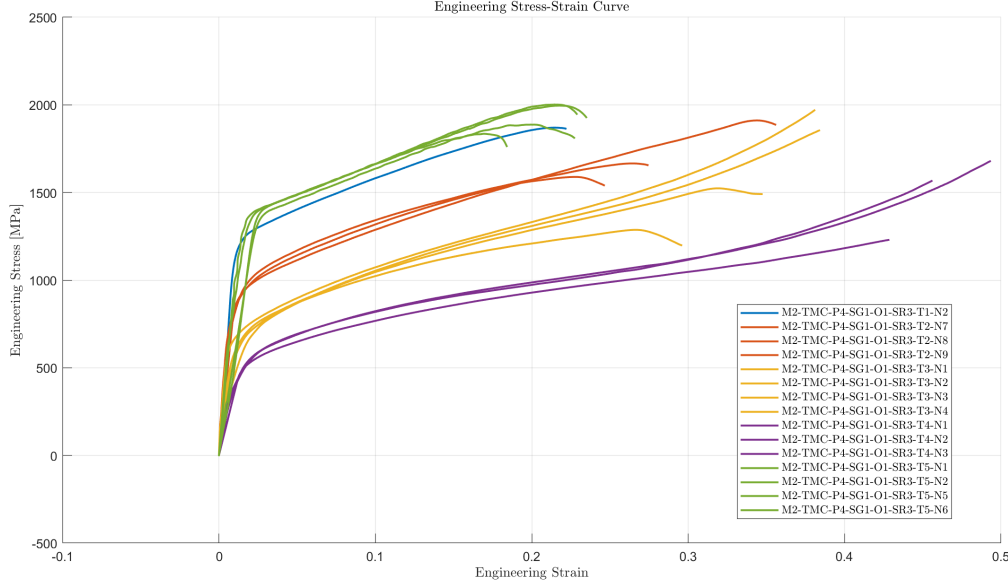


Figure 3.2: Temperature Effect for Compression tests.

3.3.1. Tension

Stress-Strain Relationship at Room Temperature

Among all the test at Room Temperature just one has been chosen to represent the group of data and to be processed. For tensions tests it is M2-TMT-P4-SG1-01-SR3-T1-N5. The true stress-strain relationship has been found following the approach described in section 2.2.3.

Using equation 2.4 and a Young's modulus of 110 Gpa the plastic strain-stress relationship was determined. To identify the necking point, the true strain-stress curve underwent a 9-point moving average. Equations 2.15 and 2.16, which involve taking the derivative of stress with respect to strain, were then applied to generate the tangent modulus curve. This curve was further smoothed with another 9-point moving average. The intersection of the smoothed tangent modulus curve and the true strain-stress curve defined the necking point, as illustrated in Figure 3.3. The true stress and strain values at necking were documented, and the corresponding plastic strain at this point was calculated using Equation 2.12. The hardening curve beyond necking was excluded, while the extrapolation of the curve past necking was performed using Equation 2.13. A total of 32 hardening curves were generated by varying the exponent n between approximately 0.1 and 0.5 (Figure 3.4), using non-uniform incremental steps. The remaining parameters, ε_e and k , were derived using Equation 2.16. MATLAB was used to carry out the extrap-

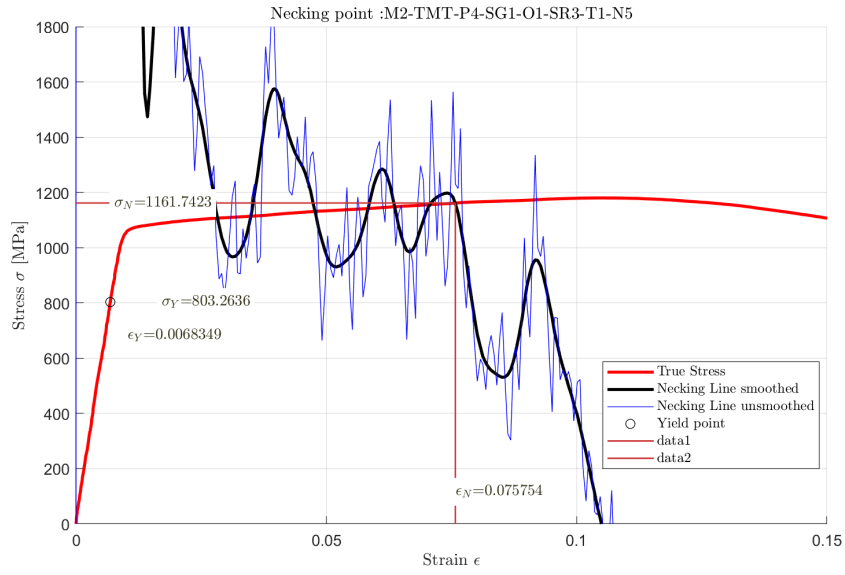


Figure 3.3: True stress-strain relationship and necking point judgment.

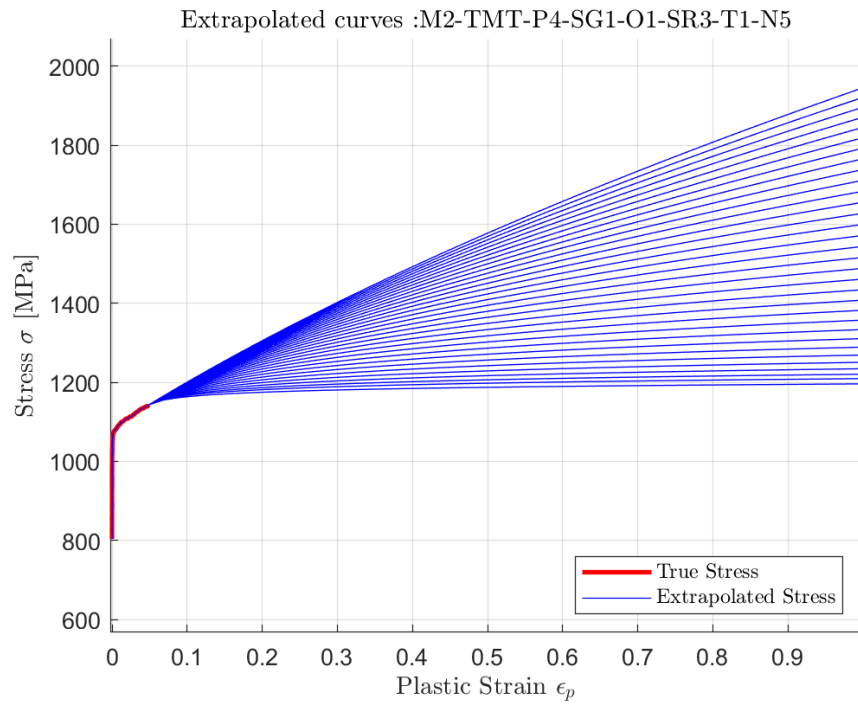


Figure 3.4: Plastic strain versus stress extrapolation curves.

olation. Each generated hardening curve was incorporated into an LS-DYNA *MAT_224 input deck to simulate the test. The model used sample dimensions matching test specimen M2-TMT-P3-SG1-O1-SR3-T1-N5, with a width of 2.019 mm and a thickness of 0.814 mm. The *DATABASE_CROSS_SECTION keyword was used to monitor the cross-sectional force,

and the displacement of two nodes representing the extensometer's base points was recorded in the NODOUT file (refer to Figure 3.5). The difference in their z -direction displacement provided the simulated elongation of the extensometer, which had an initial gauge length of 4 mm. The cross-sectional force measurement was taken at the specimen's midpoint. A force-elongation curve derived from this simulation was compared directly to the experimental force-displacement data.

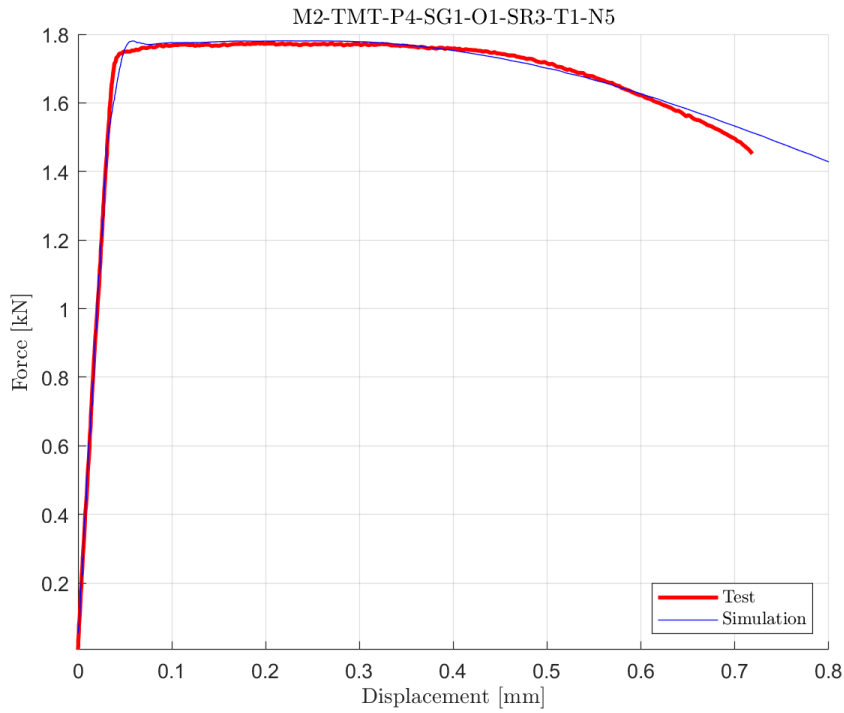


Figure 3.5: Force-Displacement Result, Curve 8.

This process was repeated for all extrapolated candidate curves until a match was achieved between the simulation and the test data. The stress-strain curve in Figure 3.6 represents the best fit, as shown in Figure 3.5.

Additionally, Figure 3.7 compares a simulation contour of the strain in the load direction to a DIC image from the experiment taken just before failure, showing strong agreement between the two.

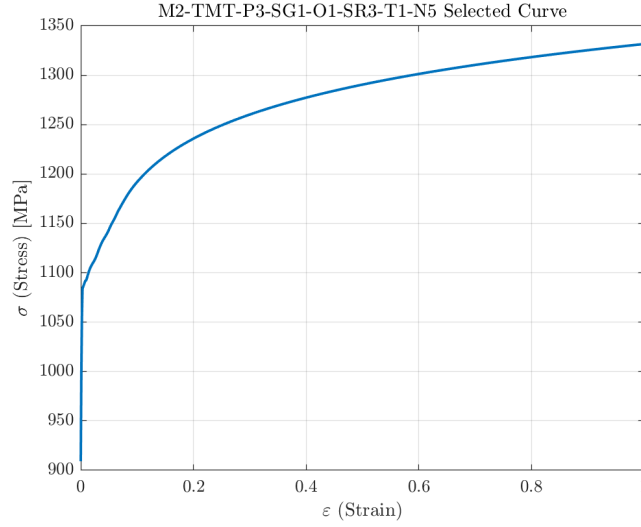


Figure 3.6: Selected Stress-Strain input curve.

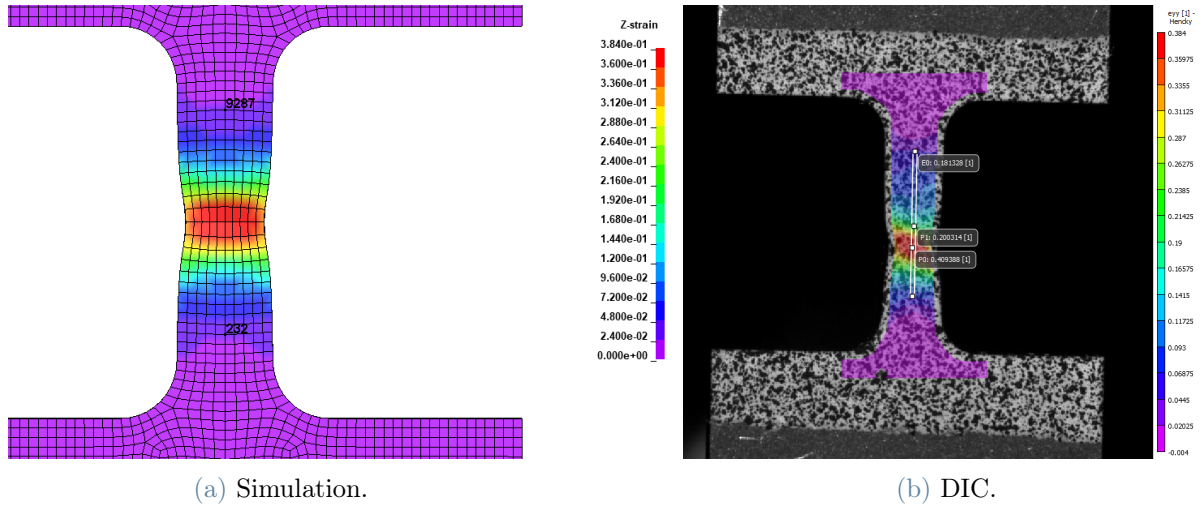


Figure 3.7: Strain comparison in the load direction at Room Temperature.

Stress-Strain Relationship at Other Temperatures

The same procedure described in Section 3.3.1 is applied to the tests at others temperatures. The stress-strain input curves used as input for the LCKT table of the `*MAT_224_GYS` are plotted in 3.8. It is possible to notice that there is no intersection between the curves at different temperatures.

Ti64 exhibits a clear thermal softening behavior [14]. As temperature increases:

- Yield strength decreases.
- Ultimate tensile strength decreases.

- Strain to failure (ductility) increases.

Intersecting stress-strain curves would contradict this material behavior.

Moreover, LS-DYNA uses the LCKT table to interpolate stress-strain data across different temperatures: intersecting curves would create numerical artifacts during interpolation, potentially leading to instabilities in high-rate simulations.

Ti64 is often used in dynamic applications, such as aerospace and automotive compo-

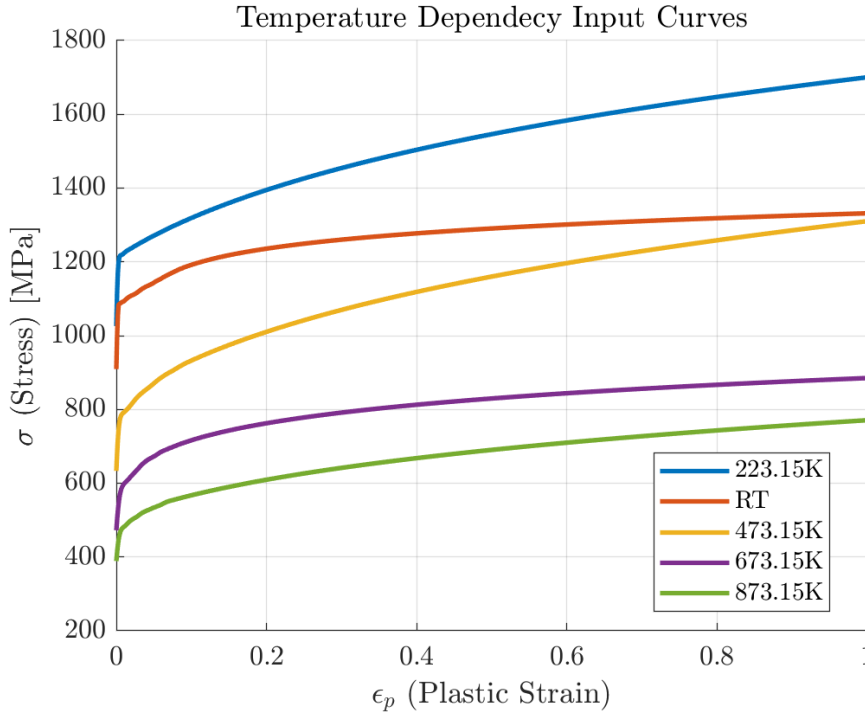


Figure 3.8: Selected Stress-Strain input curves.

nents, where thermal effects due to high strain rates and adiabatic heating are critical. Non-intersecting LCKT curves ensure the model's behavior remains consistent and physically accurate under these conditions. In Figures 3.9, 3.10, 3.11, and 3.12, the force-displacement comparisons between the simulation and the test data for T2, T3, T4, and T5 are presented. All the results demonstrate an excellent agreement.

Additionally, for the tests at T2, T3, and T4, DIC images were provided, enabling a comparison of the strain in the load direction between the simulation and the DIC results (3.13, 3.14, 3.15).

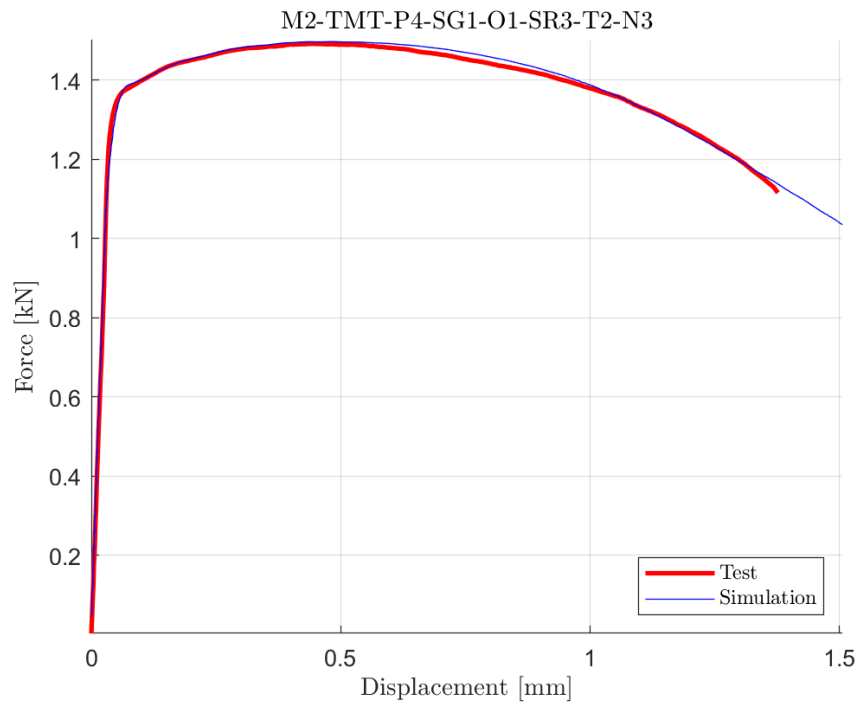


Figure 3.9: Force-Displacement Result for T2, Curve 20.

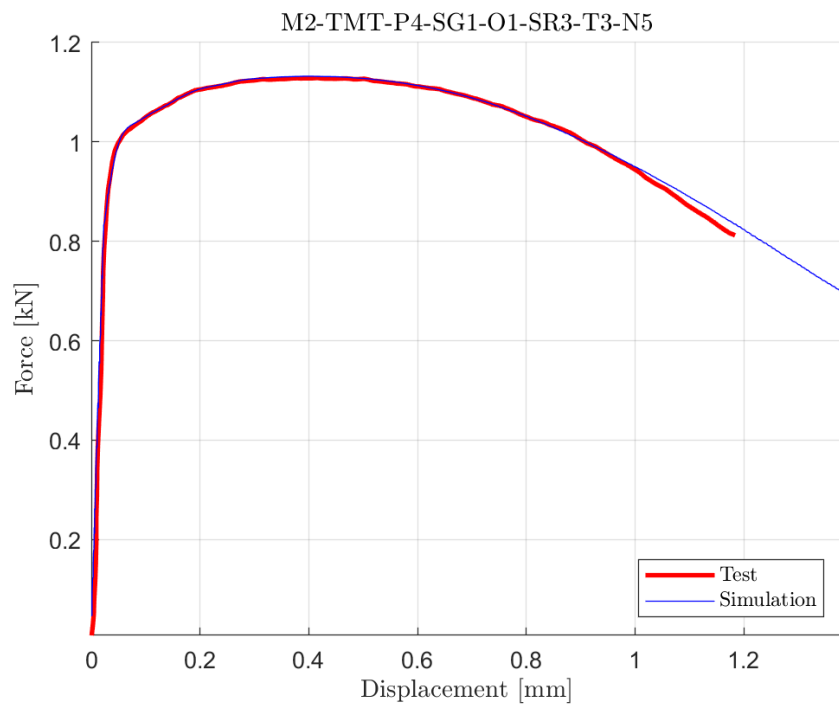


Figure 3.10: Force-Displacement Result for T3, Curve 13.

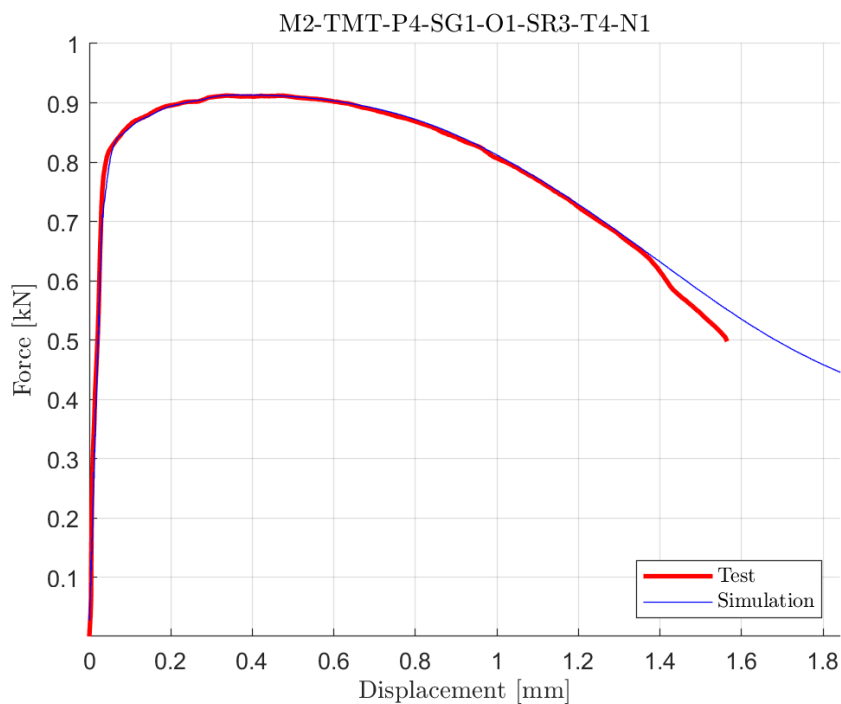


Figure 3.11: Force-Displacement Result for T4, Curve 19.

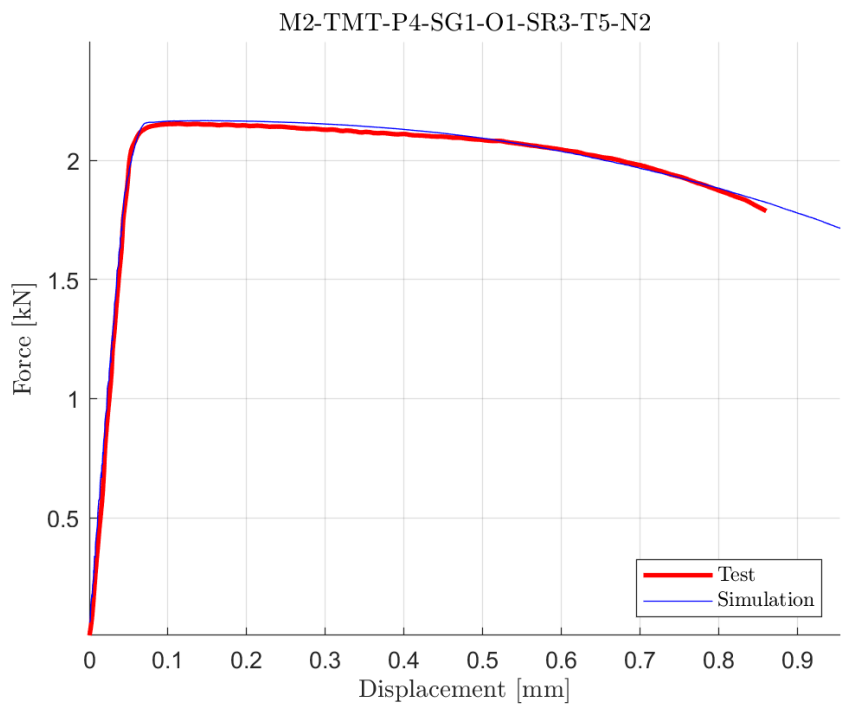
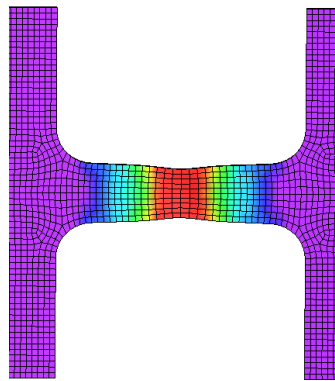
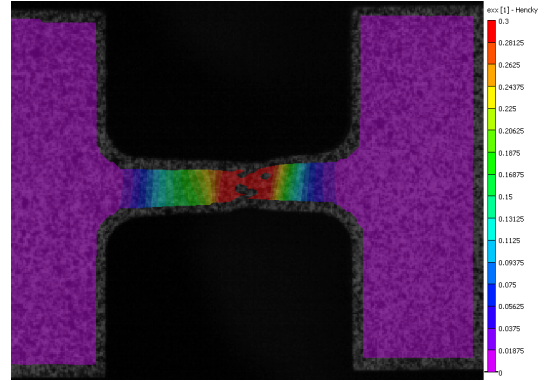


Figure 3.12: Force-Displacement Result for T5, Curve 18.

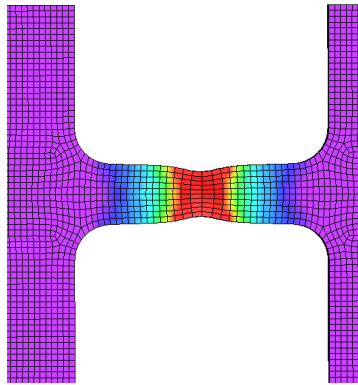


(a) Simulation.

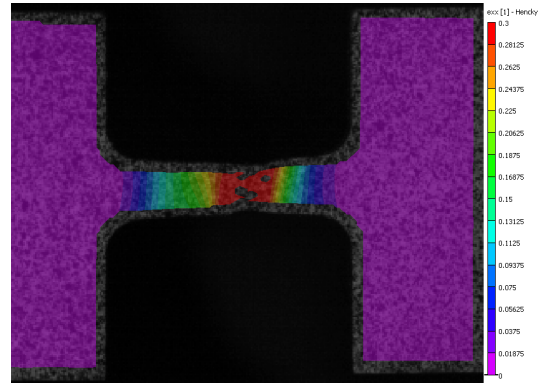


(b) DIC.

Figure 3.13: Strain comparison in the load direction at 200° C.

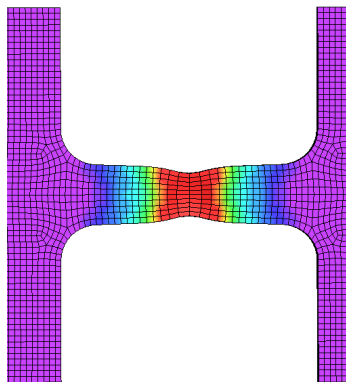


(a) Simulation.

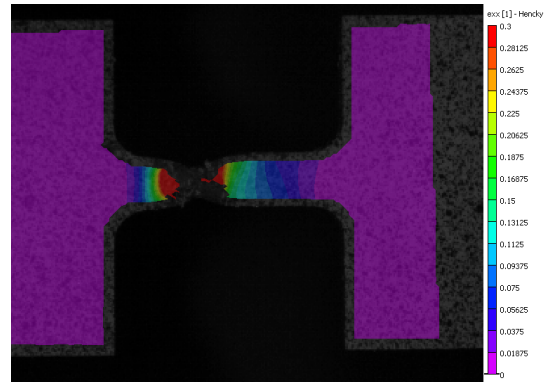


(b) DIC.

Figure 3.14: Strain comparison in the load direction at 400° C.



(a) Simulation.



(b) DIC.

Figure 3.15: Strain comparison in the load direction at 600° C.

3.3.2. Compression

Stress-Strain Relationship at Room Temperature

Among all the compression tests at Room Temperature it has been chosen M2-TMC-P4-SG1-O1-SR3-T1-N2 to represent the group of data and to be processed.

As described in Section 2.3, an extrapolation is performed also for compression tests in order to have a curve that reaches a strain value of $\varepsilon = 1$, avoiding numerical problems on LS-DYNA.

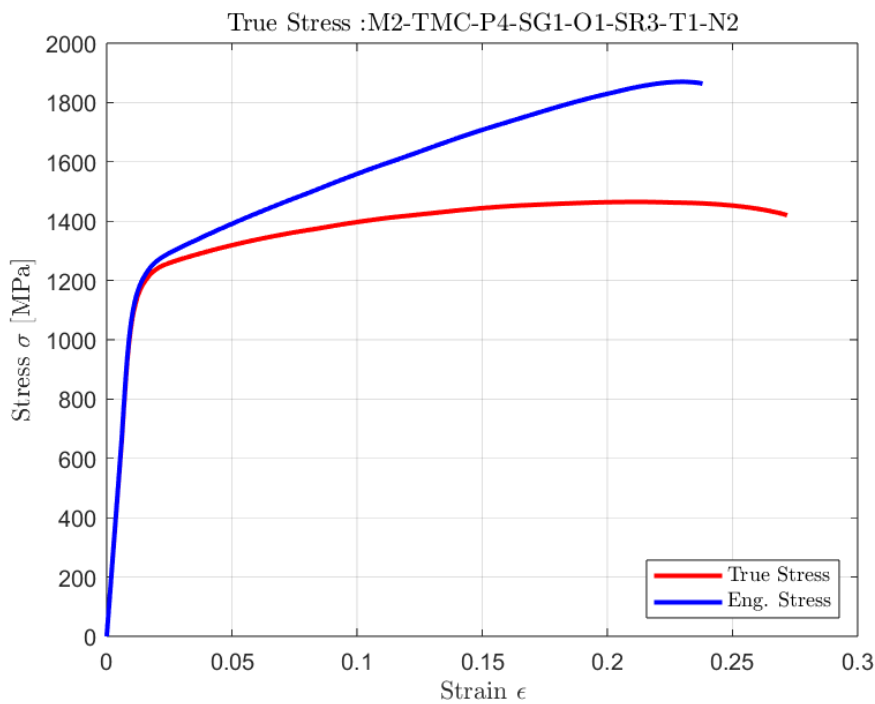


Figure 3.16: Engineering and True Stress-Strain Relationship.

In Figure 3.16, it can be observed that the engineering stress-strain curve lies above the true stress-strain curve. This behavior is opposite to what occurs in tension tests and is attributed to the increase in the cross-sectional area of the compression specimen during deformation.

The extrapolation is subsequently performed (Figure 3.17), generating 32 curves that are simulated to identify the one that best matches the force-displacement experimental test data (Figure 3.18).

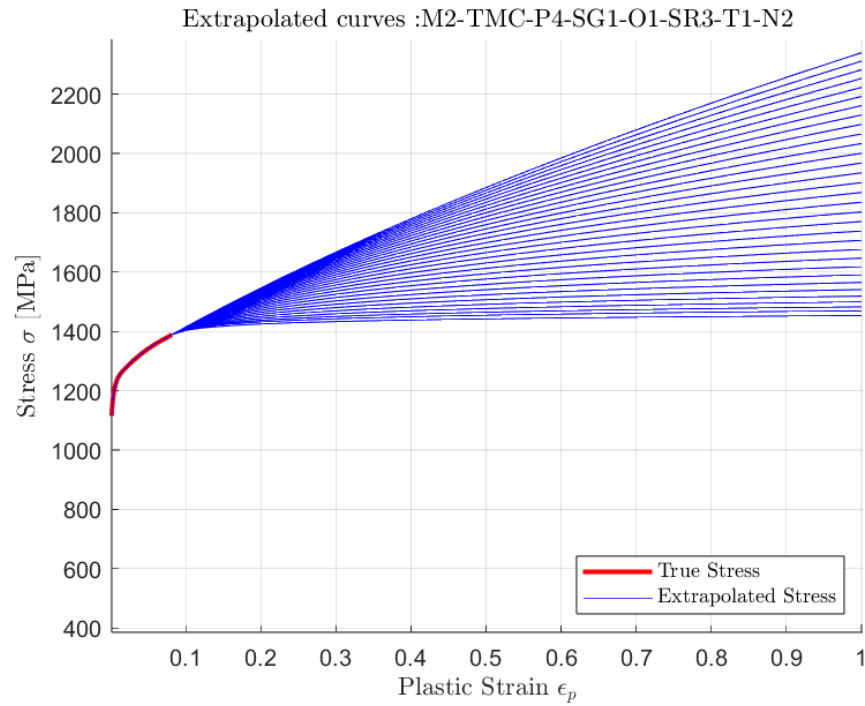


Figure 3.17: Plastic strain versus stress extrapolation curves.

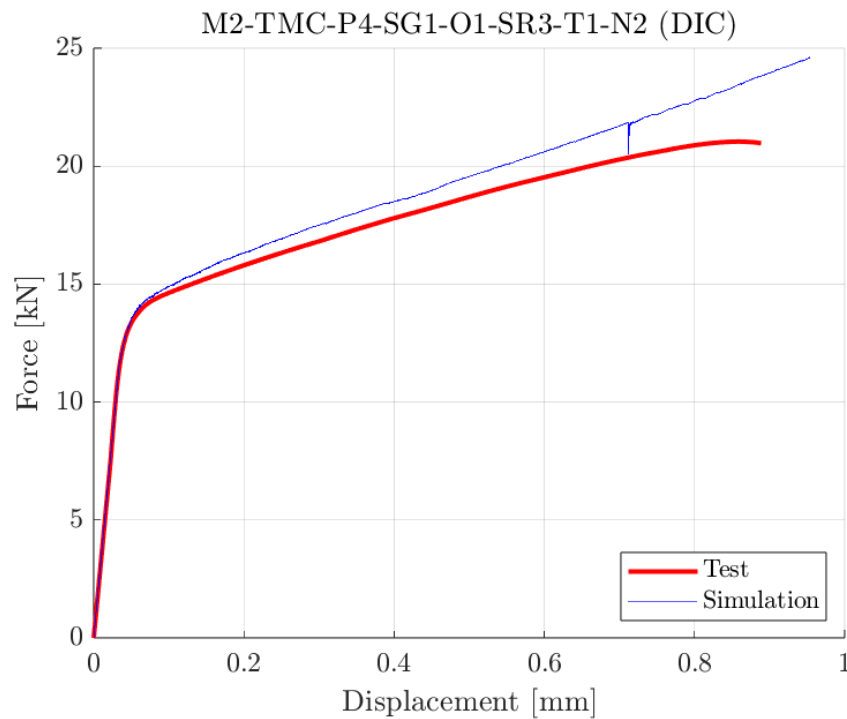


Figure 3.18: Force-Displacement Result, Curve 16.

The selected curve is then used as input for the temperature table LCCT in the MAT_224_GYS model at room temperature, Figure 3.19 .

Furthermore, the strain in the load direction obtained from the DIC and the simulation is compared. Although the quality of the DIC images is not optimal and the experimental test exhibits some asymmetry, a similarity can still be observed between the two contours and the strain values (Figure 3.20).

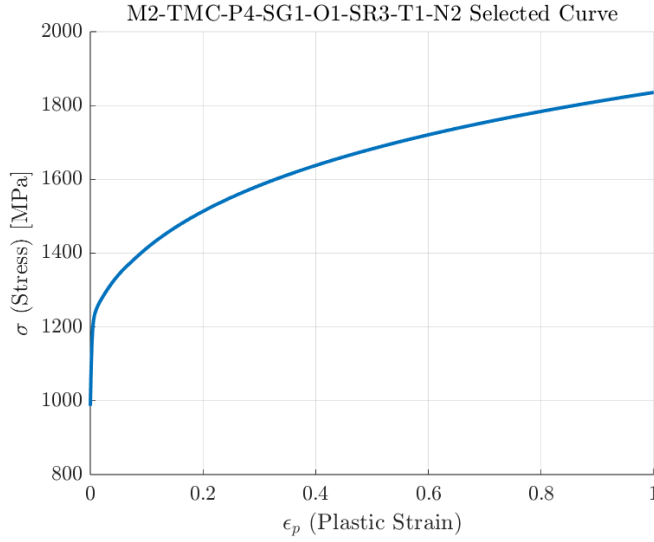


Figure 3.19: Selected Stress-Strain input curve.

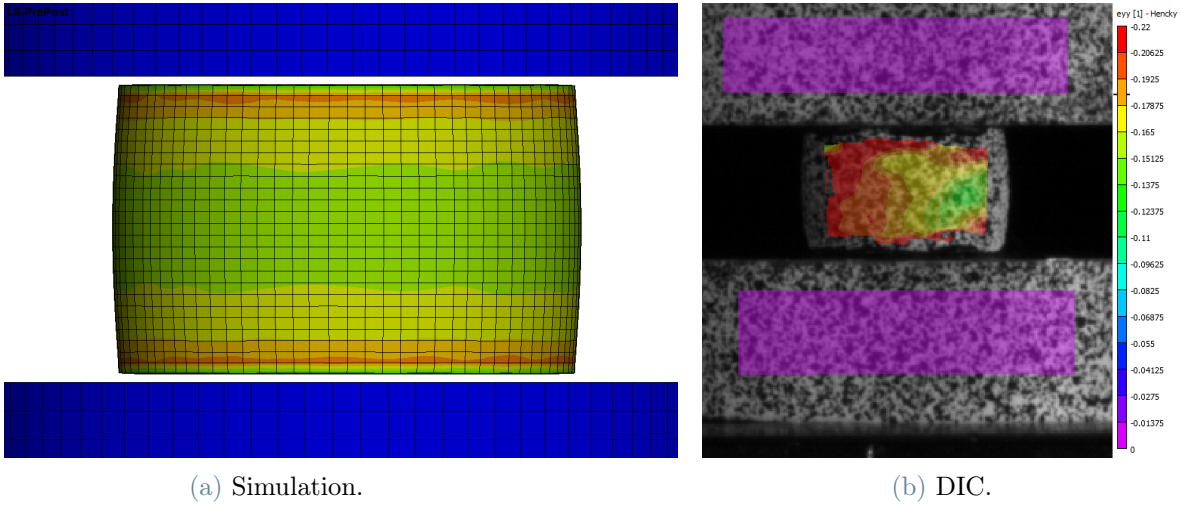


Figure 3.20: Strain comparison in the load direction at Room Temperature.

Stress-Strain Relationship at Other Temperatures

The same procedure and consideration discussed for tension tests are applied to tests conducted at other temperatures. The stress-strain curves used as input for the LCCT table of the `*MAT_224_GYS` model are plotted in Figure 3.21 . It can be observed that the curves at different temperatures do not intersect.

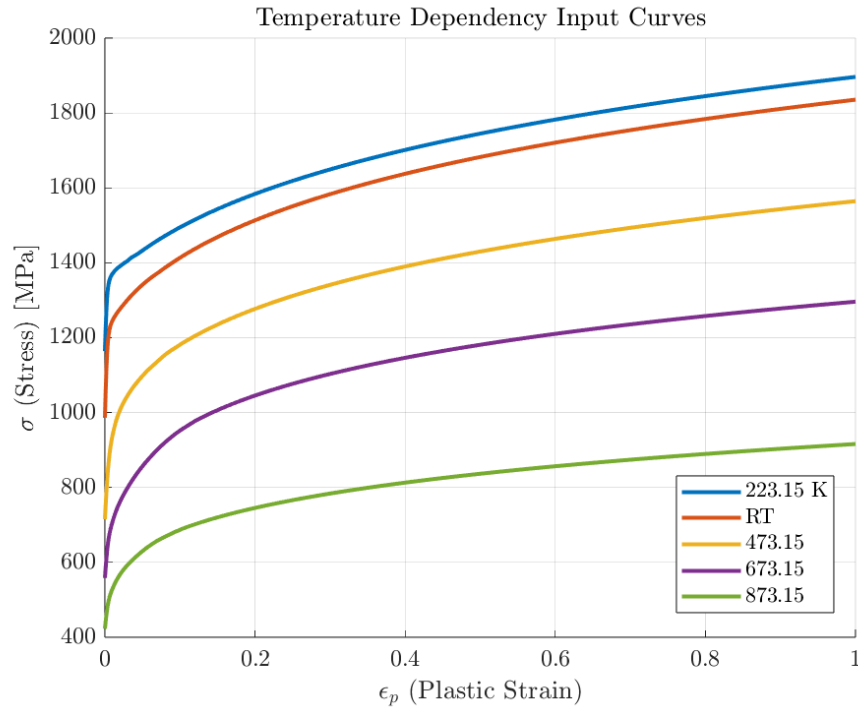


Figure 3.21: Selected Stress-Strain input curves.

Figures 3.22, 3.23 , 3.24 and 3.25 present the force-displacement comparisons between the simulation and test data for T2, T3, T4, and T5, respectively. All results show good agreement. For the compression tests, some of the DIC images are either missing or of low quality and are therefore deemed unreliable for presentation.

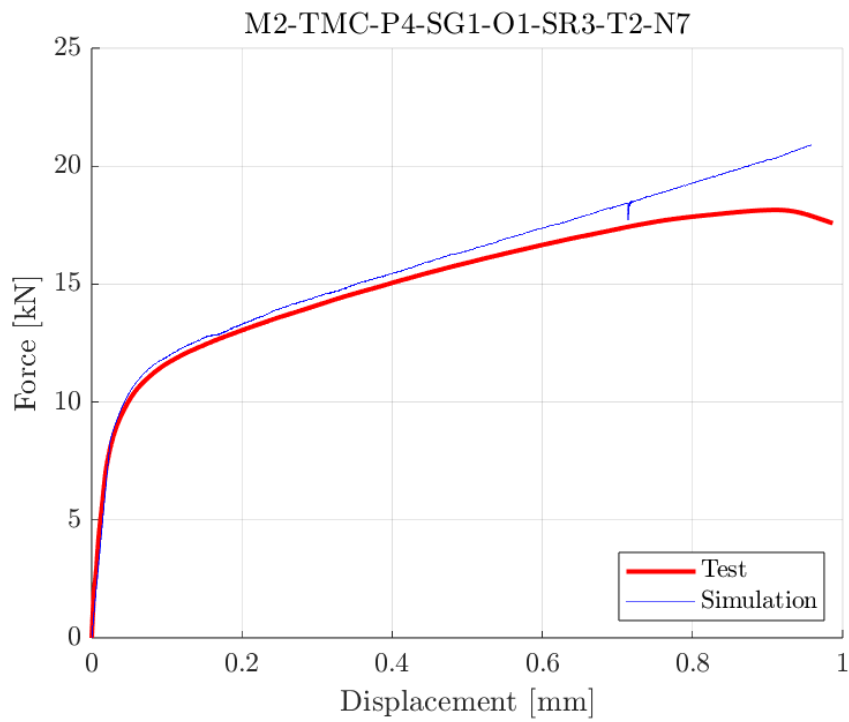


Figure 3.22: Force-Displacement Result for T2, Curve 16.

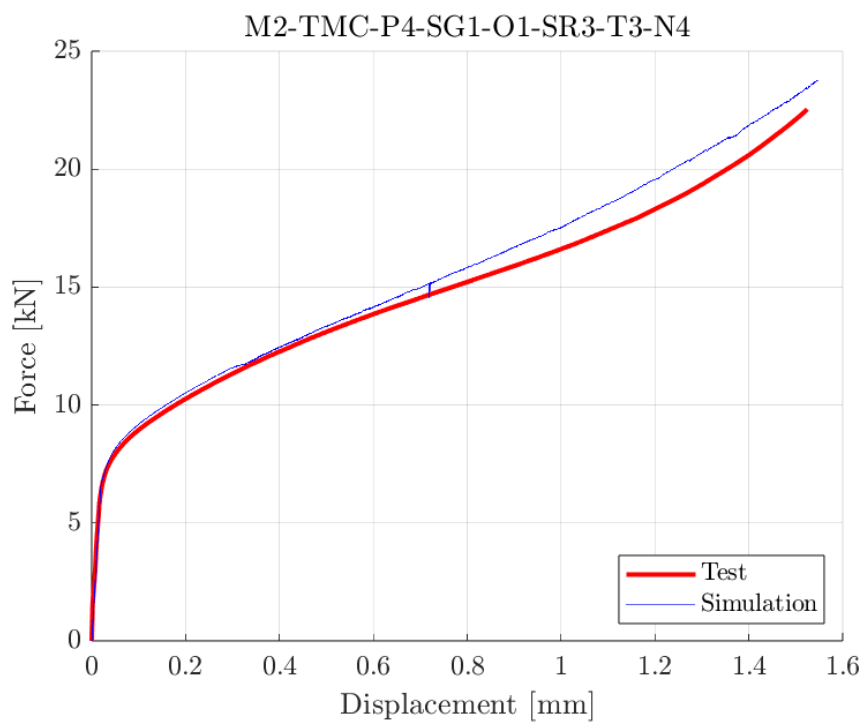


Figure 3.23: Force-Displacement Result for T3, Curve 16.

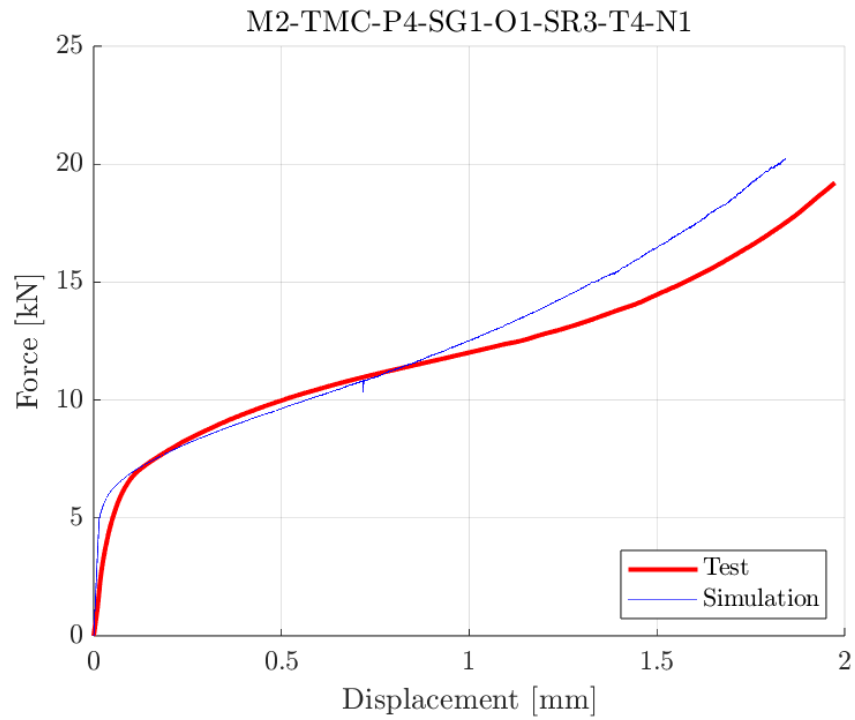


Figure 3.24: Force-Displacement Result for T4, Curve 16.

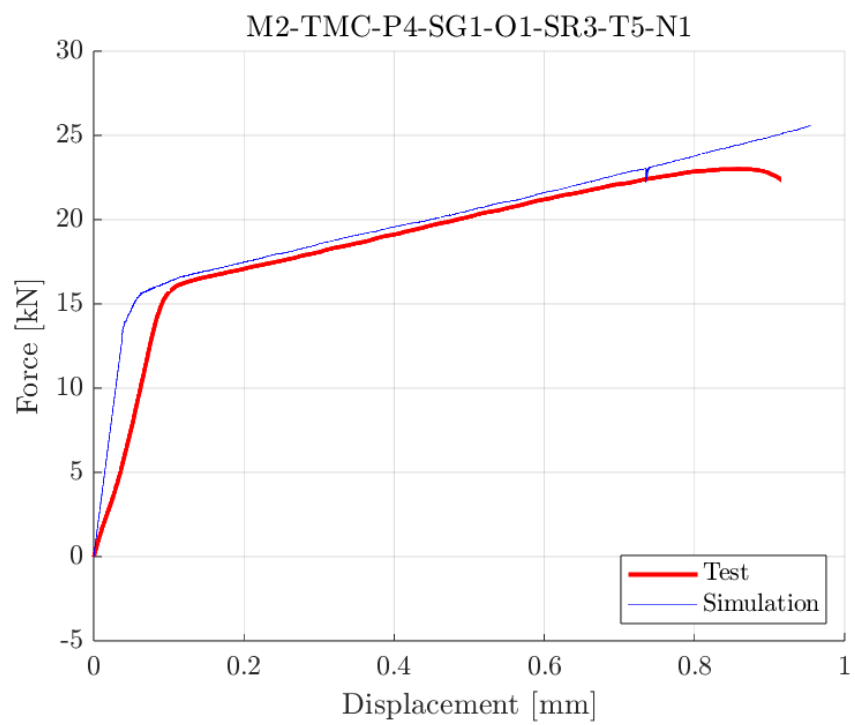


Figure 3.25: Force-Displacement Result for T5, Curve 16.

3.4. Stress strain relationship at a single, nominal quasi-static strain rate

3.4.1. Tension

The quasi-static tests conducted at a strain rate of 10^{-4} s^{-1} are listed in Table 3.7.

Table 3.7: Tension Tests at strain rate 10^{-4} s^{-1} .

Series	Test Name	Stock	Specimen	Orientation	SR [1/s]	Temp. [°C]
Tension	M2-TMT-P4-SG1-O1-SR1-T1-N1	0.5"	Flat Dogbone	Rolled	0.0001	RT
Strain	M2-TMT-P4-SG1-O1-SR1-T1-N2	0.5"	Flat Dogbone	Rolled	0.0001	RT
Rate	M2-TMT-P4-SG1-O1-SR1-T1-N7	0.5"	Flat Dogbone	Rolled	0.0001	RT
Series	M2-TMT-P4-SG1-O1-SR1-T1-N8	0.5"	Flat Dogbone	Rolled	0.0001	RT
	M2-TMT-P4-SG1-O1-SR1-T1-N9	0.5"	Flat Dogbone	Rolled	0.0001	RT

Among these tests, M2-TMT-P4-SG1-O1-SR1-T1-N1 was identified as the most representative at this strain rate. For the lower rate tests, flat dog-bone specimens were pulled at room temperature using the Instron machine. The simulations presented herein were conducted at a constant loading speed of 1 m/s, employing a single stress-strain curve. Following the procedures outlined in Section 2.2.3, the true stress-strain curve was compared with the tangent modulus curve, and the intersection of these curves was identified as the necking point. The plastic strain at necking was determined to be 0.13119 (see Figure 3.26).

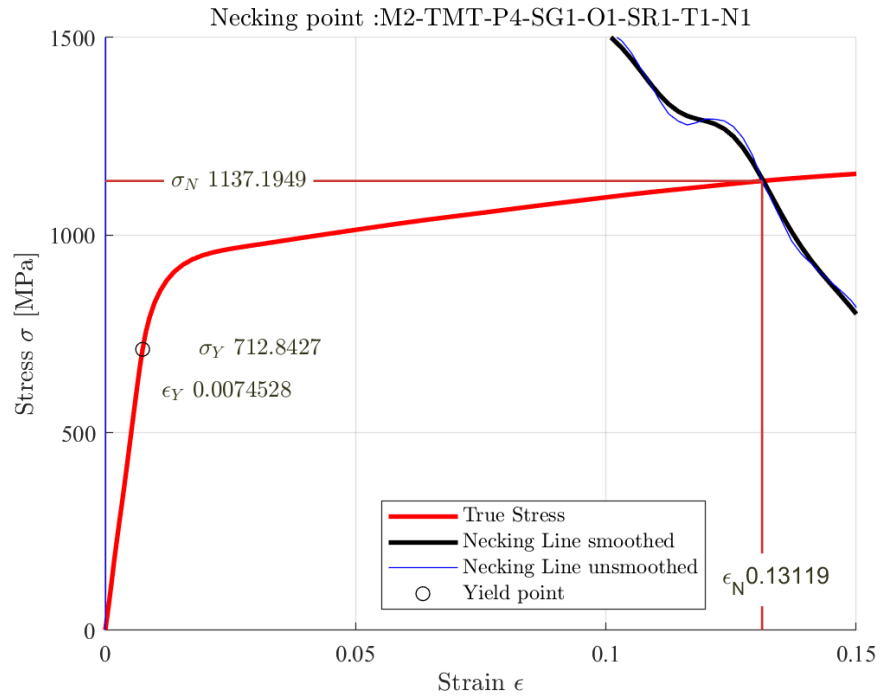


Figure 3.26: True stress-strain relationship and necking point judgment.

A total of 32 trial curves were generated through exponential extrapolation (Figure 3.27). Each of these derived stress-strain curves was utilized to generate a corresponding *MAT_224 keyword input, subsequently employed in the simulation of the tensile test.

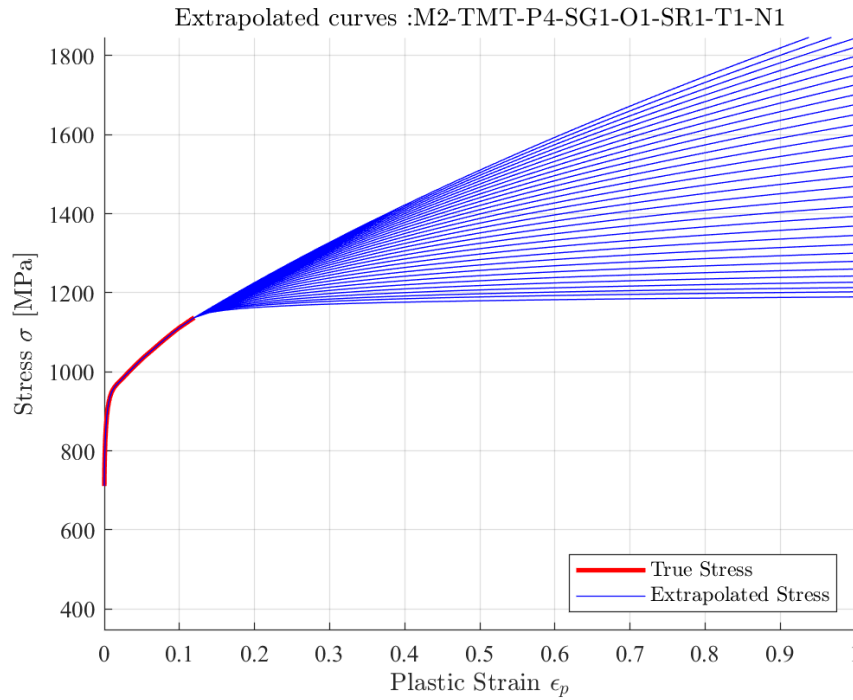


Figure 3.27: Plastic strain versus stress extrapolation curves.

As discussed in Section 2.2.3, a cross-plot of elongation versus cross-sectional force was compared against the force-displacement curve obtained from the experiment. This iterative process involved repeating simulations using each extrapolated candidate input curve until a match with the experimental force-displacement curve was achieved (Figure D.1).

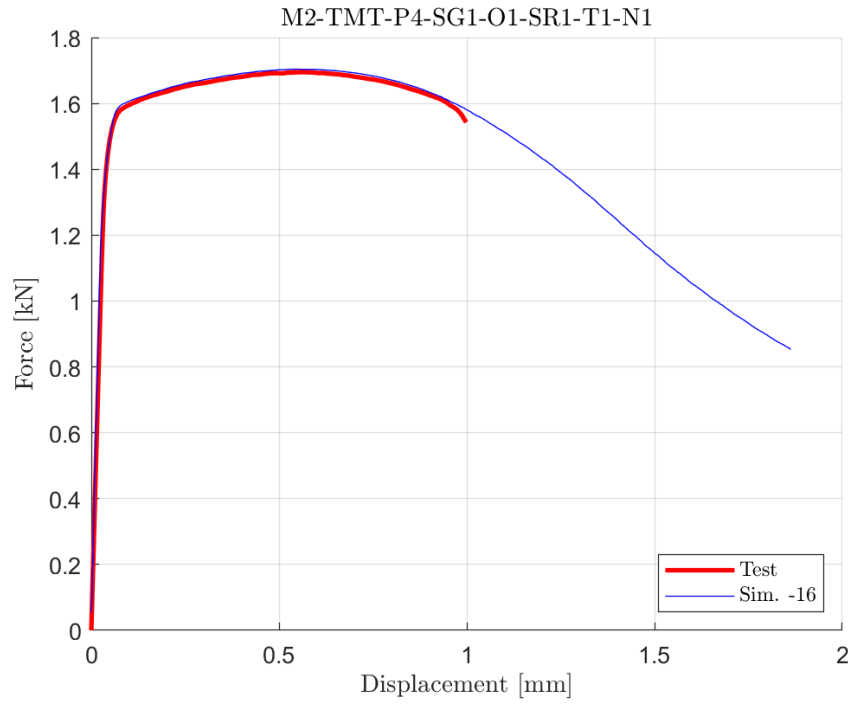


Figure 3.28: Force-Displacement Result, Curve 16.

A simulation contour depicting the 1st principal strain from this simulation was compared with the DIC image acquired immediately before fracture during the test, showing a favorable agreement (Figure 3.29).

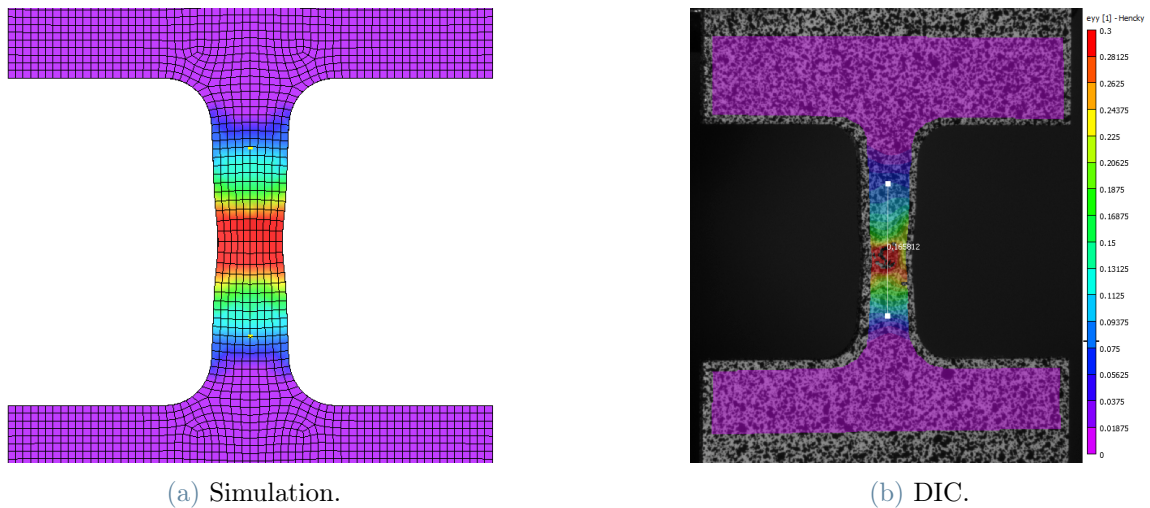


Figure 3.29: Strain comparison in the load direction.

3.4.2. Compression

Similarly to the approach used for tension, but accounting for differences such as the absence of necking (as explained in 2.3), the compression test M2-TMC-P4-SG1-O1-SR1-T1-N4 was selected as representative of tests at a strain rate of 10^{-4} s^{-1} .

Table 3.8: Compression Tests at strain rate 10^{-4} s^{-1} .

Series	Test Name	Stock	Specimen	Orientation	SR [1/s]	Temp. [°C]
Compression	M2-TMC-P4-SG1-O1-SR1-T1-N4	0.5"	Cylindrical	Rolled	0.0001	RT
Strain Rate	M2-TMC-P4-SG1-O1-SR1-T1-N5	0.5"	Cylindrical	Rolled	0.0001	RT
Series	M2-TMC-P4-SG1-O1-SR1-T1-N6	0.5"	Cylindrical	Rolled	0.0001	RT

In Figure 3.30, the comparison between simulation and experimental test results for force-displacement graphs is shown.

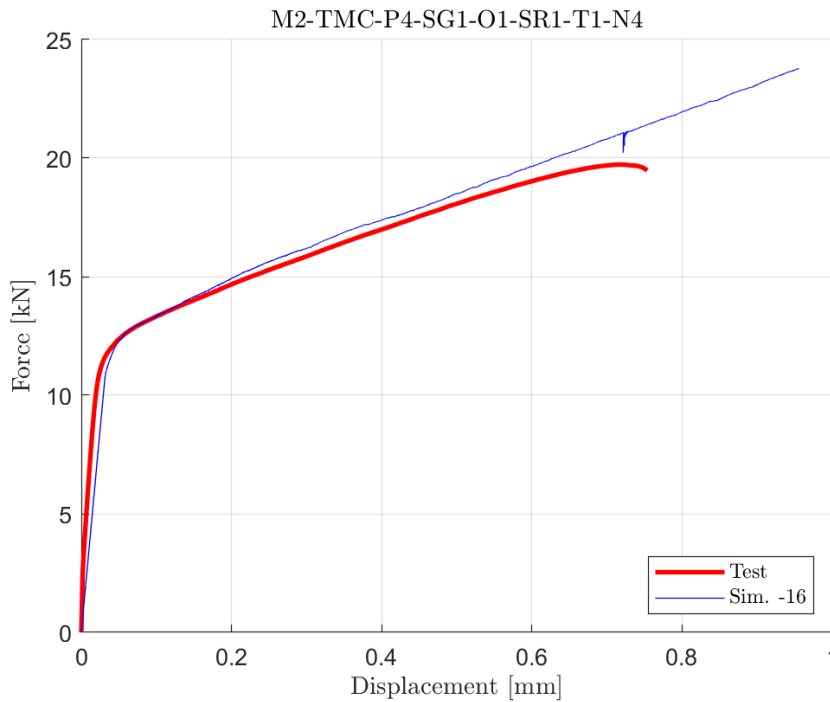


Figure 3.30: Force-Displacement Result, Curve 16.

Furthermore, the Digital Image Correlation (DIC) image can be compared with the simulation's strain contour at the same displacement, immediately prior to failure (Figure 3.31).

It is worth noting that the test displays asymmetries resulting from imperfect alignment of the specimen, in contrast to the simulation.

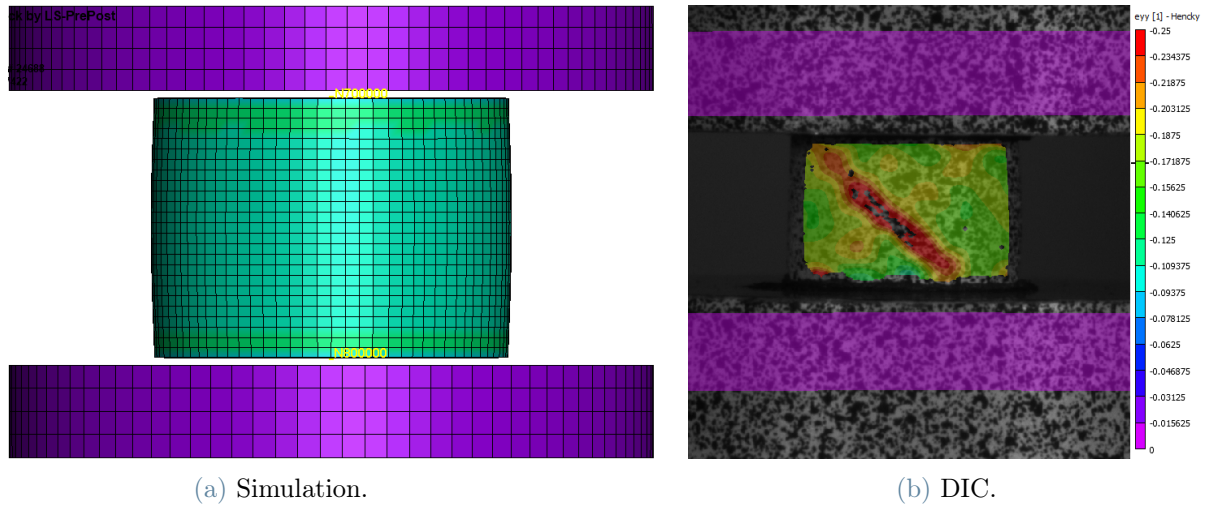


Figure 3.31: Strain comparison in the load direction.

3.5. Stress strain tabulated input of multiple strain rates and temperatures

The high strain rate testing used to generate the higher rate Ti-6Al-4V stress-strain curves is commonly referred to as split-Hopkinson (SHB) bar or Kolsky bar tests (see Appendix B). This technique differs from lower rate testing in that, instead of being displacement-controlled, the specimen is subjected to impulsive loading. The impulsive loading and smaller specimen size allow for higher strain rates to be achieved.

A consequence of the impulsive nature of the loading, which impacts the analysis, is that the test's nominal strain rate description becomes even less precise than in the lower rate tests, due to the varying strain rate during the test. However, the DIC strain measurements accurately capture the actual strain rates, which vary both spatially and temporally.

The method for creating higher rate stress-strain curves from lower rate stress-strain data, using the strain rate sensitivity measured in the higher rate tension and compression tests, was introduced in Section 2.5.3. *MAT_224 input stress-strain curves must be defined both at a constant temperature and at a constant strain rate.

Due to the requirement for isothermal and isorate input curves, it is not feasible to directly derive the higher rate input curves from the split-Hopkinson bar tests, as these tests are neither isorate nor isothermal. In contrast, the lower rate tests are isothermal, and the curves derived from them can serve as a baseline for synthesizing high strain rate stress-strain curves. The 10^{-4} s^{-1} isothermal stress-strain curve served as the baseline for the

Ti-6Al-4V higher strain rate curves. To ensure numerical accuracy, the number of higher rate curves generated was greater than the number of high strain rate tests performed.

The higher rate stress-strain curves were initially synthesized by appropriately offsetting the 10^{-4} s^{-1} baseline curve to match the stress at 2.5% strain of the higher rate responses, following the trend indicated by the nominal strain rates.

It has been chosen the stress at 2.5 % strain because of the need of having a point between the yielding point and the necking point.

Since the nominal strain rates do not accurately reflect the varying strain rates that occur in a split-Hopkinson bar test, this initial set of curves will not produce simulations that match the higher rate tests. An iterative process is required in which the stress offset is varied. This iterative process is further complicated by the transitioning rate sensitivity between the logarithmic and linear regions (see Section 2.5.3).

Each split-Hopkinson bar test provides unique information, as the range of strain rates encountered in each test is distinct. Therefore, each of the high strain rate tests (SHB apparatus) listed in the Tension Strain Rate Dependence Table 3.5 and Compression Strain Rate Dependence Table 3.8 was simulated multiple times, varying the stress offsets until a satisfactory match to the test data from each test was achieved. Forty iterations were conducted before the simulation predictions matched all the high strain rate test tension data, including force versus displacement, strain rate versus strain, force versus strain, temperature versus time, temperature versus strain and the strain contours just before fracture (when available). For the compression tests, only eight iterations were needed.

The final strain rate sensitivity curves for tension and compression are plotted in Figure 3.32 and Figure 3.33.

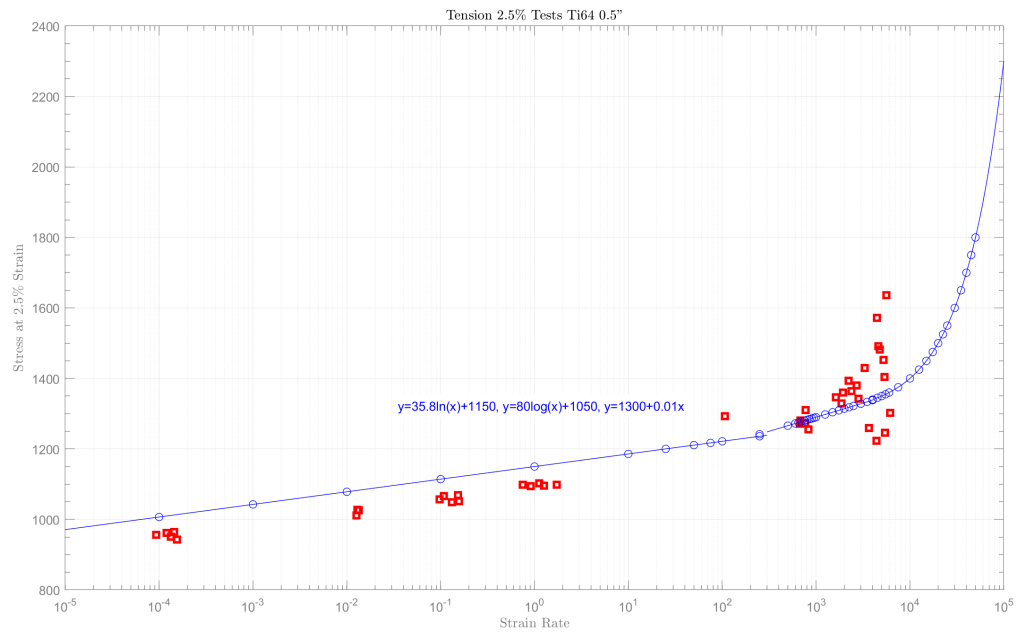


Figure 3.32: Strain-Rate sensitivity curve in tension.

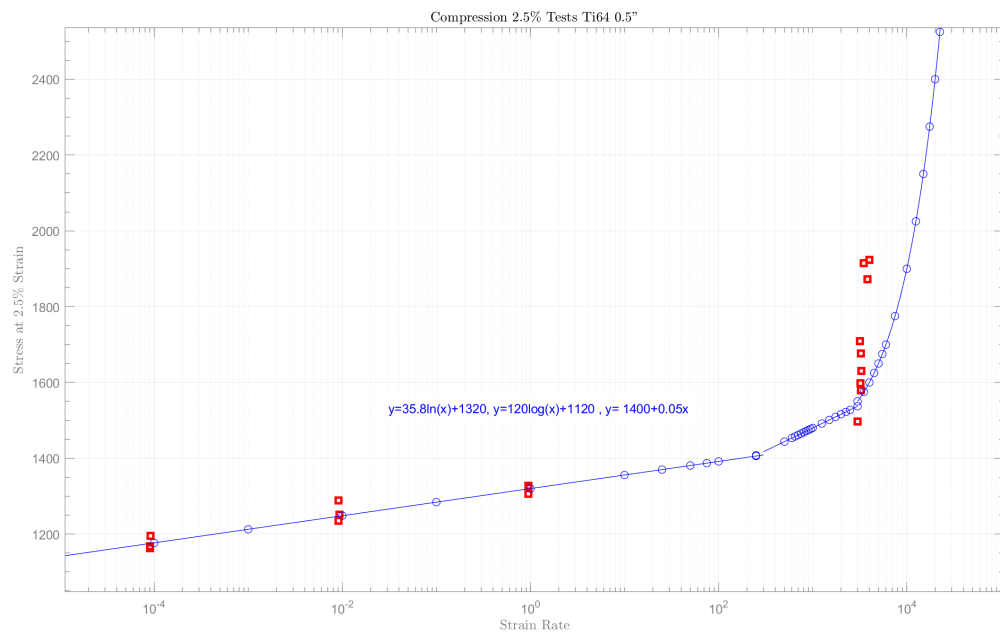


Figure 3.33: Strain-Rate sensitivity curve in compression.

The complete table of all stress-strain curves was used in the *MAT_224 input for the

split-Hopkinson bar test simulations. These simulations were performed by applying the test displacements, obtained from DIC, as boundary conditions.

The fixed end of the split-Hopkinson bar tension tests was not truly fixed, and the applied displacement at the translating boundary was most accurately defined by the displacements measured by DIC. The details on how a Split Hopkinson Bar test is conducted are provided in Appendix B.

3.5.1. Tension

Ti-6Al-4V is a material that exhibits early and extreme localization at higher strain rates. As a result, it is challenging to accurately capture the strain rate in the region of maximum localization with a mesh size on the order of 0.2mm. Consequently, the strain rate is slightly underestimated.

Additionally, the tests reveal a sudden change in slope in the temperature curves, which is also due to high localization and elevated strain rates. These conditions do not allow the material enough time to dissipate heat, causing it to accumulate and resulting in a temperature increase.

However, the force values obtained from the simulations align well with those from the experimental tests, thereby validating their reliability.

It can be observed that the Young's Modulus of the material for the high strain rate tests appears to differ from that of the simulations. This is due to the fact that a specific amount of time is required to reach dynamic equilibrium. As a consequence it is not possible to determine the elastic modulus of a given material through experimental tests using a Hopkinson bar. Indeed, since equilibrium generally occurs after a certain level of strain, which may vary in magnitude, the data corresponding to the initial portion of the stress-strain curve cannot be considered reliable [17],[28] .

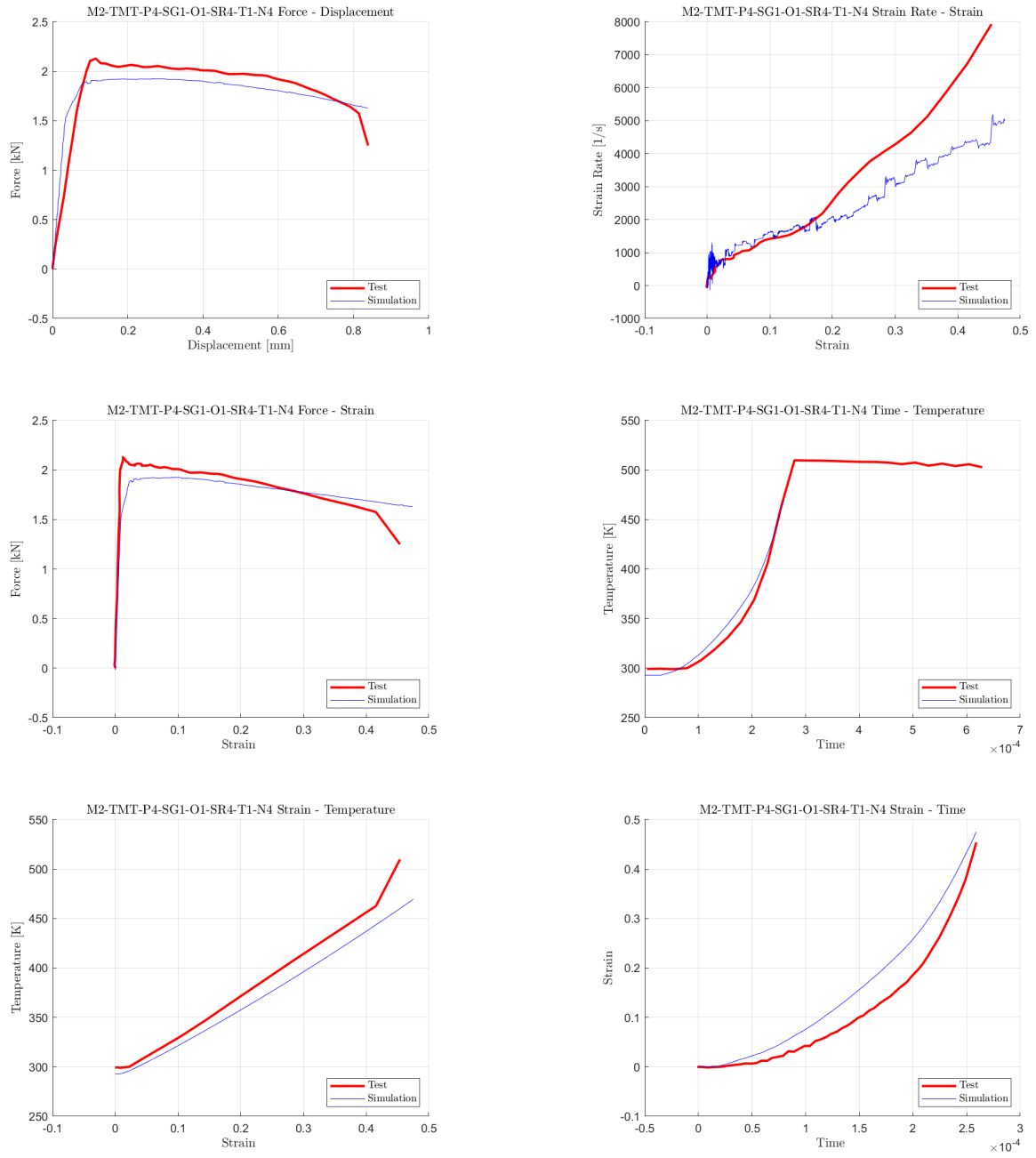


Figure 3.34: Test M2-TMT-P4-SG1-O1-SR4-T1-N4.

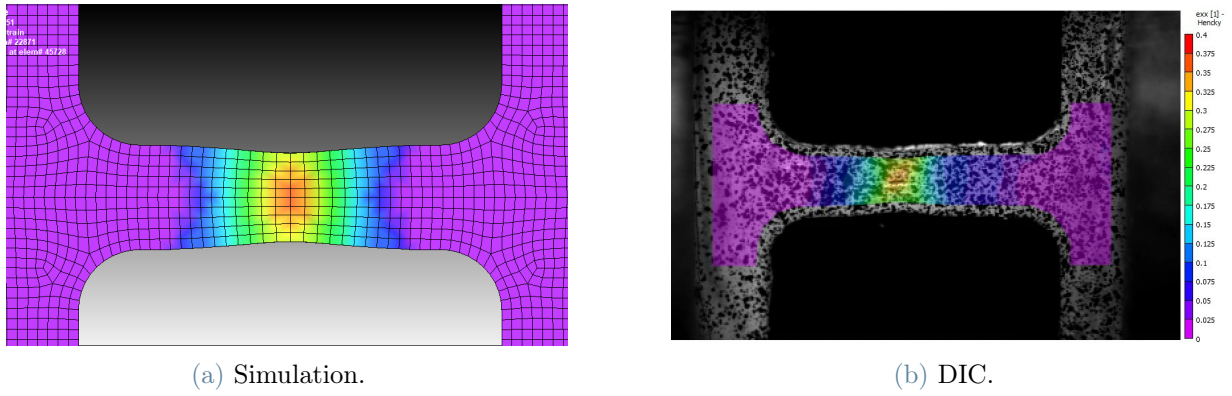


Figure 3.35: M2-TMT-P4-SG1-O1-SR4-T1-N4 Strain comparison.

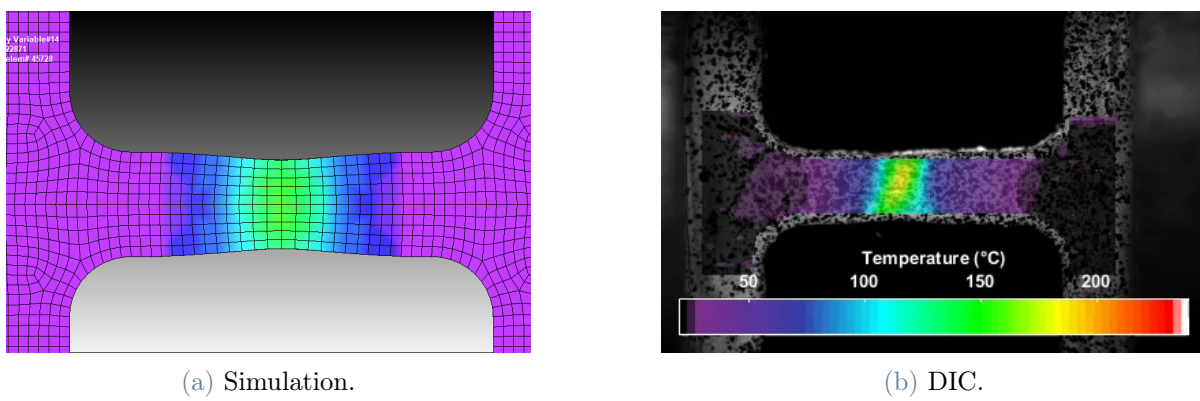


Figure 3.36: M2-TMT-P4-SG1-O1-SR4-T1-N4 Temperature comparison.

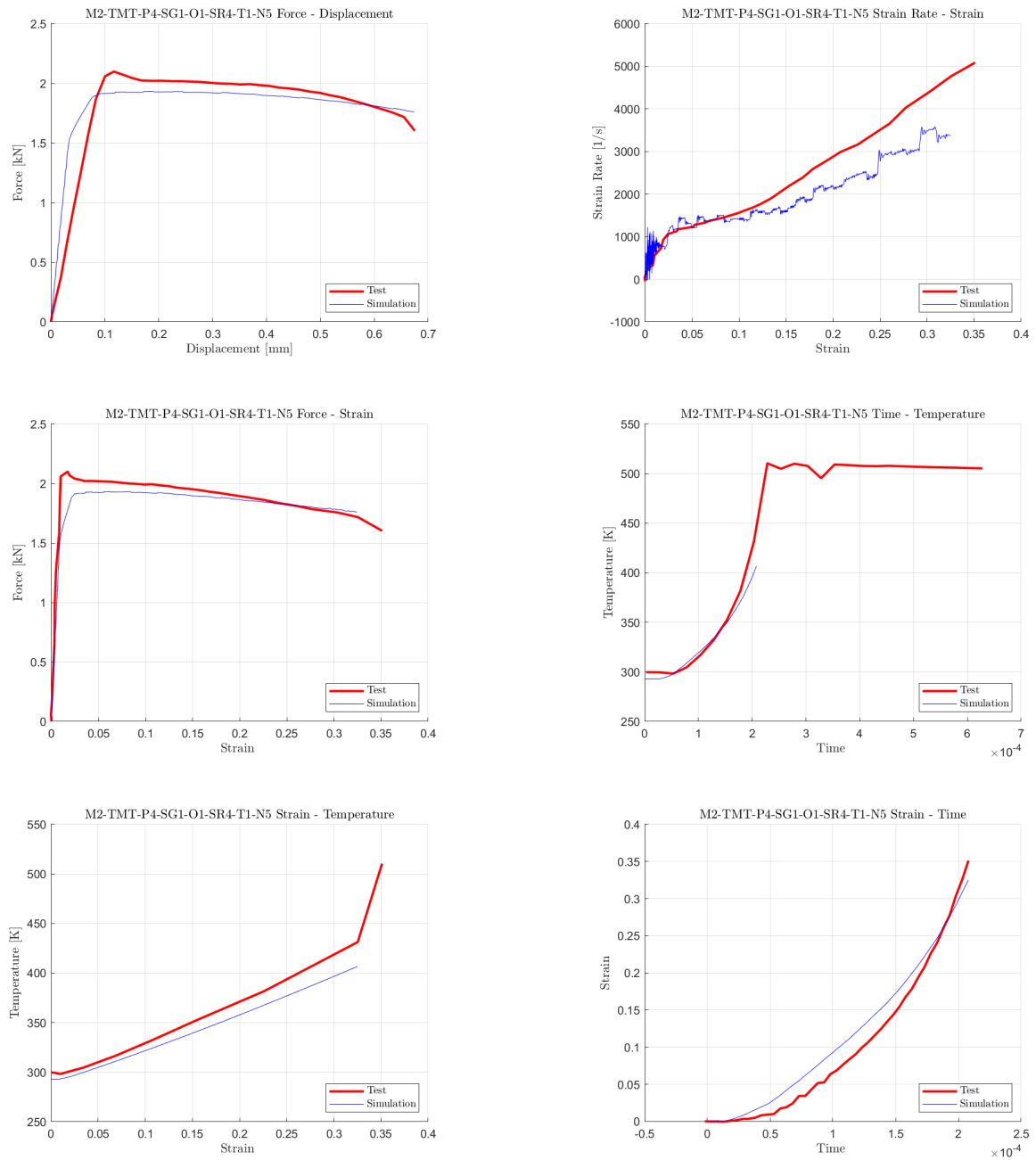


Figure 3.37: Test M2-TMT-P4-SG1-O1-SR4-T1-N5.

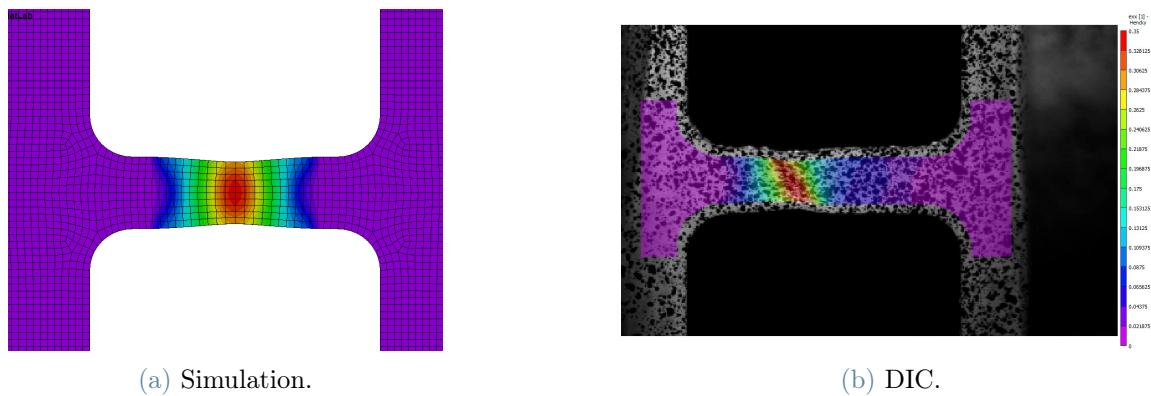


Figure 3.38: M2-TMT-P4-SG1-O1-SR4-T1-N5 Strain comparison.

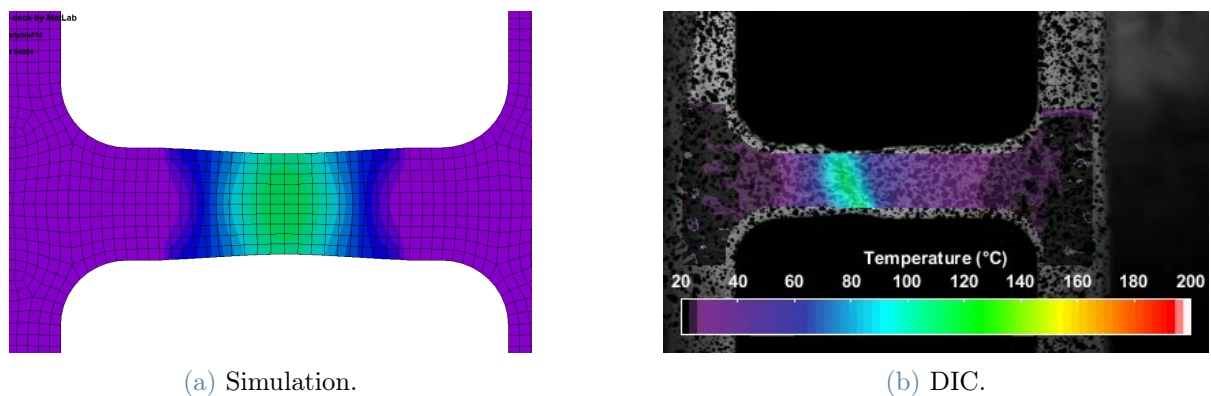


Figure 3.39: M2-TMT-P4-SG1-O1-SR4-T1-N5 Temperature comparison.

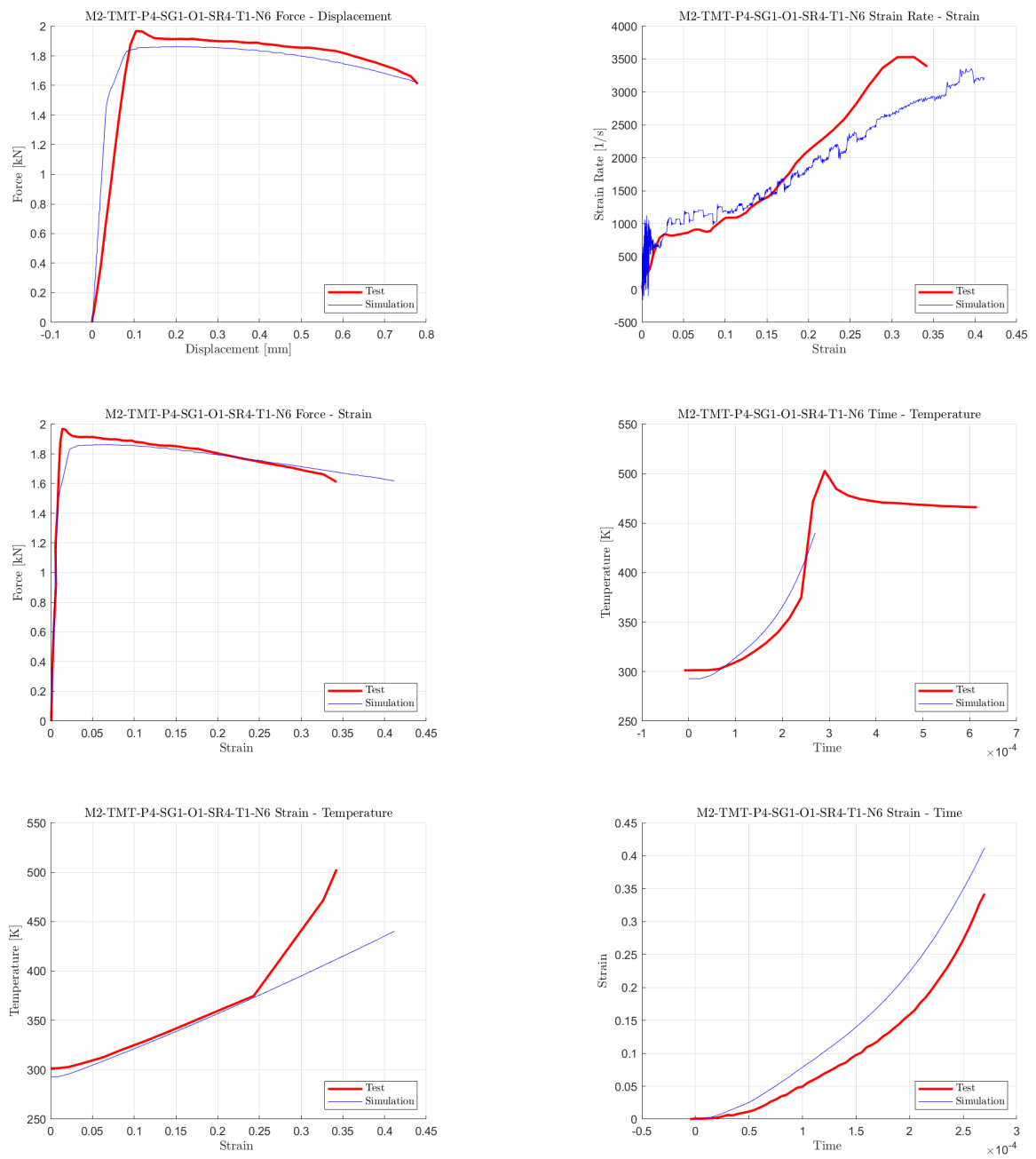


Figure 3.40: Test M2-TMT-P4-SG1-O1-SR4-T1-N6.

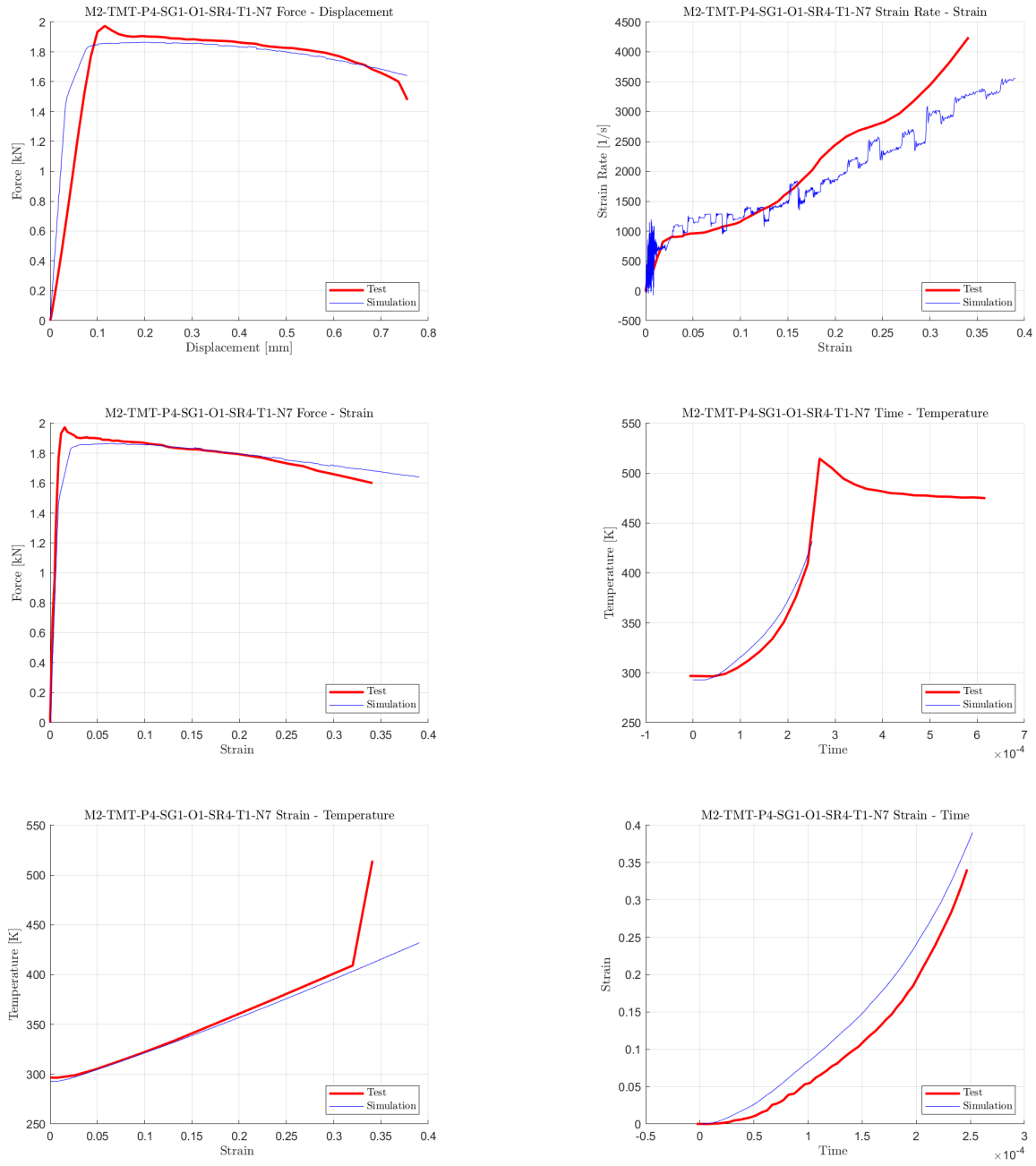


Figure 3.41: Test M2-TMT-P4-SG1-O1-SR4-T1-N7.

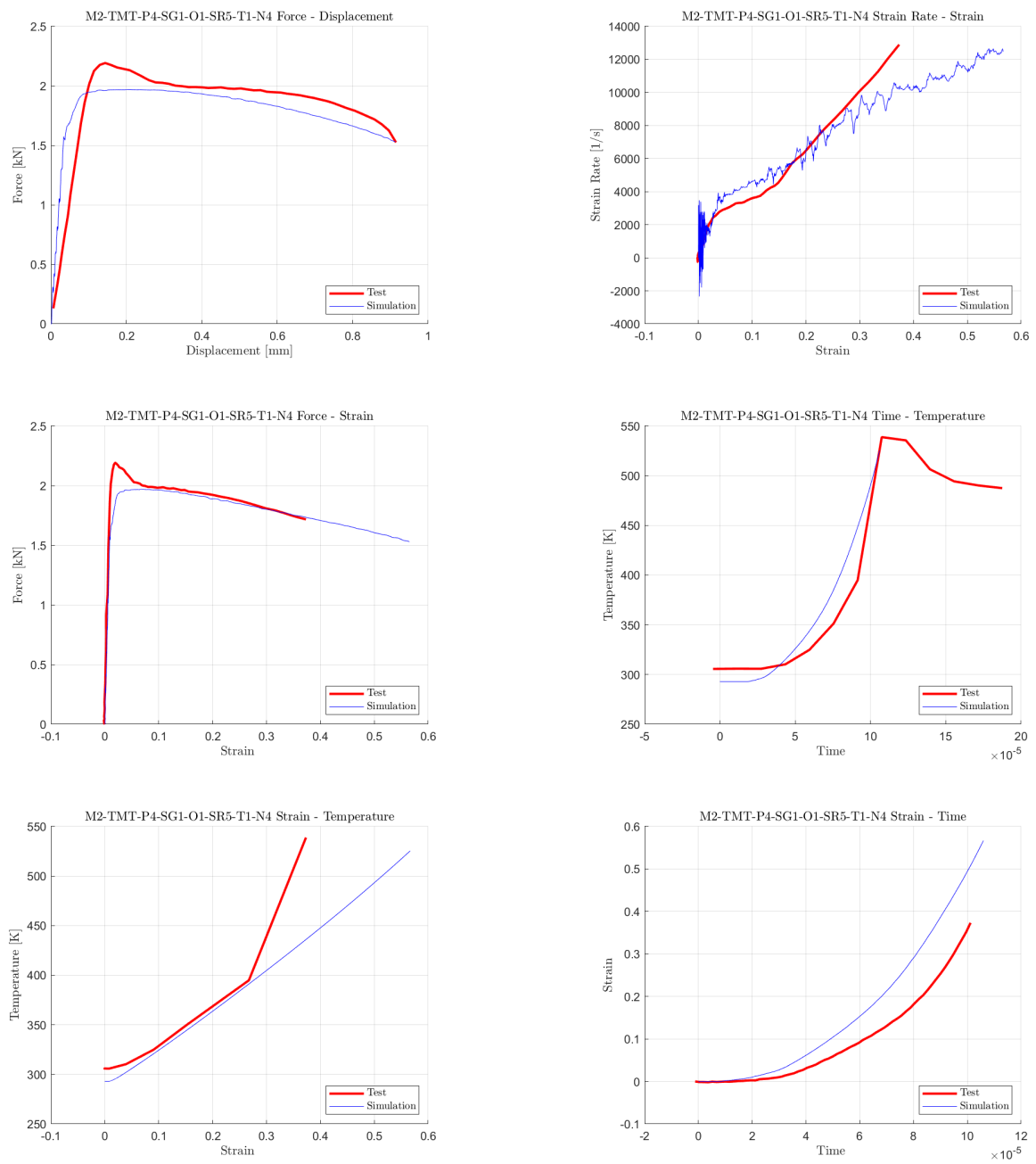


Figure 3.42: Test M2-TMT-P4-SG1-O1-SR5-T1-N4.

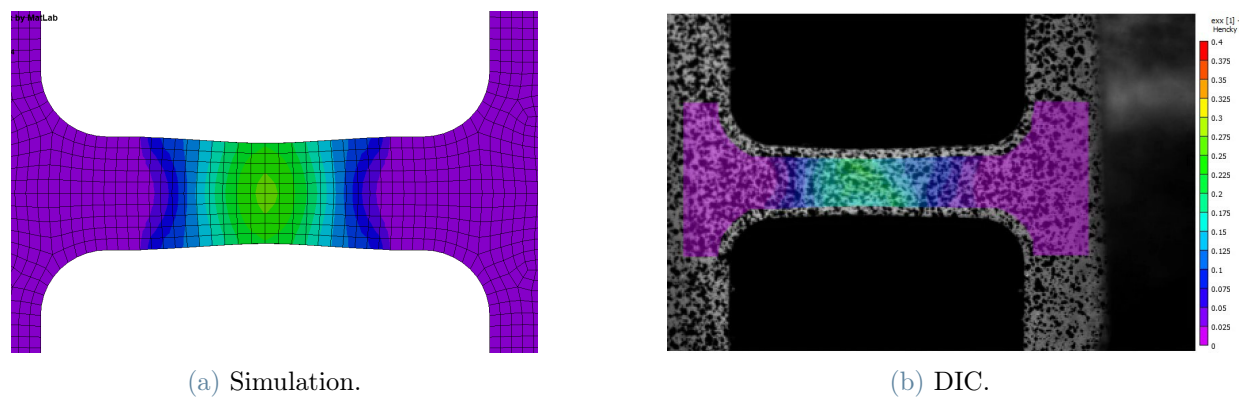


Figure 3.43: M2-TMT-P4-SG1-O1-SR5-T1-N4 Strain comparison.

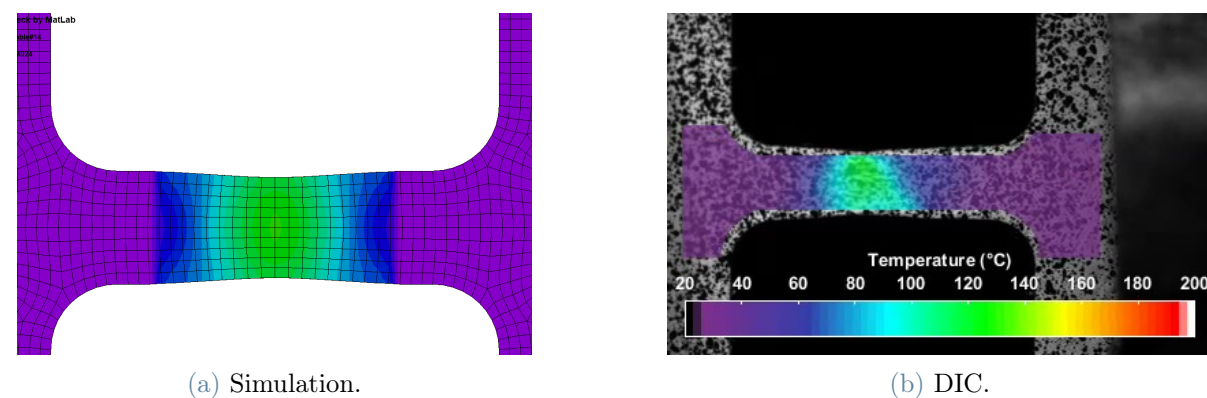


Figure 3.44: M2-TMT-P4-SG1-O1-SR5-T1-N4 Temperature comparison.

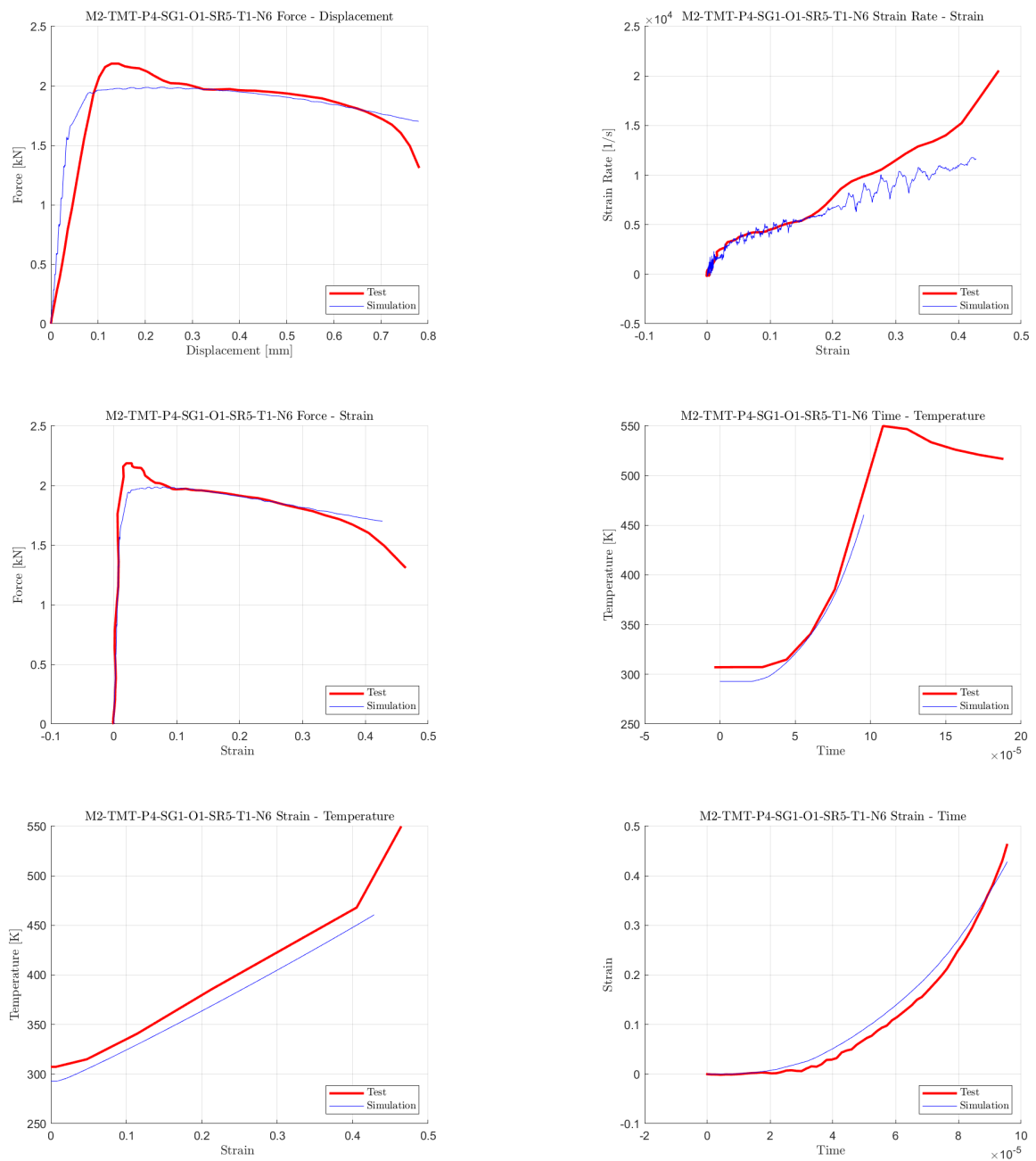


Figure 3.45: Test M2-TMT-P4-SG1-O1-SR5-T1-N6.

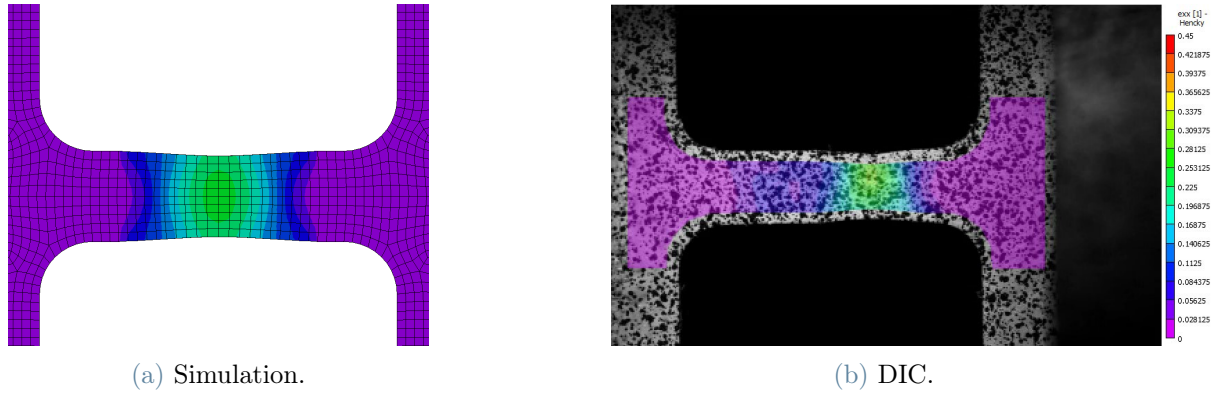


Figure 3.46: M2-TMT-P4-SG1-O1-SR5-T1-N6 Strain comparison.

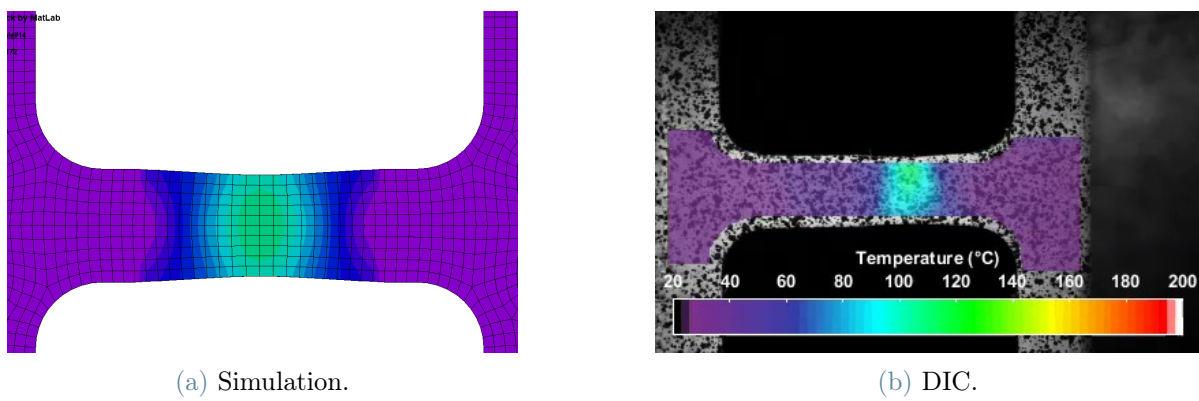


Figure 3.47: M2-TMT-P4-SG1-O1-SR5-T1-N6 Temperature comparison.

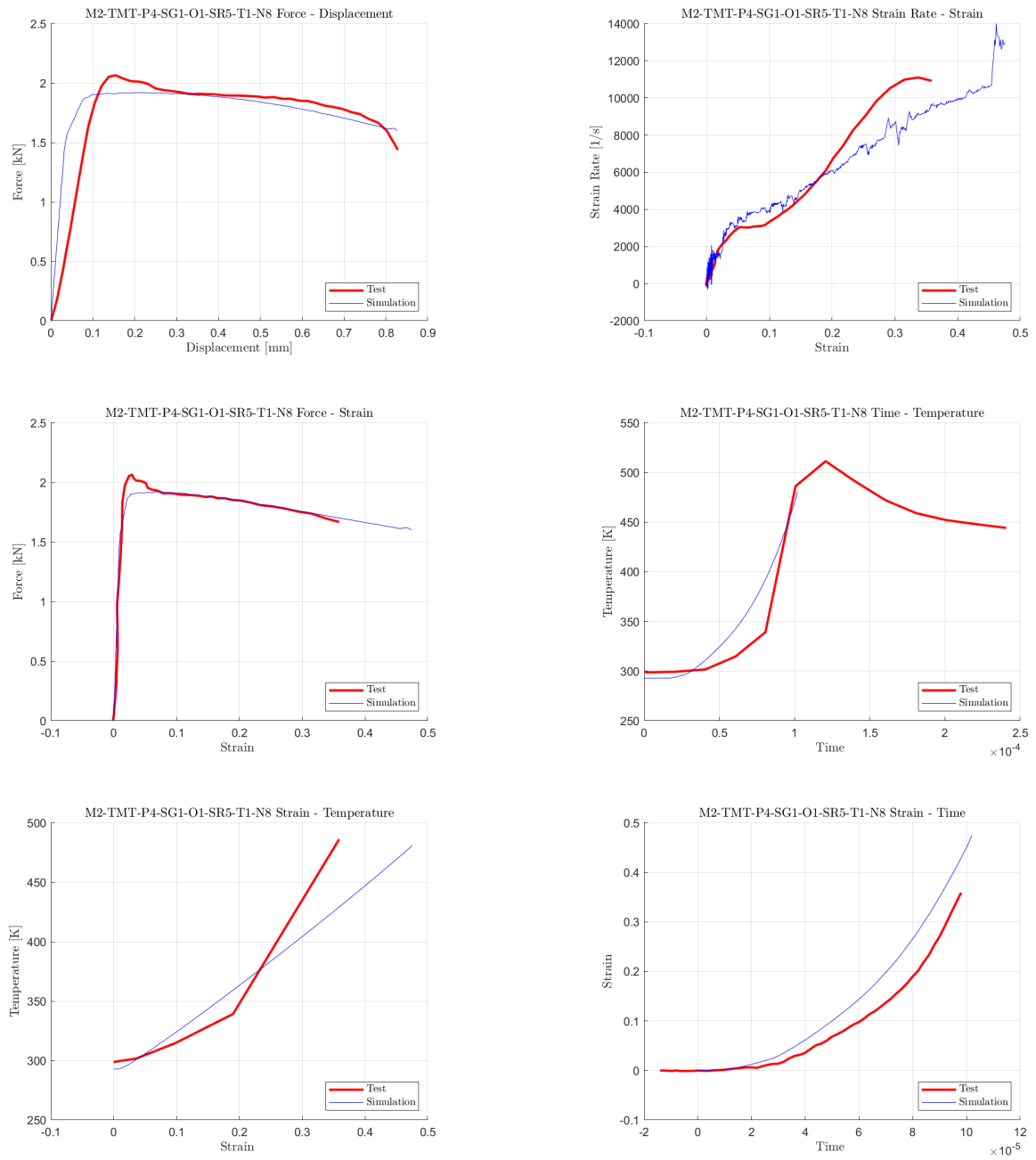


Figure 3.48: Test M2-TMT-P4-SG1-O1-SR5-T1-N8.

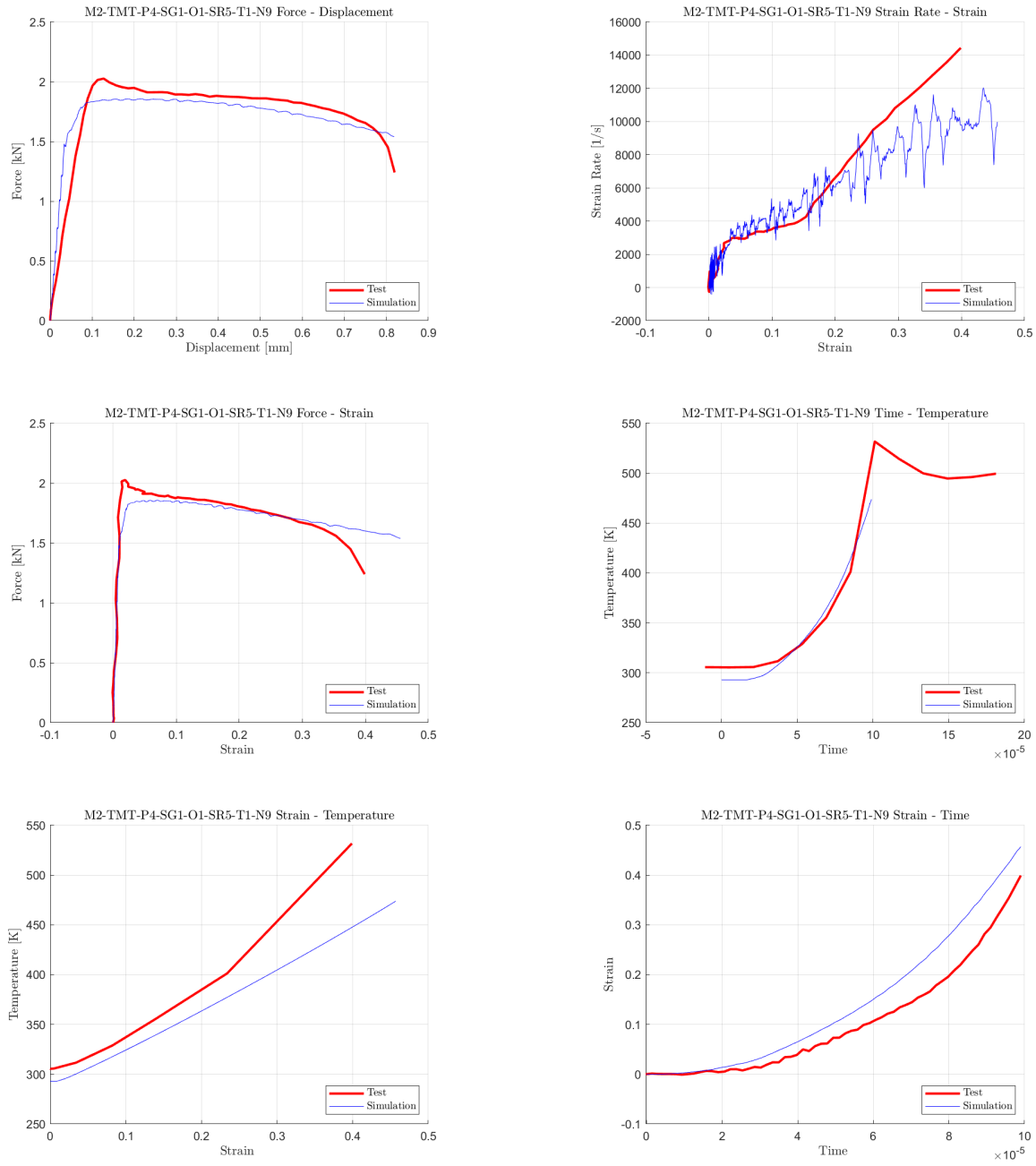


Figure 3.49: Test M2-TMT-P4-SG1-O1-SR5-T1-N9.

3.5.2. Compression

For the high-strain rate compression tests, there is a strong correlation between the simulations and experimental results, as the compression tests are significantly more stable than the tensile tests, yielding more reliable outcomes. However, temperature data is not available for the compression tests, and therefore cannot be compared with the simulations. Additionally, the DIC images suffer from low quality due to challenges in achieving perfect symmetry in the load application. As a result, only the DIC images deemed usable and effectively comparable to the simulations are included.

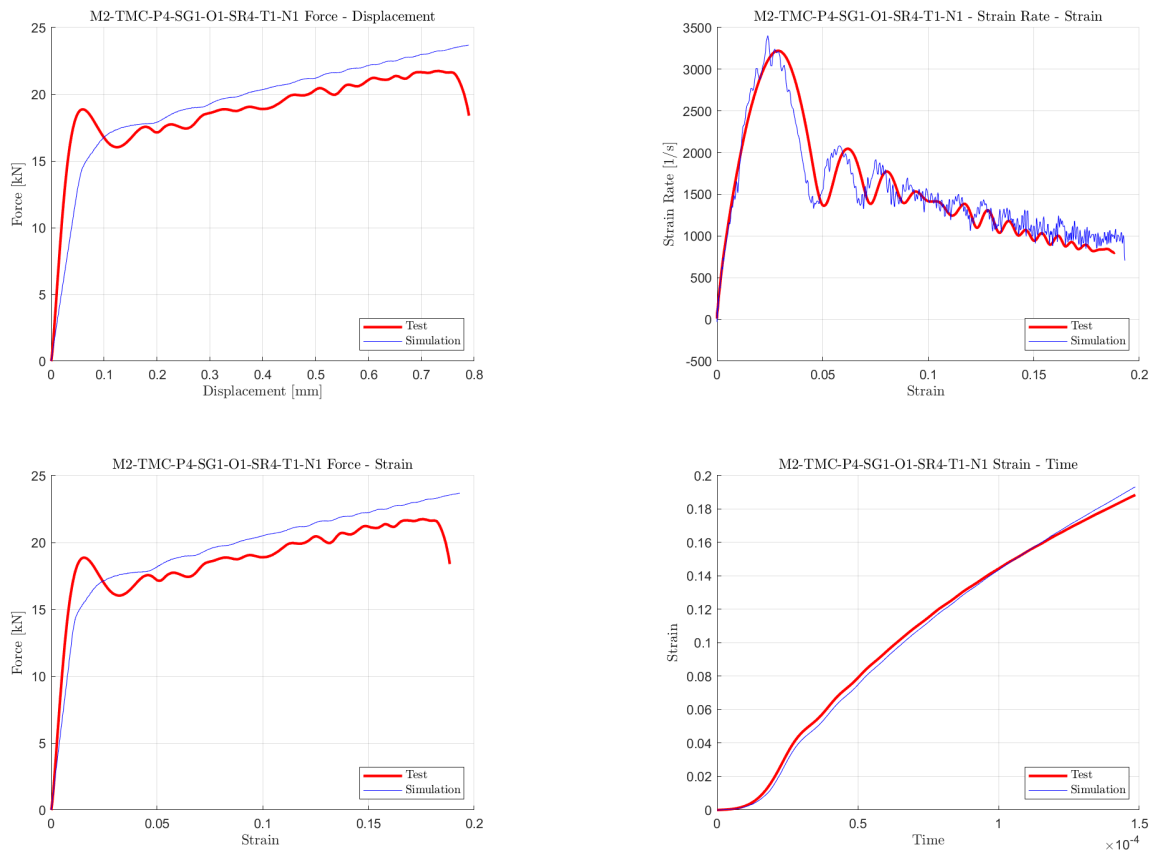
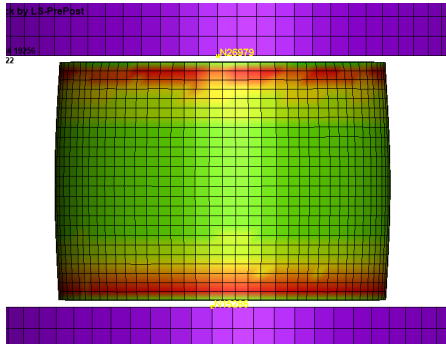
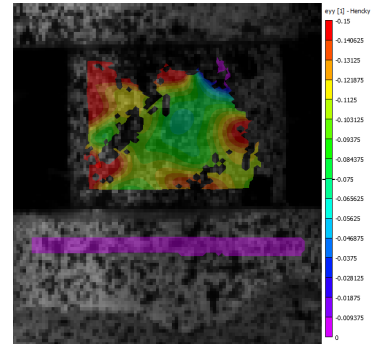


Figure 3.50: Test M2-TMC-P4-SG1-O1-SR4-T1-N1.



(a) Simulation.



(b) DIC

Figure 3.51: M2-TMC-P4-SG1-O1-SR4-T1-N1 Strain comparison.

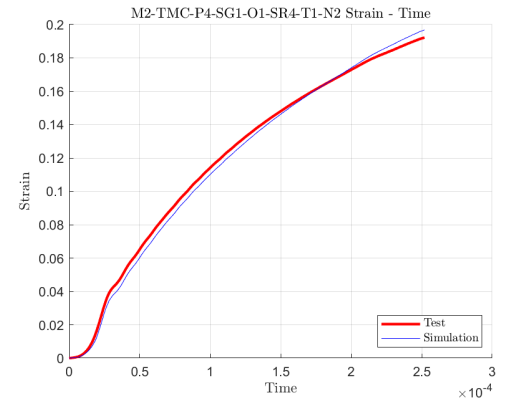
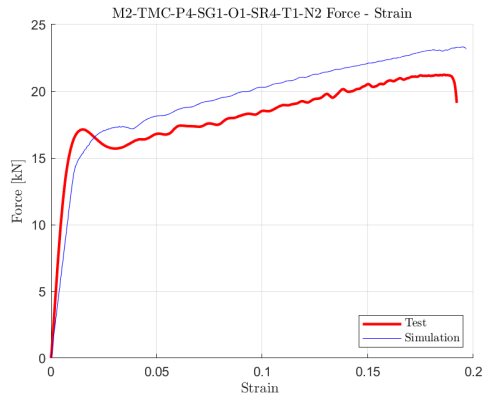
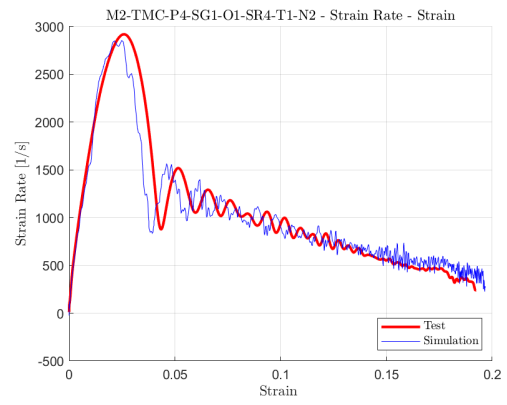
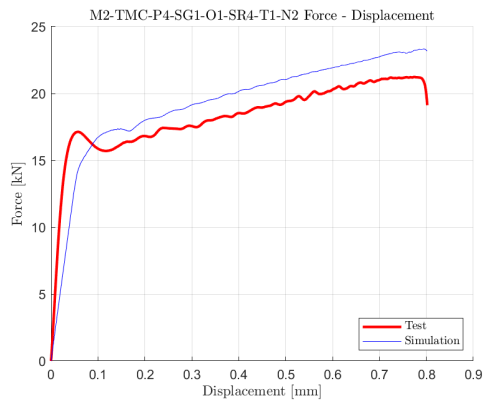


Figure 3.52: Test M2-TMC-P4-SG1-O1-SR4-T1-N2.

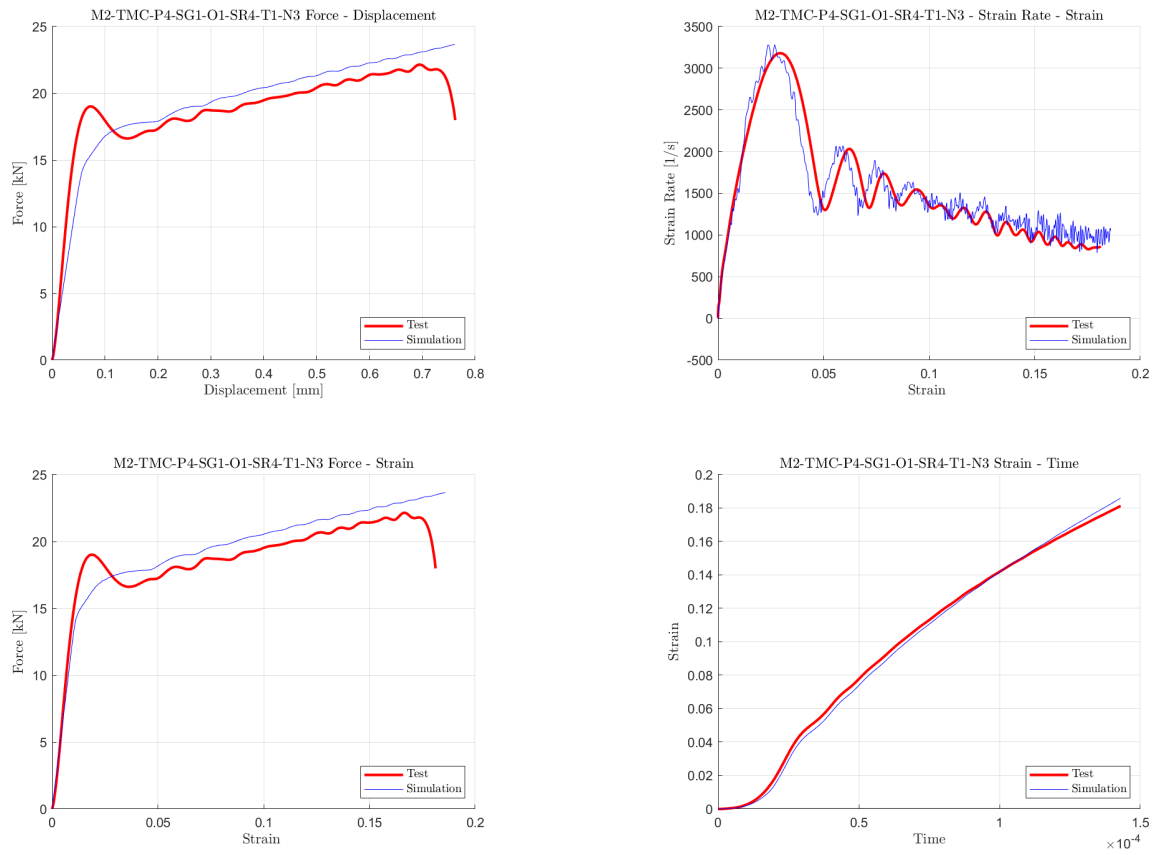


Figure 3.53: Test M2-TMC-P4-SG1-O1-SR4-T1-N3.

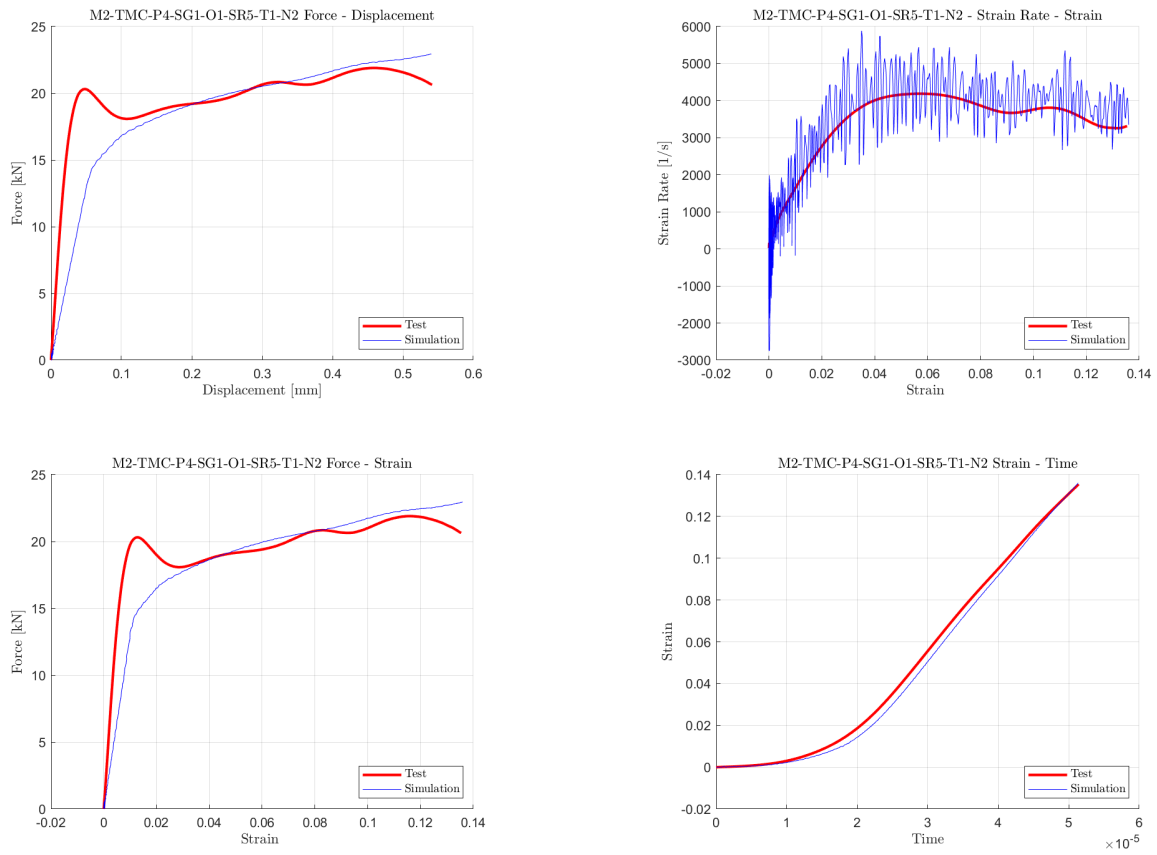


Figure 3.54: Test M2-TMC-P4-SG1-O1-SR5-T1-N2.

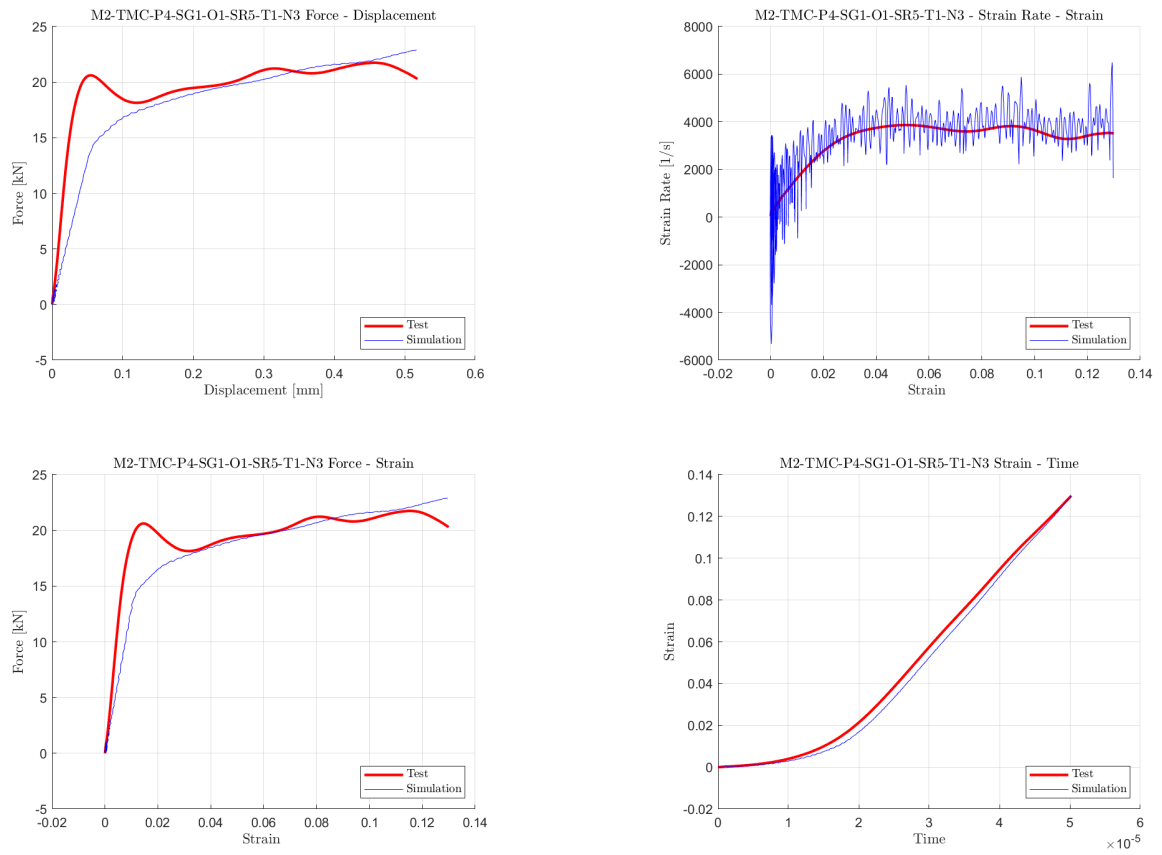


Figure 3.55: Test M2-TMC-P4-SG1-O1-SR5-T1-N3.

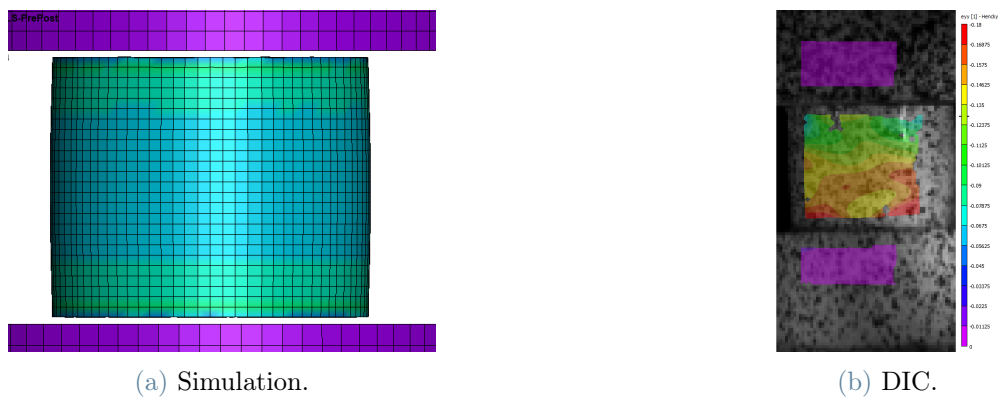


Figure 3.56: M2-TMC-P4-SG1-O1-SR5-T1-N3 Strain comparison.

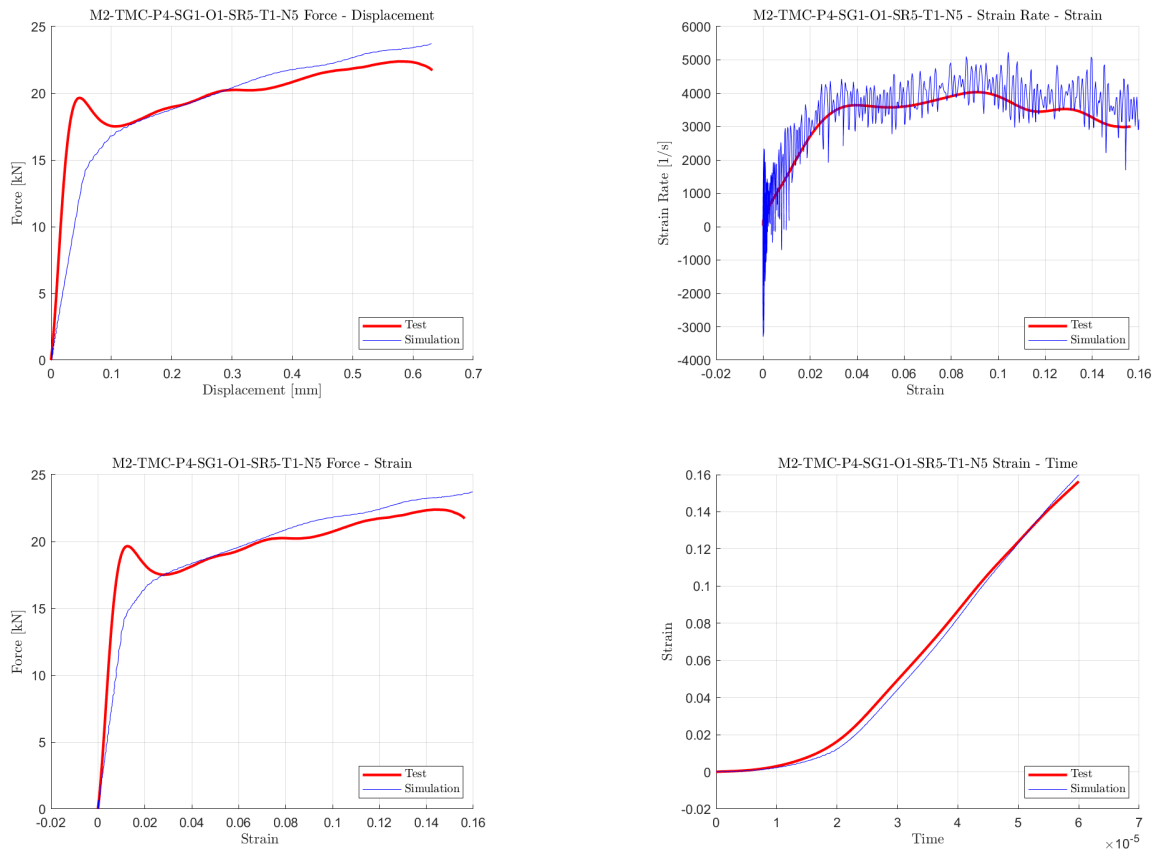


Figure 3.57: Test M2-TMC-P4-SG1-O1-SR5-T1-N5.

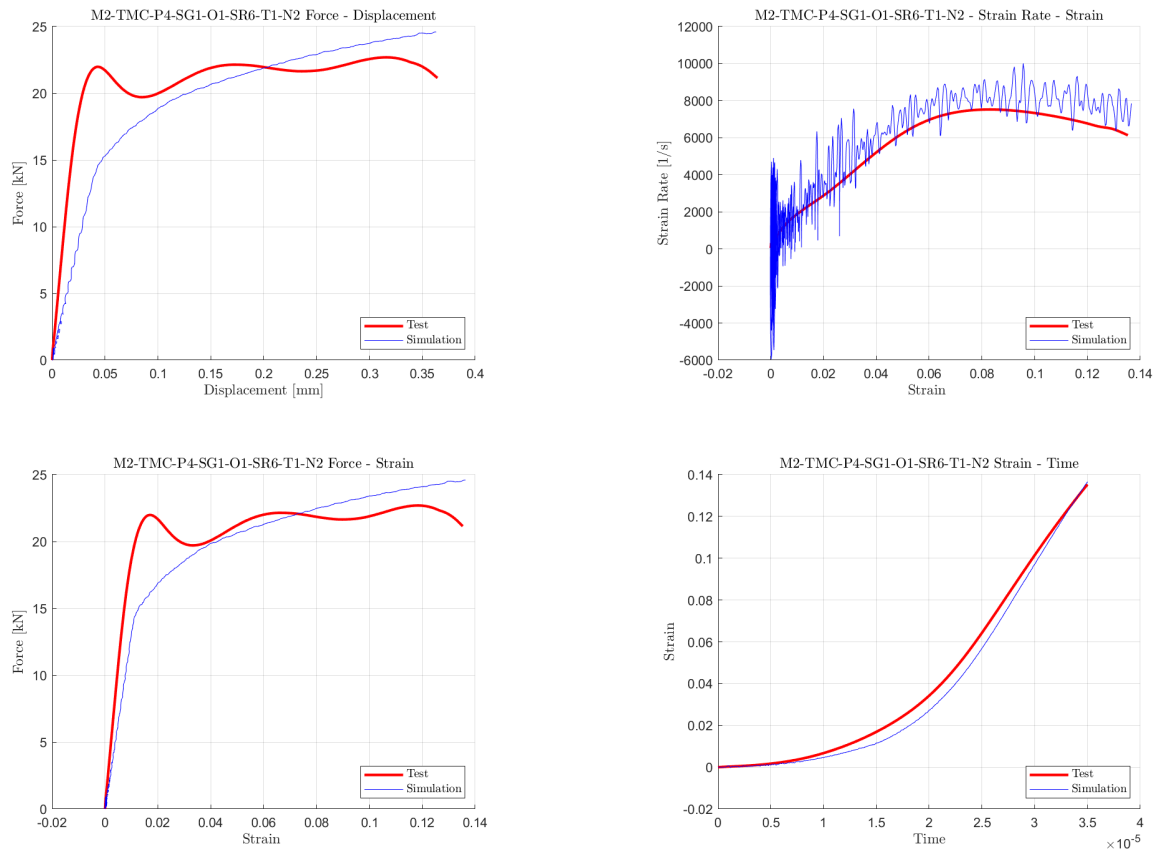


Figure 3.58: Test M2-TMC-P4-SG1-O1-SR6-T1-N2.

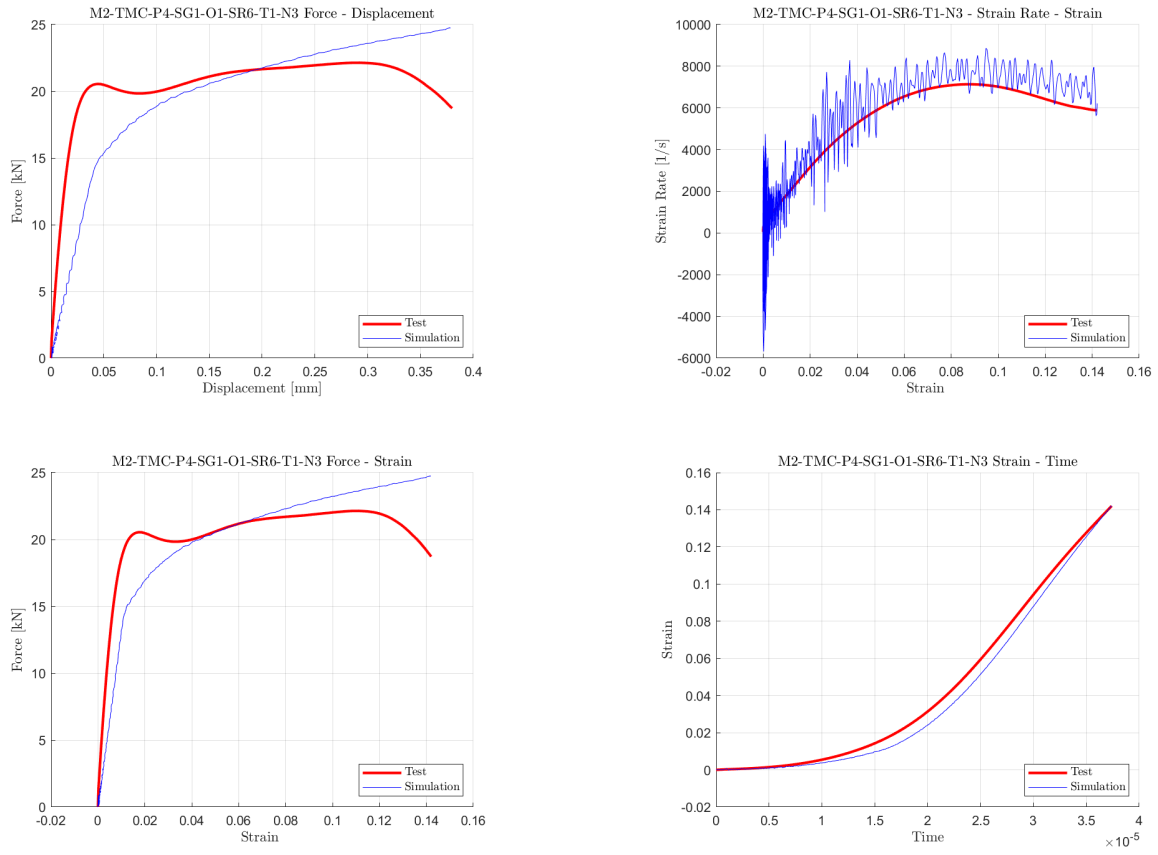


Figure 3.59: Test M2-TMC-P4-SG1-O1-SR6-T1-N3.

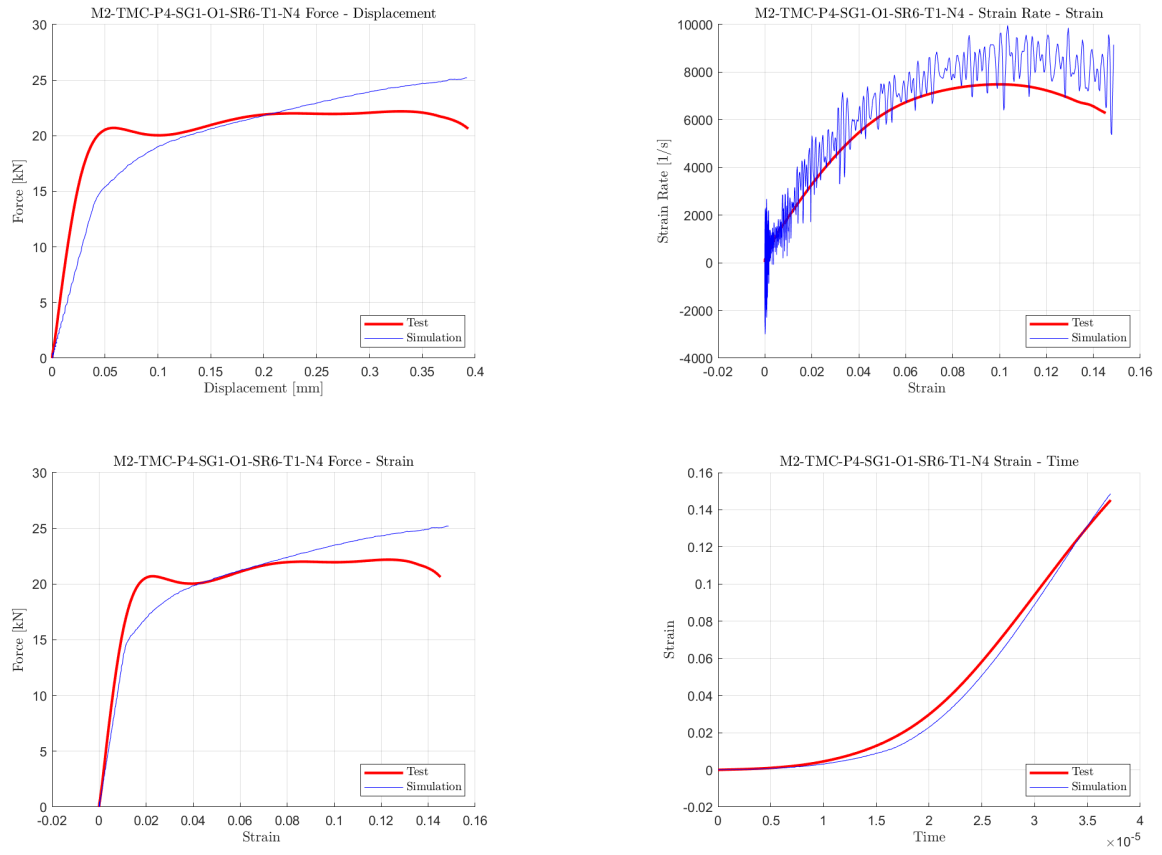


Figure 3.60: Test M2-TMC-P4-SG1-O1-SR6-T1-N4.

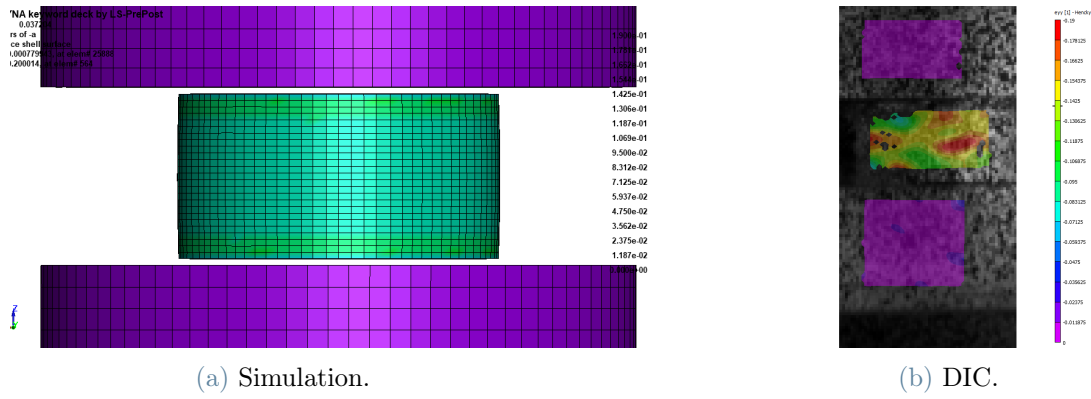


Figure 3.61: M2-TMC-P4-SG1-O1-SR6-T1-N4 Strain comparison.

4 | Methodology for Failure Model Creation

4.1. Failure Surface Overview

Element erosion in `*MAT_224_GYS` can be made dependent on four distinct curves or tables. The first table (LCF) defines the effective plastic failure strain as a function of the stress state, and is referred to as the failure surface. For solid elements, the stress state is characterized by two parameters: the triaxiality and the Lode parameter. For shell elements, a single curve defining element erosion as a function of triaxiality can be used. The second input (LCG) is a curve that scales the effective plastic strain at fracture as a function of the element strain rate. The third input (LCH) is a curve that scales the effective plastic strain at fracture as a function of the element temperature. The last input (LCI) scales the effective plastic strain as a function of element size (as a curve), which can also be made a function of triaxiality (as a table), or triaxiality and Lode parameter (as a 3D table).

Triaxiality, τ , is defined by the equation:

$$\tau = \frac{p}{\sigma_{vm}}$$

where p is the pressure and σ_{vm} is the von Mises stress. The Lode parameter, θ_L , is defined by the equation:

$$\theta_L = \frac{27s_1s_2s_3}{\sigma_{vm}^3}$$

where s_1 , s_2 , and s_3 are the principal deviatoric stresses, and σ_{vm} is the von Mises stress. Overall, the net effective plastic strain at fracture, ε_n , is defined by:

$$\varepsilon_n = \varepsilon_f(\tau, \theta_L) \cdot g(\dot{\varepsilon}_p) \cdot h(T) \cdot i(l_c, \tau, \theta_L)$$

where ε_f is the effective plastic strain at fracture from the LCF table, $\dot{\varepsilon}_p$ is the plastic strain rate, T is the temperature, and l_c is the element size. Therefore, the net effective

plastic strain, which serves as the element erosion criterion, is the stress-state fracture strain multiplied by the product of the three scale factors.

For each element, the stress state, strain rate, and temperature continually change. Consequently, a parameter must be defined to account for an element's history. A damage parameter is introduced, and the accumulated damage for each element is calculated. The element erosion criterion in `*MAT_224_GYS` is based on this accumulated damage parameter. When the damage parameter reaches or exceeds one at an integration point, the element is eroded. The damage parameter is defined by:

$$D = \int \dot{\varepsilon}_p \cdot \varepsilon_n dt$$

To create a failure surface, various types of test specimens with differing geometries are used. Each specimen geometry has a unique triaxiality and Lode parameter, which together define the fracture strain at a specific point on the failure surface. To generate an accurate and complete failure surface, as many specimen geometries as possible should be used. However, there will not be sufficient test specimens to fully define the failure surface. Interpolation between fracture strains at known triaxialities and Lode parameters is required to generate a complete failure surface, and often extrapolation is also necessary.

After generating the LCF failure surface, the scaling factor curves and tables are created. By observing how the fracture strain is influenced by strain rate and temperature, the same strain rate and temperature test series described in Section 3 can be used to create the LCG and LCH curves. Finally, by simulating selected tests in the fracture series with varying mesh densities, a 3D LCI table can be created. This table accounts for the changes in fracture strain as a function of element size, which in turn depends on the stress state.

4.2. Failure Surface Generation

It is possible to interpolate and extrapolate fracture strains from tests varying in triaxiality and Lode parameters to manually construct a failure surface. Alternatively, automation using a failure surface generation tool developed within the MathWorks MATLAB environment is also viable.

The Ti-6Al-4V material testing program at OSU conducted 21 distinct fracture tests, presenting stress states as functions of triaxiality and Lode parameter (Figure 4.1). These stress states are not constant throughout the specimens; plotted values represent average triaxiality and Lode parameter during loading. Section 5.2.2 will comprehensively detail

the fracture testing families identified in Figure 4.1

Despite the breadth of the testing program with 21 individual specimens, there are still regions with sparse or absent test data. Notably, outside the figure's bounds, where triaxiality exceeds 0.23 or falls below -1.0, no test data is available (triaxiality can vary from hydrostatic tension's $-\infty$ to hydrostatic compression's $+\infty$, while the Lode parameter varies between -1 and 1).

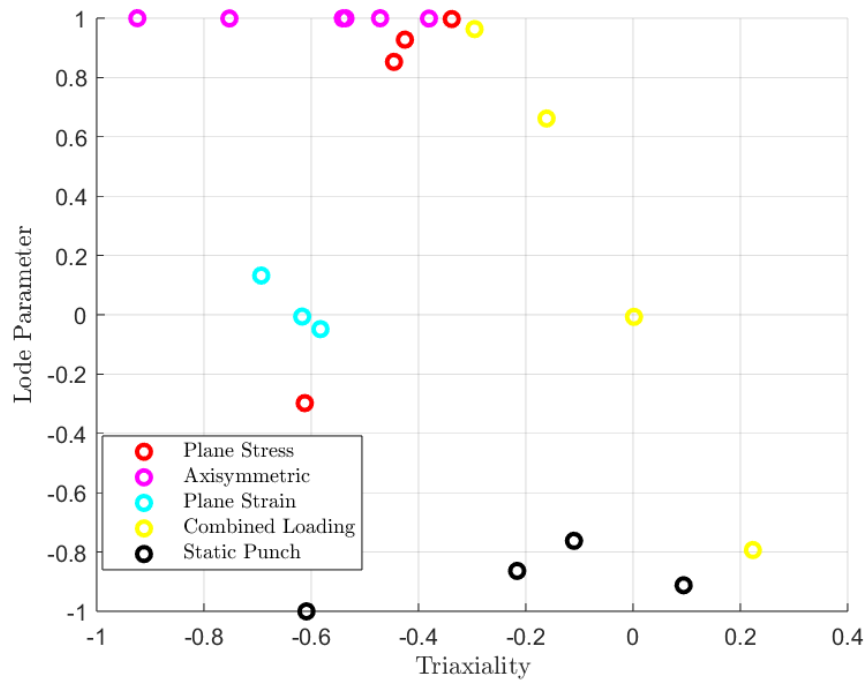


Figure 4.1: Example stress states from various material tests.

The initial step in generating the Ti-6Al-4V failure surface involved creating three-dimensional splines connecting commonly defined stress states (referenced in the legend of Figure 4.2). Each spline of fracture strain was derived through curve fitting to test data points proximate to these defined stress sets. Four splines were generated using data points from the four primary solid-line curves illustrated in Figure 4.2. Notably, these stress states do not align precisely with plane stress, plane strain, axisymmetric tension, or axisymmetric compression conditions, as evident from Figure 4.3, where data points do not perfectly overlap these lines. Figure 4.3b depicts a 3D representation, revealing the fracture strain distribution and outlining the failure surface.

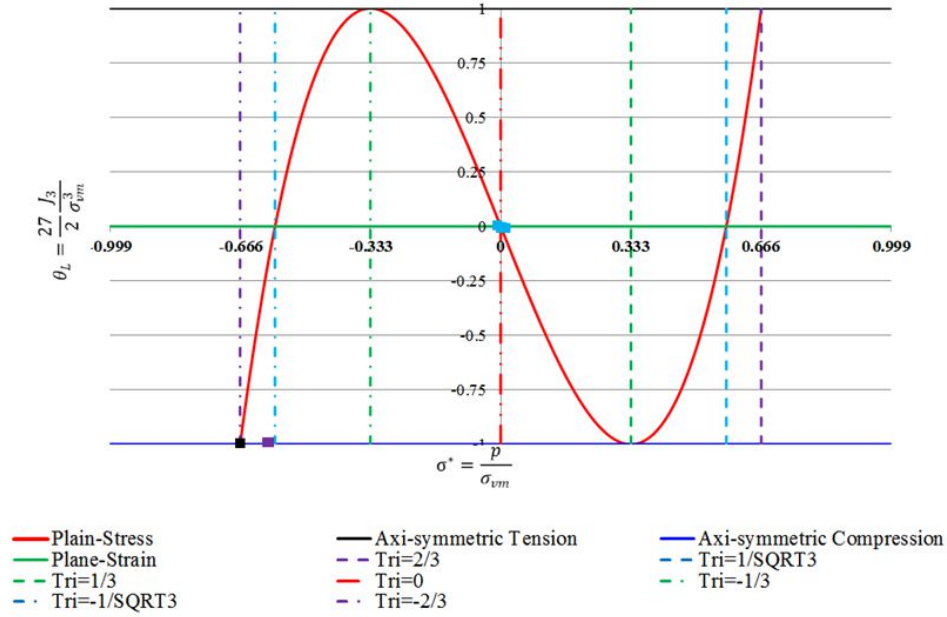


Figure 4.2: Commonly defined stress states.

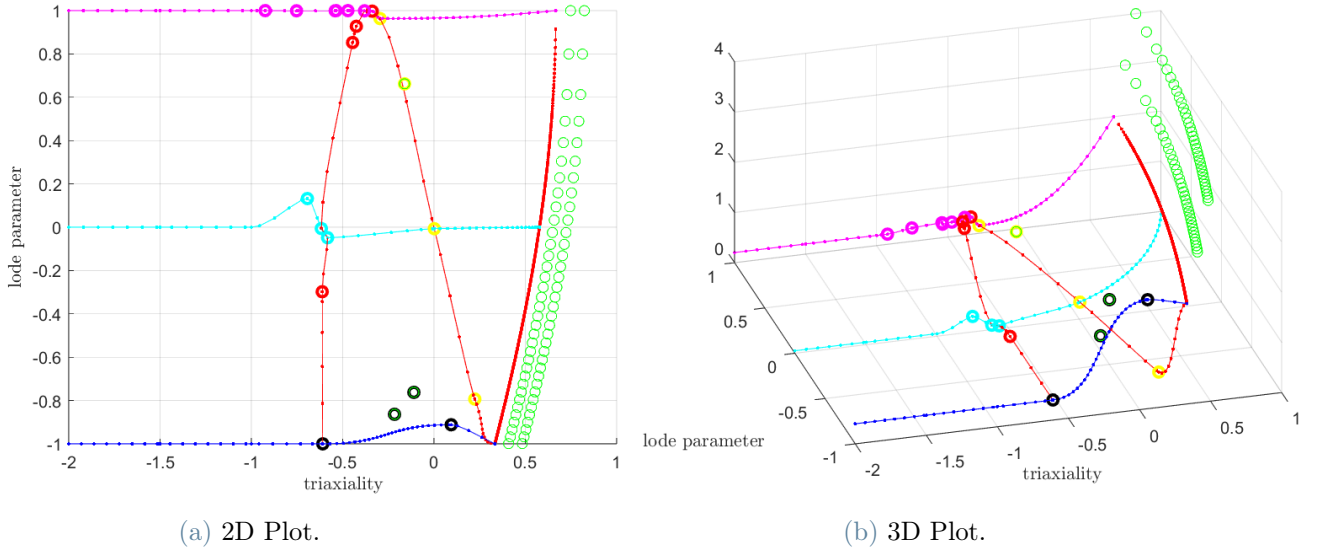


Figure 4.3: Control points of the three-dimensional splines.

Additional control points were added along these three-dimensional splines, as demonstrated in Figure 4.4, where fracture strains are defined. Mathematically, three one-dimensional vectors were created defining: 1) triaxiality of the control points, 2) Lode parameter of the control points, and 3) failure strain for each of these points.

Subsequently, a MATLAB subroutine utilizing the Curve Fitting Toolbox was employed in the next phase of failure surface creation. This subroutine processed the three one-

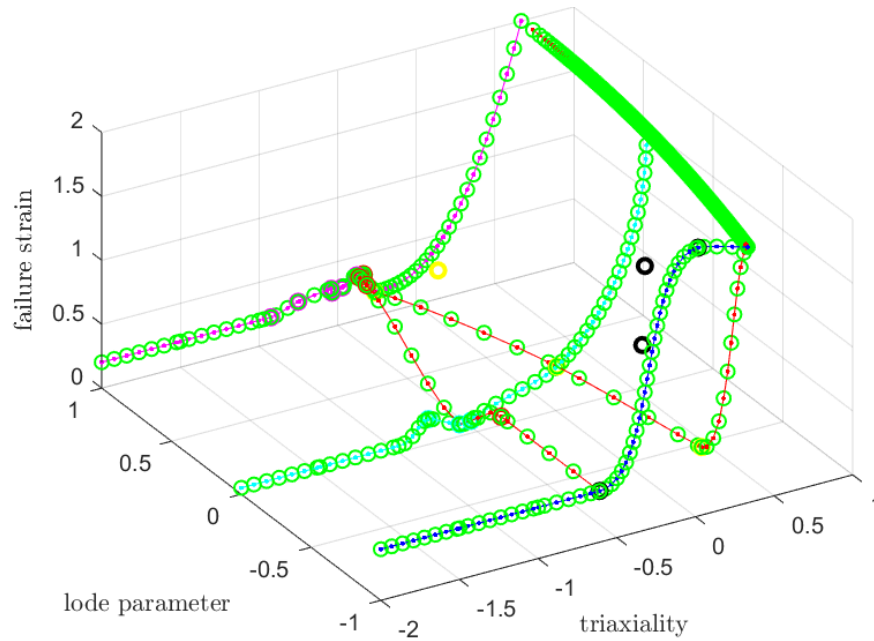


Figure 4.4: Additional control points created from the 3D splines.

dimensional vectors of the control points, interpolating them over a uniform grid and returning a surface fit to these splines. The subroutine utilized a 'v4' interpolation routine (MATLAB 4 grid data method) to generate the three-dimensional surface, with the plot shown in Figure 4.5.

The final stage of failure surface generation involved discretizing the three-dimensional surface into discrete data points. This surface was defined by 202 triaxiality values and 41 Lode parameter values, resulting in a total of 8282 discrete points, as depicted in Figure 4.6.

The concluding step in failure surface creation involved generating a keyword input file referenced by the `*MAT_224_GYS` LCF parameter. This file included a `*DEFINE_TABLE` with 41 values ranging from -1 to 1, representing Lode parameter discretization. Triaxiality discretization was defined by 41 `*DEFINE_CURVE` keywords, each encompassing 202 fracture strain values. This keyword file could then be directly integrated into simulation inputs.

Upon simulating each test specimen detailed in Section 5.2.2, fracture displacement was compared against experimental results. Adjustments to control points near the specimen's stress state were made if simulation either exceeded failure criteria too late (resulting in excessively high failure strain) or too early (resulting in excessively low failure strain), followed by immediate surface regeneration [11].

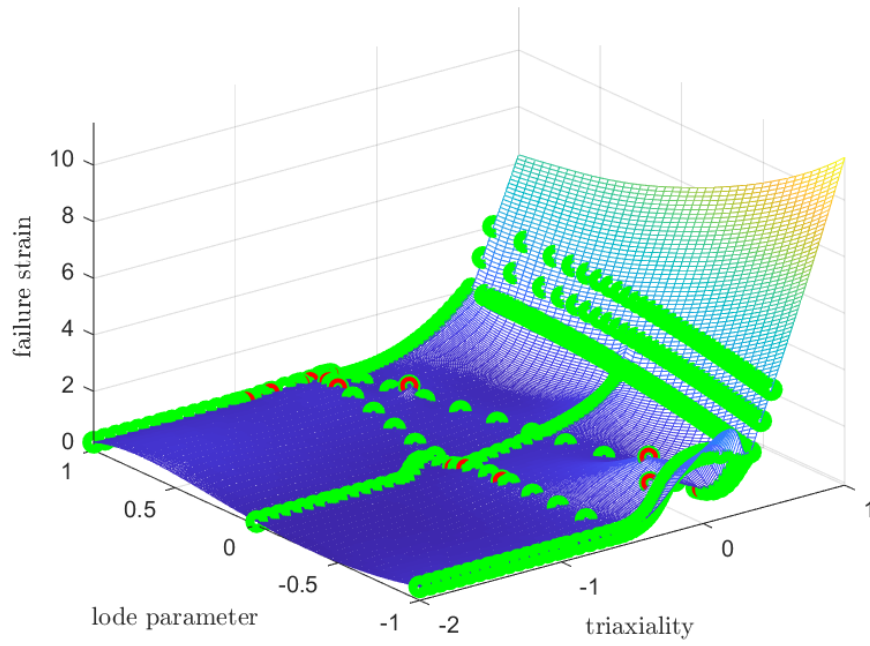


Figure 4.5: Failure surface generated by MATLAB subroutine.

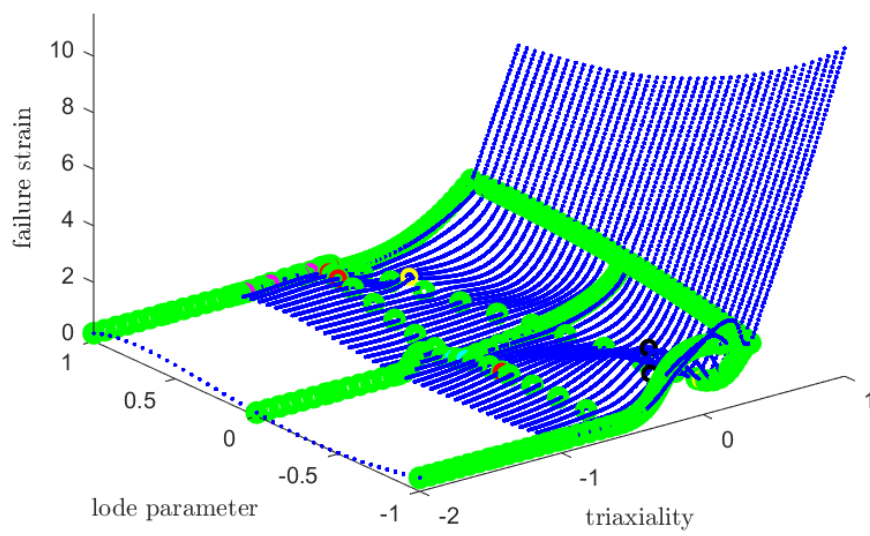


Figure 4.6: Discretized 3D failure surface.

5 | Failure Model Creation by Simulation of Mechanical Property Tests

To construct an effective failure surface, it is necessary to conduct numerous tests using various geometries that induce varying stress states. These tests must encompass a wide range of triaxiality and Lode parameters at the localization point or the failure initiation point. To ensure that the surface accurately represents a comprehensive stress state spectrum, a broad array of combinations of triaxiality and Lode parameters is necessary [20]. Inadequate sampling can lead to incomplete representation of stress states in certain regions. Achieving optimal sampling that uniformly covers the stress space is a challenge in practical implementation.

Mechanical property testing was conducted by OSU, providing specimen geometry, force, displacement, strain data, and DIC images. The failure surface model was derived from 21 different specimens, identified as follows:

- SG1: Plane stress specimen (pure tension)
- SG2, SG3, SG4: Plane stress specimens
- SG5: Axisymmetric specimen (pure tension)
- SG6 to SG10: Axisymmetric specimens
- SG11 to SG13: Plane strain specimens
- LR1, LR2: Combined (tension/torsion) specimens
- LR3: Torsion specimen
- LR4: Combined (compression/torsion) specimen
- Unbacked Punch
- Backed Punch: 0.072', 0.05', 0.035' backing plates

Note that the terms *plane stress* and *plane strain* represent specimen families, with only the initial specimen of each family inducing true plane stress or strain. Variations within each family include notches creating additional stress state variations. Each specimen and its associated finite element model will be detailed further in Sections 5.1.

5.1. Test specimen descriptions

This section outlines the process of specimen modeling, simulation of OSU’s tests, and the outcomes obtained using the failure surface generation tool. Diagram dimensions represent nominal values used for finite element model creation; actual dimensions may marginally differ between specimens. Mesh adjustments for each analysis were made to precisely match actual test specimen dimensions. All dimensions are in millimeters (mm), milliseconds (ms), kilograms (kg), and kilonewtons (kN).

5.1.1. SG1—Plane Stress Specimen (Pure Tension)

SG1 is a plane stress (pure tension) specimen previously used to determine the stress-strain relationships outlined earlier in this report. The dimensions of the specimen are shown in Figure 5.1.

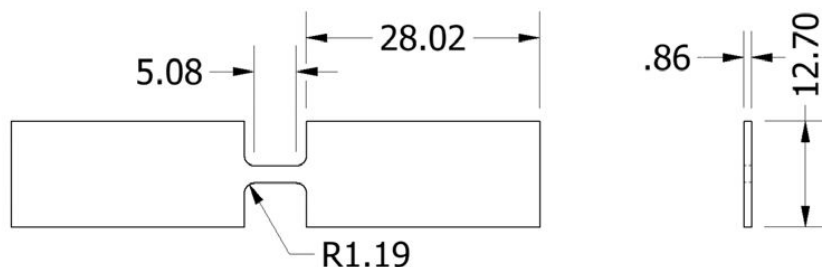


Figure 5.1: Geometry of specimen SG1.

The specimen was meshed using solid elements, with an average element size of 0.2 mm. The mesh of the SG1 specimen is shown in Figure 5.2. An enlargement of the area containing the 4.00 mm virtual (DIC) extensometer gauge length is also provided. The mesh contains approximately 73,000 solid elements, of which about 65,000 were modeled as rigid solid elements (shown in gray). Figure 5.2 illustrates the proportion of rigid solid elements and titanium elements (shown in white).

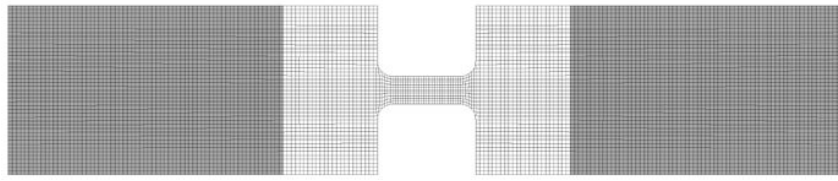


Figure 5.2: Meshed model of specimen SG1 showing rigid solid elements (gray) and titanium elements (white).

5.1.2. SG2—Plane Stress Specimen

SG2 is a variation of the plane stress specimen with a specifically chosen center geometry or notch, designed to produce a unique triaxiality and Lode parameter. The dimensions of the specimen are shown in Figure 5.3.

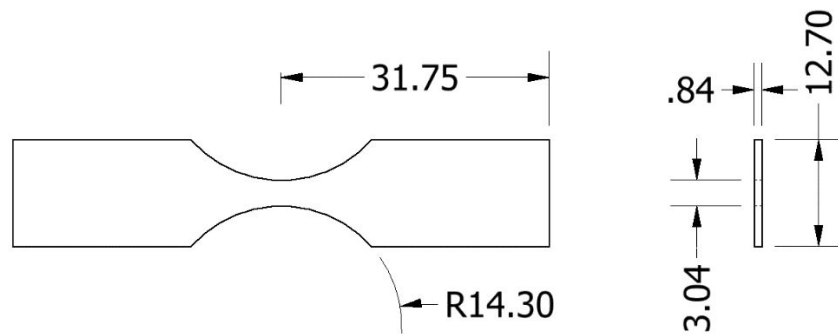


Figure 5.3: Geometry of specimen SG2.

The specimen was meshed with solid elements, using an average element size of 0.2 mm. The mesh of the SG2 specimen is shown in Figure 5.4, and an enlargement of the area containing the 4.00 mm virtual (DIC) extensometer gauge length is also provided. The mesh consists of approximately 22,000 solid elements, of which approximately 12,000 were modeled as rigid solid elements (shown in gray). Figure 5.4 shows the proportion of rigid solid elements and titanium elements (shown in white).

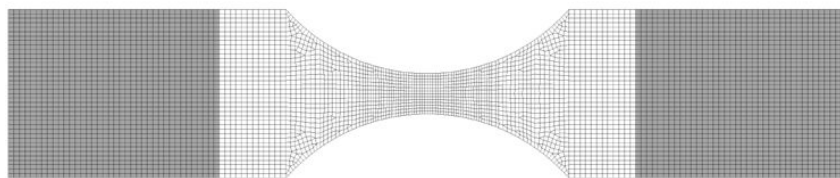


Figure 5.4: Meshed model of specimen SG2 showing rigid solid elements (gray) and titanium elements (white).

5.1.3. SG3—Plane Stress Specimen

SG3 is another variation of the plane stress specimen, designed to produce a unique triaxiality and Lode parameter through its center geometry or notch. The dimensions of the specimen are shown in Figure 5.5.

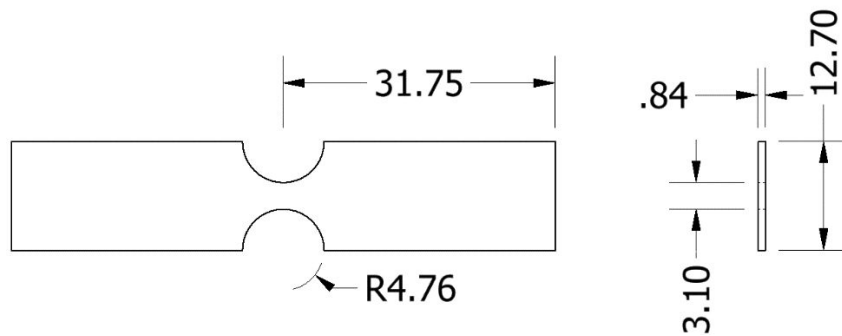


Figure 5.5: Geometry of specimen SG3.

The mesh of the SG3 specimen is shown in Figure 5.6, with an average element size of 0.2 mm. An enlargement of the area containing the 4.00 mm virtual (DIC) extensometer gauge length is provided. This specimen's mesh contains approximately 20,000 solid elements, of which around 14,000 are considered rigid solid elements (shown in gray). Figure 5.6 illustrates the distribution of rigid solid elements and titanium elements (shown in white).

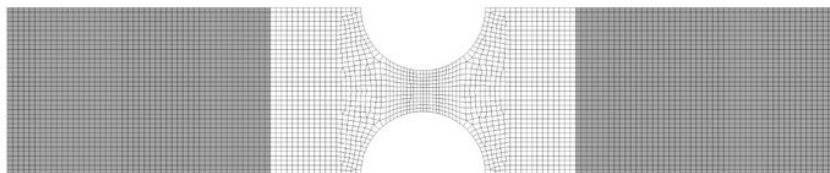


Figure 5.6: Meshed model of specimen SG3 showing rigid solid elements (gray) and titanium elements (white).

5.1.4. SG4—Plane Stress Specimen

SG4 is another variation of the plane stress specimen, with a chosen center geometry or notch to create a unique triaxiality and Lode parameter. The dimensions are shown in Figure 5.7.

The mesh of the SG4 specimen is depicted in Figure 5.8, with an average element size of 0.2 mm. An enlargement of the area containing the 4.00 mm virtual (DIC) extensometer gauge length is shown. The mesh contains approximately 41,000 solid elements, with

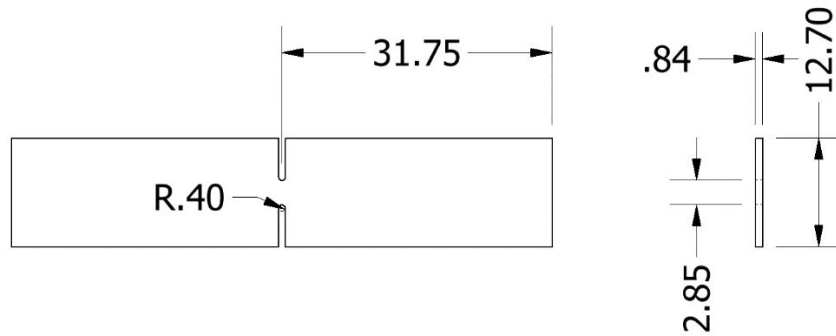


Figure 5.7: Geometry of specimen SG4.

roughly 30,000 considered rigid solid elements (shown in gray). Figure 5.8 illustrates the distribution of rigid solid elements and titanium elements (shown in white).

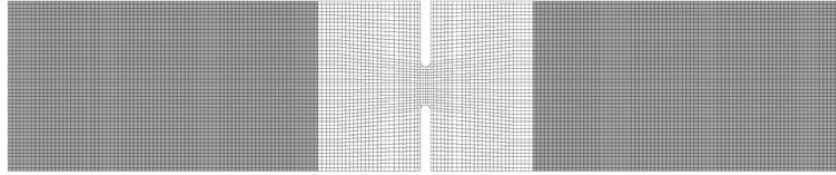


Figure 5.8: Meshed model of specimen SG4 showing rigid solid elements (gray) and titanium elements (white).

5.1.5. SG5—Axisymmetric Specimen (Pure Tension)

SG5 is an axisymmetric (cylindrical) specimen with a central section under pure tension. The dimensions are shown in Figure 5.9.



Figure 5.9: Geometry of specimen SG5.

The mesh of the SG5 specimen is shown in Figure 5.10, with an average element size of 0.2 mm. An enlargement of the area containing the 4.00 mm virtual (DIC) extensometer gauge length and the center cross-section is also shown. This specimen has approximately 471,000 solid elements, with around 300,000 considered rigid solid elements (shown in gray). Figure 5.10 illustrates the distribution of rigid solid elements and titanium elements (shown in white).

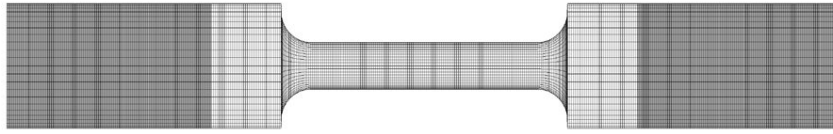


Figure 5.10: Meshed model of specimen SG5 showing rigid solid elements (gray) and titanium elements (white).

5.1.6. SG6—Axisymmetric Specimen

SG6 is a variation of the axisymmetric specimen with a specifically chosen center geometry or notch that will produce a unique triaxiality and Lode parameter. The dimensions are shown in Figure 5.11.

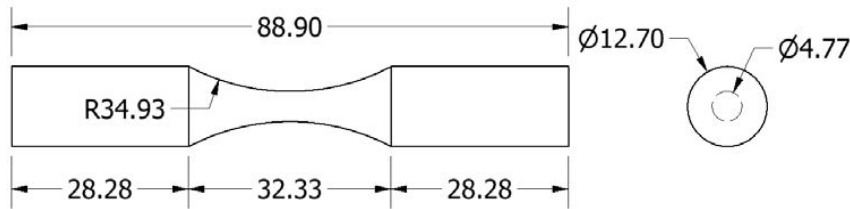


Figure 5.11: Geometry of specimen SG6.

The mesh of the SG6 specimen is shown in Figure 5.12, with an average element size of 0.2 mm. An enlargement of the area containing the 4.00 mm virtual (DIC) extensometer gauge length and the center cross-section is also shown. The mesh contains approximately 430,000 solid elements, with around 250,000 considered rigid solid elements (shown in gray). Figure 5.12 illustrates the distribution of rigid solid elements and titanium elements (shown in white).

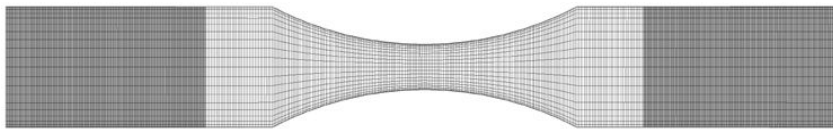


Figure 5.12: Meshed model of specimen SG6 showing rigid solid elements (gray) and titanium elements (white).

5.1.7. SG7—Axisymmetric Specimen

SG7 is a variation of the axisymmetric specimen with a specifically chosen center geometry or notch that will produce a unique triaxiality and Lode parameter. The dimensions are shown in Figure 5.13.

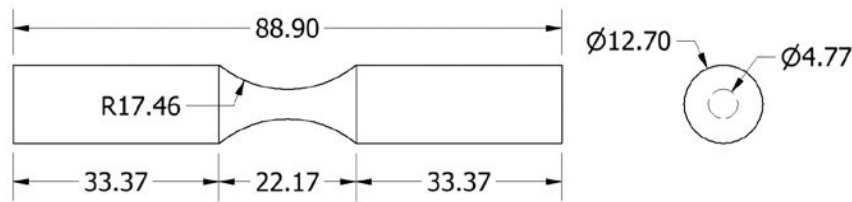


Figure 5.13: Geometry of specimen SG7.

The mesh of the SG7 specimen is shown in Figure 5.14, with an average element size of 0.2 mm. An enlargement of the area containing the 4.00 mm virtual (DIC) extensometer gauge length and the center cross-section is also shown. The mesh contains approximately 457,000 solid elements, with around 294,000 considered rigid solid elements (shown in gray). Figure 5.14 illustrates the distribution of rigid solid elements and titanium elements (shown in white).

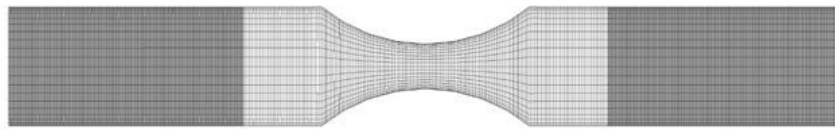


Figure 5.14: Meshed model of specimen SG7 showing rigid solid elements (gray) and titanium elements (white).

5.1.8. SG8—Axisymmetric Specimen.

SG8 is a variation of the axisymmetric specimen with a specifically chosen center geometry or notch that will produce a unique triaxiality and Lode parameter. The dimensions are shown in Figure 5.15.

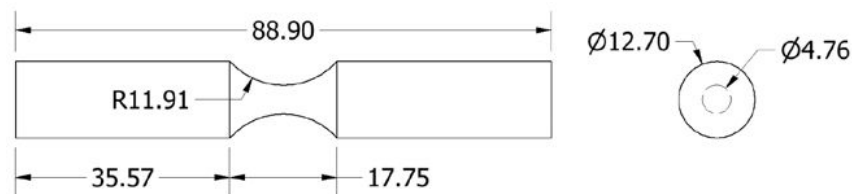


Figure 5.15: Geometry of specimen SG8.

The mesh of the SG8 specimen is shown in Figure 5.16, with an average element size of 0.2 mm. An enlargement of the area containing the 4.00 mm virtual (DIC) extensometer gauge length and the center cross-section is also shown. The mesh contains approximately 385,000 solid elements, with about 256,000 considered rigid solid elements (shown in

gray). Figure 5.16 illustrates the distribution of rigid solid elements and titanium elements (shown in white).

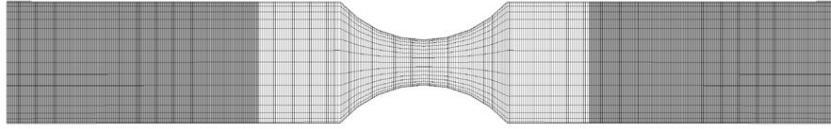


Figure 5.16: Meshed model of specimen SG8 showing rigid solid elements (gray) and titanium elements (white).

5.1.9. SG9—Axisymmetric Specimen

SG9 is a variation of the axisymmetric specimen with a specifically chosen center geometry or notch that will produce a unique triaxiality and Lode parameter. The dimensions are shown in Figure 5.17.

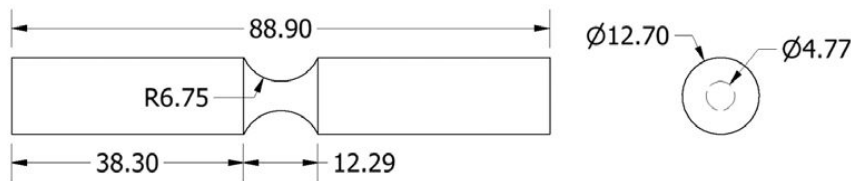


Figure 5.17: Geometry of specimen SG9.

The mesh of the SG9 specimen is shown in Figure 5.18, with an average element size of 0.2 mm. An enlargement of the area containing the 4.00 mm virtual (DIC) extensometer gauge length and the center cross-section is also shown. The mesh contains approximately 652,000 solid elements, with around 452,000 considered rigid solid elements (shown in gray). Figure 5.18 illustrates the distribution of rigid solid elements and titanium elements (shown in white).

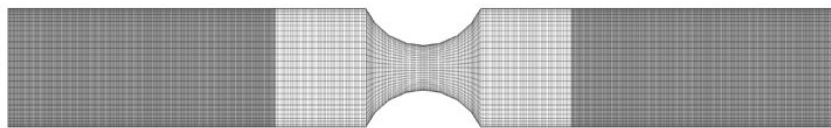


Figure 5.18: Meshed model of specimen SG9 showing rigid solid elements (gray) and titanium elements (white).

5.1.10. SG10—Axisymmetric Specimen

SG10 is a variation of the axisymmetric specimen with a specifically chosen center geometry or notch that will produce a unique triaxiality and Lode parameter. The dimensions

are shown in Figure 5.19.

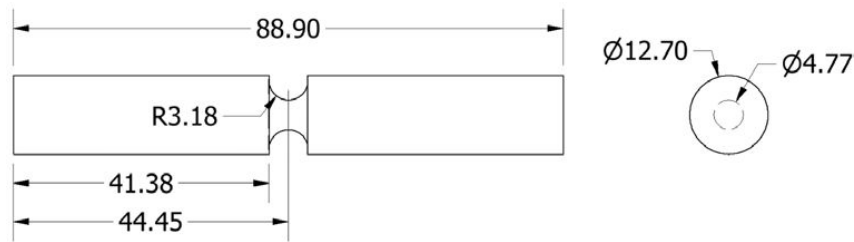


Figure 5.19: Geometry of specimen SG10.

The mesh of the SG10 specimen is shown in Figure 5.20, with an average element size of 0.2 mm. An enlargement of the area containing the 4.00 mm virtual (DIC) extensometer gauge length and the center cross-section is also shown. The mesh contains approximately 593,000 solid elements, with about 432,000 considered rigid solid elements (shown in gray). Figure 5.20 illustrates the distribution of rigid solid elements and titanium elements (shown in white).

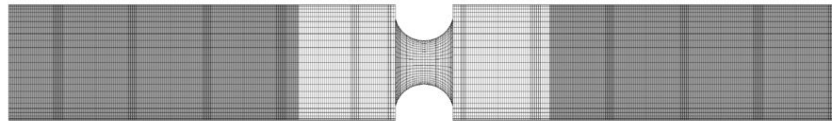


Figure 5.20: Meshed model of specimen SG10 showing rigid solid elements (gray) and titanium elements (white).

5.1.11. SG11—Plane Strain Specimen

SG11 is a plane strain specimen with a specifically chosen center geometry that is under pure tension. The dimensions are shown in Figure 5.21.

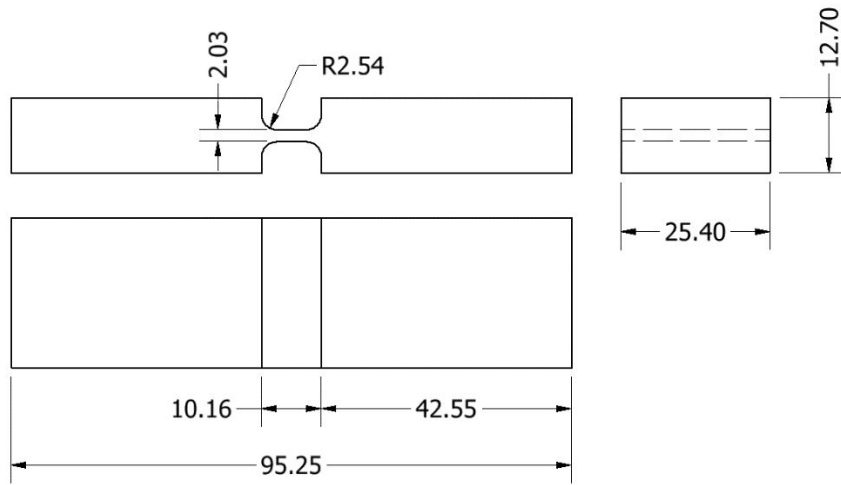


Figure 5.21: Geometry of specimen SG11.

The mesh of the SG11 specimen is shown in Figure 5.22, with an average element size of 0.2 mm. An enlargement of the area containing the 4.00 mm virtual (DIC) extensometer gauge length and the center cross-section is also shown. The mesh contains approximately 935,000 solid elements, with around 442,000 considered rigid solid elements (shown in gray). Figure 5.22 illustrates the distribution of rigid solid elements and titanium elements (shown in white).

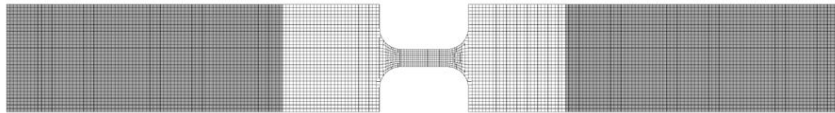


Figure 5.22: Meshed model of specimen SG11 showing rigid solid elements (gray) and titanium elements (white).

5.1.12. SG12—Plane Strain Specimen

SG12 is a variation of the plane strain specimen with a specifically chosen center geometry or notch that will produce a unique triaxiality and Lode parameter. The dimensions are shown in Figure 5.23.

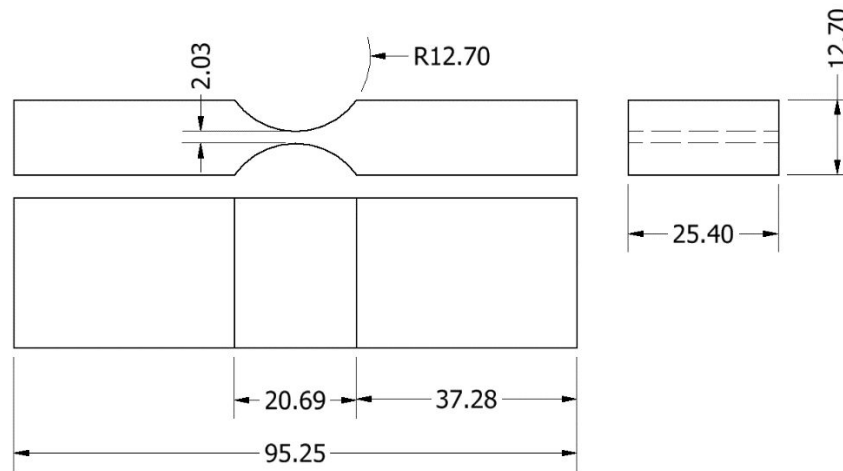


Figure 5.23: Geometry of specimen SG12.

The mesh of the SG12 specimen is shown in Figure 5.24, with an average element size of 0.2 mm. An enlargement of the area containing the 4.00 mm virtual (DIC) extensometer gauge length and the center cross-section is also shown. The mesh contains approximately 740,000 solid elements, with around 452,000 considered rigid solid elements (shown in gray). Figure 5.24 illustrates the distribution of rigid solid elements and titanium elements (shown in white).

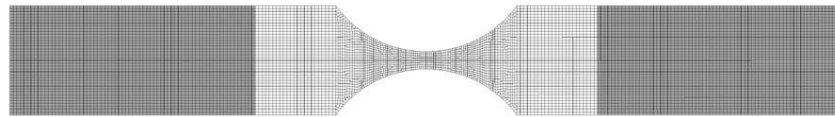


Figure 5.24: Meshed model of specimen SG12 showing rigid solid elements (gray) and titanium elements (white).

5.1.13. SG13—Plane Strain Specimen

SG13 is a variation of the plane strain specimen with a specifically chosen center geometry or notch that will produce a unique triaxiality and Lode parameter. The dimensions are shown in Figure 5.25.

The mesh of the SG13 specimen is shown in Figure 5.26, with an average element size of 0.2 mm. An enlargement of the area containing the 4.00 mm virtual (DIC) extensometer gauge length and the center cross-section is also shown. The mesh contains approximately 2,639,000 solid elements, with around 1,924,000 considered rigid solid elements (shown in gray). Figure 5.26 illustrates the distribution of rigid solid elements and titanium elements (shown in white).

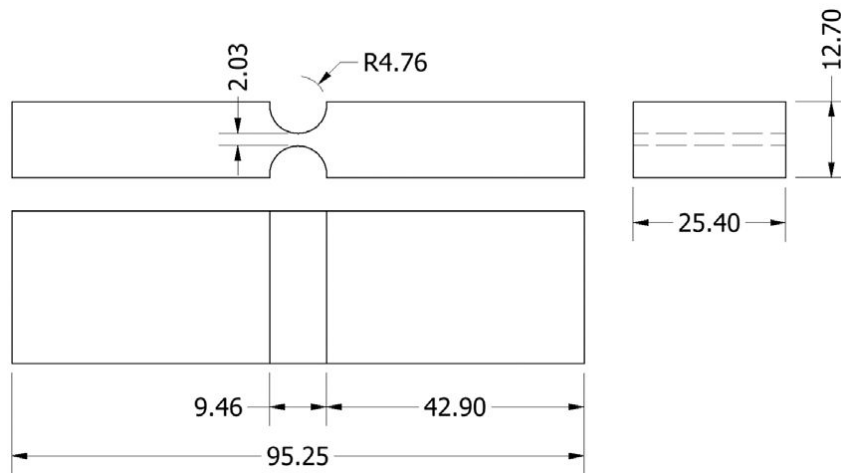


Figure 5.25: Geometry of specimen SG13.

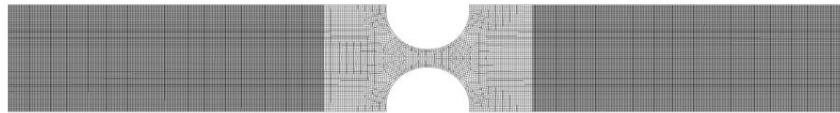


Figure 5.26: Meshed model of specimen SG13 showing rigid solid elements (gray) and titanium elements (white).

5.1.14. LR1 – Combined (Tension/Torsion) Specimen

LR1 is a combined loading specimen in which the ratio of tensile and torsional stress is adjusted so that the area of localization results in the desired triaxiality and Lode parameter. LR1, LR2, and LR3 use the same specimen and mesh, but the ratio of the tension and the torsion differs. The dimensions of the tension/torsion specimen are shown in Figure 5.27.

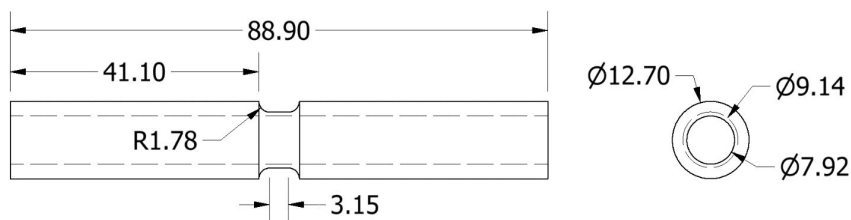


Figure 5.27: Geometry of the LR1, LR2, and LR3 specimen.

The specimen was meshed using solid elements with an average element size of 0.2 mm. The mesh of the LR1, LR2, and LR3 specimen is shown in Figure 5.28. An enlargement of the test section is also shown. The mesh for this specimen contains a total of about 814,000 solid elements. In the Instron mechanical grip sections, the elements were defined

as rigid. Of the 814,000 elements, approximately 442,000 were defined as rigid. Figure 5.28 shows the rigid elements in gray, and the titanium modeled elements in white.

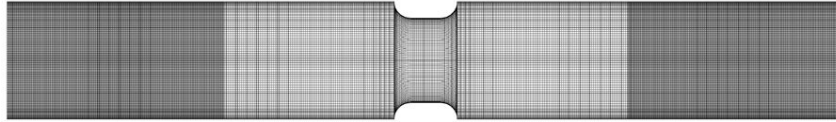


Figure 5.28: Tension/torsion combined finite element mesh.

In the combined loading tests, the ratio of the applied force and torque determines the state of stress. In the simulations, this ratio must precisely match the ratio of the tests. For these combined loading tests, the motion of the grips was controlled by an applied tension force and torque, as defined by two input curves using a `*LOAD_RIGID_BODY` keyword. These two input curves were generated using data from the LR1 tests.

5.1.15. LR2 – Combined (Tension/Torsion) Specimen

LR2 is a combined loading specimen where the ratio of tensile and torsional stress is adjusted so that the area of localization results in a unique triaxiality and Lode parameter. The specimen geometry is approximately the same as the LR1 specimen described in Section 5.1.14. The tension and torque curves were generated using data from the LR2 tests, and were applied using the `*LOAD_RIGID_BODY` keyword input.

5.1.16. LR3 – Torsion Specimen

LR3 is a pure torsion test specimen that has the same geometry as the LR1 and LR2 specimens described in Section 5.1.14. Unlike the LR1 and LR2 combined loading tests, the LR3 test does not include an applied tension load. The mesh shown in Figure 5.28 and mechanical grip positions for the LR3 simulations were the same as for LR1 and LR2. The tension curve was generated using data from the LR3 tests, and was applied using the `*LOAD_RIGID_BODY` keyword input.

5.1.17. LR4 – Combined (Compression/Torsion) Specimen

LR4 is a combined loading specimen where the ratio of compressive and torsional stress is adjusted so that the area of localization results in the desired triaxiality and Lode parameter. LR4 and LR5 use the same specimen and mesh, but the ratio of compression and torsion differs. The dimensions of the compression/torsion specimen are shown in Figure 5.29.

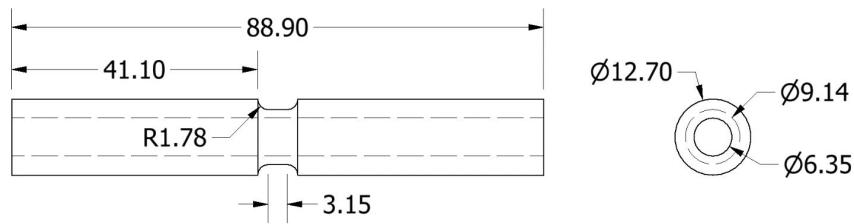


Figure 5.29: Geometry of the LR4 and LR5 specimen.

The specimen was meshed using solid elements with an average element size of 0.2 mm. The mesh of the LR4 and LR5 specimen is shown in Figure 5.30. An enlargement of the test section is also shown. The mesh for this specimen contains a total of about 1,093,000 solid elements. In the Instron mechanical grip sections, the elements were defined as rigid. Of the 1,093,000 elements, approximately 742,000 were defined as rigid. Figure 5.30 shows the rigid elements in gray, and the titanium modeled elements in white.

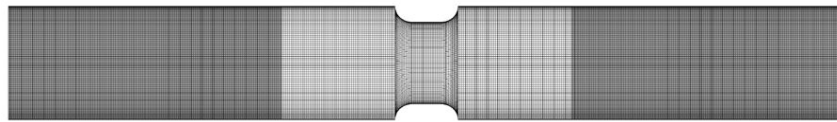


Figure 5.30: Compression/torsion combined finite element mesh.

For these combined loading tests, the motion of the grips was controlled by an applied compression force and torque, as defined by two input curves using a *LOAD_RIGID_BODY keyword. These two input curves were generated using data from the LR4 tests.

5.1.18. Punch: Unbacked

Punch4 is a test where a small diameter punch is forced into the center of a titanium cylindrical plate until fracture occurs. The smaller punch head creates a stress state close to biaxial tension on the titanium plate's side opposite from the punch, where the fracture occurs. The dimensions for the unbacked test, including both the punch and the titanium plate, are shown in Table 5.1.

Dimensions	[mm]
Specimen Thickness	0.688
Clamp Diameter	25.4
Punch Diameter	2.2987
Punch Length	6.15

Table 5.1: Punch dimensions.

The nominal size for the elements in the Punch finite element mesh was approximately 0.15 mm. The simulation took advantage of the test's symmetry, using a $\frac{1}{4}$ axisymmetric mesh of both the plate and punch (Figure 5.31). The finite element mesh had a total of 150,022 elements, including 9,120 shell elements and 140,902 solid elements, with 294 rigid and 149,728 deformable elements. Since the tungsten carbide punch exhibited compressive elastic deformation, it was modeled as elastic.

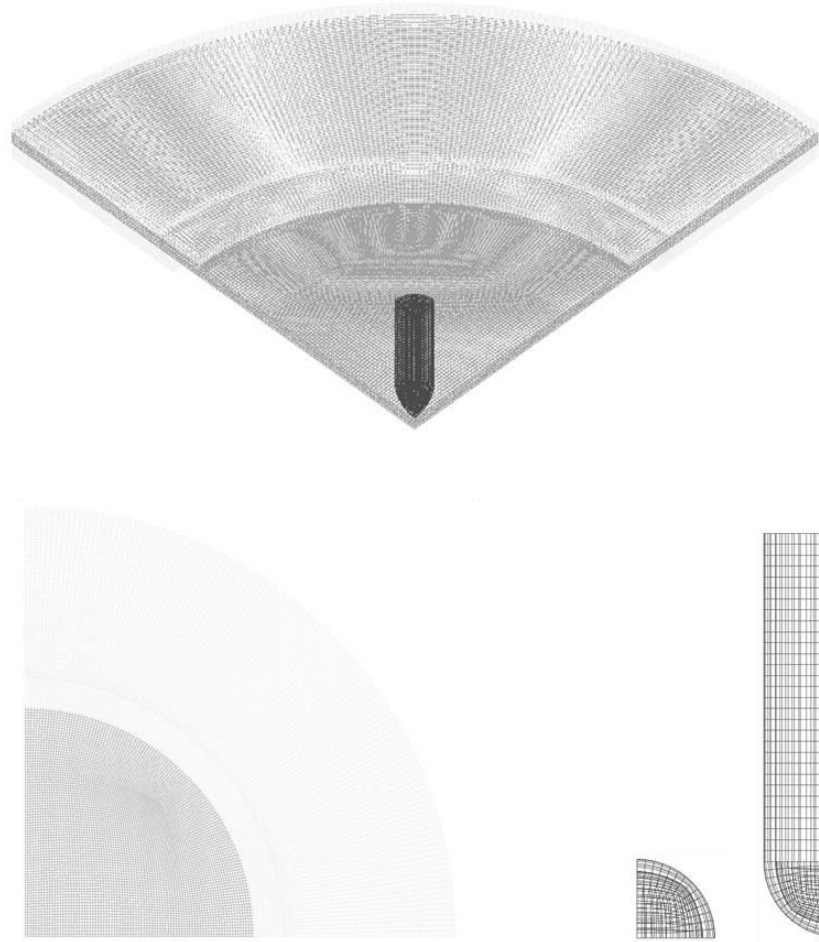


Figure 5.31: Unbacked test mesh, unbacked plate (left), and punch (right).

5.1.19. Punch: Backed tests

The backed tests involve a small diameter punch is forced into the center of a titanium cylindrical plate until fracture occurs. Opposite of the punch side, there is a thick Copper backing plate behind the titanium plate. For this research 3 backing plates with different thickness have been used: 0.072', 0.05', and 0.035'. This backing plate creates compression in the titanium plate, resulting in a Lode parameter around -1. The fracture occurs on the surface of the titanium plate where it contacts the backing plate. The dimensions for

the backed Punch tests, including the punch, the titanium plate, and the Copper backing plate, are shown in Tables 5.2.

Dimension	Value (mm)
Specimen Thickness	0.6515
Clamp Diameter	25.4
Punch Diameter	1.6129
Punch Length	66.8
Backing Plate Thickness	1.83642

Table 5.2: 0.072' Backed Test dimensions.

Dimensions	Value (mm)
Specimen Thickness	0.6604
Clamp Diameter	25.4
Punch Diameter	2.2987
Punch Length	66.8
Backing Plate Thickness	1.26238

Table 5.3: 0.05' Backed Test dimensions.

Dimensions	Value (mm)
Specimen Thickness	0.6833
Clamp Diameter	25.4
Punch Diameter	2.2987
Punch Length	66.8
Backing Plate Thickness	0.8865

Table 5.4: 0.035' Backed Test dimensions.

The nominal size for the elements in the Punch finite element mesh was approximately 0.15 mm. The simulation used a $\frac{1}{4}$ axisymmetric mesh of both the plate and punch (Figure 5.32). The finite element mesh had a total of 398,761 elements, including 11,040 shell elements and 387,715 solid elements, with 430 rigid and 398,331 deformable elements. The tungsten carbide punch was modeled as elastic.

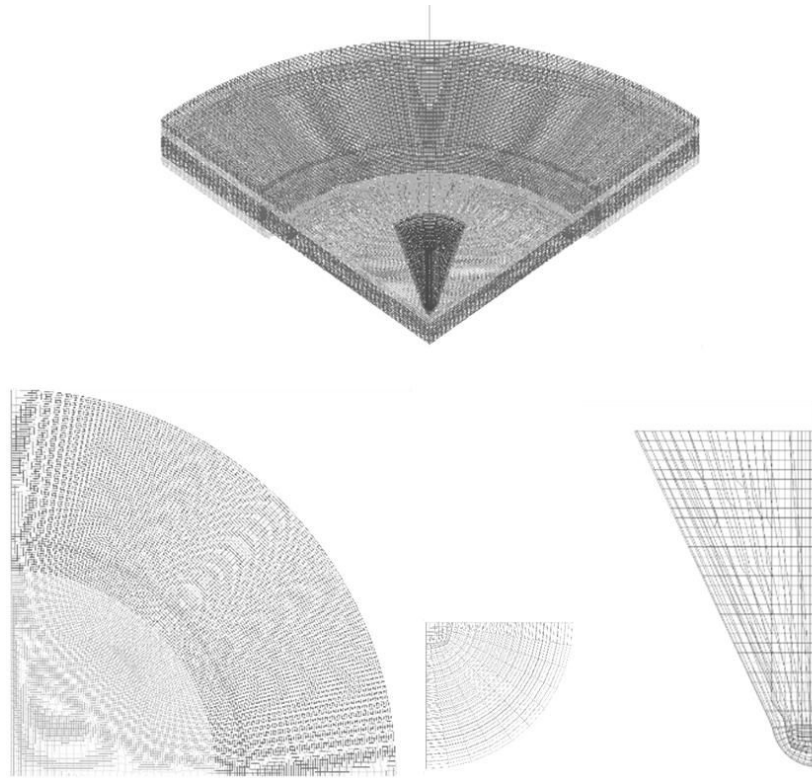


Figure 5.32: Backed test mesh, thick plate (left), and punch (right).

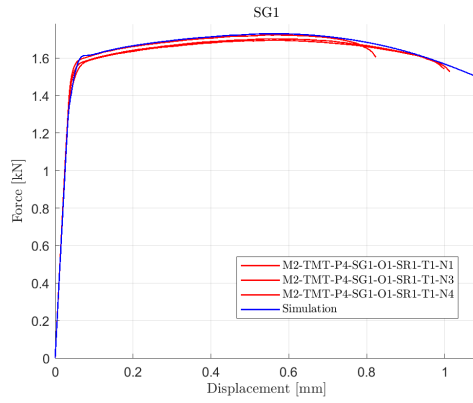
5.2. Simulation results of mechanical property tests

A single representative test was selected from multiple repeated tests of each specimen design series. The selected test was simulated using the precise geometry of the specimen without incorporating a failure surface. Predictions of force versus displacement from each selected test simulation were compared against the complete set of test repetitions. Additionally, in combined loading tests, torque versus twist angles were compared. Comparison between simulated full-field strains from contour plots and Digital Image Correlation (DIC) test images was also conducted. Upon achieving a satisfactory correlation between simulation and test results, initial inputs for creating the failure surface were estimated from these results.

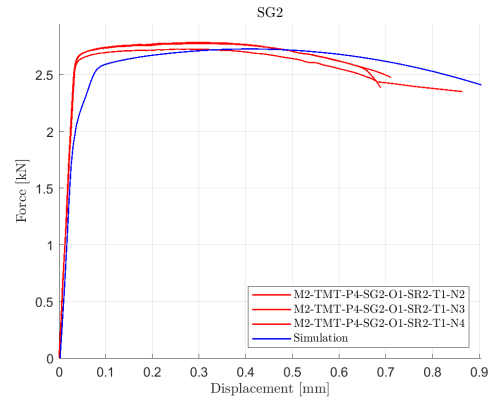
To ensure accurate displacement comparisons, extensometer locations from the tests were aligned with nodes from each finite element mesh. Differences between nodal displacements were utilized in comparison with test results. For simulations involving combined loading, the twist angle was derived from nodal displacements. The twist angle was directly compared with measurements obtained from a Rotary Variable Differential Transformer (RVDT) test. To obtain the forces, the `*DATABASE_CROSS_SECTION_PLANE` key-

word input was defined at the center of the specimen. The normal vector of the cross-section was oriented in the direction of the applied load. The comparison of force versus displacement time history plots for each specimen set is presented in Figure 5.33. It is important to note that in the punch tests, fracture does not occur abruptly with a sharp decrease in load-carrying capability. Instead, fracture develops gradually.

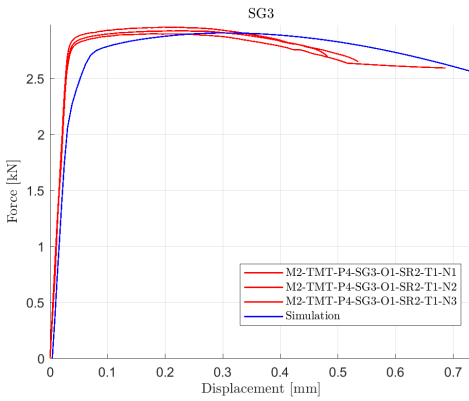
For accurate comparison of strain contour images between the simulation and the test, the virtual strain gauge length and element size in the simulation must be similar. Localization in the strain contour plots, just before fracture, can be compared by ensuring the same normalization in both images. The strain contour comparisons for each specimen set are shown in Figures 5.34 to 5.47.



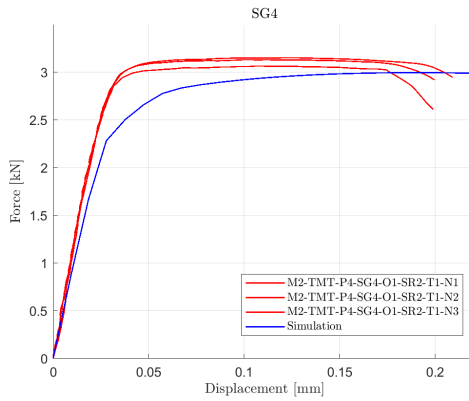
(a) SG1



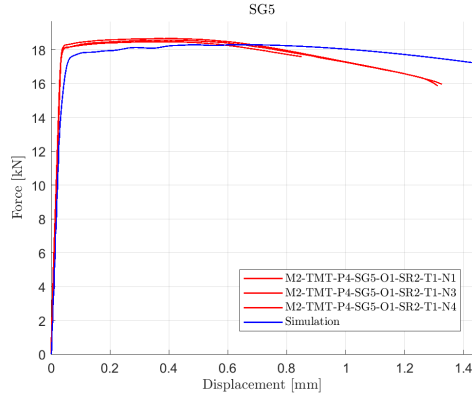
(b) SG2



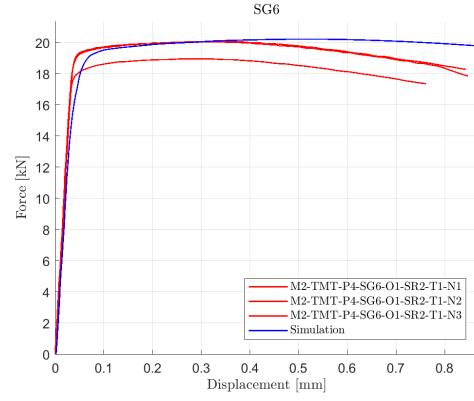
(c) SG3



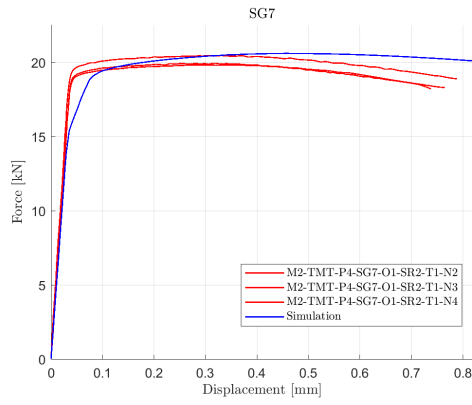
(d) SG4



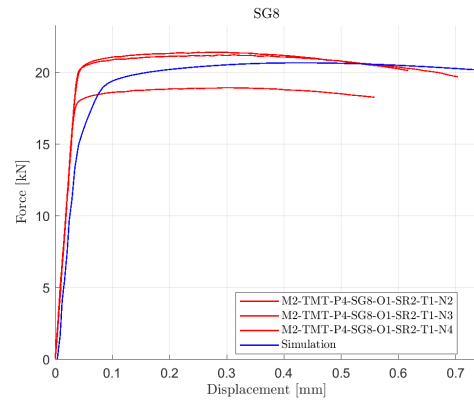
(e) SG5



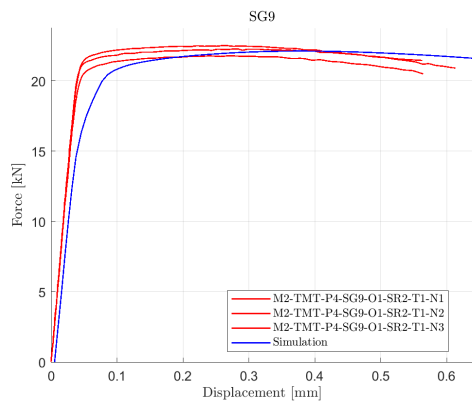
(f) SG6



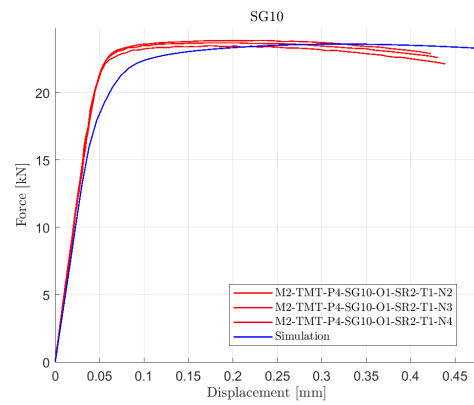
(g) SG7



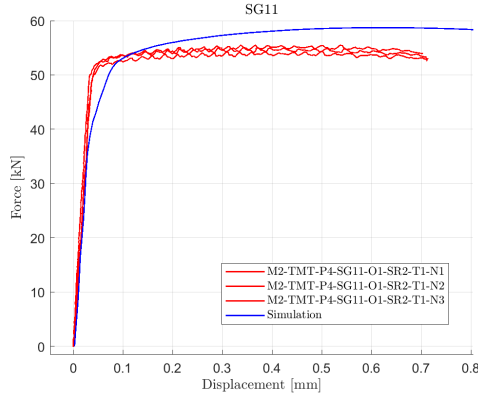
(h) SG8



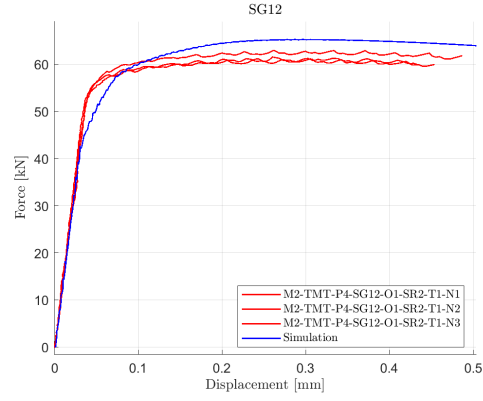
(i) SG9



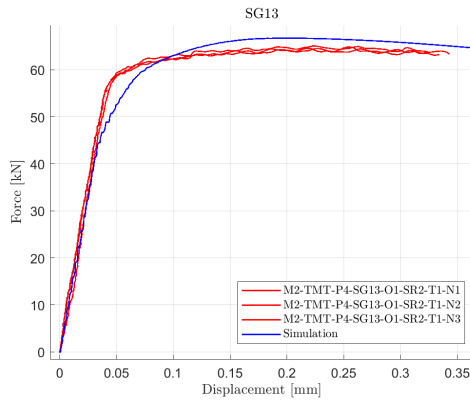
(j) SG10



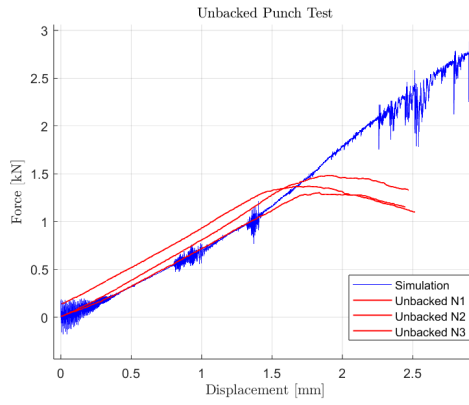
(k) SG11



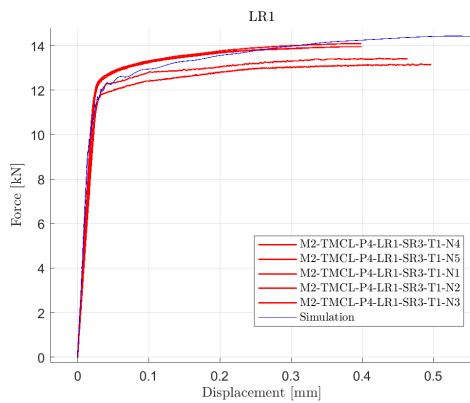
(l) SG12



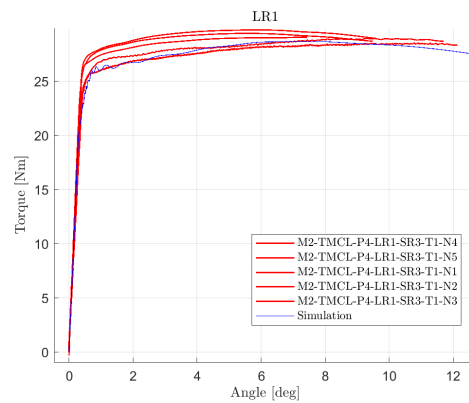
(m) SG13



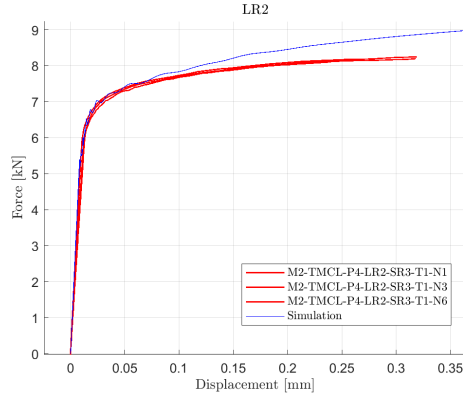
(n) Unbacked



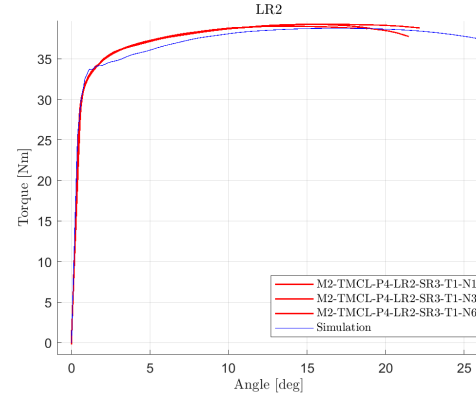
(o) LR1



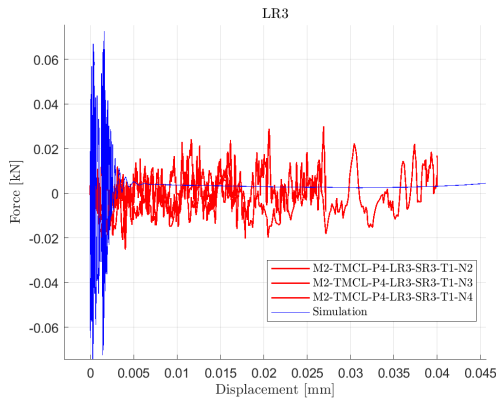
(p) LR1



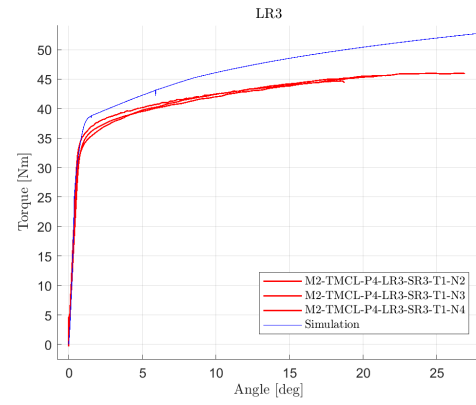
(q) LR2



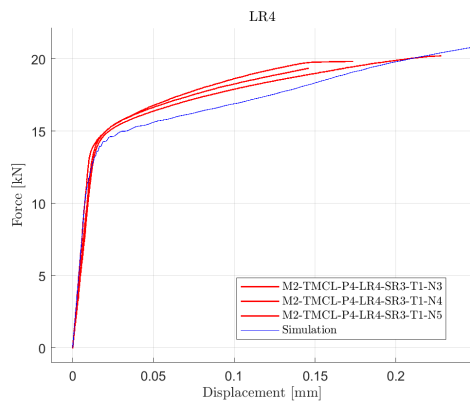
(r) LR2



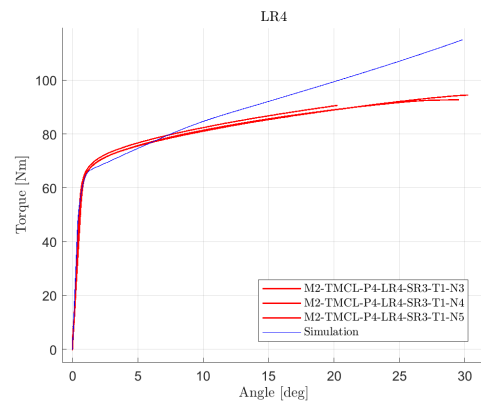
(s) LR3



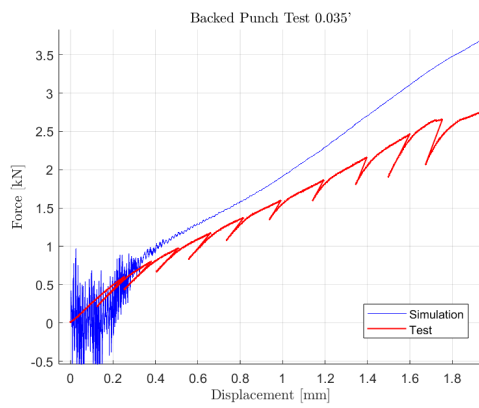
(t) LR3



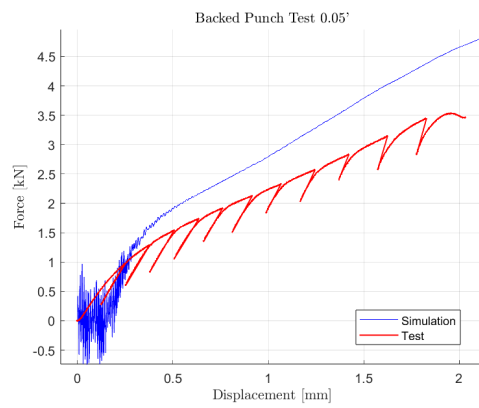
(u) LR4



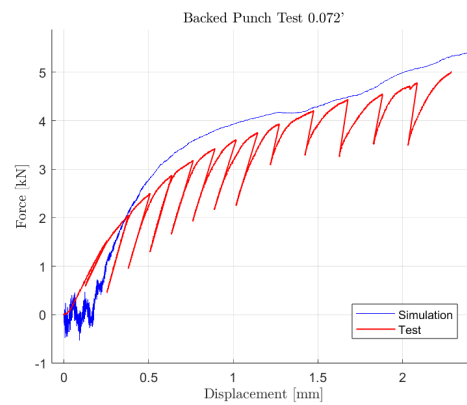
(v) LR4



(w) Backed 0.035'



(x) Backed 0.05'



(y) Backed 0.072'

Figure 5.33: Force-Displacement comparison.

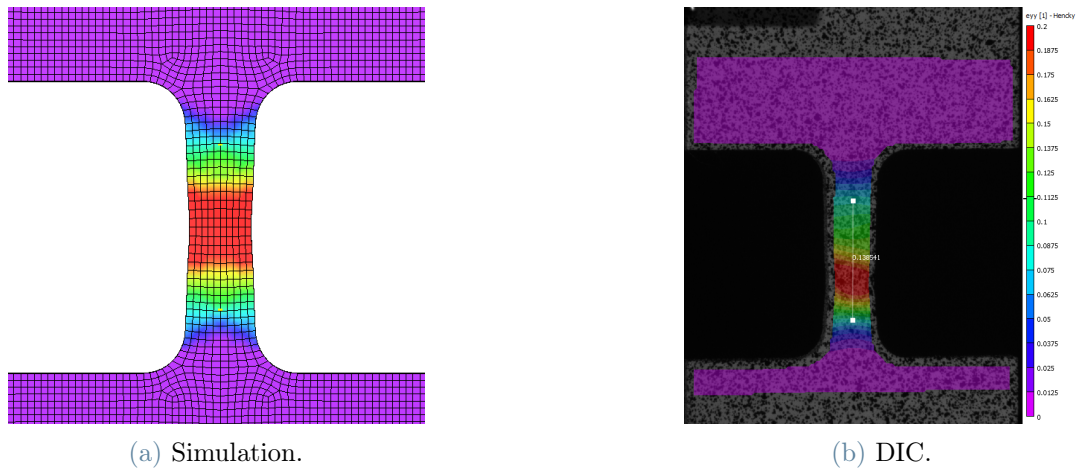


Figure 5.34: SG1 Strain comparison.



Figure 5.35: SG2 Strain comparison.

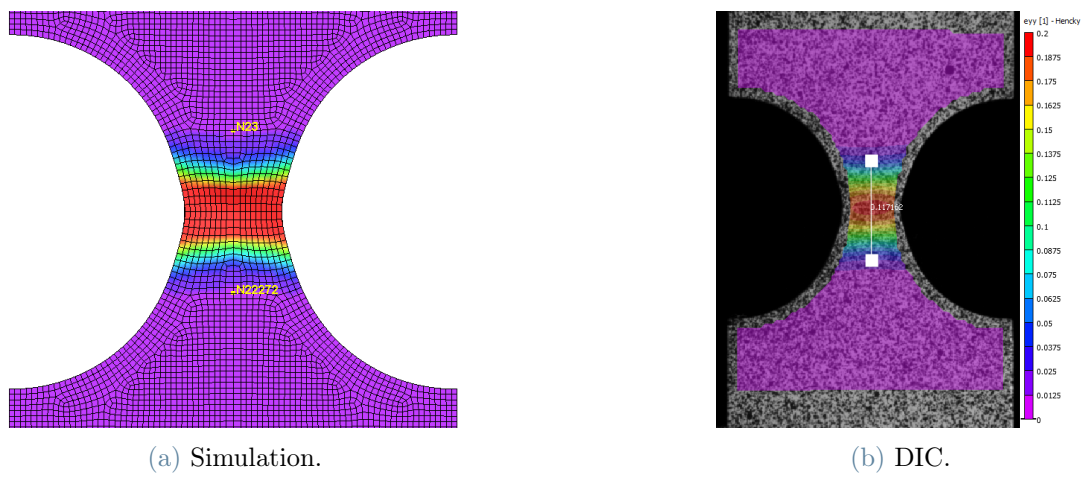


Figure 5.36: SG3 Strain comparison.

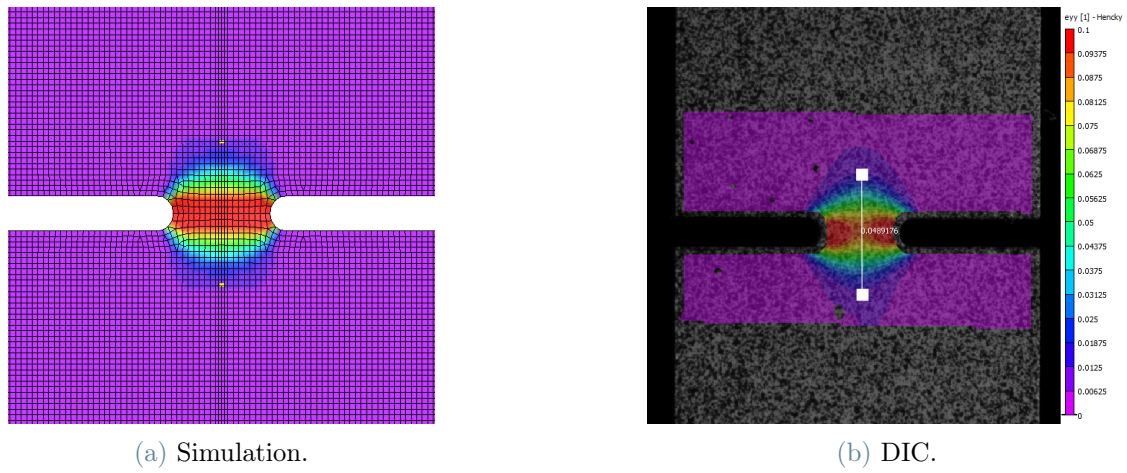


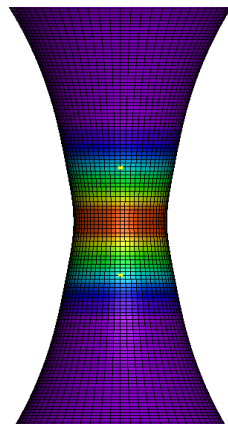
Figure 5.37: SG4 Strain comparison.



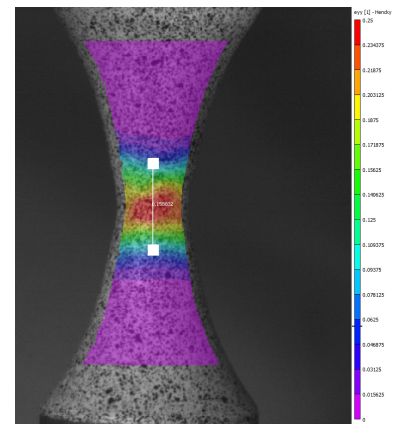
Figure 5.38: SG5 Strain comparison.



Figure 5.39: SG6 Strain comparison.

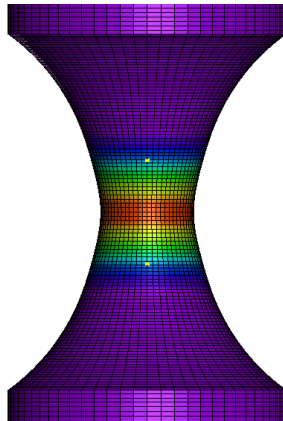


(a) Simulation.

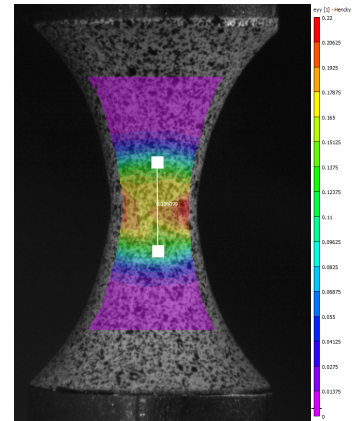


(b) DIC.

Figure 5.40: SG7 Strain comparison.

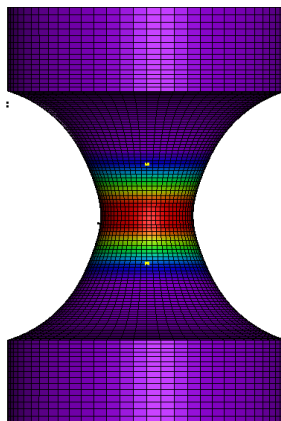


(a) Simulation.

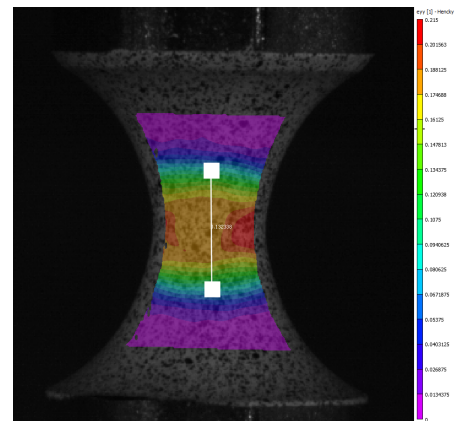


(b) DIC.

Figure 5.41: SG8 Strain comparison.

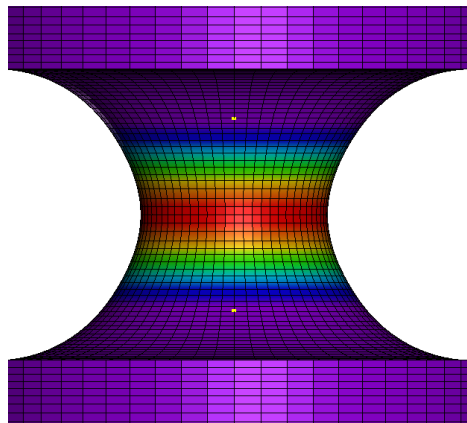


(a) Simulation.

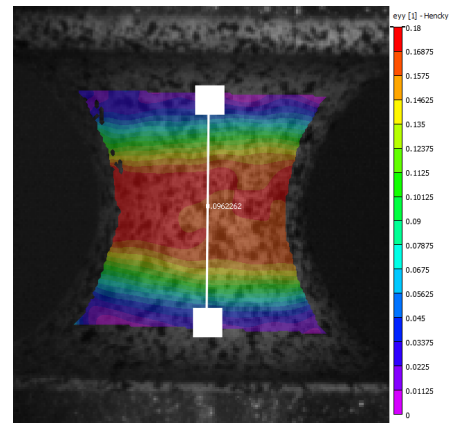


(b) DIC.

Figure 5.42: SG9 Strain comparison.

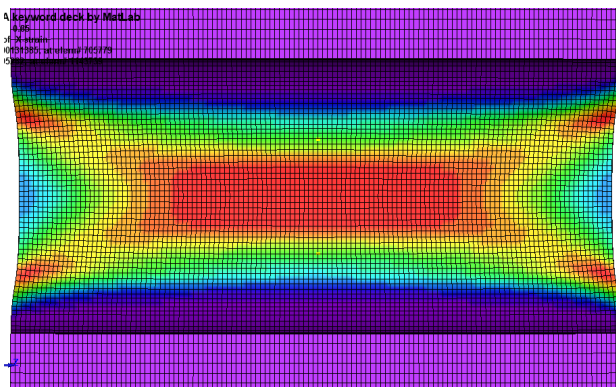


(a) Simulation.

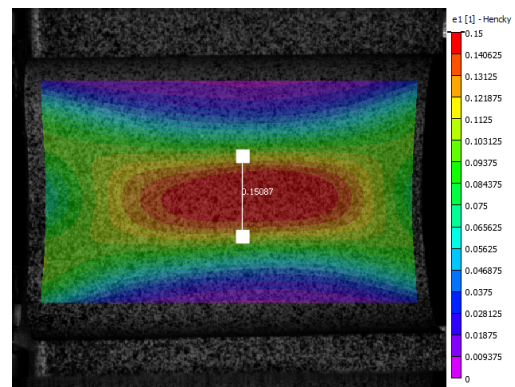


(b) DIC.

Figure 5.43: SG10 Strain comparison.

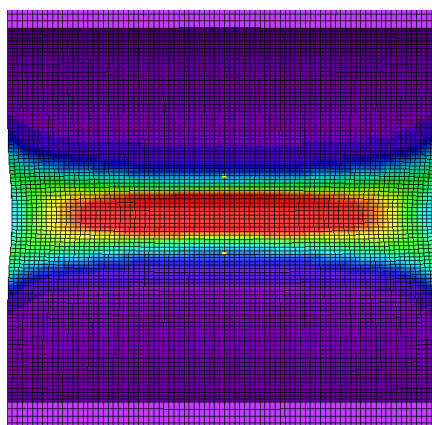


(a) Simulation.

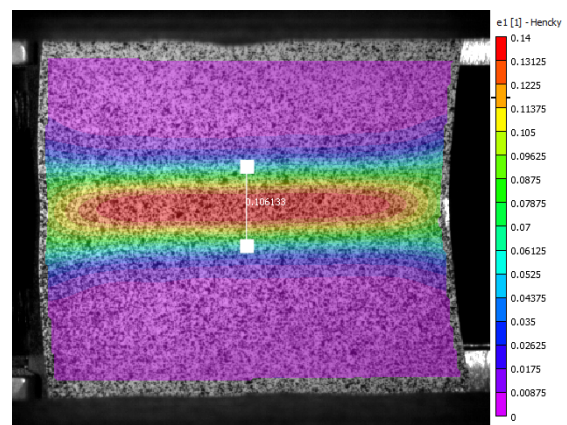


(b) DIC.

Figure 5.44: SG11 Strain comparison.



(a) Simulation.



(b) DIC.

Figure 5.45: SG12 Strain comparison.

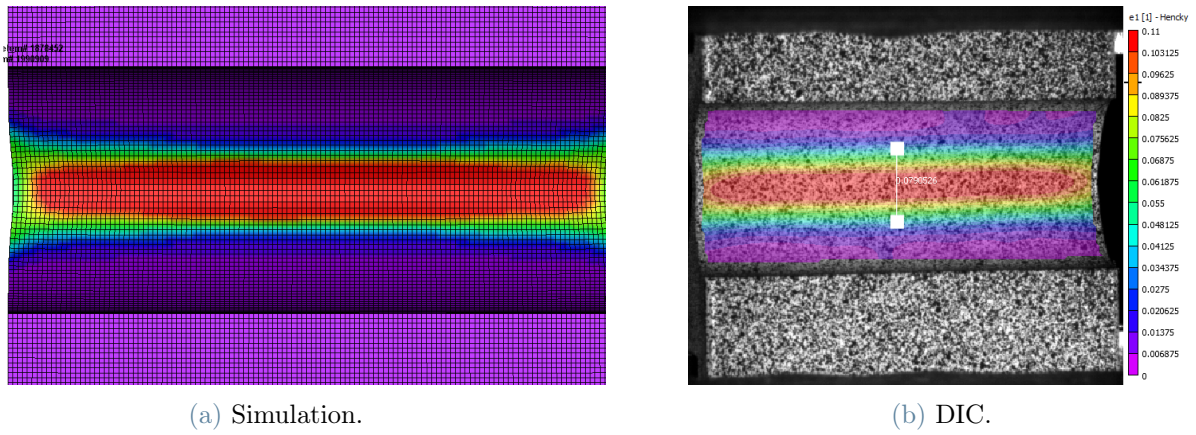


Figure 5.46: SG13 Strain comparison.

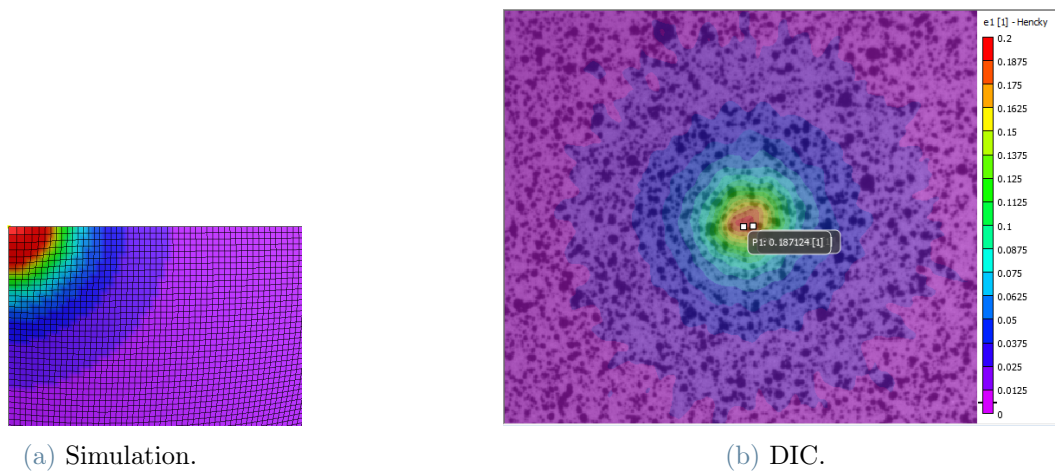


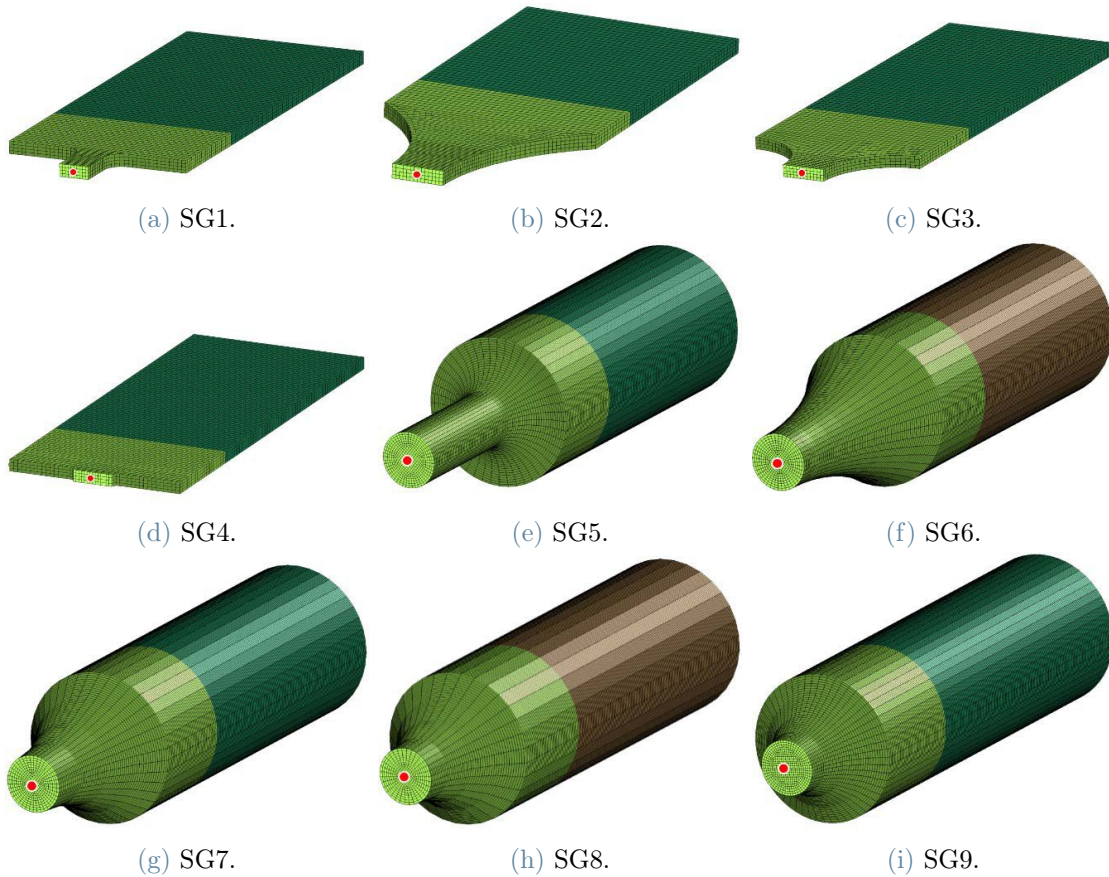
Figure 5.47: Unbacked Test Strain Comparison.

The comparisons between experimental and numerical results, as illustrated in Figure 5.33 and Figures 5.34 to 5.47 indicate a satisfactory level of agreement. The discrepancies observed in the Punch tests plots are likely attributed to the complexity and uncertainty associated with modeling the boundary conditions in these specific test configurations. However, these variations do not significantly impact the applicability of these tests for defining the failure surface. An initial oscillation can be observed in the punch tests, which is attributed to the initial contact dynamics, specifically the moment when the punch and the plate make contact.

It is important to clarify that for the combined loading tests, shear curves should be used, given that the torsional moment is predominant. However, this approach is not adopted, as it would result in a violation of the convexity condition of the failure surface [8].

A more detailed discussion on this matter can be found in the Appendix C.

The stress states of each test specimen are analyzed by assessing the triaxiality and Lode parameters of a single element. For each test case, an element situated at the center of the specimen, where fracture is expected to initiate, is selected. Figure 5.49 highlights the location of the chosen element with a red marker for each specimen.



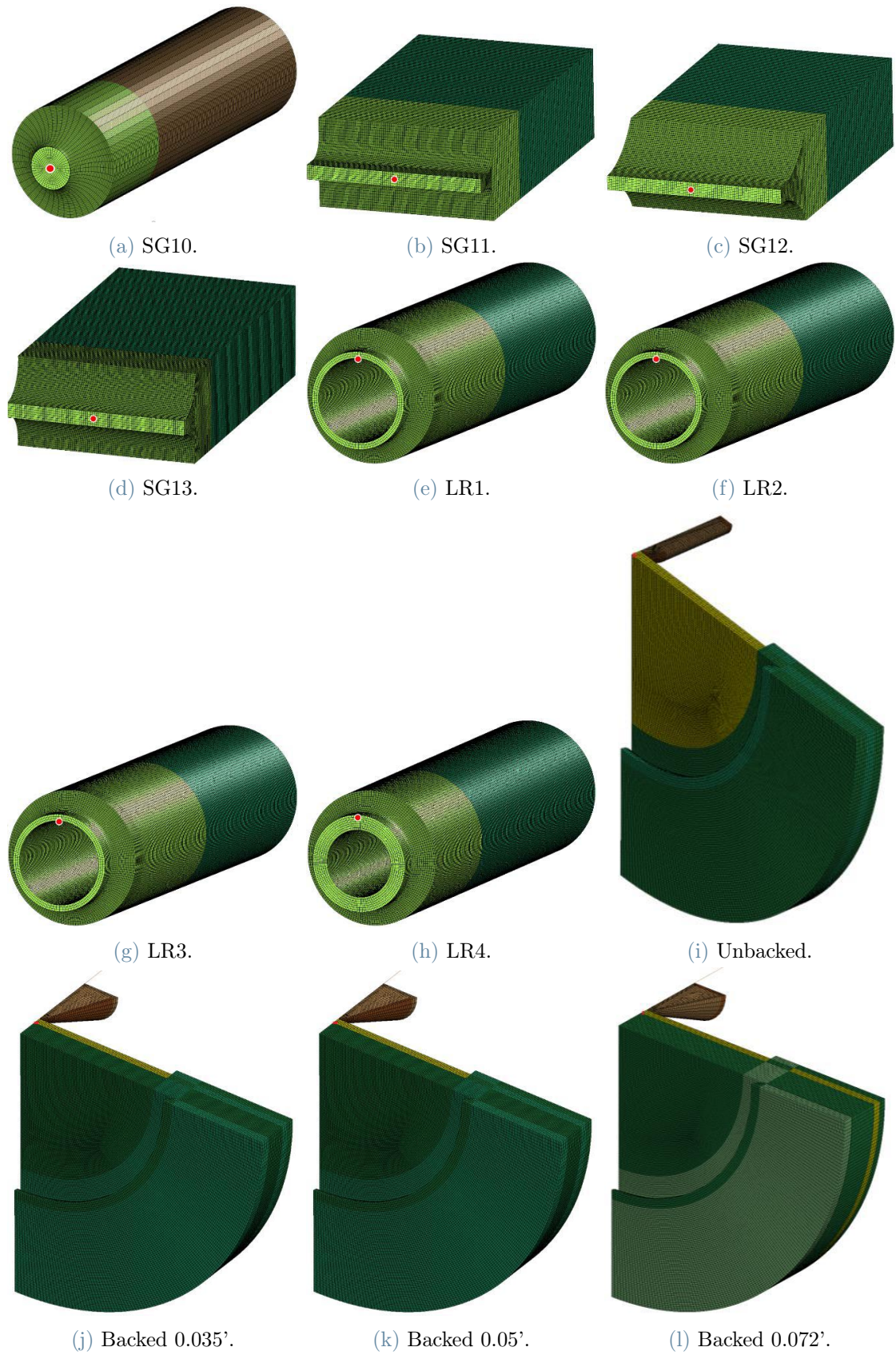
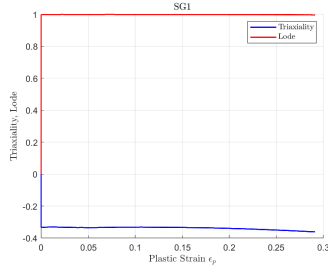
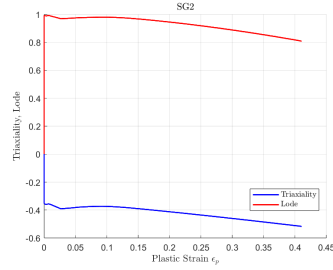


Figure 5.49: Red spot denoting selected elements for stress state evaluation.

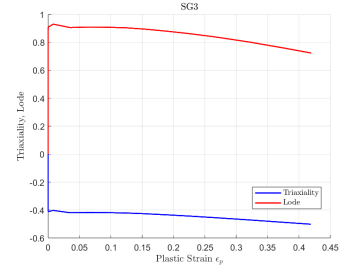
The time histories of the triaxiality and Lode parameter for the selected elements, which are most likely to failure, are presented as a function of the effective plastic strain in Figure 5.51.



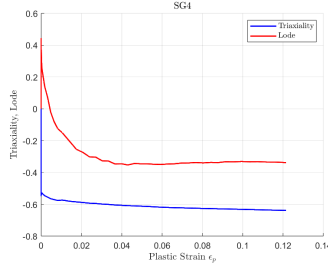
(a) SG1.



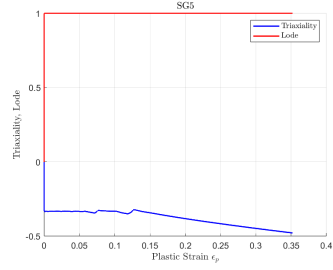
(b) SG2.



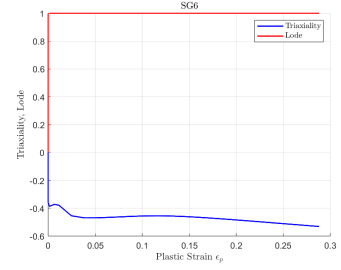
(c) SG3.



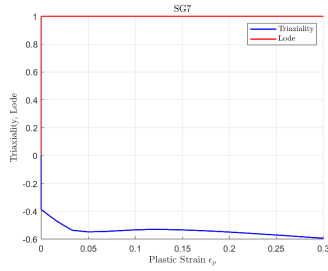
(d) SG4.



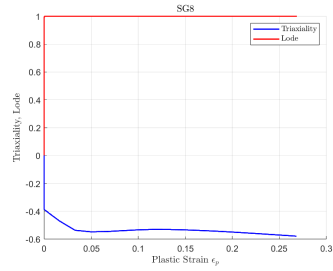
(e) SG5.



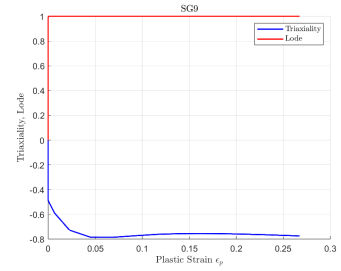
(f) SG6.



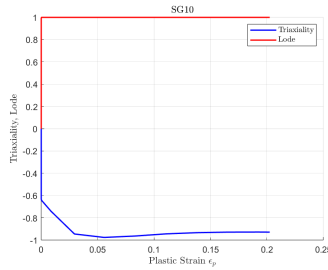
(g) SG7.



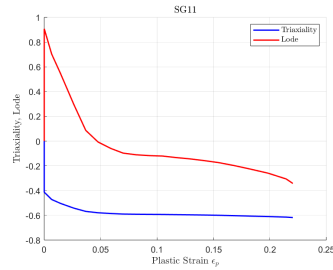
(h) SG8.



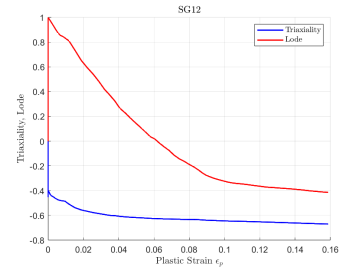
(i) SG9.



(j) SG10.



(k) SG11.



(l) SG12.

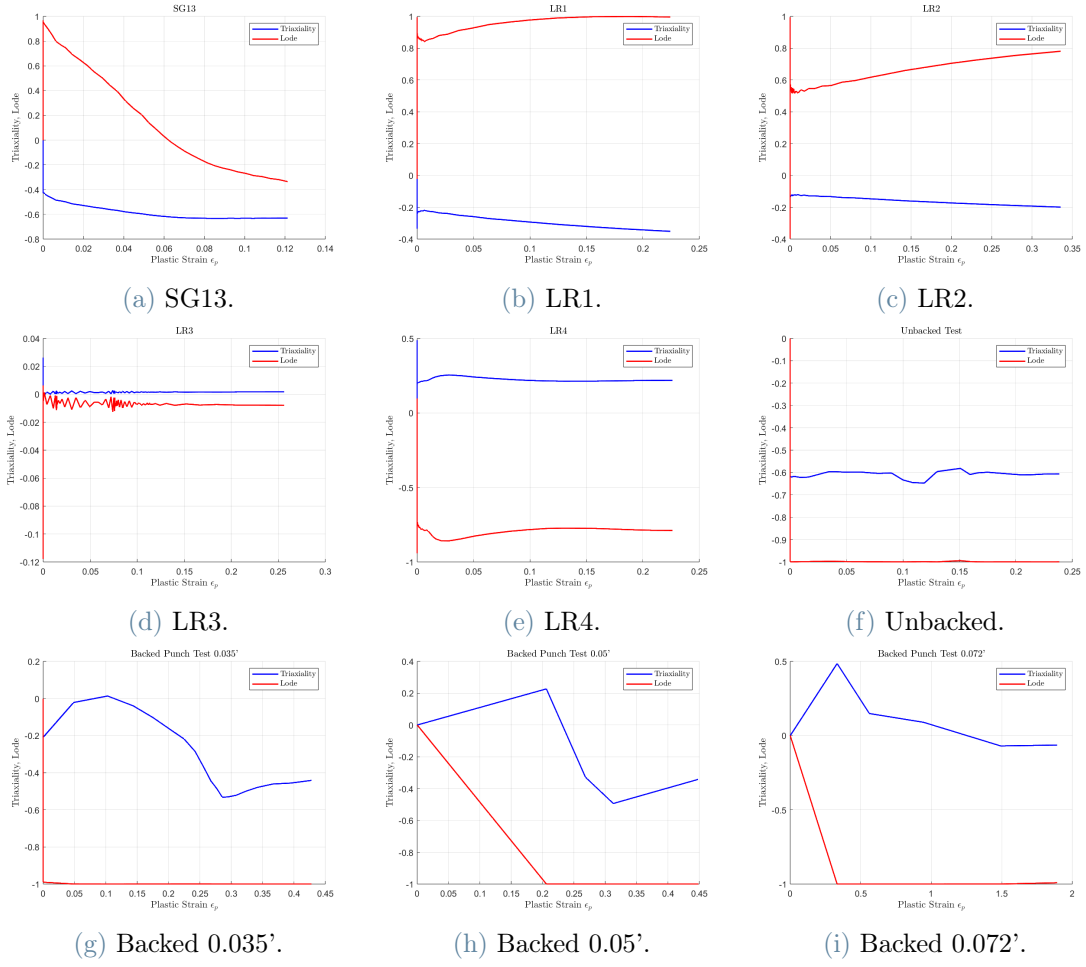


Figure 5.51: Triaxiality and lode parameter for each specimen's selected element.

To determine the average triaxiality, τ_{avg} , and the average Lode parameter, $\theta_{L\text{avg}}$, for each specimen, the following equations are employed:

$$\tau_{\text{avg}} = \frac{\int_0^{\varepsilon_{pf}} \tau d\varepsilon_p}{\varepsilon_{pf}} \quad (5.1)$$

$$\theta_{L\text{avg}} = \frac{\int_0^{\varepsilon_{pf}} \theta_L d\varepsilon_p}{\varepsilon_{pf}} \quad (5.2)$$

where τ represents the triaxiality as a function of the effective plastic strain ε_p , θ_L is the Lode parameter as a function of the effective plastic strain, and ε_{pf} denotes the final effective plastic strain.

It is important to note that, in the numerical simulations, triaxiality and the Lode parameter are computed at each time step and incorporated into the damage parameter

calculation. However, the average values of triaxiality and the Lode parameter are determined solely for characterization purposes and to define the initial failure surface inputs.

The computed average values of triaxiality and the Lode parameter for each test specimen are presented in Table 5.5. The fracture strains in the simulations were estimated by analyzing the effective plastic strain of the selected elements, as indicated in Figure 5.49, and identifying the point at which the simulated nodal displacement corresponded to the displacement at which fracture occurred in the physical test. The estimated fracture strain values are also reported in Table 5.5.

Table 5.5: Computed Triaxiality, Lode Parameter, and Fracture Strain for Test Specimens.

Test Number	Type	Triaxiality	Lode Parameter	Fracture Strain
M2-TMT-P4-SG1-O1-SR1-T1-N4	Plane Stress	-0.3381	0.9973	0.2918
M2-TMT-P4-SG2-O1-SR2-T1-N2		-0.4254	0.9277	0.4105
M2-TMT-P4-SG3-O1-SR2-T1-N1		-0.4458	0.8528	0.4193
M2-TMT-P4-SG4-O1-SR2-T1-N1		-0.6121	-0.2977	0.1215
M2-TMT-P4-SG5-O1-SR2-T1-N1	Axi-Symmetric	-0.3806	0.9991	0.3525
M2-TMT-P4-SG6-O1-SR2-T1-N1		-0.4717	1.0000	0.2880
M2-TMT-P4-SG7-O1-SR2-T1-N2		-0.5412	0.9994	0.3001
M2-TMT-P4-SG8-O1-SR2-T1-N2		-0.5363	1.0000	0.2684
M2-TMT-P4-SG9-O1-SR2-T1-N1		-0.7527	0.9993	0.2677
M2-TMT-P4-SG10-O1-SR2-T1-N2		-0.9243	1.0000	0.2025
M2-TMT-P4-SG11-O1-SR2-T1-N2	Plane Strain	-0.5829	-0.0483	0.2200
M2-TMT-P4-SG12-O1-SR2-T1-N1		-0.617	-0.006	0.1590
M2-TMT-P4-SG13-O1-SR2-T1-N1		-0.6934	0.1324	0.1212
M2-TMCL-LR1-P4-SR3-T1-N1	Combined Loading	-0.2956	0.9635	0.224
M2-TMCL-LR2-P4-SR3-T1-N1		-0.1614	0.662	0.339
M2-TMCL-LR3-P4-SR3-T1-N2		0.0016	-0.0069	0.2570
M2-TMCL-LR4-P4-SR3-T1-N3		0.2232	-0.7933	0.2270
Unbacked	Punch	-0.6090	-1.0000	0.238
Backed 0.035'		-0.2162	-0.8636	0.495
Backed 0.05'		-0.1103	-0.7622	0.453
Backed 0.072'		0.0941	-0.9119	1.8900

5.2.1. Failure surface generation

The average triaxiality values, Lode parameters, and fracture strains presented in Table 5.5 serve as input parameters for the MATLAB routine used to generate the failure surface. An initial failure surface is constructed by performing a curve-fitting procedure, as outlined in Section 4.2.

Since the initial failure surface was derived from stress state averages and estimated fracture strains, modifications were expected to achieve a closer alignment with experimental data. The input fracture strain values were iteratively refined until the numerical simulations, incorporating the revised failure surface, produced fracture responses within the observed range of experimental fracture strains. The final set of test simulation fracture strains utilized for this calibration is summarized in Table 5.6.

Following these refinements, the failure surface generation routine was executed again using the updated inputs, yielding the final failure surface depicted in Figure 5.52.

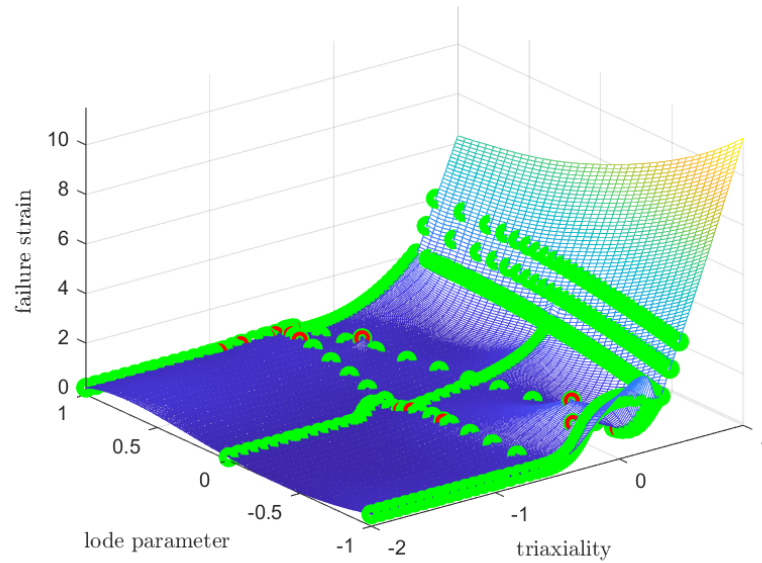


Figure 5.52: Final failure surface obtained after refinement of input parameters.

Table 5.6: Control point iterations and adjustments for each specimen.

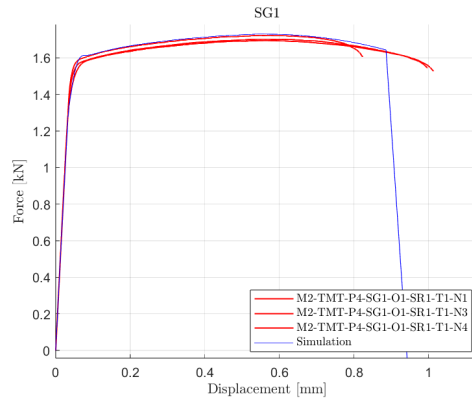
Test Number	Type	Triaxiality	Lode Parameter	Fracture Strain
M2-TMT-P4-SG1-O1-SR1-T1-N4	Plane Stress	-0.3381	0.9973	0.35 (+0.0582)
M2-TMT-P4-SG2-O1-SR2-T1-N2		-0.4254	0.9277	0.4105
M2-TMT-P4-SG3-O1-SR2-T1-N1		-0.4458	0.8528	0.4193
M2-TMT-P4-SG4-O1-SR2-T1-N1		-0.6121	-0.2977	0.4 (+0.2785)
M2-TMT-P4-SG5-O1-SR2-T1-N1	Axi-Symmetric	-0.3806	0.9991	0.3525
M2-TMT-P4-SG6-O1-SR2-T1-N1		-0.4717	1.0000	0.2880
M2-TMT-P4-SG7-O1-SR2-T1-N2		-0.5412	0.9994	0.3001
M2-TMT-P4-SG8-O1-SR2-T1-N2		-0.5363	1.0000	0.2684
M2-TMT-P4-SG9-O1-SR2-T1-N1		-0.7527	0.9993	0.2677
M2-TMT-P4-SG10-O1-SR2-T1-N2		-0.9243	1.0000	0.2025
M2-TMT-P4-SG11-O1-SR2-T1-N2	Plane Strain	-0.5829	-0.0483	0.1500 (-0.07)
M2-TMT-P4-SG12-O1-SR2-T1-N1		-0.617	-0.006	0.1000 (-0.059)
M2-TMT-P4-SG13-O1-SR2-T1-N1		-0.6934	0.1324	0.0500 (-0.0712)
M2-TMCL-LR1-P4-SR3-T1-N1	Combined Loading	-0.2956	0.9635	0.224
M2-TMCL-LR2-P4-SR3-T1-N1		-0.1614	0.662	0.6 (+0.261)
M2-TMCL-LR3-P4-SR3-T1-N2		0.0016	-0.0069	0.35 (+0.093)
M2-TMCL-LR4-P4-SR3-T1-N3		0.2232	-0.7933	0.3 (+0.073)
Unbacked	Punch	-0.6090	-1.0000	0.4 (+0.162)
Backed 0.035'		-0.2162	-0.8636	1.3 (+0.805)
Backed 0.05'		-0.1103	-0.7622	1.8 (+1.347)
Backed 0.072'		0.0941	-0.9119	2.0 (+0.11)

5.2.2. Simulation results with failure surface

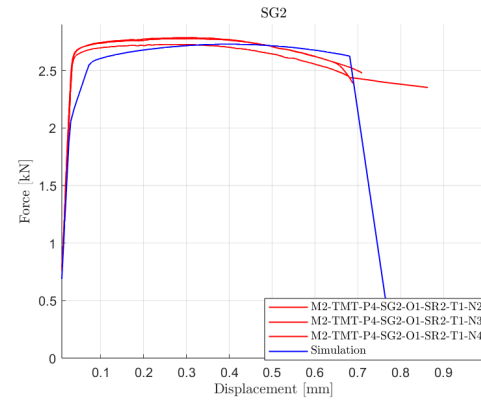
The failure surface presented in the previous section and illustrated in Figure 5.52 was implemented in the numerical simulations for each test specimen set. The force-displacement time histories obtained from the simulations were compared against the corresponding experimental data. The resulting force-displacement curves are depicted in Figure 5.53.

The simulated failure displacements were observed to occur within or in close proximity to the range of experimentally measured values, indicating a reasonable correlation between the numerical predictions and physical test results. This comparison represents the initial

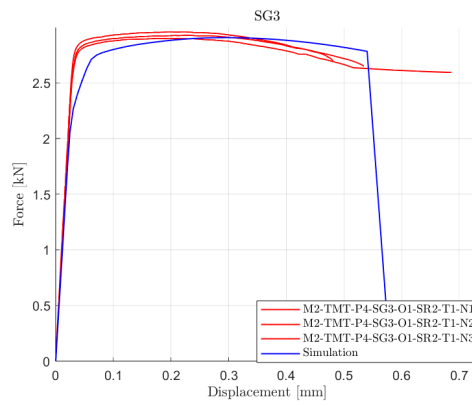
step in the verification process of the failure surface.



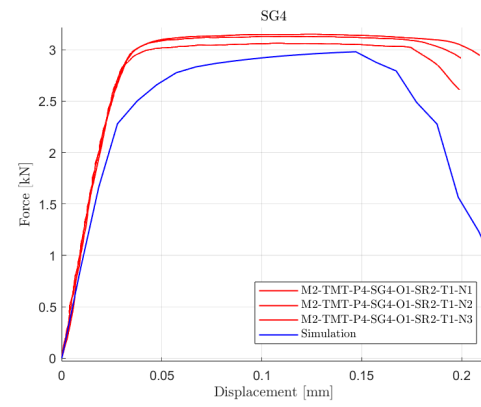
(a) SG1



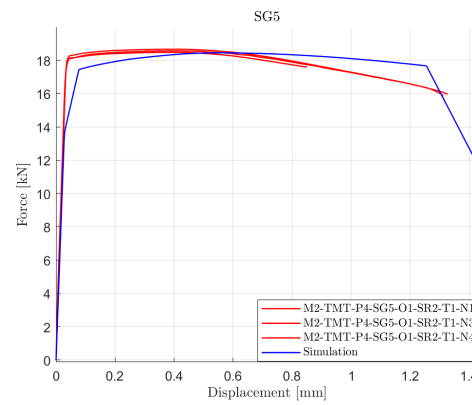
(b) SG2



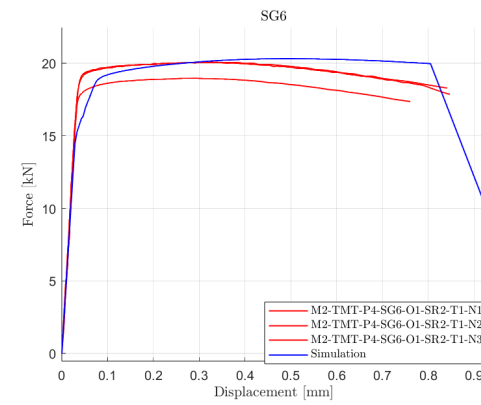
(c) SG3



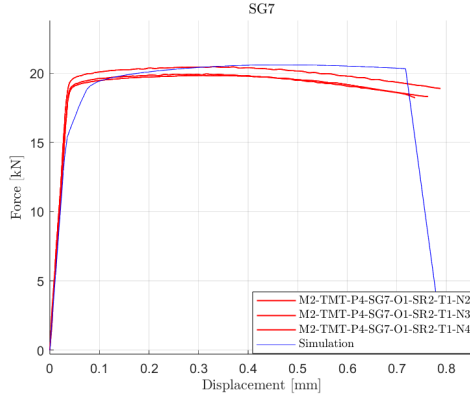
(d) SG4



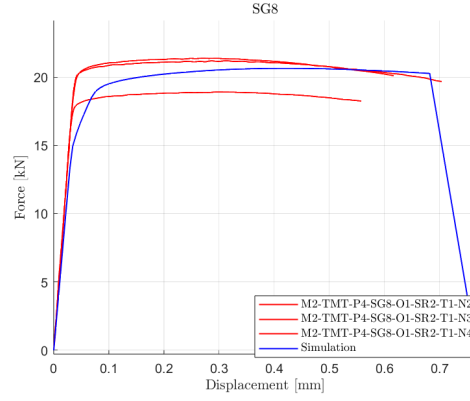
(e) SG5



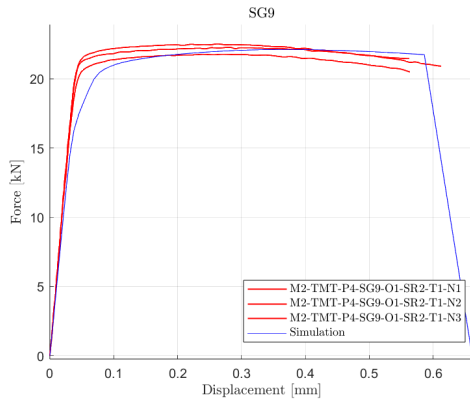
(f) SG6



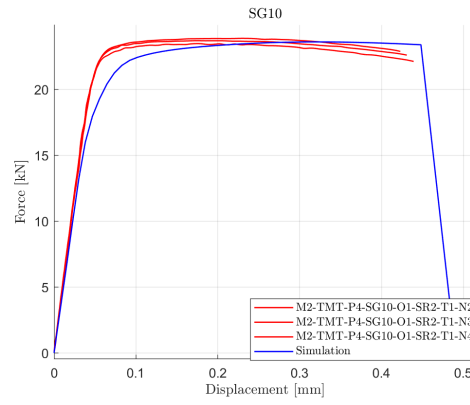
(g) SG7



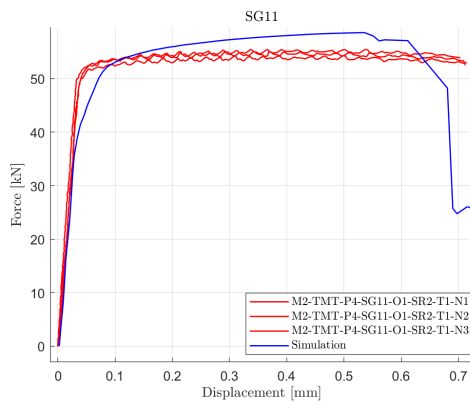
(h) SG8



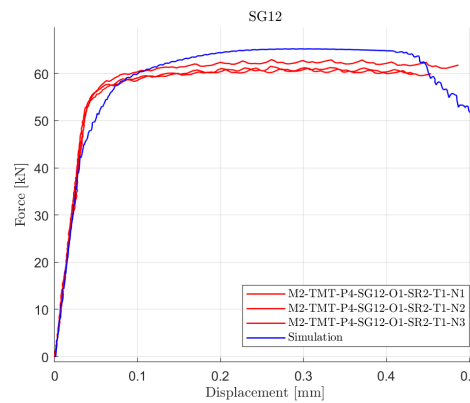
(i) SG9



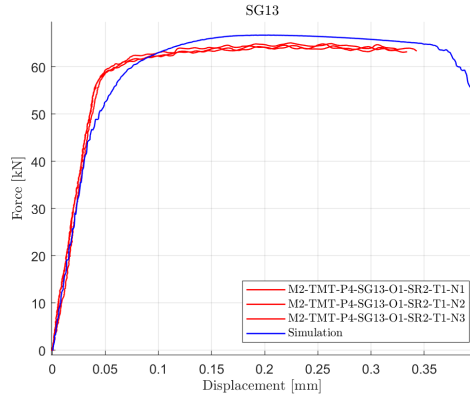
(j) SG10



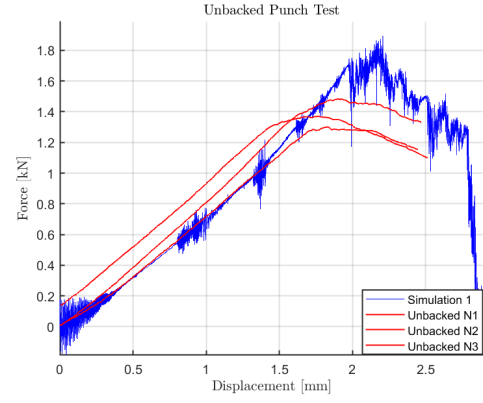
(k) SG11



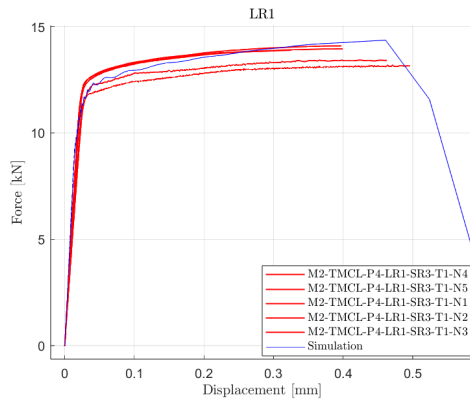
(l) SG12



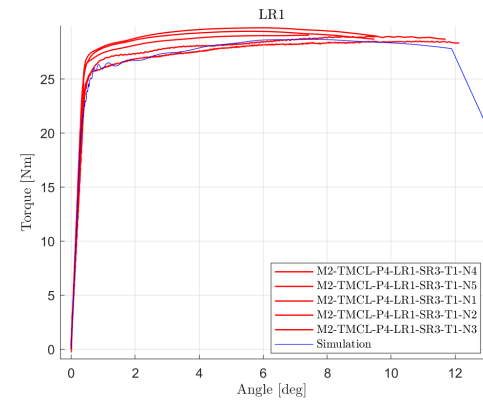
(m) SG13



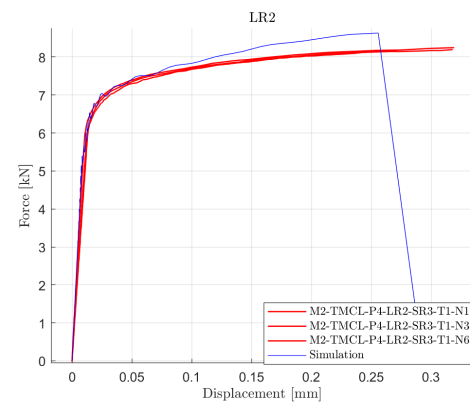
(n) Unbacked



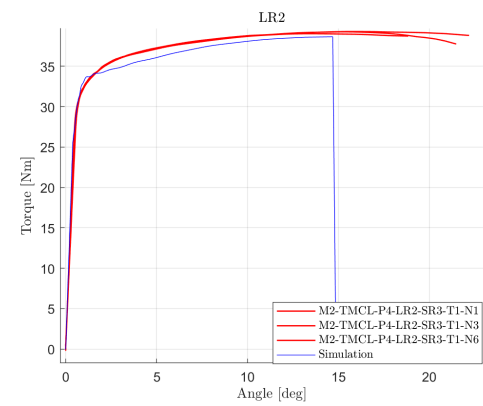
(o) LR1



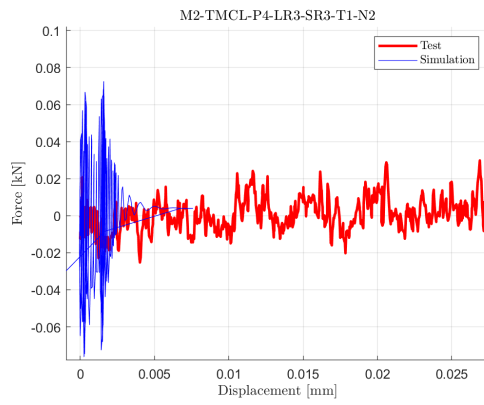
(p) LR1



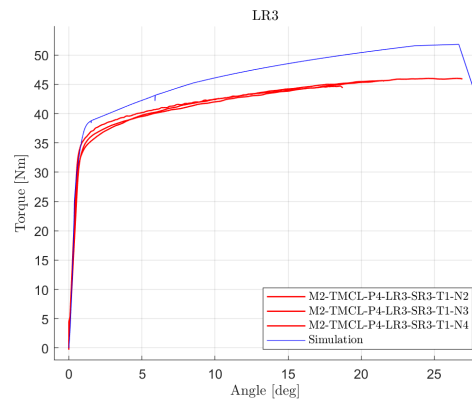
(q) LR2



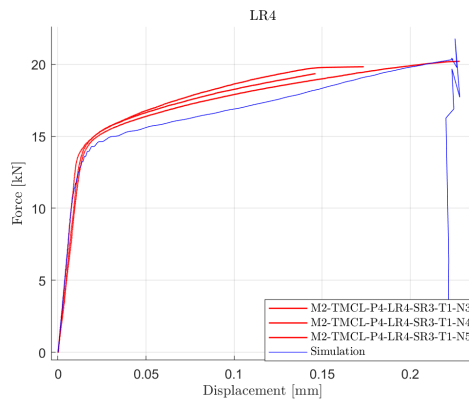
(r) LR2



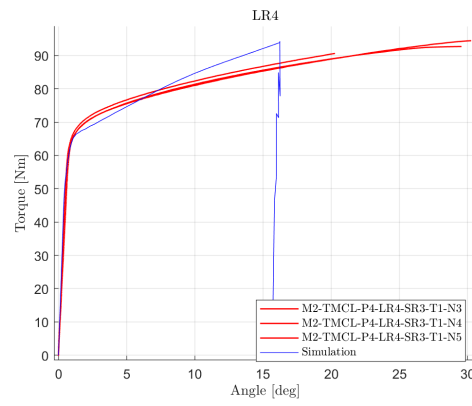
(s) LR3



(t) LR3



(u) LR4



(v) LR4

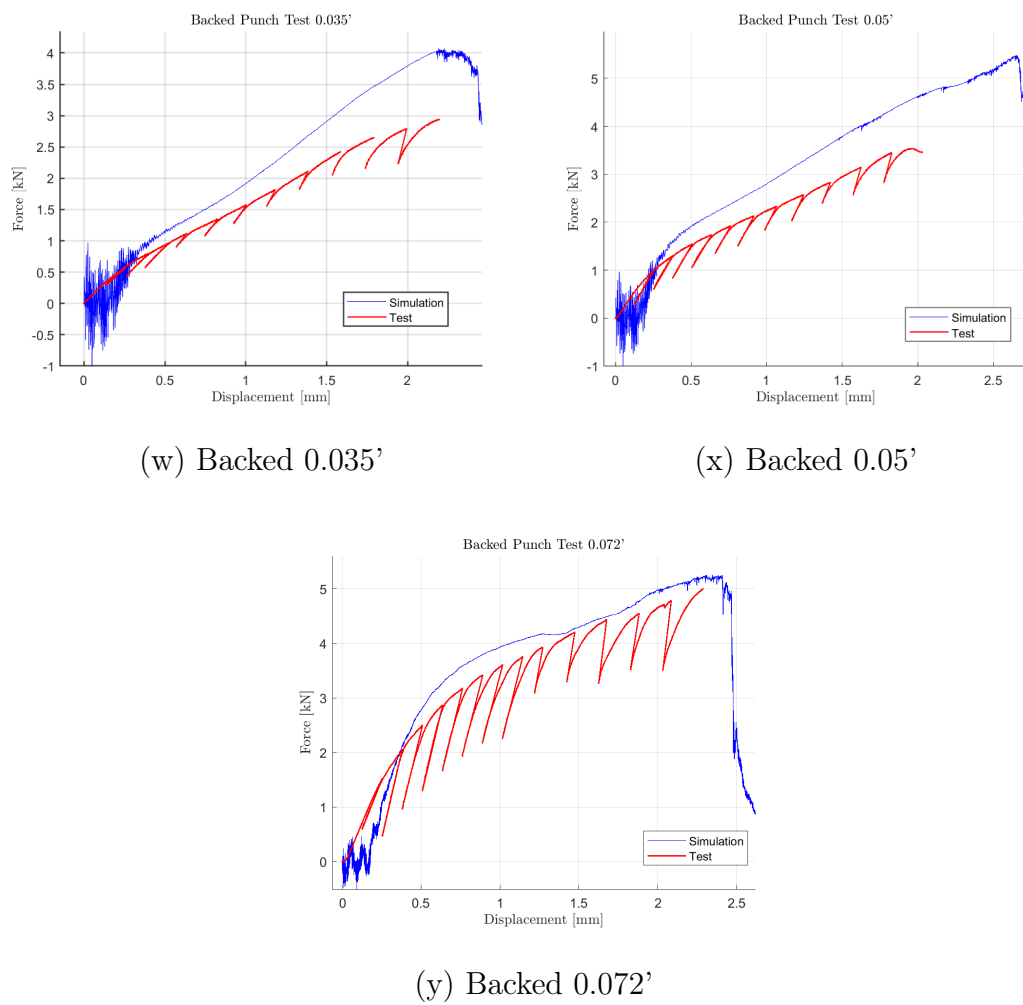


Figure 5.53: Force-Displacement comparison.

5.3. Creation of a Temperature Scaling function

The second element in the implementation of the `*MAT_224_GYS` failure model is the failure-temperature scaling function. This function acts as a scaling factor for the failure surface, which is temperature-dependent and varies with the temperature of the element at each time step. To establish this function, a temperature-testing series is necessary. In this study, five distinct temperatures were tested: 223 K, 293 K, 273 K, 673 K and 873 K. For each of these temperatures, the pure tension plane stress (SG1) specimen, as described in Section 3.3, was used.

In each simulation, a single yield curve was specified in the material keyword. A distinct yield curve was applied for each temperature since the stress-strain response differs across these temperatures. It is assumed that the temperature scaling is independent of strain rate, as the Johnson-Cook model applies temperature scaling uniformly for all strain rates. Although the failure surface was initially developed using tests conducted at a strain rate of 0.01 sec^{-1} and the temperature tests were performed at a strain rate of 1.0 sec^{-1} , this approach is valid. This is because strain rate and temperature scaling are independent and multiplicative in the Johnson-Cook law. Consequently, the impact of a temperature change remains consistent across all strain rates.

The input yield curves corresponding to each temperature are presented in Figure 5.54.

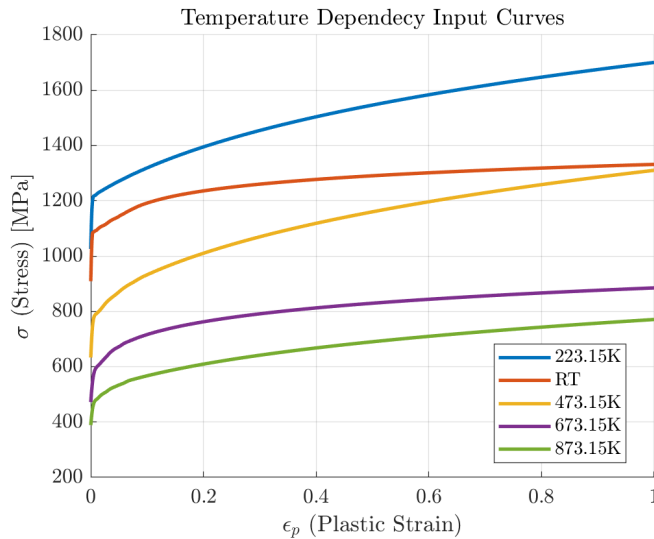


Figure 5.54: Input yield curves for each temperature.

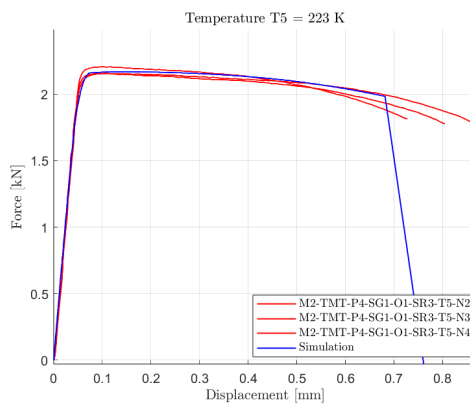
The initial verification simulations were conducted without incorporating the complete failure surface. These simulations followed the methodology outlined earlier (arbitrary speed, single load curve) but with a unique yield curve for each temperature.

By initializing each of these simulations without the failure surface, it was possible to develop a scaling function, ensuring that each temperature simulation would fail at the correct displacement.

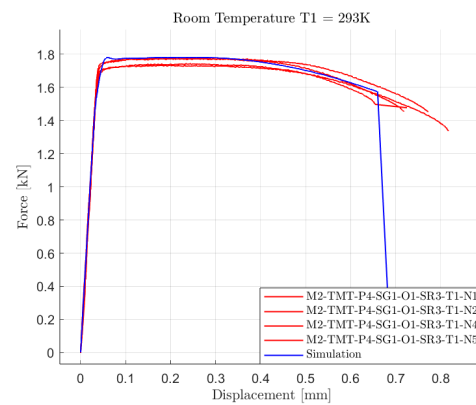
The same simulations were repeated using a unitary scaling factor for each Temperature. In these simulations, both the failure surface table and the temperature scaling function were included in the material keyword, alongside the yield curve for each specific temperature. After several simulation adjustments, the temperature scaling function was refined so that the failure displacements from the simulations aligned with the experimental spread. Additionally, the melting point of Ti-Al6-4V (1877 K) was added at the end of the curve to prevent exceedingly high scaling factors at very high temperatures due to extrapolation. The final temperature scaling function is presented in Table 5.7, and the resulting force-displacement plots are shown in Figure 5.55.

Temp (K)	Scaling Factor
0	0.982
223	0.982
293	1.000
473	1.364
673	1.364
873	3.636
1877	3.636

Table 5.7: Scaling factors by temperature.



(a) $T_5 = 223$ K



(b) Room Temperature $T_1 = 293$ K

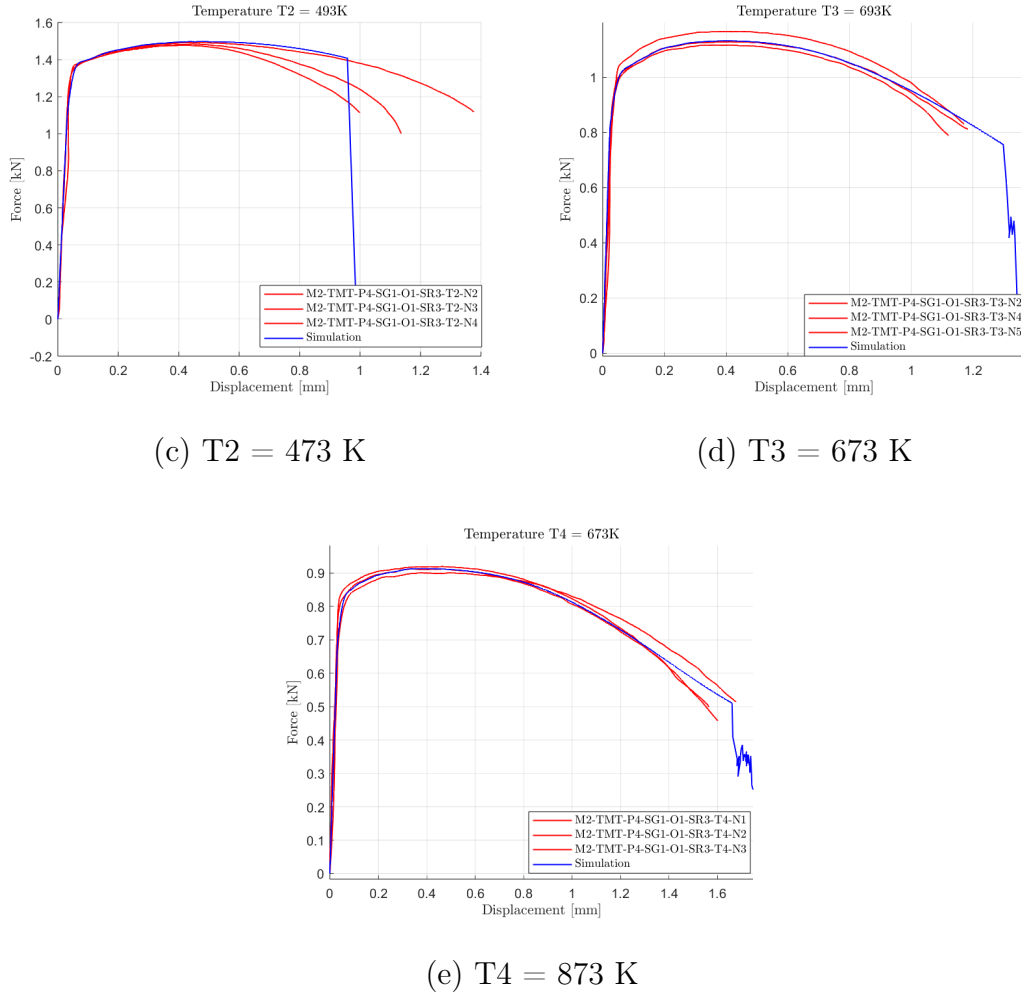


Figure 5.55: Force-Displacement plots with scaling function for each Temperature.

It is observed that at Temperature $T_3 = 673 \text{ K}$, the Force-Displacement curve does not perfectly match the experimental data. However, the decision was made not to reduce the scaling factor for this temperature in order to maintain the monotonicity of the scaling function, as this is considered the most logical assumption.

5.4. Creation of a Strain Rate Scaling function

Similar to the temperature scaling function discussed in Section 5.3, a scaling function for failure can also be developed for varying strain rates. Since the failure surface was initially based on a global strain rate of 0.01 sec^{-1} , other strain rates are not directly represented within the failure surface. To accommodate this, a scaling function can be employed to adjust the failure surface according to the elemental strain rate. In order to construct this scaling curve, the same strain rate testing series outlined in Section 3.5 was

utilized.

Each of these strain rate tests was simulated following the identical procedure used in the original SG1 simulation, except that the complete material model (including strain rate curves, temperature curves, failure surface, and temperature scaling function) was implemented. Consequently, these rate-dependent tests were considered to include both rate and thermal effects. The strain rate curves, which were already described in Section 2.5.1, are presented in Figure 5.56.

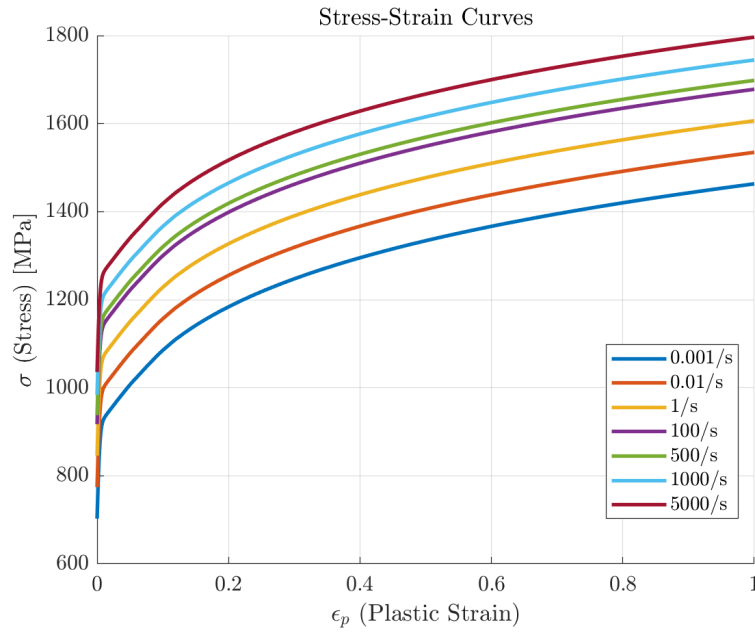


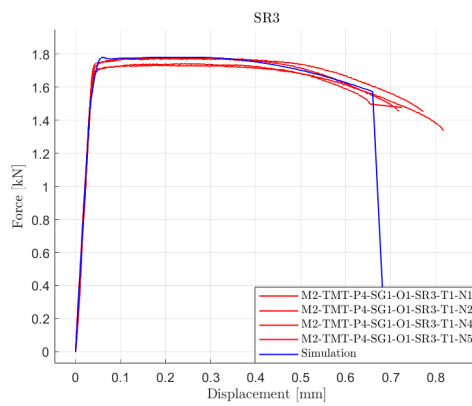
Figure 5.56: Strain rate input curves.

The goal of these simulations was to derive the strain rate scaling curve. An initial scaling curve was formulated and subsequently refined until all specimens failed within the experimental data spread. The strain rates used in the table were selected by analyzing the strain rates at the elements surrounding the failure zone, which differs from the average global strain rates provided by OSU. The final strain rate scaling data is summarized in Table 5.8.

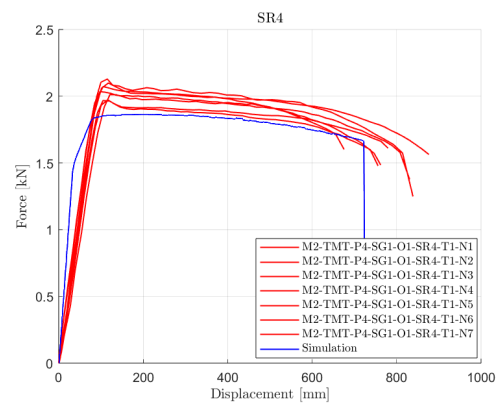
The final force-displacement curves, incorporating the strain rate scaling function as presented in Table 5.8, were plotted alongside the original experimental test data. The resulting plots for SR3, SR4, and SR5 analyses are shown in Figures 5.57.

Strain Rate (msec^{-1})	Scaling Factor
0.0001	1.0
0.0100	1.0
1.00	1.0
100.00	0.9
500.00	0.9
1000.00	0.9

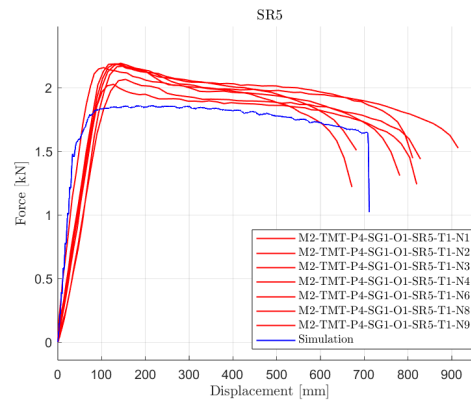
Table 5.8: Scaling factors for varying strain rates.



(a) SR3



(b) SR4



(c) SR5

Figure 5.57: Final force-displacement curves plotted against physical test data for (a) SR3, (b) SR4, and (c) SR5.

5.5. Creation of an Element Size fracture regularization curve

The final component of the Ti-6Al-4V *MAT_224_GYS material model is the mesh-size regularization scaling function, which plays a crucial role in element erosion simulations. It is well-established that simulations involving element erosion do not converge when the mesh size is reduced [30]. This scaling function defines the plastic failure strain as a function of the element size. The mesh size used in regularization is calculated by dividing the volume of the element by the area of its largest side. It is important to note that this corresponds precisely to the side length of a perfectly cubical element (i.e., when the aspect ratio is equal to 1). Only in this specific case the regularization function will behave optimally. Therefore, for such applications, elements should be used with an aspect ratio as close to unity as possible.

The regularization curve was developed by simulating the tension (SG1) specimen with different mesh sizes. Initially, all specimens had a mesh size of 0.2 mm. These specimens were then re-meshed with element sizes of 0.1 mm and 0.4 mm. The element configurations for each mesh size are depicted in Figures 5.58, 5.59, and 5.60.

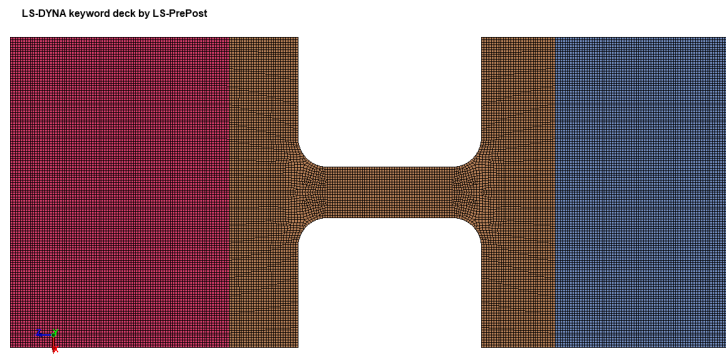


Figure 5.58: Element configuration with 0.10 mm mesh (557,856 elements).

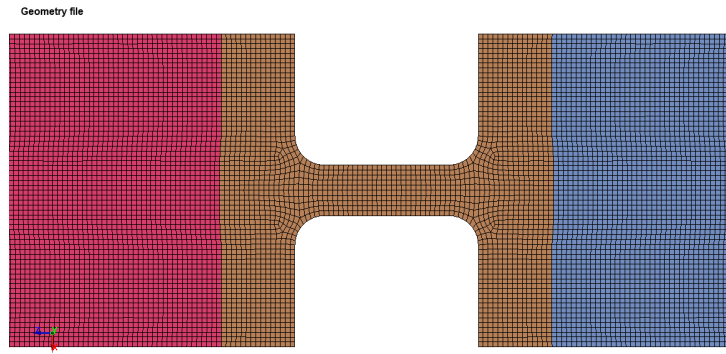


Figure 5.59: Element configuration with 0.20 mm mesh (73,184 elements).

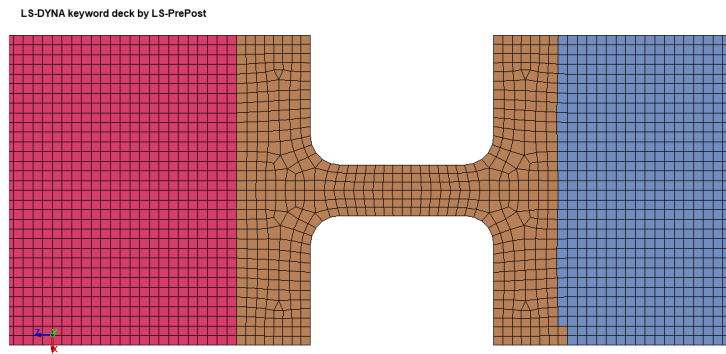


Figure 5.60: Element configuration with 0.40 mm mesh (8088 elements).

Each of these simulations was carried out in the same manner as for the original failure surface, using a single load curve and the failure surface, without applying any additional scaling factors. In order to generate the regularization scaling curve, each mesh was initially simulated with a scaling factor of 1.0. If the specimen failed before reaching the desired displacement, the scaling factor was increased. Conversely, if the specimen failed at a higher displacement than observed in the physical test, the scaling factor was reduced. After several iterations, the final regularization scaling factor was established. Additional data points were included to avoid extrapolation at very small and large mesh sizes. The final regularization scaling curve is presented in Table 5.9. It is important to note that users of this material model, with mesh sizes smaller than 0.1 mm or larger than 0.4 mm, should conduct further analyses to extend this scaling curve.

Mesh Size (mm)	Scaling Factor
0.00 mm	1.1
0.10 mm	1.1
0.20 mm	1.000
0.40 mm	0.83
0.50 mm	0.83

Table 5.9: Scaling factors by mesh size.

The force-displacement plots for the 0.10 mm, 0.20 mm, and 0.40 mm mesh sizes are shown in Figure 5.61. With the application of the scaling factors, all three specimens exhibit failure at nearly identical displacements, specifically 0.889 mm.

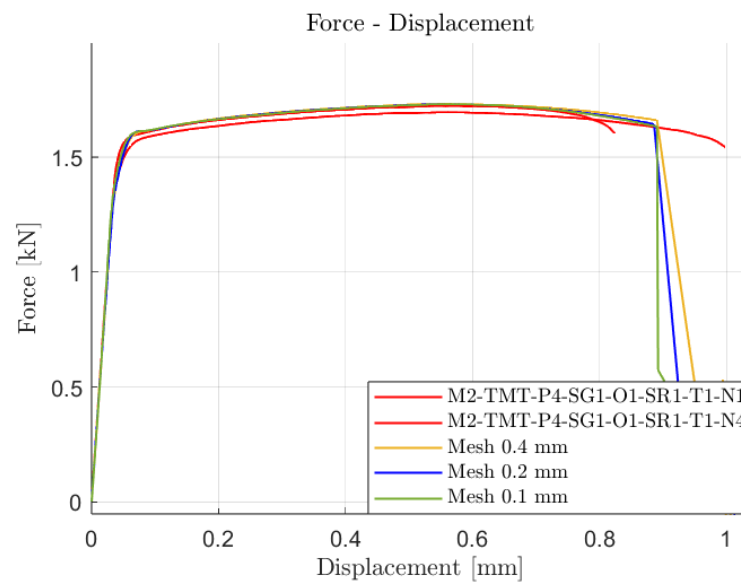


Figure 5.61: Comparison of force-displacement plots for mesh sizes of 0.10 mm, 0.20 mm, and 0.40 mm.

6 | Validation of the Model

To assess the accuracy and predictive capabilities of the Ti-6Al-4V material model, dynamic impact simulations were performed and compared to experimental test results. A series of ballistic impact tests were simulated to determine the ballistic limit of the Ti-6Al-4V material model. The complete material model was implemented in all simulations, incorporating strain rate tables, temperature tables, the failure surface, the strain-rate-failure scaling function, the temperature-failure scaling function, and the mesh-regularization scaling function.

6.1. NASA Ballistic Test Series

In 2013, NASA conducted a series of ballistic impact tests, the results of which are documented in the report [37]. This test campaign included ballistic experiments where a 19.0-mm diameter cylindrical A2 tool steel projectile impacted a 381-mm square Ti-6Al-4V plate. The plate had a thickness of 12.7 mm (0.5 inches) and was constrained such that a circular impact area of 254 mm remained free. The projectile was precisely aligned to strike the center of the plate.

The geometric details of both the plate and projectile are depicted in Figure 6.1, while Figures 6.3 and 6.4 illustrate the orientation of the finite element model and the mesh configuration of the projectile, respectively.

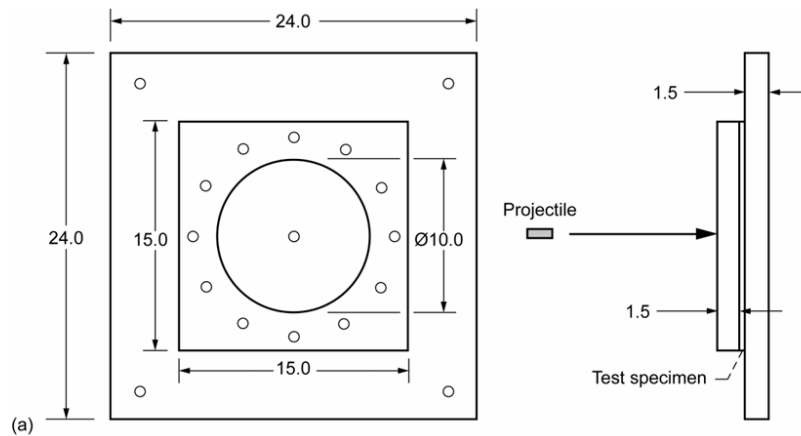


Figure 6.1: Geometric dimensions of the plate (in inches).

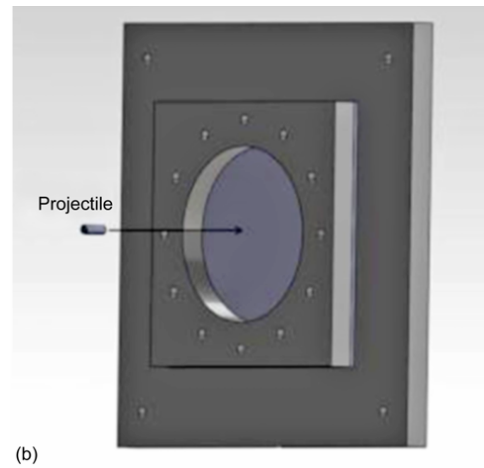


Figure 6.2: Clamp Fixture Assembly.

The projectile was modeled as an elastic body, justified by the test report's observation that *no evidence of plasticity or macro deformation [was] seen in the hardened A2 projectiles* [37]. Consequently, the numerical model accounted for elastic deformation but excluded plastic deformation.

The properties of the projectile are reported in Table 6.1.

Table 6.1: Projectile Penetration Velocity for the Panel Impact Tests.

Target Material	Thickness (in.)	Projectile Material	Hardness (HRC)	Length (in.)	Diameter (in.)	Mass (g)
Ti-6Al-4V	0.5	A2 Tool Steel	62-63	2.25	0.75	126.2

Additionally, the boundary condition, represented by the outer ring of the plate, was modeled as rigid, stationary, solid elements. Given the large ratio between the plate diameter and projectile diameter, boundary effects were assumed to be negligible.

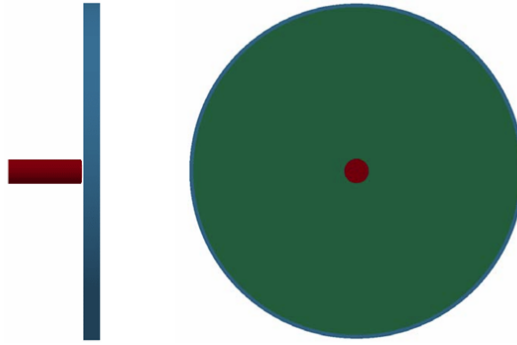


Figure 6.3: Orientation of the finite element model.

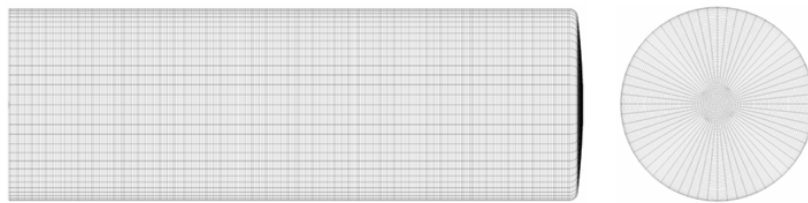


Figure 6.4: Mesh configuration of the projectile.

A matrix was developed based on the available experimental data. The primary independent variable was the projectile impact velocity, while the dependent variable was the projectile's exit velocity. Some of the impact and exit velocities close to the ballistic limit (minimum velocity at which a projectile can completely perforate the plate) recorded in the physical tests are summarized in Table 6.2.

Impact Velocity (m/s)	Exit Velocity (m/s)
196.9	46.33
182	0
192	0

Table 6.2: Impact and exit velocities from the experimental tests.

Three simulations were performed at the test velocities in Table 6.2, and all three cases resulted in containment. This outcome was expected due to the fact that the phenomenon of adiabatic shear banding is not accounted for in this material model: the mesh density

is too low to accurately capture the extreme localization of adiabatic shear bands. The analysis does not predict the rise in temperature caused by adiabatic heating in the corresponding elements [12].

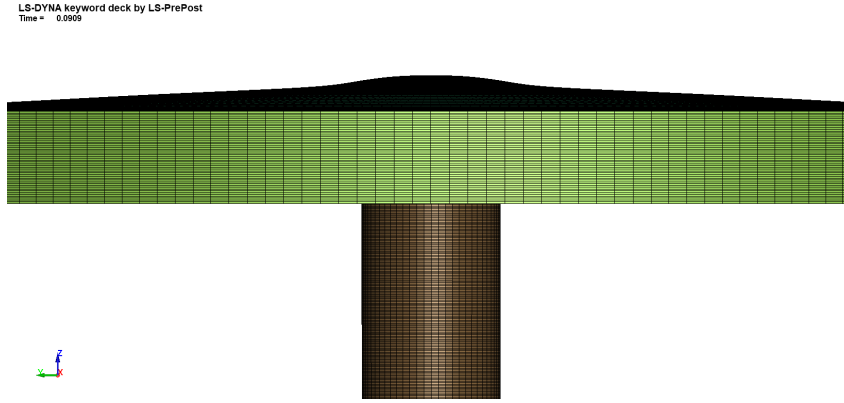


Figure 6.5: Finite Element Simulation of Ballistic Test.

6.1.1. Adiabatic Shear Band

Impact tests on thick plates of metal alloys under high-speed impact have shown that failure primarily occurs through adiabatic shear banding (ASB). Validated two-dimensional numerical simulations indicate that the standard Johnson-Cook (J-C) material model can accurately predict this failure mode only when the mesh is refined to element sizes on the same order of magnitude as the ASB width [11].

Since the ASB width in certain high-performance metal alloys can be as small as 1 μm , the J-C material model becomes impractical for real-world applications where such fine mesh resolutions are computationally infeasible. To address this limitation, modifications have been implemented in the MAT_224 model, enabling the formation of adiabatic shear bands under appropriate loading conditions even when using element sizes suitable for practical engineering applications.

The enhanced material model has been shown to accurately predict ballistic limits and failure modes in impact scenarios while utilizing mesh resolutions compatible with modern computational resources. These improvements were achieved by modifying the LS-DYNA source code for this specific material model. However, this implementation is not yet available in MAT_224_GYS and cannot be currently used for this work. This explains why no penetration occurs even in the ballistic test conducted at the highest velocity.

7 | Conclusions and Future Developments

This research focused on the development of an advanced plasticity and failure model based on `MAT_224_GYS` for Ti-6Al-4V, specifically tailored for high-strain-rate impact conditions, such as those encountered in uncontained turbine engine failures. The goal was to enhance the predictive capabilities of LS-DYNA simulations, reducing reliance on costly experimental testing while ensuring accuracy across a wide range of loading conditions.

The `MAT_224_GYS` model developed in this study introduces several key advancements:

- **Asymmetric Plasticity for Tension and Compression:** The model differentiates between the material's response under tensile and compressive loading, accurately capturing the anisotropic yield behavior of Ti-6Al-4V.
- **Strain Rate and Temperature Dependence:** The material behavior is defined through input tables, incorporating strain rate- and temperature-dependent yield curves to ensure realistic response under dynamic conditions.
- **Taylor-Quinney Coefficient Implementation:** The model accounts for the conversion of plastic deformation into heat, allowing for the influence of thermal softening at high strain rates.
- **Failure Surface with Scaling Functions:** The failure surface has been refined based on experimental data and includes temperature scaling, strain rate scaling and element size regularization, ensuring failure occurs at the correct displacement across different conditions.

The material model is not yet fully validated due to the absence of adiabatic shear band (ASB) update in `MAT_224_GYS`. The inability to explicitly model ASB prevents accurate predictions at higher impact velocities, like ballistic tests, where shear localization becomes a dominant failure mechanism.

The `MAT_224_GYS`-based model developed in this study represents a significant improve-

ment for aerospace structural simulations, offering a realistic and robust alternative to traditional plasticity models.

While the current model successfully enhances material behavior predictions, several areas require further refinement:

- **Implementation of Adiabatic Shear Banding (ASB):** To improve high-speed impact predictions, ASB initiation and growth criteria should be incorporated into the material model. This would allow the accurate representation of failure at extreme strain rates and ballistic impact conditions.
- **Expanded Experimental Validation:** Additional high-strain-rate and high-temperature experimental data would further validate and refine the model, ensuring its reliability for aerospace impact applications.
- **Enhancement of the Failure Surface:** Further experimental tests should be conducted using specimens of different geometries to obtain a wider range of tri-axiality and Lode parameter values. This would allow for a more comprehensive characterization of failure behavior and contribute to the development of a more robust and reliable failure surface.
- **Development of a MAT_264 Model for Anisotropy Consideration:** If a sufficient number of tests covering various loading directions are available to fully populate the required material tables, developing a MAT_264 model would be a valuable advancement, as it accounts for the material's anisotropy. However, in practice, obtaining such a large dataset is challenging. Without comprehensive test coverage, the model's effectiveness would be limited, but with complete input tables, it could further improve impact simulation accuracy and expand applicability in aerospace structural analysis.

Overcoming these challenges will facilitate the development of a fully validated, high-fidelity material model for impact simulations, enhancing the safety, efficiency, and cost-effectiveness of aerospace structural designs.

Bibliography

- [1] Y. Bai and T. Wierzbicki. Application of extended Mohr–Coulomb criterion to ductile fracture. *International Journal of Fracture*, 161:1–20, 2010.
- [2] Y. Bao. *Prediction of ductile crack formation in uncracked bodies*. PhD thesis, Massachusetts Institute of Technology, 2003.
- [3] Y. Bao and T. Wierzbicki. On fracture locus in the equivalent strain and stress triaxiality space. *International Journal of Mechanical Sciences*, 46:81–98, 2004.
- [4] I. Barsoum. *The effect of stress state in ductile failure*. PhD thesis, KTH, 2008.
- [5] I. Barsoum and J. Faleskog. Rupture mechanisms in combined tension and shear Experiments. *International Journal of Solids and Structures*, 44:1768–1786, 2007.
- [6] F. A. Bower. *Applied Mechanics of Solids*. CRC Press, Boca Raton, FL, 2010.
- [7] J. D. Campbell and W. G. Ferguson. The temperature and strain-rate dependence of the shear strength of mild steel. *The Philosophical Magazine: A Journal of Theoretical Experimental and Applied Physics*, 21(169):63–82, 1970. doi: 10.1080/14786437008238397.
- [8] K. Carney, P. Du Bois, K. Sengoz, L. Wang, and C.-D. Kan. Development of a Generalized Yield Surface for Isotropic, Pressure-Insensitive Metal Plasticity with Differing Tension, Compression, and Shear Yield Strengths. *Technical Report TC19-42*, 2020.
- [9] H. Conrad. *The Relation Between the Structure and Mechanical Properties of Metals*. Her Majesty’s Stationery Office, London, 1963.
- [10] D. Cordasco, W. Emmerling, and P. D. Bois. A Status Review of Failure Simulation at the Federal Aviation Administration. In *11th European LS-DYNA Conference 2017*, 2017.
- [11] S. Dolci. *The Influence of Strain Rate, Temperature Effects, and Instabilities in Failure Modeling for Metal Alloys*. PhD thesis, George Mason Univer-

- sity, 2021. URL <http://mutex.gmu.edu/login?url=https://www.proquest.com/dissertations-theses/influence-strain-rate-temperature-effects/docview/2573003826/se-2>.
- [12] S. Dolci, K. Carney, L. Wang, P. DuBois, and C.-D. Kan. The Effect of Inconel-718 High Strain Rate Sensitivity on Ballistic Impact Response using *MAT_224. In *15th International LS-DYNA Users Conference*. Center for Collision Safety and Analysis, George Mason University, USA, 2018.
 - [13] S. Dolci, K. Carney, L. Wang, P. D. Bois, and C.-D. Kan. Development of an Inconel-718 LS-DYNA[®] Material Model and *MAT_224 Input Parameters. Technical report, George Mason University, Center for Collision Safety and Analysis, December 2023.
 - [14] M. J. Donachie. *Titanium: A Technical Guide*. ASM International, Materials Park, OH, 1988. Comprehensive guide on the thermomechanical behavior of titanium alloys, including Ti-6Al-4V.
 - [15] D. C. Drucker. A definition of stable inelastic material. Technical Report NR-064-424, Office of Naval Research, 1950.
 - [16] R. N. Elshaer and K. M. Ibrahim. Applications of Titanium Alloys in Aerospace Manufacturing: A Brief Review. *The Bulletin of Tabbin Institute for Metallurgical Studies (TIMS)*, 111, 2022.
 - [17] M. I. Follansbee and U. F. Kocks. A Constitutive Description of the Deformation of Copper Based on the Hopkinson Bar. *Acta Metallurgica*, 36(4):81–87, 1988.
 - [18] X. Gao et al. Application of Digital Image Correlation to Study Deformation and Fracture Mechanisms in Polycrystalline Materials. *Materials Science and Engineering A*, 527(23):6329–6337, 2010.
 - [19] A. Gilat and T. Matrka. A new compression intermediate strain rate testing apparatus. *Dynamic Behavior of Materials*, 1:425–429, 2011.
 - [20] S. Haight, L. Wang, P. D. Bois, K. Carney, and C.-D. Kan. Development of a Titanium Alloy Ti-6Al-4V Material Model Used in LS-DYNA. Technical report, George Mason University, Center for Collision Safety and Analysis, 2016.
 - [21] J. Hallquist. *LS-DYNA Keyword User's Manual, Volume II*. 2025.
 - [22] J. Hancock and A. Mackenzie. On the mechanisms of ductile failure in high-strength steels subjected to multi-axial stress-states. *Journal of the Mechanics and Physics of Solids*, 24(2-3):147–160, 1976.

- [23] K. Inagaki, Y. Shirai, T. Takechi, and N. Ariyasu. Application and Features of Titanium for the Aerospace Industry. *Nippon Steel & Sumitomo Metal Technical Report*, (106), July 2014.
- [24] G. Johnson and W. Cook. Fracture Characteristics of Three Metals Subjected to Various Strains, Strain Rates, Temperatures, and Pressures. *Engineering Fracture Mechanics*, 21:31–48, 1985.
- [25] G. R. Johnson and W. H. Cook. Fracture of Materials Under High Rates of Strain. *Journal of Engineering Materials and Technology*, 107(4):324–329, 1985.
- [26] H. Kolsky. An investigation of the mechanical properties of materials at very high rates of loading. *Proceedings of the Physical Society. Section B*, 62(11):676, 1949.
- [27] J. Krafft, A. Sullivan, and C. Tipper. The effect of static and dynamic loading and temperature on the yield stress of iron and mild steel in compression. 1954.
- [28] Lai, S. H. and Chen, C. H. and Rittel, D. The Split Hopkinson Pressure Bar: A Comprehensive Review. *Experimental Mechanics*, 33(3):230–242, 1993.
- [29] S. Li and C. Chen. Study of the Influence of Surface Quality on the Digital Image Correlation Results. *Journal of Strain Analysis for Engineering Design*, 46(1):58–69, 2011.
- [30] LS-DYNA Aerospace Working Group. Awg modeling guidelines document. <http://awg.lstc.com/tiki/tiki-index.php?page=MGD>. Accessed: 2025-02-12.
- [31] A. Mackenzie, J. Hancock, and D. Brown. On the influence of state of stress on ductile failure initiation in high strength steels. *Engineering Fracture Mechanics*, 9(1):167–188, 1977.
- [32] H. J. McQueen. High-Rate Deformation of Metals. *Metallurgical Transactions A*, 27(10):2855–2862, 1996.
- [33] D. Mohr and S. Marcadet. Micromechanically-motivated phenomenological Hosford–Coulomb model for predicting ductile fracture initiation at low stress triaxialities. *International Journal of Solids and Structures*, 67-68:40–55, 2015.
- [34] T. Okura. Materials for Aircraft Engines. Technical report, Final Report for ASEN 5063 Aircraft Propulsion, 2015.
- [35] B. Pan, H. Xie, and J. Yan. Digital Image Correlation and its Applications to Experimental Mechanics. *Experimental Mechanics*, 49(3):383–406, 2009.

- [36] C.-K. Park, K. Carney, P. D. Bois, and C.-D. Kan. Development of Effective Taylor-Quinney Coefficient Tables of *MAT_224 for Aluminum 2024-T351, Titanium 6Al-4V, and Inconel 718 Alloys. 2023. URL <https://doi.org/10.21949/1528232>.
- [37] J. M. Pereira, D. M. Revilock, B. A. Lerch, and C. R. Ruggeri. Impact Testing of Aluminum 2024 and Titanium 6Al-4V for Material Model Development. Technical Report NASA/TM—2013-217869, DOT/FAA/TC-12/58, NASA Glenn Research Center, Cleveland, Ohio, 2013.
- [38] M. Peters, C. Leyens, J. Kumpfert, and S. Wilmes. Titanium Alloys for Aerospace Applications. *Advanced Engineering Materials*, 5(6):419–427, 2003. doi: 10.1002/adem.200310095.
- [39] A. Rosenfield and G. Hahn. *Transactions of the American Society for Metals*, 59, 1966.
- [40] N. Spulak. Investigations into Ductile Fracture and Deformation of Metals Under Combined Quasi-static Loading and Under Extremely High-rate Compressive Impact Loading. Technical thesis, Federal Aviation Administration, William J. Hughes Technical Center, Aviation Research Division, October 2020.
- [41] M. A. Sutton, J. J. Orteu, and H. W. Schreier. *Image Correlation for Shape, Motion and Deformation Measurements: Basic Concepts, Theory and Applications*. Springer, 2009.
- [42] G. Taylor. The use of flat-ended projectiles for determining dynamic yield stress I. Theoretical considerations. *Proceedings of the Royal Society of London. Series A. Mathematical and Physical Sciences*, 194(1038):289–299, 1948.
- [43] G. I. Taylor. The Use of a High-velocity Impact Apparatus for the Study of Plastic Flow in Metals. *Journal of the Mechanics and Physics of Solids*, 1(1):26–32, 1948.
- [44] L. Wang, P. DuBois, K. Carney, and C.-D. Kan. A Temperature and Strain Rate Dependent Material Model with Tension-Compression Asymmetry for 0.25 inch Ti-6Al-4V Plate. In *15th International LS-DYNA Users Conference*. Center for Collision Safety and Analysis, George Mason University, USA, 2018.
- [45] T. Wierzbicki, Y. Bao, Y. Lee, and Y. Bai. Calibration and evaluation of seven fracture models. *International Journal of Mechanical Sciences*, 47(4-5):719–743, 2005.
- [46] J. C. Williams and R. R. Boyer. Opportunities and Issues in the Application of Titanium Alloys for Aerospace Components. *Metals*, 10(6), 2020. ISSN 2075-4701. doi: 10.3390/met10060705. URL <https://www.mdpi.com/2075-4701/10/6/705>.

A | Digital Image Correlation

Digital Image Correlation (DIC) is an advanced non-contact optical technique widely employed for full-field strain and displacement measurement during mechanical testing. The technique involves capturing sequential digital images of a specimen's surface at different stages of deformation and comparing them to extract displacement and strain information. The primary advantage of DIC lies in its ability to measure full-field responses, capturing spatial and temporal variations in strain and displacement across a specimen, in contrast to traditional, localized measurement methods such as strain gauges or extensometers [41]. This makes DIC particularly valuable for applications requiring high spatial resolution, such as material testing under complex loading conditions, where traditional methods may be insufficient.

A.1. Working Principle

The underlying principle of DIC is based on the analysis of pixel intensity variations within images captured at different deformation stages. A random speckle pattern is applied to the specimen surface, and the images are captured using high-resolution digital cameras. The speckle pattern serves as a unique marker that enables the DIC algorithm to track local displacement between successive images.

A.2. Differences in SHPB Testing for Tensile and Compression Tests

The DIC process can be divided into two main phases: image acquisition and data analysis. During image acquisition, two or more images of the specimen are taken at distinct time intervals, typically one before loading and another during deformation. The images are then compared through a cross-correlation algorithm. In the data analysis step, subsets of pixels (small regions within the image) are tracked and matched between consecutive images. These pixel shifts are used to calculate the displacement field. The displacement data can then be used to derive strain fields by numerically differentiating

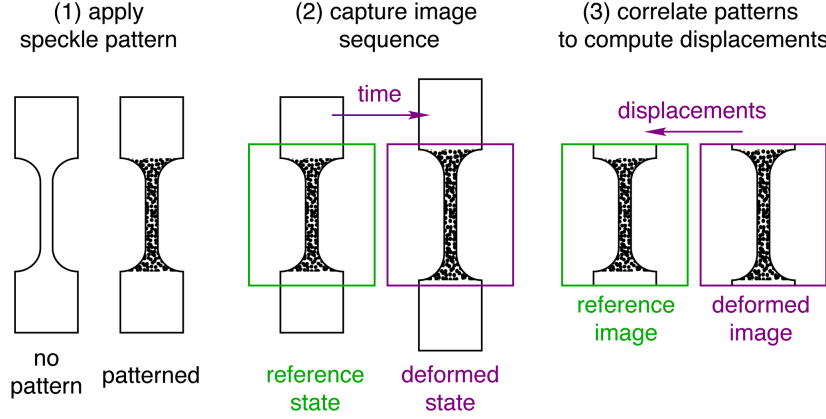


Figure A.1: Digital Image Correlation Process.

the displacement fields [35]. The strain tensor is generally obtained using the following formulation:

$$\varepsilon_{ij} = \frac{1}{2} \left(\frac{\partial u_i}{\partial x_j} + \frac{\partial u_j}{\partial x_i} \right)$$

where u_i and u_j are the displacements in the x_i and x_j directions, respectively, and ε_{ij} is the strain tensor.

This approach allows for accurate and comprehensive mapping of displacement and strain across the entire surface of the specimen, which is critical for understanding the material behavior under both uniform and non-uniform deformation conditions.

A.3. DIC in Tensile and Compression Testing

DIC is widely used in tensile and compression testing due to its ability to provide detailed full-field strain and displacement maps. In tensile tests, DIC allows for the visualization of local strain distributions and the evolution of deformation, which can help detect early signs of plasticity, necking, or fracture. The technique is particularly valuable for evaluating heterogeneous material responses, such as those seen in advanced alloys or composite materials, where localized deformation patterns often precede macroscopic failure. DIC can capture the initiation and progression of damage, providing critical insights into material behavior, such as strain localization, plastic zone development, and the eventual fracture point [29].

In compression tests, DIC is similarly beneficial for tracking the material response under

compressive loading conditions. It enables the detection of localized plastic flow, shear band formation, and buckling behavior, which are often difficult to observe with traditional techniques. Additionally, DIC can detect the formation of damage such as void nucleation, shear localization, and necking in materials under compression, making it a crucial tool for studying material failure under high stress states. In cases of localized deformation or when strain heterogeneities are present, DIC provides a more accurate and holistic view of the material's response than conventional strain gauges [18].

A.4. Advantages and Limitations

DIC offers several advantages over traditional experimental methods. One of its main strengths is the ability to provide full-field data over the entire surface of a specimen, as opposed to localized measurements from strain gauges. This makes DIC especially valuable for capturing non-uniform deformation and detecting localized failure modes that may be missed with traditional measurement techniques. Furthermore, DIC does not require physical contact with the specimen, which is beneficial when working with delicate, small, or fragile specimens that could be damaged by conventional gauges.

Another significant advantage is the capability to capture large deformation fields, making DIC highly suitable for studying both small and large strains. This is particularly beneficial in applications where material undergoes significant plastic deformation, as DIC can provide high spatial resolution even in the post-yield region [41]. Additionally, DIC is versatile and can be applied to a wide range of materials, including metals, polymers, and composites.

However, DIC also has some limitations. The accuracy of DIC measurements is sensitive to surface quality. The surface of the specimen must be carefully prepared to ensure that the speckle pattern is random and uniform. Surface imperfections such as scratches, coatings, or smooth regions may interfere with the speckle pattern and affect the quality of the data. Furthermore, proper lighting and camera calibration are essential to avoid errors in image analysis. Another limitation is the computational cost associated with processing large image datasets. Advanced image processing techniques and high-performance computing resources are often required to obtain precise and reliable results [29].

A.5. DIC for Strain and Displacement Calculation

The displacement fields obtained from DIC are directly related to the material behavior under loading. DIC provides displacement data at each point of the surface, which

can be used to compute strain fields. In tensile and compression testing, strain fields provide insight into how the material deforms across the specimen's surface. By differentiating the displacement field with respect to the coordinates, the strain tensor can be calculated, providing both normal and shear strain components. This data is vital for understanding complex material responses, especially in the case of anisotropic materials or heterogeneous microstructures [18].

Moreover, DIC allows for the accurate tracking of strain localization, a phenomenon often seen in necking during tensile tests or shear banding during compression. By accurately mapping strain fields, DIC can identify the precise location of strain concentration, which is crucial for predicting failure and assessing material ductility.

In compression tests, DIC helps in identifying the onset of plastic deformation, tracking shear bands, and understanding failure mechanisms such as buckling or crushing. These details are often difficult to assess with traditional methods, and DIC offers an unprecedented level of insight into the material's response to compressive forces [35].

B | Split-Hopkinson Pressure Bar

The Split Hopkinson Pressure Bar (SHPB), also known as the Kolsky bar, is one of the most widely used experimental techniques for measuring material behavior at high strain rates. This technique allows the study of materials under dynamic loading conditions, typically in the range of 10^2 to 10^4 s^{-1} , which is essential for simulating real-world applications like impact events, automotive crash testing, ballistic testing, and the response of materials during explosive loading.

The SHPB was first introduced by Kolsky in 1949 and remains an invaluable tool in experimental mechanics due to its versatility and effectiveness in characterizing materials under extreme deformation conditions. The SHPB is designed to generate a high-strain-rate load on a specimen, allowing researchers to measure the material's response to dynamic stress and strain. While it is predominantly used for metallic materials, the SHPB is also suitable for testing polymers, ceramics, and composite materials [26, 43].

The fundamental principle of the SHPB test is based on the propagation of stress waves through bars. When a specimen is subjected to a compressive force, the resulting stress wave travels through the specimen, interacting with the incident and transmission bars that are in contact with the specimen. By analyzing the incident, reflected, and transmitted stress waves, the true stress-strain response of the material can be calculated. This method allows for the determination of material properties such as yield strength, flow stress, and failure mechanisms under high-strain-rate loading [28].

B.1. Differences in SHPB Testing for Tensile and Compression Tests

While the Split Hopkinson Pressure Bar is widely used for testing materials under dynamic loading in both tension and compression, the experimental setup and the way the stress waves are generated differ significantly between the two test types.

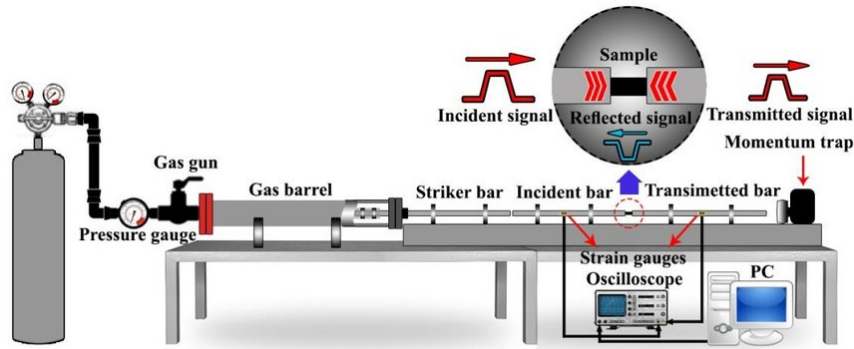


Figure B.1: Split Hopkinson Pressure Bar Schematics.

B.1.1. Compression Testing with the SHPB

In the typical compression configuration, the specimen is interposed between two cylindrical bars—the incident bar and the transmission bar. The specimen is subjected to a compressive force generated by a striker bar that impacts the incident bar, producing a compressive stress wave that propagates through the specimen and into the transmission bar. The stress wave is reflected at the specimen-bar interface, and a portion of it passes through the specimen to the transmission bar. Strain gauges placed on the incident and transmission bars measure the strain in these waves, from which the stress-strain data of the specimen can be derived [25, 26]. This configuration is straightforward and effective for materials under compression.

B.1.2. Tensile Testing with the SHPB

Tensile testing with the SHPB is more complex due to the need to induce a tensile stress state in the specimen. Typically, a special setup is used where the specimen is threaded or shaped (e.g., dog-bone geometry) to allow for the transmission of tensile forces. Unlike the compression configuration, in this case, the compression wave generated by the striker bar passes through the incident bar and reaches the specimen, but due to the setup, it results in a tensile wave being applied to the specimen after the reflection from the specimen ends. This setup allows the SHPB to generate a tensile stress in the specimen, which is critical for studying materials in tension under high strain rates.

Tensile testing often requires more careful specimen preparation, especially when using threads or geometrically complex shapes to ensure uniform stress distribution and avoid premature failure at localized points.

B.1.3. Material Behavior Under High Strain Rates

The SHPB is particularly effective in studying materials that exhibit different behaviors under tensile and compressive stress states. For instance, ductile materials, such as metals, typically show different strain-hardening characteristics under compression versus tension. In high strain-rate conditions, some materials such as titanium alloys and steels can exhibit substantial changes in yield stress and ductility when subjected to tension compared to compression [17, 32]. Similarly, polymers and composites may show different failure modes under dynamic tension and compression, making the SHPB essential for understanding these material behaviors.

B.1.4. Geometrical Considerations

A notable difference in SHPB testing for tension versus compression lies in specimen geometry. While cylindrical specimens are commonly used in compression tests, tensile tests require specimens with specific geometries, such as threaded or dog-bone shapes, to ensure the correct distribution of tensile forces. The geometry of the specimen must be carefully selected to prevent non-uniform stress distribution, which can lead to inaccurate data or premature failure. In compression testing, the stress state tends to be more uniform, but in tension tests, the geometry plays a more significant role in the outcome of the test. The specimen length-to-diameter (or length-to-width) ratio must be carefully considered to ensure one-dimensional stress conditions and avoid artifacts in the test data [28].

C | Convexity Algorithm of the GYS Model

The convexity of the GYS model is thoroughly discussed in [8], which covers convexity conditions, regions of convexity, and comparisons with other models. In this appendix, some of the key aspects are summarized. For a more rigorous and detailed analysis, the reader is encouraged to refer to the aforementioned article.

In plasticity analysis, convexity of the yield surface is a necessary condition for ensuring a unique solution. The requirement for yield surface convexity was first demonstrated by Drucker [15], who introduced the concept of stable plastic materials and stated that one of the key conditions for stability is that the yield surface must be convex. Moreover, a material that is stable in this context must satisfy the principle of maximum plastic resistance.

The principle of maximum plastic resistance, as described by Bower [6], can be expressed mathematically as the scalar product of the stress and plastic strain rate vectors:

$$(\sigma_{ij} - \sigma_{ij}^*) \cdot (d\varepsilon_{ij}^p) \geq 0 \quad (\text{C.1})$$

where σ_{ij}^* is the stress that just satisfies the yield criterion. Equation C.1 indicates that the angle between the vectors $(\sigma_{ij} - \sigma_{ij}^*)$ and $d\varepsilon_{ij}^p$ must be less than 90° for all stresses and strain rates. This condition holds true only when the yield surface is convex, and the plastic strain rate vector is normal to the yield surface.

A yield surface is considered convex if its curvature is non-negative everywhere on its surface. More formally, the curvature of the yield function in two mutually perpendicular directions in the tangent plane at any given point on the surface must be non-negative. Mathematically, this condition requires that the curvature tensor be positive definite.

In the context of plasticity analysis, for there to be a unique solution, the convexity of the yield surface is a critical requirement. There exists a condition, referred to as first

convexity condition, which when satisfied ensures convexity. This condition states:

$$c_1 + 18c_3 - 8c_2(\cos 3\theta) - 35c_3(\cos 3\theta)^2 \geq 0 \quad (\text{C.2})$$

It is expressed in terms of the GYS material coefficients (hardening parameters) c_1 , c_2 , and c_3 , as well as the Lode parameter $\cos 3\theta$. The GYS material coefficients are:

$$\sigma_{vm} = \sigma_y = \sigma_t \quad (\text{C.3})$$

$$c_1 + c_2 + c_3 = 1, \quad c_1 - c_2 + c_3 = \frac{\sigma_t}{\sigma_c}, \quad c_1 = \frac{\sigma_t}{\sqrt{3}\sigma_s} \quad (\text{C.4})$$

For the yield function to be convex, these parameters need to be restricted to a specific numerical range. To facilitate visualization, the GYS material coefficients c_1 , c_2 , and c_3 can also be expressed in terms of the ratio of pure-shear yield stress to uni-axial tension yield stress $\left(\frac{\sigma_s}{\sigma_t}\right)$ and the ratio of uni-axial compression yield stress to uni-axial tension yield stress $\left(\frac{\sigma_c}{\sigma_t}\right)$:

$$c_1 = \frac{1}{\frac{\sigma_s}{\sigma_t}\sqrt{3}}, \quad c_2 = \frac{1}{2} \left(1 - \frac{1}{\frac{\sigma_c}{\sigma_t}} \right), \quad c_3 = 1 - c_1 - c_2 \quad (\text{C.5})$$

$$c_3 = 1 - \frac{1}{\frac{\sigma_s}{\sigma_t}\sqrt{3}} - \frac{1}{2} \left(1 - \frac{1}{\frac{\sigma_c}{\sigma_t}} \right) = \frac{1}{2} - \frac{1}{\frac{\sigma_s}{\sigma_t}\sqrt{3}} + \frac{1}{\frac{\sigma_c}{\sigma_t}} \quad (\text{C.6})$$

The first convexity condition can thus be rewritten in terms of three parameters: the ratio of uni-axial compression yield to uni-axial tension yield $\left(\frac{\sigma_c}{\sigma_t}\right)$, the ratio of pure-shear yield to uni-axial tension yield $\left(\frac{\sigma_s}{\sigma_t}\right)$, and the Lode parameter $\cos 3\theta$:

$$\left(\frac{1}{\frac{\sigma_s}{\sigma_t}\sqrt{3}} \right) + 18 \left(\frac{1}{2} - \frac{1}{\frac{\sigma_s}{\sigma_t}\sqrt{3}} + \frac{1}{\frac{\sigma_c}{\sigma_t}} \right) - 4 \left(1 - \frac{1}{\frac{\sigma_c}{\sigma_t}} \right) (\cos 3\theta) - 35 \left(\frac{1}{2} - \frac{1}{\frac{\sigma_s}{\sigma_t}\sqrt{3}} + \frac{1}{\frac{\sigma_c}{\sigma_t}} \right) (\cos 3\theta)^2 \geq 0. \quad (\text{C.7})$$

D | Material Property Summary

The following is the Ti-6Al-4V 1/2-inch plate material property summary, as reported by Michael Pereira of the NASA John H. Glenn Research Center.

rev 12-16-11		draft summary 10-31-11		6Al-4V, Condition A, AMS-4911L		
Material number	Sheet/Plate Thickness	Material Supply Source	Ingot Source	Heat #	Rolling Source from Cert sheets	
4	0.50"	Titanium Industries	TIMET (Henderson, NV)	H13980	TIMET (Toronto, OH)	
Tensile Test Source	UTS- Long.	UTS- Trans.	0.2% Yield Long	0.2% Yield Transverse	% Elong. Long.	% Elong. Transverse
	ksi (mPa)	ksi (mPa)	ksi (mPa)	ksi (mPa)		
TIMET (Toronto, Ohio)	144-145 (993-1000)	150-150 (1034-1034)	133-133 (917-917)	139-139 (958-958)	18-18	18-18
	(~1050-1100)	(~1000-1050)				
[NASA-GRC chemical analysis in ()]						
Chemistry Analysis	Al	V	Fe	O	C	N
TIMET Henderson Process Lab	6.27 (6.64)	4.08 (4.04)	0.16 (0.13)	0.170 (0.190)	0.016 (0.011)	0.006 (0.006)

Figure D.1: Force-Displacement Result, Curve 16.

E | Vendor-Supplied Material Certifications

Titanium Industries, Inc.				Packing List			
Titanium Industries, Inc. 18 Green Pond Road, Rockaway, NJ 07866 Ship-To J. MICHAEL PEREIRA NASA GLENN RESEARCH CENTER, MS 49-8 2100 BROOKPARK ROAD CLEVELAND, OH 44135				Issued from Titanium Industries, Inc., Rockaway Service Center 18 Green Pond Road Rockaway, NJ 07866 Sold-To FAA WM. J. HUGHES TECHNICAL CENTER ATLANTIC CITY INTL AIRPORT, ATTN: DONALD ALTOBELLI(BLDG 202) ATLANTIC CITY, NJ 08405			
Packing List Cust/Ship to		11009-1 5770		Shipment Dt 4/23/2010			
Divy Mthd Carrier		Common Carrier C.H.ROBINSON		To Ref 261267867			
Item		Product		Vehicle No Trailer No			
Our Order		Your PO		credit card (4/20/2010)			
1-1 Titanium Plate 6AL-4V US Titanium Plate 0.500" x 36" x 48"		Ven Tag ID CRP 20447		Heat H13952-E10211			
Shp MI 2 0		Certificate Mill Test Cert		Tag 4233AA			
Lift 2		Pcs 2		LBS 283			
Total for the Shipment 1 Wood Skid (2)				Gross 345			
				Tare 62			
				Net (LBS) 283			
Inside Slip		Dan DiNapoli		(973) 983-6235			
Taken-by Slip		Dan DiNapoli		(973) 983-2573			
				(973) 983-2573			
				(973) 983-2573			

The contents of this order have been inspected by:

Customer copy



4/23/2010 03:38 PM 1


Titanium Industries, Inc.		Certificate of Analysis	
FAA WM. J. HUGHES TECHNICAL CENTER ATLANTIC CITY INT'L AIRPORT ATTN: DONALD ALTOBELLI(BLDG 292) ATLANTIC CITY, NJ 08405		Cert Number 1058 Test Reference 8740 4/23/2010	
Sold To: FAA WM. J. HUGHES TECHNICAL CENTER, ATLANTIC CITY INT'L AIRPORT, ATTN: DONALD ALTOBELLI(BLDG 292), ATLANTIC CITY, NJ 08405 Ship To: J. MICHAEL PEREIRA, NASA GLENN RESEARCH CENTER, MS 49-8, 2100 BROOKPARK ROAD, CLEVELAND, OH 44135		Issued from Titanium Industries, Inc. Rockaway Service Center 18 Green Pond Road Rockaway, NJ 07866	
Customer 57/0 Our Order 9811-1-1		Your Order Packing List	
Titanium Plate 6AL-4V US Titanium Plate 0.500" x 36" x 48"		Reference credit card (4/20/2010) 11009-1 (4/23/2010)	
Shipped Heats H13962-E10211 Conform To AMS-4911 8/28/2008		Product Information Heat H13962-E10211 Tag 4233AA Pcs 2 LBS 283	
Chemical Composition			
N	C	Fe	O
0.006	0.016	0.16	0.17
H		Al	
0.0085		6.27	
V		Y	
4.08		0.0004	
Physical Tests			
Tensile L	Tensile T	Yield L	Yield T
148 KSI	145 KSI	137 KSI	136 KSI
Elongation L		Elongation T	
16 %		16 %	
<p style="text-align: center;">CERTIFICATE OF COMPLIANCE</p> <p>ALL ITEMS FURNISHED ARE IN FULL COMPLIANCE WITH PURCHASE ORDER AND SPECIFICATION REQUIREMENTS LISTED. THE MATERIAL APPLIED DID NOT COME IN CONTACT WITH MERCURY NOR WAS ANY WELD REPAIR PERFORMED DURING PROCESSING BY TITANIUM INDUSTRIES, INC.</p> <p>THE MATERIAL SUPPLIED MEETS THE VISUAL AND DIMENSIONAL REQUIREMENTS OF THE PURCHASE ORDER AND TEST REPORTS/CERTIFICATIONS REPRESENT THE ACTUAL ATTRIBUTES OF THE ITEMS FURNISHED.</p> <p>AUTHORIZED SIGNATURE: <u><i>David Johnson</i></u> <u><i>4/23/10</i></u></p>			

The contents of this order have been inspected by:

Our Order 9811-1-1 Your Order credit card

Packing List 11009-1 (4/23/2010) Img No 7621 (4/23/2010)

		Titanium Metals Corporation 100 Titanium Way, Toronto, OH 43964 Telephone (740) 537-5694, Fax (740) 537-5653		Approved Certificate Page 1 of 3	
		CERT ID HI13980-A1X 26-FEB-2010 18:28:05 GMT		PURCHASE ORDER 20060408	
HEAT NUMBER HI13980		GRADE TIMETAL®6-4		SHIP TO CUSTOMER TIMET Service Center St. Louis 109 Interstate Drive, Wentzville, MO 63385	
TEST NUMBER E10225					
PRODUCT DESCRIPTION .500" SQ Plate					
DELIVERY CONDITION Annealed					
Specifications This material complies with the following specifications: AMS 4911 L					
Release Statements 1. TIMET-Toronto has a Quality Management System that is in compliance with ISO 9001:2000, ANSI/ISO/ASQ Q9001-2000 and AS 9100:2001 Revision B, Certificate No. UQA 0113328, through Lloyd's Register Quality Assurance, effective 24-Jul-03.					
Melt Method 3-VAR		Melt/Process Location TIMET - Henderson, NV, USA / TIMET - Toronto, OH, USA			
Compliance Statements 1. In accordance with AMS-T-9046 B cancellation notice, material is tested and certified to Table 1 superseding specification AMS 4911 Rev L. 2. Surface free from alpha case and product conforms to the other technical requirements of the referenced specification(s). 3. Microstructure examined and acceptable to the order specifications. 4. Immersion ultrasonic tested to a #3 FBH per AMS 2631 C Class A1 and acceptable. 5. Material meets the special flatness requirements of the purchase order. 6. TIMET-Toronto is an approved supplier of this product per DMS QPL 1592 Issue 18. Ingot melted in accordance with DMS 2442; TIMET-Henderson, NV, is an approved Ingot source per DMS QPL-2442 Issue 18.					
 Accredited Multiple Testing Laboratory ISO 9001:2000 Nondestructive Testing Heat Treating REGISTERED ISO 9001/AS9100 FACILITY		This test report shall not be reproduced except in full, without the written approval of TIMET. The intentional recording of false, fictitious, or fraudulent statements or entries on the certificate may be punished as a felony under federal law.			
First in Titanium Worldwide					

	Titanium Metals Corporation 100 Titanium Way, Toronto, OH 43964 Telephone (740) 537-5694, Fax (740) 537-5653	Approved Certificate Page 2 of 3
CERT ID H13980-A1X 26-FEB-2010 18:28:05 GMT	PURCHASE ORDER 20060408	SOLD TO CUSTOMER TIMET Service Center St. Louis 109 Interstate Drive, Wentzville, MO 63385

Ingot Chemical Analysis
(Weight percent)

Unless otherwise noted, Ingot Chemical Analysis performed at Henderson Process Lab, 181 N. Water Street, Henderson, NV, 89015, US

Sample ID	Fe	V	Al	C	O	N	Y
TOP	0.16	4.05	6.28	0.015	0.18	0.008	<0.0004
BOTTOM	0.15	4.00	6.25	0.016	0.19	0.007	<0.0004

Product Analysis
(Weight percent)

Unless otherwise noted, Product Analysis performed at Toronto Laboratory, 100 Titanium Way, Toronto, OH, 43964, US

Sample ID	H
1	46
2	69

Chemistry Statements

- Hydrogen values reported in PPM. Hydrogen determined by inert gas fusion per ASTM E1447. Carbon determined by combustion per ASTM E1941. Oxygen and Nitrogen determined by inert gas fusion per ASTM E1409. Henderson Melt: Metallics determined by Inductively Coupled Plasma-Atomic Emission Spectrometry (ICP-AES) per ASTM E2371. Morgantown Melt: Copper and Boron by atomic spectrometry (Ingot only) and all other elements by x-ray fluorescence spectrometry.
- Residual elements each less than 0.10% maximum, 0.40% maximum total.
- Balance titanium.

Mechanical Properties


Unless otherwise noted, testing performed at Toronto Laboratory, 100 Titanium Way, Toronto, OH, 43964, US

RTT - Longitudinal (ASTM E 8)
Test Condition: Mill VCF 8 Hours Minimum @ 1400°F

Sample ID	0.2YS ksi	U.T.S. ksi	4DEL %
1	133	144	18
2	133	145	18

RTT - Transverse (ASTM E 8)
Test Condition: Mill VCF 8 Hours Minimum @ 1400°F

Sample ID	0.2YS ksi	U.T.S. ksi	4DEL %
1	139	150	18
2	139	150	18




REGISTERED ISO 9001/AS9100 FACILITY

This test report shall not be reproduced except in full, without the written approval of TIMET.

The intentional recording of false, fictitious, or fraudulent statements or entries on the certificate may be punished as a felony under federal law.

First in Titanium Worldwide

	Titanium Metals Corporation 100 Titanium Way, Toronto, OH 43964 Telephone (740) 537-5694, Fax (740) 537-5653	Approved Certificate Page 3 of 3
CERT ID H13980-A1X 26-FEB-2010 18:28:05 GMT	PURCHASE ORDER 20060408	SOLD TO CUSTOMER TIMET Service Center St. Louis 109 Interstate Drive, Wentzville, MO 63385



Tests on Other Material


Unless otherwise noted, testing performed at Toronto Laboratory, 100 Titanium Way, Toronto, OH, 43964, US

Batch: H13550-31 (J9833)
 RTT - Longitudinal (ASTME 8)
 Test Condition: Periodic Test: Mill Annealed 60 Minutes 1400°F AC + Lab Annealed 20 Minutes @ 1325°F AC

Sample ID	0.2YS	U.T.S.	4DEL	R.A.
	ksi	ksi	%	%
1	126	137	15	31

Results are from TIMET Quality Control Records on file
 Sales Order # 273575 Item # 10
 v.1



 Bill Williamson - Certification Specialist



Accredited
Nadcap
190160 17025
Nondestructive Testing
Heat Treating

This test report shall not be reproduced except in full, without the written approval of TIMET.

The intentional recording of false, fictitious, or fraudulent statements or entries on the certificate may be punished as a felony under federal law

First in Titanium Worldwide

REGISTERED ISO 9001/AS9100 FACILITY



St. Louis Mill Sales
109 Interstate Drive
WENTZVILLE MO 63386
USA
Tel: 800-763-1550 Fax: 636-887-9088
Shipping Plant: St. Louis Service Center

Sold-to Address
Titanium Industries Inc
18 Green Pond Road
ROCKAWAY NJ 07866
USA

Attachment to Product Certification

Customer P.O. Number/Date
CRP-20447-KS/Feb 26, 2010
TIMET Sales Order Number/Date
281118/Feb 26, 2010
TIMET Packing List Number/Scheduled Ship Date
80417460/Apr 02, 2010

Ship-to Address
Titanium Industries Inc
18 Green Pond Road
ROCKAWAY NJ 07866
USA

TIMET Item #	Material #	Material Description	Quantity	Weight
Customer Item #	Customer Material #			
000010	110357	TIMETAL® 6-4 Titanium Aero Plate		
Heat Treatment		: Mill Annealed		
Specifications		: 01 AMS 4911 * L		
		: 02 AMS 2631 * C CL A1		
		: 03 AMS-STD-2154 TY1 CL A		
		: 04 AMS-T-9046 * A AB-1 COND A		
		: 05 ASTM B 265 * -09AE1 GR 6		
		: 08 DMS 1592 * G		
		: 09 MIL-STD-2154 ORG TY1 CL A		
		: 10 MIL-T-9046 J AMD2 AB-1 CD A		
Batch Number		: H13962-Y16	489.000LB	489.000LB
Batch Dimensions		: 0.500" X 48.000" X 120.000"		
Batch Number of Pieces		: 1.000		
Country of Origin		: USA		
Heat Number		: H13962		
Test Number		: E10211		
Batch Number		: H13980-Y03	489.000LB	489.000LB
Batch Dimensions		: 0.500" X 48.000" X 120.000"		
Batch Number of Pieces		: 1.000		
Country of Origin		: USA		
Heat Number		: H13980		
Test Number		: E10225		



St. Louis Mill Sales
109 Interstate Drive
WENTZVILLE MO 63386
USA
Tel: 800-753-1880 Fax: 636-867-9088
Shipping Plant: St. Louis Service Center

Sold-to Address
Titanium Industries Inc
18 Green Pond Road
ROCKAWAY NJ 07866
USA

Attachment to Product Certification
Customer P.O. Number/Date CRP-20447-KS/Feb 25, 2010
TIMET Sales Order Number/Date 281118/Feb 26, 2010
TIMET Packing List Number/Scheduled Ship Date 80417460/Apr 02, 2010

Ship-to Address
Titanium Industries Inc
18 Green Pond Road
ROCKAWAY NJ 07866
USA

TIMET Item #	Material #	Material Description	Quantity	Weight
	Customer Item #	Customer Material #		
B-Additional customer req				
GEAE S-400 Approved Laboratory				
GEAE S-1000 Supplier Quality Req'ts				
Beta Transus Temperature Reading Required				
PWA300				
MCL F-17/F-14 Controlled				
EN10204.3.1.				
Inspection tolerances are to LN8297				
Billing based on scale weight of gauge shown above				
Fax Copy of Bill of Lading, packing slip and test reports at time of shipment to TI Inds Inc Rockaway NJ Location Attn: K Speer - Fax# 973.983.8016 email: kspeer@titanium.com				
The following notes must appear on certificate of test:				
1. During manufacturing, handling, testing and inspection this material did not come in direct contact with mercury or any device employing a single boundary of containment.				
2. The recording of false, fictitious or fraudulent statements or entries may be punishable as a felony under federal statutes including federal law, title 18, chapter 47.				
3. No weld repair has been performed on this material				
4. Material has not been exposed to radioactive contamination.				
Melted and Manufactured in USA must appear on test report				
Amount is required quantity, do not short ship.				



St. Louis M/I Sales
109 Interstate Drive
WENTZVILLE MO 63386
USA
Tel: 800-753-1860 Fax: 636-887-8088
Shipping Plant St. Louis Service Center

Sold-to Address
Titanium Industries Inc
18 Green Pond Road
ROCKAWAY NJ 07866
USA

Attachment to Product Certification
Customer P.O. Number/Date CRP-20447-KS/Feb 26, 2010
TIMET Sales Order Number/Date 281118/Feb 26, 2010
TIMET Packing List Number/Scheduled Ship Date 80417460/Apr 02, 2010

Ship-to Address
Titanium Industries Inc
18 Green Pond Road
ROCKAWAY NJ 07866
USA

TIMET Item #	Material #	Material Description	Quantity	Weight
Customer Item #	Customer Material #			

Results are from TIMET Quality Control Records on file. The undersigned has verified that the information on the attached mill product certification meets the requirements of the above referenced order. This Attachment to Product Certification is specific to your referenced order, is an integral part of and amends the physical and chemical test reports attached. All specification(s) and revision(s) that differ from the attached have been approved for inclusion by the producing facility.

Authorized TIMET Signature

Kennoth Renshaw
Kennoth Renshaw
NASC Quality Supervisor

Date MAR 8 1 2010

List of Figures

1	Fan blade-off test of the Trent XWB.	2
1.1	Airbus A350 XWB.	5
1.2	Rolls-Royce Trent 900 fan blades.	7
2.1	MAT_224_GYS Model Definition.	14
2.2	Standard tensile test.	17
2.3	LS-DYNA input deck of a piecewise liner plasticity material model of a typical test result.	18
2.4	The necking judgment line and stress-strain curve.	22
2.5	Plastic strain versus stress extrapolation curves.	23
2.6	Candidate material plastic strain versus stress curves for tensile test simu- lation.	24
2.7	Von Mises stress contour of simulated tensile test.	24
2.8	Force-displacement results from tensile test simulation.	25
2.9	Strain comparison in the load direction at Room Temperature.	25
2.10	Plastic strain-stress relationship of rolled Ti-6Al-4V sheet under different strain rates.	27
2.11	Length of uniformly deformed material significantly shortens post-necking.	28
2.12	Strain-Rate sensitivity curve in tension.	30
2.13	Strain-Rate sensitivity curve in compression.	31
3.1	Temperature Effect for Tension tests.	37
3.2	Temperature Effect for Compression tests.	38
3.3	True stress-strain relationship and necking point judgment.	39
3.4	Plastic strain versus stress extrapolation curves.	39
3.5	Force-Displacement Result, Curve 8.	40
3.6	Selected Stress-Strain input curve.	41
3.7	Strain comparison in the load direction at Room Temperature.	41
3.8	Selected Stress-Strain input curves.	42
3.9	Force-Displacement Result for T2, Curve 20.	43

3.10	Force-Displacement Result for T3, Curve 13.	43
3.11	Force-Displacement Result for T4, Curve 19.	44
3.12	Force-Displacement Result for T5, Curve 18.	44
3.13	Strain comparison in the load direction at 200° C.	45
3.14	Strain comparison in the load direction at 400° C.	45
3.15	Strain comparison in the load direction at 600° C.	45
3.16	Engineering and True Stress-Strain Relationship.	46
3.17	Plastic strain versus stress extrapolation curves.	47
3.18	Force-Displacement Result, Curve 16.	47
3.19	Selected Stress-Strain input curve.	48
3.20	Strain comparison in the load direction at Room Temperature.	48
3.21	Selected Stress-Strain input curves.	49
3.22	Force-Displacement Result for T2, Curve 16.	50
3.23	Force-Displacement Result for T3, Curve 16.	50
3.24	Force-Displacement Result for T4, Curve 16.	51
3.25	Force-Displacement Result for T5, Curve 16.	51
3.26	True stress-strain relationship and necking point judgment.	53
3.27	Plastic strain versus stress extrapolation curves.	54
3.28	Force-Displacement Result, Curve 16.	55
3.29	Strain comparison in the load direction.	55
3.30	Force-Displacement Result, Curve 16.	56
3.31	Strain comparison in the load direction.	57
3.32	Strain-Rate sensitivity curve in tension.	59
3.33	Strain-Rate sensitivity curve in compression.	59
3.34	Test M2-TMT-P4-SG1-O1-SR4-T1-N4.	61
3.35	M2-TMT-P4-SG1-O1-SR4-T1-N4 Strain comparison.	62
3.36	M2-TMT-P4-SG1-O1-SR4-T1-N4 Temperature comparison.	62
3.37	Test M2-TMT-P4-SG1-O1-SR4-T1-N5.	63
3.38	M2-TMT-P4-SG1-O1-SR4-T1-N5 Strain comparison.	64
3.39	M2-TMT-P4-SG1-O1-SR4-T1-N5 Temperature comparison.	64
3.40	Test M2-TMT-P4-SG1-O1-SR4-T1-N6.	65
3.41	Test M2-TMT-P4-SG1-O1-SR4-T1-N7.	66
3.42	Test M2-TMT-P4-SG1-O1-SR5-T1-N4.	67
3.43	M2-TMT-P4-SG1-O1-SR5-T1-N4 Strain comparison.	68
3.44	M2-TMT-P4-SG1-O1-SR5-T1-N4 Temperature comparison.	68
3.45	Test M2-TMT-P4-SG1-O1-SR5-T1-N6.	69
3.46	M2-TMT-P4-SG1-O1-SR5-T1-N6 Strain comparison.	70

3.47	M2-TMT-P4-SG1-O1-SR5-T1-N6 Temperature comparison.	70
3.48	Test M2-TMT-P4-SG1-O1-SR5-T1-N8.	71
3.49	Test M2-TMT-P4-SG1-O1-SR5-T1-N9.	72
3.50	Test M2-TMC-P4-SG1-O1-SR4-T1-N1.	73
3.51	M2-TMC-P4-SG1-O1-SR4-T1-N1 Strain comparison.	74
3.52	Test M2-TMC-P4-SG1-O1-SR4-T1-N2.	74
3.53	Test M2-TMC-P4-SG1-O1-SR4-T1-N3.	75
3.54	Test M2-TMC-P4-SG1-O1-SR5-T1-N2.	76
3.55	Test M2-TMC-P4-SG1-O1-SR5-T1-N3.	77
3.56	M2-TMC-P4-SG1-O1-SR5-T1-N3 Strain comparison.	77
3.57	Test M2-TMC-P4-SG1-O1-SR5-T1-N5.	78
3.58	Test M2-TMC-P4-SG1-O1-SR6-T1-N2.	79
3.59	Test M2-TMC-P4-SG1-O1-SR6-T1-N3.	80
3.60	Test M2-TMC-P4-SG1-O1-SR6-T1-N4.	81
3.61	M2-TMC-P4-SG1-O1-SR6-T1-N4 Strain comparison.	81
4.1	Example stress states from various material tests.	85
4.2	Commonly defined stress states.	86
4.3	Control points of the three-dimensional splines.	86
4.4	Additional control points created from the 3D splines.	87
4.5	Failure surface generated by MATLAB subroutine.	88
4.6	Discretized 3D failure surface.	88
5.1	Geometry of specimen SG1.	90
5.2	Meshed model of specimen SG1 showing rigid solid elements (gray) and titanium elements (white).	91
5.3	Geometry of specimen SG2.	91
5.4	Meshed model of specimen SG2 showing rigid solid elements (gray) and titanium elements (white).	91
5.5	Geometry of specimen SG3.	92
5.6	Meshed model of specimen SG3 showing rigid solid elements (gray) and titanium elements (white).	92
5.7	Geometry of specimen SG4.	93
5.8	Meshed model of specimen SG4 showing rigid solid elements (gray) and titanium elements (white).	93
5.9	Geometry of specimen SG5.	93
5.10	Meshed model of specimen SG5 showing rigid solid elements (gray) and titanium elements (white).	94

5.11 Geometry of specimen SG6.	94
5.12 Meshed model of specimen SG6 showing rigid solid elements (gray) and titanium elements (white).	94
5.13 Geometry of specimen SG7.	95
5.14 Meshed model of specimen SG7 showing rigid solid elements (gray) and titanium elements (white).	95
5.15 Geometry of specimen SG8.	95
5.16 Meshed model of specimen SG8 showing rigid solid elements (gray) and titanium elements (white).	96
5.17 Geometry of specimen SG9.	96
5.18 Meshed model of specimen SG9 showing rigid solid elements (gray) and titanium elements (white).	96
5.19 Geometry of specimen SG10.	97
5.20 Meshed model of specimen SG10 showing rigid solid elements (gray) and titanium elements (white).	97
5.21 Geometry of specimen SG11.	98
5.22 Meshed model of specimen SG11 showing rigid solid elements (gray) and titanium elements (white).	98
5.23 Geometry of specimen SG12.	99
5.24 Meshed model of specimen SG12 showing rigid solid elements (gray) and titanium elements (white).	99
5.25 Geometry of specimen SG13.	100
5.26 Meshed model of specimen SG13 showing rigid solid elements (gray) and titanium elements (white).	100
5.27 Geometry of the LR1, LR2, and LR3 specimen.	100
5.28 Tension/torsion combined finite element mesh.	101
5.29 Geometry of the LR4 and LR5 specimen.	102
5.30 Compression/torsion combined finite element mesh.	102
5.31 Unbacked test mesh, unbacked plate (left), and punch (right).	103
5.32 Backed test mesh, thick plate (left), and punch (right).	105
5.33 Force-Displacement comparison.	110
5.34 SG1 Strain comparison.	111
5.35 SG2 Strain comparison.	111
5.36 SG3 Strain comparison.	111
5.37 SG4 Strain comparison.	112
5.38 SG5 Strain comparison.	112
5.39 SG6 Strain comparison.	112

5.40	SG7 Strain comparison.	113
5.41	SG8 Strain comparison.	113
5.42	SG9 Strain comparison.	113
5.43	SG10 Strain comparison.	114
5.44	SG11 Strain comparison.	114
5.45	SG12 Strain comparison.	114
5.46	SG13 Strain comparison.	115
5.47	Unbacked Test Strain Comparison.	115
5.49	Red spot denoting selected elements for stress state evaluation.	117
5.51	Triaxiality and lode parameter for each specimen's selected element.	119
5.52	Final failure surface obtained after refinement of input parameters.	121
5.53	Force-Displacement comparison.	127
5.54	Input yield curves for each temperature.	128
5.55	Force-Displacement plots with scaling function for each Temperature.	130
5.56	Strain rate input curves.	131
5.57	Final force-displacement curves plotted against physical test data for (a) SR3, (b) SR4, and (c) SR5.	132
5.58	Element configuration with 0.10 mm mesh (557,856 elements).	133
5.59	Element configuration with 0.20 mm mesh (73,184 elements).	134
5.60	Element configuration with 0.40 mm mesh (8088 elements).	134
5.61	Comparison of force-displacement plots for mesh sizes of 0.10 mm, 0.20 mm, and 0.40 mm.	135
6.1	Geometric dimensions of the plate (in inches).	138
6.2	Clamp Fixture Assembly.	138
6.3	Orientation of the finite element model.	139
6.4	Mesh configuration of the projectile.	139
6.5	Finite Element Simulation of Ballistic Test.	140
A.1	Digital Image Correlation Process.	148
B.1	Split Hopkinson Pressure Bar Schematics.	152
D.1	Force-Displacement Result, Curve 16.	157

List of Tables

2.1	Taylor-Quinney Coefficient Curve.	32
3.1	Material Mechanical Properties.	33
3.2	Material Chemical Composition.	33
3.3	Tension temperature tests series provided by OSU.	34
3.4	Compression strain rate tests series provided by OSU.	34
3.5	Tension strain rate tests series provided by OSU.	35
3.6	Compression temperature tests series provided by OSU.	36
3.7	Tension Tests at strain rate 10^{-4} s^{-1}	52
3.8	Compression Tests at strain rate 10^{-4} s^{-1}	56
5.1	Punch dimensions.	102
5.2	0.072' Backed Test dimensions.	104
5.3	0.05' Backed Test dimensions.	104
5.4	0.035' Backed Test dimensions.	104
5.5	Computed Triaxiality, Lode Parameter, and Fracture Strain for Test Specimens.	120
5.6	Control point iterations and adjustments for each specimen.	122
5.7	Scaling factors by temperature.	129
5.8	Scaling factors for varying strain rates.	132
5.9	Scaling factors by mesh size.	135
6.1	Projectile Penetration Velocity for the Panel Impact Tests.	138
6.2	Impact and exit velocities from the experimental tests.	139

List of Symbols

Variable	Description	SI unit
β	Taylor-Quinney Coefficient	-
ε	Real Strain	-
ε_p	Plastic Strain	-
ε_p^{eff}	Effective Plastic Strain	-
ε_{eng}	Engineering Strain	-
$\dot{\varepsilon}$	Strain Rate	1/sec
σ	Real Stress	MPa
σ_{eng}	Real Stress	MPa
σ_{vm}	Real Stress	MPa
σ_y	Yield Stress	MPa
$\sigma_1, \sigma_2, \sigma_3$	Principal Stress	MPa
τ	Triaxiality	-
D	Damage Parameter	-
L	Lode Parameter	-
T	Temperature	K / °C
T_H	Homologous Temperature	K / °C
T_{melt}	Melting Temperature	K / °C
T_{ref}	Reference Temperature	K / °C

List of Abbreviations

Abbreviation	Description
ACFPR	Aircraft Catastrophic Failure Prevention Research Program
CAD	Computer-Aided Design
CFRP	Carbon Fiber Reinforced Plastics
DIC	Digital Image Correlation
FAA	Federal Aviation Administration
GMU	George Mason University
GRC	Glenn Research Center
GYS	Generalized Yield Surface
J2	Second Stress Tensor Invariant
J3	Third Stress Tensor Invariant
NASA	National Aeronautics and Space Administration
OSU	Ohio State University
SHB	Split-Hopkinson Bar
Ti64	Ti-6Al-4V
TQC	Taylor-Quinney Coefficient
XWB	Extra Wide Body

Acknowledgments

Arrivato alla conclusione di questo percorso universitario e al completamento del lavoro di tesi sono tante le persone a cui sento di dover dire grazie.

Al Prof. Marco Anghileri, per la straordinaria opportunità concessami di svolgere la tesi oltreoceano.

Al Prof. Cing-Dao Kan ed a tutto il Center for Collision Safety and Analysis (CCSA) alla George Mason University, per avermi accolto ed avermi consentito di crescere professionalmente e umanamente.

Al Prof. Stefano Dolci, per il continuo supporto e il preziosissimo aiuto nello svolgere il lavoro di tesi, per tutti i consigli e gli incoraggiamenti, ma soprattutto per avermi trattato come un amico. Le sarò sempre riconoscente per tutto ciò che ha fatto per me.

A Luca ed Alessandro, per aver condiviso quest'esperienza con me. Avervi al mio fianco mi ha aiutato nei momenti più difficili e vi auguro il successo che meritate da brillanti ingegneri quali siete.

Ai miei genitori Alba e Rodolfo. Queste poche righe non possono bastare ad esprimere tutta la mia gratitudine e riconoscenza nei vostri confronti. Mi avete sempre sostenuto ed incoraggiato in qualsiasi idea, sogno o aspirazione che avessi. Avete creduto in me fermamente, insegnandomi a non accontentarmi e a non pormi limiti. Mi avete dato la possibilità di sognare e ambire ai traguardi più alti. Questo risultato e tutti gli altri che raggiungerò sono solo vostri e spero un giorno di poter dare ai miei figli tutte le opportunità che voi avete dato a me.

A Riccardo, per il meraviglioso fratello che sei. Sei per me l'unica persona con cui posso davvero confidarmi, che mi conosce alla perfezione e che sa darmi sempre i giusti consigli. Grazie per il modo in cui sai ascoltarmi, per le mille volte in cui mi hai incoraggiato in questi anni, per come sei in grado di farmi riflettere. Sei senza dubbio una persona fuori dall'ordinario, con una sensibilità ed un'intelligenza fuori dal comune. Sei per me la persona più importante al mondo e so che ci sarò sempre per te.

A tutta la famiglia, zii e cugini, per tutto il supporto che sapete darmi e il vostro esempio

che mi sprona a fare sempre meglio.

Ai miei amici *di giù*, con cui sono cresciuto e ho fatto le prime esperienze di vita. Siete per me un porto sicuro dove trovare rifugio e sostegno indipendentemente dai chilometri di distanza e so di poter contare su di voi per sempre.

Ai miei amici di Milano, i coinquilini e gli amici dell'università, per gli incredibili anni trascorsi insieme e i bellissimi ricordi che ci accompagneranno per sempre. Avete reso questo difficile percorso un bellissimo viaggio.

A tutti gli amici conosciuti in Francia e negli US, per aver condiviso le esperienze più belle della mia vita, arricchendole ancor di più e rendendole tali.

A tutte le persone che mi hanno aiutato e sostenuto in questi anni, a quelle che mi hanno fatto riflettere e crescere come persona, a tutte quelle che sono entrate ed uscite dalla mia vita.

A chi ho dimenticato di ringraziare.